
Engineering a 3D ultrasound system for image-guided vascular modelling

Steven James Hammer



A thesis submitted for the degree of Doctor of Philosophy.
The University of Edinburgh.
May 2008

Abstract

Atherosclerosis is often diagnosed using an ultrasound (US) examination in the carotid and femoral arteries and the abdominal aorta. A decision to operate requires two measures of disease severity: the degree of stenosis measured using B-mode US; and the blood flow patterns in the artery measured using spectral Doppler US. However other biomechanical factors such as wall shear stress (WSS) and areas of flow recirculation are also important in disease development and rupture. These are estimated using an image-guided modelling approach, where a three-dimensional computational mesh of the artery is simulated.

To generate a patient-specific arterial 3D computational mesh, a 3D ultrasound (3DUS) system was developed. This system uses a standard clinical US scanner with an optical position sensor to measure the position of the transducer; a video capture card to record video images from the scanner; and a PC running Stradwin software to reconstruct 3DUS data. The system was characterised using an industry-standard set of calibration phantoms, giving a reconstruction accuracy of ± 0.17 mm with a 12 MHz linear array transducer. Artery movements from pulsatile flow were reduced using a retrospective gating technique. The effect of pressure applied to the transducer moving and deforming the artery was reduced using an image-based rigid registration technique.

The artery lumen found on each 3DUS image was segmented using a semi-automatic segmentation technique known as ShIRT (the Sheffield Image Registration Toolkit). Arterial scans from healthy volunteers and patients with diagnosed arterial disease were segmented using the technique. The accuracy of the semi-automatic technique was assessed by comparing it to manual segmentation of each artery using a set of segmentation metrics. The mean accuracy of the semi-automatic technique ranged from 85% to 99% and depended on the quality of the images and the complexity of the shape of the lumen.

Patient-specific 3D computational artery meshes were created using ShIRT. An idealised mesh was created using key features of the segmented 3DUS scan. This was registered and deformed to the rest of the segmented dataset, producing a mesh that represents the shape of the artery. Meshes created using ShIRT were compared to meshes created using the Rhino solid modelling package. ShIRT produced smoother meshes; Rhino reproduced the shape of arterial disease more accurately. The use of 3DUS with image-guided modelling has the potential to be an effective tool in the diagnosis of atherosclerosis. Simulations using these data reflect in vivo studies of wall shear stress and recirculation in diseased arteries and are comparable with results in the literature created using MRI and other 3DUS systems.

Declaration of originality

I hereby declare that the research recorded in this thesis and the thesis itself was composed and originated entirely by myself in the Department of Medical Physics at The University of Edinburgh.

Exceptions:

- The initial design of a transducer holder for the phantom scanner presented in chapter 2
- The development of an algorithm to measure the curvature of an artery centreline in chapter 4
- CFD simulations described in chapter 7
- Creation of idealised artery geometries for registration-based artery mesh creation in chapter 7
- Creation of a diseased artery geometry using ShIRT in chapter 7

Steven James Hammer

Acknowledgements

Having spent so long on preparing this thesis and working at Medical Physics at the University of Edinburgh, I realise that I've met a lot of amazing people and learned a lot from getting to know them. I'll start from the bottom up.

Many thanks to all the volunteers who participated in my research study. They taught me a lot about the human side of disease: the development of new technology to diagnose disease isn't just about biological phenomena that happen in a test tube in a lab, but it affects people's quality of life and ultimately their lifespan. It was a humbling experience to learn about this.

Thanks to Irene in Medical Physics for scan bran cake, sympathy, sarcasm, and fantastic secretarial support. Thanks to Wilma, the secretary at Radiology, and Janice, the secretary at the Vascular Lab, for all the time spent looking for patients and sending them invitation forms for my study, and time spent organising room bookings amidst everything else that they do. Thanks go to Kev and George in the SEE workshops for interpreting my drawings and making things that were more or less what I wanted.

Thanks to Sarah-Jane, Karen, Scott and Maggie in the Vascular Lab for showing me how patients are supposed to be scanned using ultrasound. Thanks also to Paul Allan in Radiology for the time spent sorting out ethics applications and other challenges that appear when dealing with research in a hospital setting.

Many thanks to my collaborators from The University of Sheffield (Rod Hose, David Barber and Adam Jeays) for providing their segmentation and registration software. Thanks also to Tom MacGillivray for his image processing advice and software. Thanks also to Richard Prager, Graham Treece and Andrew Gee at the University of Cambridge for providing software and technical support.

Thanks to my (former) colleagues in the wider project for their support and enlightenment in my time at Medical Physics: Tom Anderson, Norman McDicken, Kate Fraser, Siobhan Meagher, Michael Bennett, Mairead Butler, James Blake, Pavel Stroeve, Jason Beech-Brandt, Chaoquan Chen, Judith Dineley, Tamie Poepping and William Lee.

Thanks are due to my supervisors, Peter Hoskins and Bill Easson, for seeing the potential that

I had and encouraging me to stretch myself and persevere.

Thanks to Jocelyn, Ben and (eventually) Ian for putting up with me talking about arteries and taking work home with me. Thanks for your patience.

Finally, a quote:

Natural perspicacity is a gift of God, and the liberal arts and the sciences, by which wisdom is acquired, are gifts of God...They must occupy the place of handmaid, not of mistress.

John Calvin, Cor. I:145

I hope that my work has demonstrated the exercise of one of these gifts of God. I praise Him for the skill and knowledge He has given me through this work, and the opportunity to contribute a little bit to our knowledge of 3D ultrasound.

Contents

Declaration of originality	iii
Acknowledgements	iv
Contents	vi
List of figures	xii
List of tables	xvii
Acronyms and abbreviations	xix
1 Introduction	1
1.1 Cardiovascular disease	1
1.1.1 Summary	2
1.2 The treatment of cardiovascular disease	2
1.2.1 Summary	4
1.3 The diagnosis of cardiovascular disease	4
1.3.1 Imaging cardiovascular disease	4
1.3.2 Assessing the severity of cardiovascular disease	6
1.3.3 Summary	8
1.4 Ultrasound imaging of arterial disease	8
1.4.1 The physics of ultrasound imaging	9
1.4.2 Ultrasound image processing	17
1.4.3 3D ultrasound imaging	17
1.4.4 Summary	20
1.5 The biomechanics of arterial disease	21
1.5.1 Summary	22
1.6 Modelling arterial disease using image-guided modelling	22
1.6.1 Summary	24
1.7 Critical analysis	24
1.8 Aim	24
1.9 Thesis outline	24
2 Mechanical 3D ultrasound for <i>in-vitro</i> flow models	26
2.1 Introduction	26
2.2 Materials & methods	27
2.2.1 Phantom scanning system	27
2.2.2 Ultrasound system	30
2.2.3 Data capture and display	30
2.2.4 ECG gating	31
2.2.5 Operation	31
2.3 Results	34
2.4 Discussion	36
2.5 Conclusion	37
3 Characterisation of a 3D freehand ultrasound system	38
3.1 Introduction	38

3.2	Methods	41
3.2.1	3D US system	41
3.2.2	Assessing whole system accuracy (3D reconstruction accuracy) using a test phantom	42
3.2.3	Assessing calibration precision	52
3.2.4	Assessing precision of optical tool and transducer holder replacement	54
3.3	Results	59
3.3.1	Reconstruction accuracy	59
3.3.2	Calibration Precision	59
3.3.3	Optical tool and transducer holder replacement precision	61
3.4	Discussion	61
3.4.1	Assessment of whole system reconstruction accuracy	61
3.4.2	Assessment of calibration precision	61
3.4.3	Replacement precision	62
3.4.4	Whole system characterisation	62
3.5	Conclusion	62
4	An analysis of probe pressure correction using Stradwin	64
4.1	Introduction	64
4.2	Methods	67
4.2.1	Lofting registered and unregistered surfaces in Rhino	67
4.2.2	Measuring arterial curvature	68
4.2.3	Assessing the effect of registration using a statistical test	70
4.3	Results	70
4.3.1	Graphically assessing the effect of registration on lofted artery surface models	70
4.3.2	Summary of changes in curvature	76
4.3.3	Statistical test results	76
4.4	Discussion	77
4.4.1	Corrugated surface models	77
4.4.2	Statistical test results	78
4.5	Conclusion	81
5	Gating ultrasound data	82
5.1	Introduction	82
5.2	Methods	83
5.2.1	Scanning straight phantoms to assess variation in gating methods and scanning mode	83
5.2.2	Measuring phantom area using thresholding	84
5.2.3	Retrospective gating using Stradx	85
5.2.4	Statistical Analysis	89
5.3	Results	90
5.3.1	Straight phantom areas	90
5.3.2	Summaries of the data	90
5.3.3	Statistical test results	94
5.4	Discussion	94
5.4.1	Statistical analysis of area with and without SonoCT compounding	94

5.4.2	Statistical analysis of retrospective and ECG gating	95
5.5	Conclusion	96
6	Segmentation of 3D ultrasound data	98
6.1	Introduction	98
6.2	Methods	99
6.2.1	Methods to measure the accuracy and precision of segmentation techniques	100
6.2.2	Assessing the precision of ShIRT	107
6.2.3	Comparing ShIRT to a set of intraobserver segmentations	108
6.2.4	Assessing the accuracy of ShIRT on full artery scans	110
6.3	Results	117
6.3.1	Assessing the precision of ShIRT	117
6.3.2	Comparing ShIRT to a set of intraobserver segmentations	119
6.3.3	Assessing the accuracy of ShIRT on full artery scans	122
6.4	Discussion	129
6.4.1	Assessing the precision of ShIRT	129
6.4.2	Comparing ShIRT to a set of intraobserver segmentations	129
6.4.3	Assessing the accuracy of ShIRT on full artery scans	130
6.4.4	How appropriate is ShIRT for use with ultrasound data?	130
6.5	Conclusion	132
7	Image-guided flow modelling of patient-specific artery geometries	133
7.1	Introduction	133
7.2	Methods	134
7.2.1	Artery geometry creation	134
7.2.2	Simulating flow patterns and wall shear stress	142
7.3	Results	146
7.3.1	Assessing the realism of artery models	146
7.3.2	Simulating flow patterns and wall shear stress	155
7.4	Discussion	163
7.5	Conclusion	164
8	Evaluation of arterial wall motion software	165
8.1	Introduction	165
8.2	Wall motion phantom design	166
8.2.1	Wall motion phantom assembly	166
8.2.2	Wall position	169
8.2.3	Generating wall motion waveforms	170
8.2.4	Removal of stepper motor interference	171
8.2.5	Assessment of wall motion phantom accuracy	174
8.2.6	TDI-based wall motion software assessment	174
8.3	Results	179
8.3.1	Wall motion phantom accuracy	179
8.3.2	Measurement accuracy using a range of physiological wall motions	179
8.3.3	Minimum resolvable displacement	180
8.3.4	Change in accuracy with change in wall velocity	181

8.4	Discussion	182
8.4.1	Assessment of wall motion test phantom	182
8.4.2	Assessment of wall motion software	183
8.4.3	Conclusion	186
9	Critically evaluating the 3D ultrasound system for image-guided modelling	187
9.1	Introduction	187
9.2	Comparisons with other IGM work	187
9.2.1	3DUS acquisition system	188
9.2.2	Creating patient-specific artery geometries	190
9.2.3	CFD simulations based on 3DUS data	191
9.2.4	Summary	192
9.3	Evaluating 3DUS imaging in healthy and diseased arteries	192
9.3.1	3DUS imaging of the carotid artery	193
9.3.2	3DUS imaging of the femoral artery	194
9.3.3	3DUS imaging of the abdominal aorta	196
9.3.4	Successful arterial 3DUS scanning	198
9.4	Computational modelling of arteries	199
9.4.1	Summary	199
9.5	Conclusion	200
10	Conclusions	201
A	Papers and conference presentations	203
A.1	Papers and published conference proceedings	203
A.2	Conference presentations and posters	203
B	Manually segmenting ultrasound data using Analyze	205
B.1	Write all Stradwin images to a sequence of bitmap files	206
B.2	Load the images into Analyze	206
B.3	Create an Object Map	209
B.4	Use the spline tool to outline the lumen	210
B.5	Save the Object Map as a series of bitmap images	211
B.6	Convert the bitmap images to a Stradwin image file	212
B.7	Threshold the images in Stradwin to produce spatially registered 3D contours	212
C	Generating a Stradwin image file from a series of bitmap graphics files	214
C.1	Save a series of sequentially-numbered bitmaps	214
C.2	Renumber the images if required using XnView	214
C.3	Run BMP2SXIarray.vi to create a Stradwin image file	215
C.4	Modify the Stradwin header file (.sw) to suit the new image file.	216
D	Development of surface models of bifurcating arteries using Rhino	217
D.1	Introduction	217
D.2	Importing segmented points into Rhino	217
D.3	Rebuilding the segmented contours	219
D.4	Removing misregistered contours	220
D.5	Lofting the CCA/ICA/ECA	221

D.6	Filling the bifurcation area	222
D.6.1	Extracting wireframes from the lofted artery sections	222
D.6.2	Connecting wireframes using interpolated curves	222
D.6.3	Creating a network surface between the upper part of the CCA and the ECA/ICA	224
D.6.4	Splitting the bifurcation segments	226
D.6.5	Creating a smoothed bifurcation surface	226
D.6.6	Splitting and joining the bifurcation surfaces	231
D.6.7	Tidying and checking the mesh	232
D.6.8	Joining all the surfaces	233
D.7	Meshing the geometry and exporting it to STL	233
E	Remeshing STL files with Materialise Magics	235
E.1	Create a solid model in Rhino and export it as an STL file	235
E.2	Load the STL file into Magics	235
E.3	Automatic fixing with the Fix Wizard	236
E.4	Slice the outlets and/or inlets parallel to the vessel centreline	237
E.5	Remesh operations	237
E.6	Save remeshed file	241
F	Software documentation	242
F.1	Introduction	242
F.2	BMP2SXIarray.vi	242
F.2.1	Connector Pane	243
F.2.2	Front Panel	243
F.2.3	List of SubVIs and Express VIs	243
F.3	SW threshold and segment images SM.vi	244
F.3.1	Connector Pane	244
F.3.2	Front Panel	245
F.3.3	List of SubVIs and Express VIs	245
F.4	SW create OBJ file from segmented file.vi	249
F.4.1	Connector Pane	250
F.4.2	Front Panel	250
F.4.3	List of SubVIs and Express VIs	250
F.5	SW gate to sxp peaks.vi	251
F.5.1	Connector Pane	251
F.5.2	Front Panel	252
F.5.3	List of SubVIs and Express VIs	252
F.6	SW_SelectSW.vi	255
F.6.1	Connector Pane	255
F.6.2	Front Panel	256
F.6.3	List of SubVIs and Express VIs	256
F.7	state demo with fake physio.vi	258
F.7.1	Connector Pane	258
F.7.2	Front Panel	259
F.7.3	List of SubVIs and Express VIs	259
F.8	SW evaluate segmentation with Udupa methods using BMPs.vi	260

F.8.1	Connector Pane	261
F.8.2	Front Panel	261
F.8.3	List of SubVIs and Express VIs	261
F.9	calculate Udupa interobserver percent statistic.vi	264
F.9.1	Connector Pane	264
F.9.2	Front Panel	265
F.9.3	List of SubVIs and Express VIs	265
F.10	calculate Udupa segmentation precision.vi	266
F.10.1	Connector Pane	266
F.10.2	Front Panel	266
F.10.3	List of SubVIs and Express VIs	267

References		268
-------------------	--	------------

List of figures

1.1	Development of an arterial plaque showing how atheroma is formed and its effect on blood flow.	3
1.2	A screenshot of a B-mode US image.	10
1.3	A simplified representation of the beam shape in an array transducer.	13
1.4	Axial resolution is defined as the minimum resolvable distance measured in the axial plane between two separate reflectors imaged by the US system.	14
1.5	Lateral resolution is defined as the minimum resolvable distance between two separate reflectors that are displaced laterally with respect to the US beam.	14
1.6	A screenshot of a colour Doppler US image.	15
1.7	An image of a duplex spectral Doppler display.	16
2.1	A rendered 3D CAD model of the phantom scanner.	28
2.2	Rotation of the US transducer around the curved surface covering the piezoelectric elements.	29
2.3	The phantom holder.	33
2.4	Two phantom datasets scanned using the phantom scanner and reconstructed using GEM MicroView.	35
3.1	A screenshot from the Stradwin program.	39
3.2	The 3D US system	42
3.3	Dimensions of the filaments in the CIRS 055A phantom.	44
3.4	An image of the CIRS055A phantom showing the arrangement of filaments.	44
3.5	A reconstructed panorama from a 3DUS scan of the CIRS 055A filament phantom.	45
3.6	A comparison of images of the CIRS055A filament phantom from a panoramic reconstruction of a 3DUS scan and a single image of the filament phantom.	46
3.7	Banding artefacts due to interpolation from remapping 3DUS images to a voxel dataset.	48
3.8	A view of the two egg-shaped volumes of the CIRS 055 volume reconstruction phantom created using the segmentation tools of Stradwin.	50
3.9	A highly attenuated image of the smaller egg-shaped volume of the CIRS 055 volume reconstruction phantom. The egg-shaped volume could not be thresholded clearly enough to calculate its volume.	51
3.10	Filling in small spaces in the thresholded image of the CIRS 055 volume reconstruction phantom.	52
3.11	Using the larger depth settings of the C5-2 transducer, the Stradwin calibration facility cannot clearly image the top surface of the bar.	53
3.12	The L12-5 transducer clamped to a workbench to assess replacement precision of the transducer holder.	55
3.13	The Traxtal Adaptrax optical position sensor tool clamped to a workbench to assess tool replacement precision.	55

3.14	The C5-2 curvilinear array transducer and the transducer holder designed to hold the Traxtal Adaptrax optical tool.	57
3.15	The L12-5 38mm linear array transducer and the transducer holder designed to hold the Traxtal Adaptrax optical tool.	58
4.1	The effect of probe pressure during scanning on a straight artery.	66
4.2	The steps taken to produce a registered (or unregistered) artery geometry for curvature measurement.	68
4.3	An osculating circle connecting three contiguous points along the centreline of a 3D artery model.	69
4.4	A comparison of registered and unregistered datasets for AA1	71
4.5	A comparison of registered and unregistered datasets for CA1	71
4.6	A comparison of registered and unregistered datasets for CA2	72
4.7	A comparison of registered and unregistered datasets for CA3	72
4.8	A comparison of registered and unregistered datasets for CA4	73
4.9	A comparison of registered and unregistered datasets for FE1	73
4.10	A comparison of registered and unregistered datasets for FE2	74
4.11	A comparison of registered and unregistered datasets for FE3	74
4.12	A comparison of registered and unregistered datasets for FE4	75
4.13	A comparison of different styles of lofting using Rhino.	79
4.14	Loose-lofted surfaces for CA1 and FE2.	80
5.1	Steering of the US beam in SonoCT to produce a compound image.	83
5.2	Straight phantom datasets (L to R: ECG gated, B-mode, B-mode with SonoCT).	84
5.3	Calculating the cardiac activity waveform.	86
5.4	Cardiac activity and phase angle compared for three different US scans, one <i>in-vitro</i> on a straight tube phantom and two <i>in-vivo</i> from a healthy volunteer and a patient.	87
5.5	The LabVIEW VI used to gate a Stradwin dataset using a .sxp file. The program finds the peaks (or troughs) of the CA waveform automatically. The user can scroll through the peaks and add or remove other images to the list of peaks. The list can be saved as a text file.	88
5.6	The image processing path used to create retrospectively-gated datasets.	88
5.7	Thresholded areas of the flow phantom measured from a scan without SonoCT (labelled as “normal” on the chart), a scan with SonoCT, and an ECG gated scan. SonoCT areas are consistently larger than areas measured without SonoCT. The image resolution (pixels/mm) is the same for each of the three scans, so the different numbers of pixels correspond to different measured areas.	90
5.8	Histograms of ungated phantom areas.	91
5.9	Box-whisker plots of phantom area measured without SonoCT (labelled “normal”) and with SonoCT image compounding.	92
5.10	Histograms of gated phantom areas	92
5.11	Box-whisker plots of phantom area measured from a retrospectively gated 3DUS dataset with SonoCT and an ECG gated dataset.	93
5.12	Comparing closeups of video captured images from the straight tube phantom imaged with and without SonoCT compounding.	95

5.13	A comparison of cardiac activity to thresholded phantom area. Cardiac activity consistently leads phantom area.	96
6.1	An example of how the directionality of US imaging affects the clarity of the lumen outline.	99
6.2	A schematic showing how ShIRT is used to register and segment 3DUS images.	101
6.3	Using ShIRT to segment US images.	102
6.4	The image processing path used to create segmented 3DUS images.	103
6.5	An illustration of the different scenes used to define a set of segmentation error metrics.	105
6.6	The effect of changes in the automatically-defined segmentation C_d^M on the value of the $TNAF$ and $TPAF$ metrics.	106
6.7	Three segmented arteries (L to R: abdominal aorta, carotid artery, femoral artery).	107
6.8	Some images from the abdominal aorta of a healthy volunteer.	112
6.9	Some images from the common carotid of a healthy volunteer.	113
6.10	Some images from the common carotid of a patient with a complex plaque near the bulb.	114
6.11	Some images from the superficial femoral artery of a healthy volunteer.	115
6.12	Some images from the superficial femoral artery of a patient.	116
6.13	Box-whisker plots of precision (PR) for the three manually segmented datasets.	118
6.14	Box-whisker plots of precision (PR) for the three datasets segmented using ShIRT.	118
6.15	False Negative Area Fraction ($FNAF$) calculated for the five repeatedly segmented scans from three healthy arteries.	120
6.16	False Positive Area Fraction ($FPAF$) calculated for the five repeatedly segmented scans from three healthy arteries.	121
6.17	$TPAF$ for the healthy AA.	123
6.18	$TNAF$ for the healthy AA.	123
6.19	$TPAF$ for the healthy CA.	124
6.20	$TNAF$ for the healthy CA.	125
6.21	$TPAF$ for the healthy FE.	126
6.22	$TNAF$ for the healthy FE.	126
6.23	$TPAF$ for the diseased CA.	127
6.24	$TNAF$ for the diseased CA.	127
6.25	$TPAF$ for the patient FE.	128
6.26	$TNAF$ for the patient FE.	128
6.27	Segmentation of a poor quality image, comparing manual segmentation and ShIRT.	131
7.1	An excerpt from an STL file, showing how triangular elements are defined using three corner points and a normal.	135
7.2	Comparing a surface mesh to a volume mesh.	136
7.3	Creating a patient-specific artery mesh from 3D US data.	140
7.4	A schematic diagram showing the processes used in creating a 3D artery model.	141
7.5	The main features of the carotid artery and areas of flow recirculation.	145
7.6	The healthy carotid artery mesh compared to the original segmented contours.	147
7.7	The bifurcation region of the healthy carotid artery mesh.	148

7.8	The diseased carotid artery mesh compared to the original segmented contours.	150
7.9	Segmented contours of disease shown with US images for the diseased carotid artery.	151
7.10	A closeup of the diseased portion of an artery geometry created using the 3D method.	152
7.11	A closeup of the diseased portion of an artery geometry created using the 2D method.	153
7.12	The bifurcation region of the diseased carotid artery mesh.	154
7.13	Flow streamlines in the healthy carotid artery mesh.	156
7.14	Velocity profiles in the healthy carotid artery mesh.	157
7.15	Contours of high WSS in the healthy carotid artery mesh.	158
7.16	Flow streamlines in the diseased carotid artery mesh.	160
7.17	Velocity profiles in the diseased carotid artery mesh.	161
7.18	Contours of high WSS in the diseased carotid artery mesh.	162
8.1	The wall motion test phantom.	168
8.2	A US image of the test phantom walls.	170
8.3	The effect of stepper motor noise on recorded AWM displacements.	172
8.4	Stepper motor noise removal and its effect on recorded AWM displacements.	173
8.5	Seven physiological AWM displacement waveforms.	176
8.6	The first constant velocity and variable displacement waveform used to determine d_{crit} .	177
8.7	The second constant velocity and variable displacement waveform used to determine d_{crit} .	177
8.8	The first constant displacement and variable velocity waveform used to find the effect of changing velocity on accuracy.	178
8.9	The second constant displacement and variable velocity waveform used to find the effect of changing velocity on accuracy.	179
8.10	Error as a function of displacement for the seven physiological wall motion waveforms.	180
8.11	Accuracy of measured displacement from the two constant velocity and variable displacement waveforms shown in figures 8.6 and 8.7.	181
8.12	Accuracy of measured displacement from the two constant displacement and variable velocity waveforms shown in figures 8.8 and 8.9.	182
8.13	Variation in recorded AWM displacement.	185
9.1	Subcutaneous fat in this carotid image from a patient causes strong reflections at the top of the image, attenuating the signal and preventing clear imaging of the carotid artery.	194
9.2	Changes in image quality of US scans of the femoral artery as it approaches the knee.	195
9.3	Some images of the abdominal aorta scanned from healthy volunteers.	197
9.4	Various high-quality US images captured using the freehand 3DUS system.	198
B.1	The Analyze main screen.	206
B.2	The Analyze Import/Export tool.	207
B.3	The Volume tool, used to load bitmap files into Analyze.	207

B.4	The Save As... window.	208
B.5	The Image Edit window.	209
B.6	The Image Size window.	210
B.7	The Objects window.	210
B.8	The Spline Tool.	211
B.9	Save the object map as a series of bitmap images.	212
B.10	Thresholding segmented blobs using Stradwin	213
C.1	The front panel of “BMP2SXIarray.vi”	215
D.1	SW create OBJ file from outer edges of contours.vi	217
D.2	SW create OBJ file from segmented file.vi	218
D.3	OBJ and XYZ files imported onto different layers. The OBJ file is imported to “contours” and the XYZ file to “centrelines”	219
D.4	Rebuilding the imported OBJ file contours using the “Rebuild” command.	220
D.5	Smoothing the imported OBJ file contours using the “Smooth” command.	220
D.7	Using “ExtractWireframe” to form the shape of the three lofted arteries.	222
D.8	Joining the upper and lower wireframes using the “InterpCrv” command.	223
D.9	Matching the curvature of the interpolated curves using the “Match” command.	223
D.10	Creating the upper curve that creates the start of the bifurcation outline at the top of the CCA.	225
D.11	Creating a network surface to match the top of the CCA to the bottom of the ECA.	225
D.12	The bifurcation region before splitting.	226
D.13	The bifurcation region after splitting.	226
D.14	Extracted wireframes on the bifurcation region.	227
D.15	Matched interpolated curves that will make up the shape of the bifurcation surface.	228
D.16	Joining the central bifurcation lines with the “InterpCrvOnSrf” command. The line is endpoint connected to the central lines.	229
D.17	The surface which will become the region joining the two side sections of the bifurcation.	230
D.18	Using the side rail curves of the bifurcation to split the side surfaces.	231
D.19	Matching the curvature or tangency of the bifurcation surface using “MatchSrf”.	232
D.20	Checking the curvature and the continuity of the surface sections using “Zebra”.	233
D.21	Exporting the created mesh to an STL file. The “Export open objects” option should be used in case the surface mesh is not fully closed.	234
E.1	Importing the STL file into Magics	236
E.2	The Fix Wizard window.	236
E.3	Using Cut & Punch to slice the vessel outlets.	237
E.4	The Remesh window	239
E.5	Any remesh operation should be done locally. The ends of the geometry should be unmarked to prevent shape change at the inlet/outlets.	239

List of tables

2.1	Slice spacing recorded in the literature for various 3DUS systems designed for scanning patients.	36
3.1	US scanner settings used in scanning the CIRS phantoms.	43
3.2	Volumes of the two egg shaped objects in the CIRS 055 volume reconstruction phantom.	49
3.3	Parameters calculated from calibrations performed with Stradwin.	54
3.4	Calibration settings used for the Stradwin calibration procedure for the L12-5 38mm and C5-2 transducers.	54
3.5	Reconstruction accuracy of filament position for the two transducers.	59
3.6	Reconstruction precision of filament position for the two transducers.	59
3.7	Volume reconstruction error of the 3D US system using the C5-2 transducer.	59
3.8	Analysis of five calibrations of the L12-5 transducer at the 3.9 cm depth setting.	60
3.9	Analysis of five calibrations of the C5-2 transducer at the 8.7 cm depth setting.	60
3.10	Values of replacement precision measured for four different methods with the two US transducers.	61
4.1	A summary of the changes in artery curvature κ due to rigid registration.	76
4.2	Wilcoxon Test Results	77
5.1	Mann-Whitney U-test results for the ungated datasets	94
5.2	Mann-Whitney U-test results for the gated datasets	94
6.1	Settings used with ShIRT to register and segment US data.	108
6.2	Median precision (PR) \pm 95% confidence interval for ShIRT and manual segmentations of the three arteries.	117
6.3	Mann-Whitney U-test results for comparing the precision (PR) of ShIRT segmentations to the precision of manually-segmented segmentations for the three arteries.	117
6.4	Percent statistic (PS) results, testing whether a segmentation of each artery using ShIRT was as good as five manual segmentations.	119
6.5	Mean $TNAF$ and $TPAF$ for the five full artery segmentations, comparing ShIRT segmentation to manual segmentation using Analyze.	129
8.1	US machine settings for use with TDI.	175
9.1	Published works by the two image-guided modelling groups that have used extravascular 3D US.	188
9.2	Image spacing for 3DUS systems developed by different groups.	189
E.1	Normal triangle reduction options	239
E.2	Split based remesh options	240
E.3	Quality preserving triangle reduction options	240

E.4 Filter sharp triangles options 240

Acronyms and abbreviations

3DUS	Three-dimensional ultrasound
AA	Abdominal aorta
AAA	Abdominal aortic aneurysm
ABI	Ankle/brachial index
AWM	Arterial Wall Motion
BMP	Bitmap
CA	Carotid artery
CAD	Computer Aided Design
CCA	Common carotid artery (sometimes CC - Common carotid)
CFD	Computational Fluid Dynamics
CT	Computational Tomography
ECA	External carotid artery
ECG	Electrocardiogram
ECST	European Carotid Surgery Trial
FNAF	False negative area fraction
FPAF	False positive area fraction
FE	Finite Element method. Also, Femoral.
HDI	High-Definition Imaging
ICA	Internal carotid artery
IMAQ	Image acquisition
IMT	Intima-Media Thickness
IVUS	Intravascular ultrasound
LDOT	Lumen Diameter Over Time
MMP	matrix-mellanoproteinase
MRI	Magnetic Resonance Imaging
NASCET	North American Symptomatic Carotid Endarterectomy Trial
PI	Pulsatility index
PNG	Portable Network Graphics
PR	Precision

PS	Percent statistic
ROI	Region of interest
ShIRT	Sheffield Image Registration Toolkit
STL	Stereolithography. This also refers to a triangulated mesh file format often used in computational modelling and for rapid prototyping.
TDI	Tissue Doppler Imaging. A Doppler ultrasound technique that measures the Doppler shift of moving tissue instead of blood moving in a vessel as with spectral Doppler.
TNAF	True negative area fraction
TPAF	True positive area fraction
US	Ultrasound
VI	Virtual Instrument, a program written using the LabVIEW development environment.
WSR	Wall Shear Rate
WSS	Wall Shear Stress

Chapter 1

Introduction

1.1 Cardiovascular disease

Atherosclerosis is a type of arterial disease that is an important factor in stroke, the second most common cardiovascular disease reported in the world. Stroke killed 5.5 million people worldwide in 2002, mostly in developing countries. The direct and indirect cost of treatment of stroke in the UK alone was £2.5 billion in 2000 [1]. Risk factors for atherosclerosis have a genetic component (family history of disease) and a lifestyle component (physical inactivity, diet rich in fat, tobacco use). The risk of suffering from atherosclerosis increases when other conditions are present such as diabetes and high blood pressure.

Atherosclerosis is the thickening of the artery wall due to an accumulation of fatty plaques. Typically the endothelium, or artery wall, attracts and absorbs tiny fatty particles called lipids. The lipids accumulate, creating a mass that partially obstructs the flow of blood. This is called a stenosis. Stenoses in arterial disease consist of fat-filled plaques called atheroma. There are several different types of plaque [2]; one of the more vulnerable types consists of a fibrous cap that contains a liquid lipid pool. The cap may rupture, releasing the lipids into the blood stream. Figure 1.1 illustrates the process of disease initiation and growth leading to plaque rupture. The lipids may completely block some of the small arteries in the brain, causing a stroke, where a section of the brain loses all blood supply and dies. However, in many patients, stable plaques may be present which present no risk over the lifetime of the patient.

The formation of atherosclerosis is not a random phenomena [3]. It is predominantly associated with four main areas of the arterial system: the coronary arteries, the abdominal aorta, the carotid arteries, and the femoral arteries.

Plaques found in the coronary arteries are responsible for myocardial infarction, which is more commonly known as “heart attack”. Vulnerable plaques in the coronary artery rupture causing blood to form clots inside the artery. This clotting is known as thrombus. The thrombus travels into the arteries which supply the heart muscles. This causes malfunction of the muscles which

disrupts the blood supply to the rest of the body. Plaques found in the carotid arteries, which supply blood to the face and brain, are most likely to cause stroke. In the femoral arteries, if a vulnerable plaque ruptures, thrombi flow into the lower limb and cause claudication, which is limping due to lack of blood supply to the legs.

The abdominal aorta undergoes a different type of disease development to that found in the carotid and femoral arteries. The abdominal aorta increases in diameter due to the weakening of the muscle cells in the wall of the aorta. Stationary thrombus forms in the widened region of the aorta. This increase in aorta diameter accompanied by thrombus is known as abdominal aortic aneurysm (AAA). The decrease in strength of the artery wall allied to increasing tissue stress due to thrombus formation can cause rupture of the aorta. This results in severe internal bleeding which requires immediate surgery.

1.1.1 Summary

Atherosclerosis is a serious cause of death worldwide. It has life-changing and potentially fatal consequences to those who develop it. Abdominal aortic aneurysm is an important cause of death in adults over the age of 60. The causes of arterial diseases are related to lifestyle (diet, exercise, tobacco use) and genetics.

1.2 The treatment of cardiovascular disease

Where atherosclerosis is present, stroke may be prevented through surgery if it is considered serious enough. To reduce the threat of plaque rupture, the diseased area of the artery may be remodelled, bypassed or removed entirely.

Remodelling of a diseased portion of an artery is often performed using a process called angioplasty. To remodel the artery, a catheter with a small balloon is introduced into the artery away from the site of the stenosis. The catheter is guided to the correct position and monitored using X-ray imaging. Once the catheter is in place the balloon is inflated, expanding the vessel and reducing the obstruction. To prevent restenosis, a stent (a small scaffold) is placed into the diseased section of the artery. The stent is guided into place then unfolded. The expanded stent supports the artery wall and prevents collapse.

Bypassing the artery by diverting the blood flow from one side of the diseased portion to another

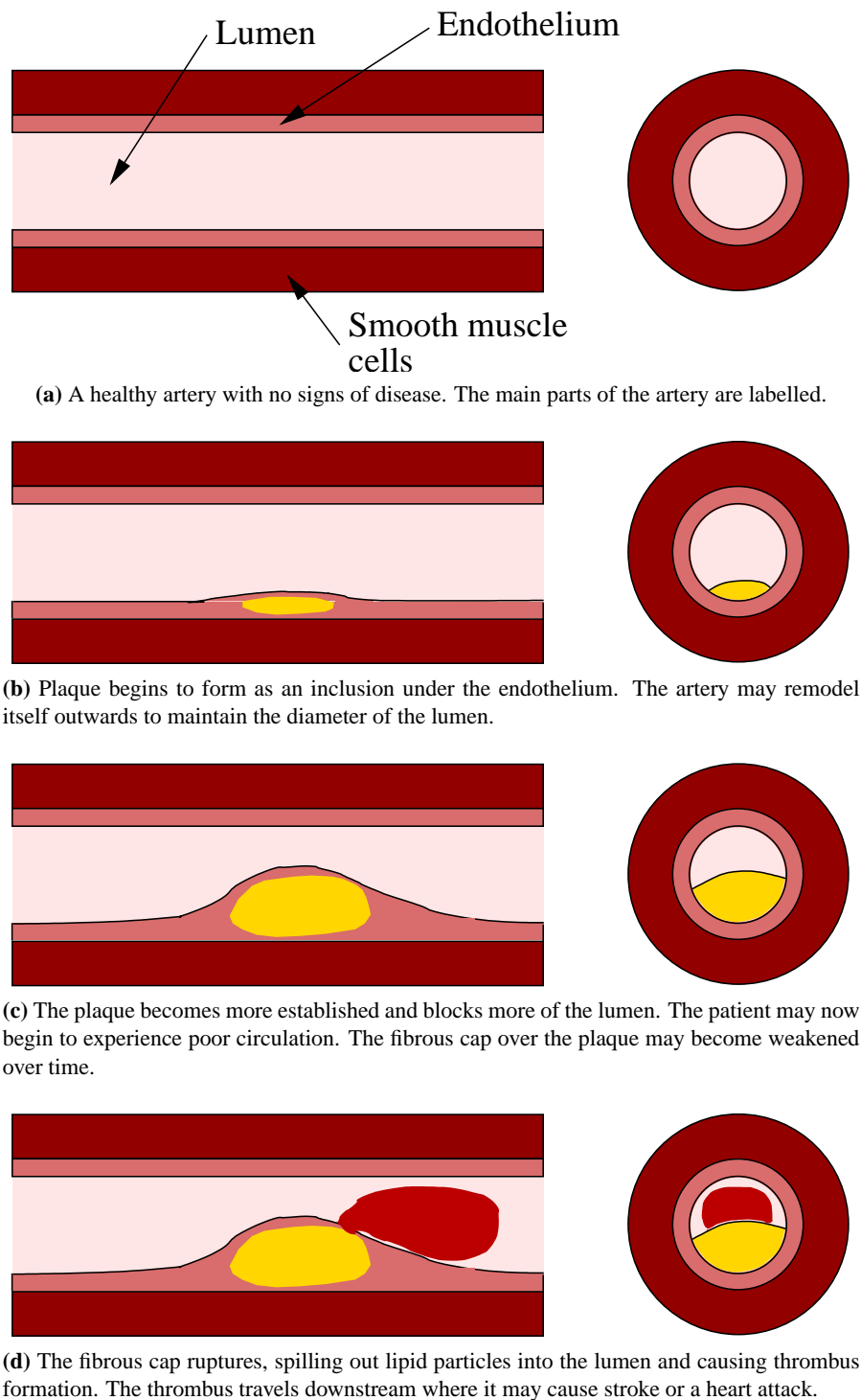


Figure 1.1: *Development of an arterial plaque showing how atheroma is formed and its effect on blood flow.*

is a common method of treating coronary artery disease. A section of the saphenous vein from the leg may be used to provide the bypass. In this way normal blood flow continues without disturbing the plaques present in the diseased coronary artery.

Removal of the diseased section of the artery is used to treat severely diseased carotid and femoral arteries. This process is called endarterectomy. The artery is incised and plaque deposits are scraped out. The weakened artery may be stented to prevent collapse post-operation.

Abdominal aortic aneurysm is treated by grafting or stenting the aorta. For grafting, the aorta is incised and a graft is inserted inside the lumen [4]. The graft diverts the flow of blood inside the aneurysm to restore flow. The graft may be made from a piece of vein from elsewhere in the body or may be made from a synthetic material. In stenting, a stent is inserted into the femoral artery in the leg [5]. A stent is a small scaffold that is used to support the artery from the inside. It is guided into position then unfolded inside the aneurysm. When the stent is opened, a clear channel is formed inside the aneurysm to restore normal blood flow. The use of either method depends on the health of the patient and the state of the AAA [6].

In cases where there is little plaque present in a diseased portion of an artery, non-surgical methods may be employed to reduce the risk of further development of disease. Changes in lifestyle (more exercise) and diet (less fatty foods) may be encouraged. Lipid-reducing drugs may be prescribed.

1.2.1 Summary

There are several methods of treating arterial disease that are dependent on its extent and location. These range from surgical intervention to lifestyle change.

1.3 The diagnosis of cardiovascular disease

1.3.1 Imaging cardiovascular disease

The severity of cardiovascular disease is usually diagnosed using some form of imaging modality. Depending on the condition of the patient and the location in the body, the most common imaging methods used are angiography, computed tomography (CT) imaging, magnetic resonance imaging (MRI) and ultrasound (US).

Angiography is an X-ray imaging technique that is used to examine the blood vessels. A contrast agent is injected into the blood stream during image acquisition. The use of a contrast agent makes the blood vessels stand out in comparison to the other anatomical structures around them. This is available as a two-dimensional technique, where sufficient planes through the artery of interest to measure the plaque are imaged, or a three-dimensional technique known as rotational angiography. The use of X-rays in angiography makes it very expensive to use in a clinical setting. Due to its long-established use in clinical practice, and its ability to image the arteries at risk of atherosclerosis formation, it is considered the “gold standard” method used in the diagnosis of arterial disease.

CT is a three-dimensional X-ray technique. X-rays are projected into the body at a variety of angles focused on the artery of interest. The multiple X-ray images are processed on a computer workstation to provide a 3D reconstruction of the patient anatomy. Measurement of the diseased portion can then be done electronically from the 3D reconstruction. CT may also be used with contrast agents to provide greater visibility of the arterial system.

In MRI imaging, a powerful magnetic field is applied to the body of the patient. In response to this field, the magnetic moments of the nuclei of hydrogen atoms in the water molecules found throughout the body are aligned. Radiofrequency (RF) coils are used to alter this field and make these magnetic moments oscillate, producing RF signals which can be detected by the scanner [7]. Through the use of various signal processing algorithms, the changes in magnetic field can be mapped into an image. The intensity of the signal produced by the hydrogen nuclei depends on its molecular environment, hence different types of tissue can be characterised in different parts of the body. Thus fat and atherosclerotic plaque may be distinguished from other tissue more easily than with US. MRI is an inherently three-dimensional technique, producing a 3D voxel (volume element) array rather than a 2D slice like US imaging. Contrast agents may also be used with MRI to accentuate the location of blood vessels in each image. Signal processing techniques such as black blood or white blood imaging also enhance the imaging of arteries. MRI produces good quality images of the arterial system in all parts of the body and can be used safely in sensitive organs such as the brain.

MRI has the significant advantage of providing a 3D image of arterial geometry when imaging the arterial system. This requires less reconstruction and registration than US-based techniques since the data is intrinsically registered in 3D space and can be used straight away to produce 3D views and measurements of arterial disease. Another significant advantage is that images

suffer from less noise artefacts than US (such as speckle and shadowing) which makes MRI more suitable for automated image processing techniques. For flow studies, MRI can also perform 3D blood flow measurement. However, MRI acquisition is more time-consuming than US acquisition, requiring more patient preparation and more time to process and display captured images. MRI is also less readily available than US due to the expensive power supply requirements of the electromagnet and the specialist training required for its operators.

A US image is made by transmitting high-frequency sound waves into the body. Arterial US imaging can be sub-divided into intra-vascular and extra-vascular types. Intravascular ultrasound (IVUS) images are formed by a small transducer in the form of a catheter which is introduced into the artery. The transducer is steered into the correct artery and images are recorded. IVUS is often used to image the coronary arteries. Extra-vascular ultrasound (hereafter referred to as US) images are formed by a hand-held transducer which is placed over the artery of interest. With each type of US, images at key areas of the diseased artery are used to diagnose the severity of disease. US as used in this fashion is typically two-dimensional; three-dimensional ultrasound techniques also exist. Three-dimensional techniques currently have limited clinical applications in cardiology and obstetrics. US is the least costly and thus the most widely-available imaging modality used to diagnose disease. However, it suffers from imaging artefacts related to the physics of US propagation in human tissue such as shadowing under diseased plaques. It has limited use in diagnosing intracranial arterial disease due to the high sonic reflectivity of bone. The presence of bowel gas when scanning the abdomen also reduces its effectiveness.

1.3.2 Assessing the severity of cardiovascular disease

In assessing atherosclerosis in the carotid artery, the NASCET (North American Symptomatic Carotid Endarterectomy Trial) and ECST (European Carotid Surgery Trial) methods are used to calculate the degree of stenosis of carotid plaque. Both methods used angiography to image diseased arteries from patients in large randomised multi-centre trials. The NASCET method measures stenosis in the internal carotid artery (ICA) based on two diameters: the minimum diameter of the ICA measured at the site of maximum stenosis ($d_{ICA,min}$), and the diameter of the ICA in a distal disease-free portion of the ICA ($d_{ICA,distal}$). To calculate the degree of

stenosis of the artery, the following equation is used:

$$100 \times \left(1 - \frac{d_{ICA,min}}{d_{ICA,distal}} \right). \quad (1.1)$$

The critical degree of stenosis for this artery using the NASCET method is set at 70%. Arteries with a degree of stenosis greater than this critical value are considered vulnerable to plaque rupture and are recommended for surgery.

The ECST trial uses a different method of calculating stenosis which gives a higher value than the NASCET trial method [8]. In the ECST trial, the minimum diameter of the ICA measured at the site of maximum stenosis ($d_{ICA,min}$) is compared to the diameter of the undiseased artery ($d_{healthy}$)(i.e. the diameter of the lumen as if it did not contain a stenosis). Degree of stenosis is calculated using

$$100 \times \left(1 - \frac{d_{ICA,min}}{d_{healthy}} \right). \quad (1.2)$$

The result of the NASCET trial method is consistently smaller than the ECST method. The ECST trial recommends that endarterectomy surgery is of most benefit to patients with $\geq 80\%$ stenosis. The NASCET trial recommends surgery on patients with $\geq 70\%$ stenosis. However, the results of the two trials are consistent when analysed in the same way [8]. These methods of measuring stenosis may also be used with US instead of angiography [9]. Other methods of measuring stenosis exist such as the Carotid Stenosis Index [10] and the Common Carotid (CC) method [9]. However, the NASCET and ECST methods are the most commonly used and have been tested widely in randomised trials to assess their accuracy.

The assessment of femoral artery disease is similar to that of carotid disease. The percent stenosis at diseased sections may be calculated using angiography. Other flow-related indices measured using spectral Doppler US may be used to assess the requirement for surgery. These include the popliteal pulsatility index (PI) or ankle/brachial index (ABI) [11].

In assessing abdominal aortic aneurysm the diameter of the aneurysm is measured using one of the imaging techniques described above. The diameter is measured using longitudinal and transverse views of the aorta. An aorta with a diameter of ≥ 4 cm is defined as an aneurysm. Patients presenting symptoms of aneurysm rupture are offered urgent repair. Asymptomatic patients are considered for repair if the diameter of the aneurysm exceeds 5.5 cm [12]. If its diameter is less than 5.5 cm, the patient is entered into a screening programme. These criteria are not perfect: 60% of AAAs with diameters greater than 5.5 cm never rupture [13]

and 10 – 20% of AAAs with a diameter less than 5.5 cm rupture [14].

1.3.3 Summary

The calculation of stenosis in femoral and carotid artery disease is used to decide whether surgery is necessary. In the case of abdominal aorta aneurysm, the maximum diameter of the aneurysm is measured.

1.4 Ultrasound imaging of arterial disease

US is an especially useful clinical imaging modality due to its wide availability, its portability and ease of use. US scanners can be very portable, with some systems available (e.g. the SonoSite system, <http://www.sonosite.com>) which are available in a lightweight laptop-computer sized format. US scanners give images in real-time at the patient bed side. They also offer the ability to measure blood flow in arteries and veins. The Doppler shift frequency of a US pulse is calculated and related to the speed of blood flow in an artery or vein [15]. US can even be used to measure the motion of the arterial wall as it is distended due to pulsatile blood flow [16]. Many applications of US are reviewed in [17].

Conventional US techniques offer a single “slice” representing a plane through the anatomy of interest. This means that the user requires training and experience to correctly interpret the image, considering factors such as the orientation of the transducer and the structures surrounding the anatomy of interest. US scanning suffers from many artefacts related to the formation of the US beam, the variable speed of sound in different tissues, and the presence of strong reflectors that cause various image artefacts [18]. A further disadvantage of US is that it provides a two-dimensional image of three-dimensional anatomy. This is a serious disadvantage when compared to 3D imaging modalities such as MRI or CT.

When imaging diseased arteries using US, the transducer is oriented to image a cross-section of the suspected site of disease. Methods such as those outlined in the NASCET and ECST trials described above are used to assess disease. The transducer has to be aligned orthogonally to the artery, otherwise false measurements of stenosis may result.

1.4.1 The physics of ultrasound imaging

There are three primary imaging modes in US used in the diagnosis of arterial disease: B-mode imaging, colour Doppler imaging, and spectral Doppler imaging. In most modern US scanners with B-mode imaging, a series of pulses are sent from an array transducer into the tissue of the patient. The array transducer is made up of an array of piezoelectric elements. When an electrical pulse is applied to each element, the element vibrates, producing a high-frequency sound signal which propagates through the tissue. Conversely, when a sound is reflected off a structure (such as an artery wall or muscle fibres) as an “echo” back to the piezoelectric element, an electrical signal is produced. Typically, each element has an electrical pulse applied in turn. In B-mode imaging, this pulse-echo method is used to create an image. To create an image, the received pulses from each element are represented by a different shade of grey, with each level of grey proportional to the strength of the reflected echo at that position. The calculation of the position in space of each reflector is based on the time to receive the US echo and the assumed speed of sound in tissue. For most clinical US machines, this is assumed to be $1540 \text{ m} \cdot \text{s}^{-1}$. In different types of tissue, the speed of sound varies as a function of the density and mechanical stiffness of the material. In practice, the use of a single assumed speed of sound does not produce significant errors in the calculation of the position of most reflectors [19]. Figure 1.2 shows a B-mode image from an arterial scan.

When using a US scanner, the image displayed on the screen gives the impression that the scanner is imaging an infinitesimally thick portion of the body, with the width of the image determined by the width of the transducer. In practice, the US beam varies in thickness with depth, and is wider than the displayed image. In an array transducer, the beam has a thickness which is determined by the shape of the echoes generated by each piezoelectric element, the frequency of the emitted pulses, and the focusing lens attached to the end of the transducer. Figure 1.3 shows a typical beam shape for a B-mode linear array transducer. Mechanical and electrical methods are available to focus the US beam to produce improved spatial resolution at the focal point of the beam [20]. An important method of focusing the US beam is to introduce delays to the triggering of the transmitted pulses. This can steer the beam and focus it to one or more focal points in the tissue.

In any discussion of an imaging modality, spatial resolution is an important concept. This is defined as the minimum size of object that can be visualised. With B-mode US, spatial resolution is made up of two components: axial and lateral resolution [21]. Axial resolution



Figure 1.2: A screenshot of a B-mode US image. This image shows a carotid artery from a healthy volunteer. The transducer is aligned with the centreline of the artery, producing a transverse sectional view. The endothelium at the top and bottom of the artery stand out clearly against the dark interior of the artery.

measures the ability of the scanner to display separate echoes from structures that lie behind each other in the direction of the beam (Figure 1.4). Using shorter ultrasonic pulses increases axial resolution. Lateral resolution measures the ability of the scanner to produce separate echoes from structures that lie across the beam (Figure 1.5). This depends on the width of the US beam at the position of the structures.

B-mode imaging (and US in general) suffers from a number of artefacts [21]. Reverberations in tissue may cause the appearance of false echoes on the B-mode display. These are especially prominent when a reflector is placed parallel to the transducer face. Shadowing artefacts may also be caused by attenuation of the transmitted pulse through a highly absorbing or reflecting material. This artefact is especially of interest in arterial imaging since atherosclerotic plaque is highly reflective and can prevent the visualisation of structures below it. These artefacts are characteristic of US pulse propagation. Other types of artefacts are a result of the shape of the US beam. The width of the US beam has the effect of causing small point targets (such as wire filaments as used in some calibration phantoms [22]) to appear as small lines on the B-mode display. This artefact varies with the proximity to the focal point of the beam; away

from the focal point, the increase in width is higher than at the focal point. Some artefacts from the signal processing electronics used to generate US images are also experienced. The TGC sliders, used in B-mode imaging to adjust the gain at different depths in the US image, can be improperly adjusted and produce an image with too high or too low amplification in different areas, rendering some important features of the image invisible. Electronic noise may also be experienced where TGC is set to maximum. This manifests itself as repeating patterns with the appearance of “rain” on the scanner display.

Some of the artefacts intrinsic to B-mode imaging may be reduced by using image compounding. An example of note is the SonoCTTM method developed by Philips Medical Systems [23]. In SonoCT, the US beam is steered to sweep back and forth along the length of the transducer. The resulting series of steered images is then compounded to produce an improved B-mode image with reduced speckle and less shadowing, especially under blood vessels. It also provides improved images of plaques, allowing their often complex structures to be more fully displayed due to the different angles of insonation used to build up an image.

Colour Doppler imaging (or 2D colour flow imaging) is routinely used in vascular US to understand the effects of plaque on blood flow patterns and identify areas of low flow in occluded arteries. A typical Doppler US image is shown in Figure 1.6. Colour Doppler imaging relies on the Doppler effect, where a change occurs in the frequency of an observed sound wave compared to the frequency of the emitted sound wave. This is due to the relative motion between the source of the sound wave (in this case the reflection from a moving structure in the body) and the receiver of the sound wave (in this case the US transducer). The Doppler frequency shift in blood flow can be related to the velocity of the blood flow using the Doppler equation

$$f_d = f_r - f_t = \frac{2 \cdot f_t \cdot v \cdot \cos \theta}{c} \quad (1.3)$$

where f_d is the Doppler shift frequency; f_r is the received frequency; f_t is the transmitted frequency; v is the velocity of blood; θ is the angle between the US beam and the direction of blood flow; and c is the speed of sound in tissue [19].

In colour Doppler imaging, the frequency shift in blood flow is recorded and its velocity relative to the direction of the US beam is calculated and displayed as a colour overlaid on the B-mode image display. Typically, shades of blue are used to show blood flowing away from the transducer and shades of red are used to show blood flow towards the transducer. The

colour flow display has to be carefully set up to provide appropriate diagnostic information. The maximum and minimum velocities to be displayed by the colour Doppler display can be preselected on the scanner. Each pixel in the colour flow display represents the Doppler shift at each pixel averaged over the area of the pixel. Because of this limitation to the sensitivity of colour Doppler imaging, spectral Doppler US is often used to measure blood flow velocity for quantitative measures of blood flow such as determining the peak flow velocity in an artery, or for boundary conditions for computational modelling of blood flow [15].

Spectral Doppler imaging also takes advantage of the Doppler effect to measure the velocity of blood flow. Unlike colour Doppler imaging, spectral Doppler is used to detect the Doppler shift in a single location within the blood vessel. In a spectral Doppler display, frequency shift is plotted against time, and the greyscale used corresponds to the amplitude of the detected US at that position in the blood vessel. Figure 1.7 shows a spectral Doppler display from a healthy volunteer. In taking a spectral Doppler measurement, scanner settings have to be carefully chosen. The size of the sample volume, which is overlaid on the B-mode image to show the location of frequency shift measurement in the blood vessel, can affect how much of the flow profile in the artery is measured. A small sample volume may incorrectly estimate the flow profile present in the blood vessel, especially in the case of pulsatile flow, where a wide range of velocities is present across the blood vessel. Several artefacts affect spectral Doppler measurements such as shadowing which leads to a loss of Doppler signal, and multiple reflections from strong reflectors which may cause the appearance of false structures on the B-mode image. An important feature of spectral Doppler US is angle dependence. The Doppler shift frequencies are dependent on the angle of insonation (as shown by the $\cos \theta$ term in Equation 1.3). As θ increases, smaller Doppler shift frequencies are measured, leading to signal loss as $\cos \theta \rightarrow 90^\circ$. Spectral Doppler signals should be angle-corrected to produce the correct blood velocity [19]. This is achieved by rearranging Equation 1.3 to give

$$v = \frac{f_d \cdot c}{2 \cdot f_t \cdot \cos \theta}. \quad (1.4)$$

The angle of insonation θ is displayed on the spectral Doppler display and can be controlled by the user.

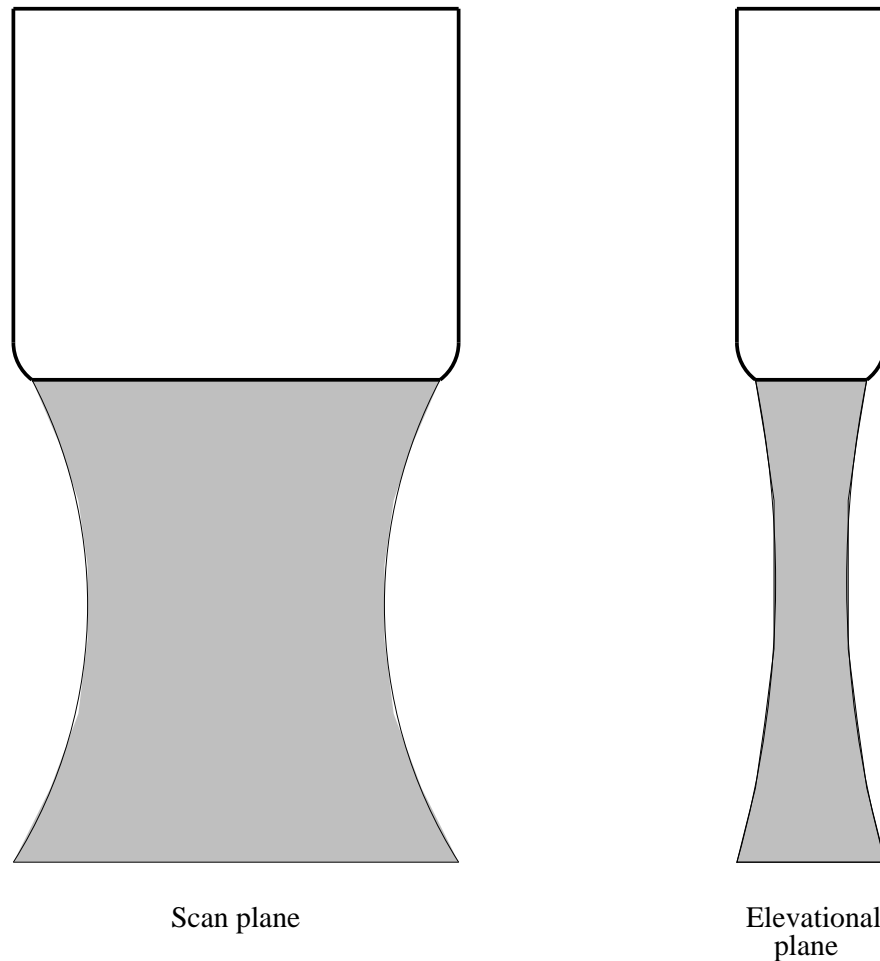


Figure 1.3: A simplified representation of the beam shape in an array transducer. The views of the scan plane (or lateral plane) and elevational plane show that the beam has a “waisted” appearance. The shape and size of the beam in each plane are usually different and may vary due to focussing and the depth setting used in acquisition. The lateral resolution of the scanner is determined by the beam width in the scan plane. The slice thickness is defined by the beam width viewed in the elevational plane.

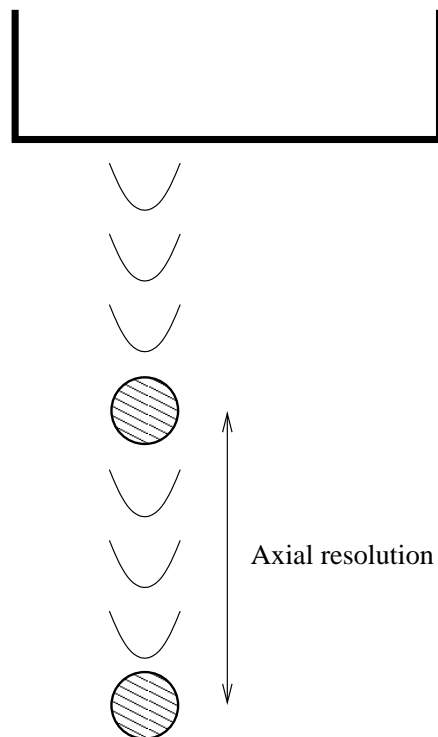


Figure 1.4: Axial resolution is defined as the minimum resolvable distance measured in the direction of the US beam between two separate reflectors. Axial resolution is determined by the pulse length used in imaging. A shorter pulse length will produce a higher axial resolution.

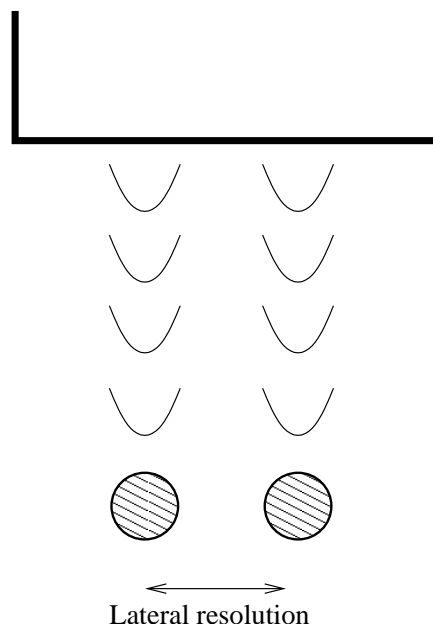


Figure 1.5: Lateral resolution is defined as the minimum resolvable distance between two separate reflectors that are displaced laterally with respect to the US beam. Lateral resolution is determined by the width of the US beam at the position of the reflectors, and is increased by using a narrower beam.

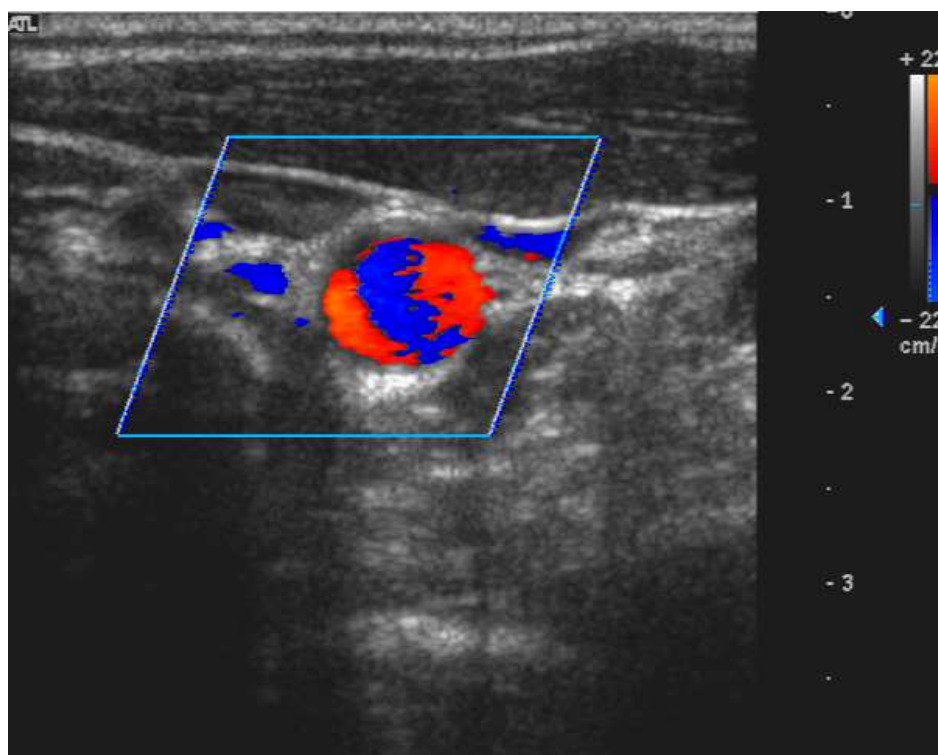


Figure 1.6: A screenshot of a colour Doppler US image. The average Doppler shift for each pixel is mapped onto the B-mode image to visualise the flow patterns present in an artery. Blue-coloured pixels show flow away from the transducer, while red-coloured pixels show flow towards the transducer.

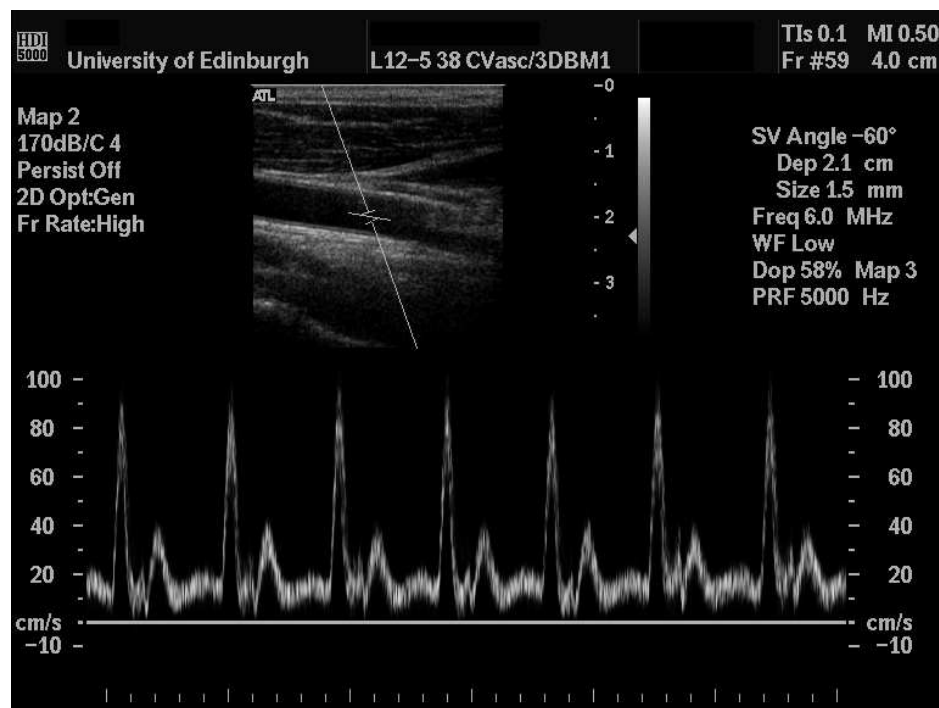


Figure 1.7: An image of a duplex spectral Doppler display. The B-mode display at the top of the image shows the position of the Doppler sample volume in the anatomy being scanned. The Doppler sample volume is shown positioned at the centreline of the artery (in this case the common carotid) to measure peak blood flow velocity. The resulting velocity profile is displayed in the lower part of the image.

1.4.2 Ultrasound image processing

An image processing task that is of interest in US imaging is segmentation. This is the process of identifying specific features of an image and performing analysis of them. An example may be identifying the shape of a fetal foot to create a 3D surface model to analyse fetal development [24]; outlining the shape of the chambers of the heart to assess heart function [25]; and tracing the shape of an artery to develop a 3D surface model for computational simulation [26]. US imaging artefacts, such as those described above, have a direct effect on the efficacy of segmentation. The speckle pattern that is characteristic of B-mode US imaging reduces the resolution of the outline of some structures, which makes them more difficult to segment. A limitation of using US images for segmentation of atherosclerosis is that shadowing artefacts under calcified plaque can obscure the outline of the vessel wall below the plaque. The directionality of the US beam also affects segmentation: when imaging a round vessel from a position orthogonal to the direction of flow, the surfaces parallel to the beam reflect more of the US echo back to the transducer. The sides of the vessel are therefore less clearly imaged, making an accurate assessment of the shape of the whole artery cross-section more difficult.

Despite the difficulties in segmenting US images, this is still an active field of research. Many researchers have developed semi-automatic means of segmenting US images [27]. Others use manual segmentation, sometimes known as “manual planimetry”, to identify features in US images [28]. In manual segmentation, an observer experienced in interpreting US images draws the location and shape of anatomical features onto the US image. This is a time-consuming and expensive process, factors which have motivated the development of semi-automatic segmentation methods.

1.4.3 3D ultrasound imaging

In research, US systems have been developed that take advantage of three-dimensional ultrasound (3DUS) technology to enhance the imaging of atherosclerosis [28, 29]. However, there is still little information on the optimisation of 3DUS techniques for arterial imaging.

Many 3DUS systems have adapted existing US technology, using the advanced imaging features of US machines alongside high-precision position sensing devices to create 3DUS images. Some current high-end clinical US scanners (e.g. the Phillips iE33 echocardiography system, <http://medical.phillips.com/ultrasound>) feature two-dimensional array transducers, giving in-

stantaneous 3DUS data without the need for any additional hardware. In obstetrics the use of mechanically-moved linear array transducers that quickly translate a linear array inside an enlarged transducer has become popular. However, both these methods can scan only a limited portion of the anatomy, meaning that scans of long arteries require several acquisitions, some form of external position sensor and a method of volume registration to align the captured volumes [30]. Commercial 2D array transducers have been developed primarily for cardiology applications, with lower frequencies and curvilinear profiles that make them unsuitable for imaging more superficial arteries such as the femoral and carotid arteries.

3DUS systems have been widely used in research outside of cardiovascular imaging. They have been used to measure ventricular volume [31], create movies of foetal movement *in-utero* [32], diagnose abnormalities in the bone structure of infants [24], visualise different anatomical features of the body during surgery [33], visualise the prostate gland [34] and visualise tumors in the breast [35].

Research 3DUS systems can be classified by the method of moving the US transducer over the skin surface of the patient [36]. Freehand scanning systems use the hand movements of the user of the US system to control the 3D position of the transducer. They typically use some kind of position sensor mounted on to the casing of the transducer to record its motion while scanning. A control program, usually run on an external computer, is used to capture images from the scanner and assemble them in 3D space with the position information from the position sensor. This can be done in real time while scanning, or after scanning has finished. The type of position sensor varies with application, budget and the required level of positional accuracy. The most accurate type of position sensor is the measuring arm, where a jointed structure holds the transducer and is moved by the user [37]. They are very resistant to interference from electromagnetic sources due to their sealed nature. However, they have a limited range of movement and can be very expensive compared to other sensors. Optical position sensors are generally the next most accurate type of position sensor [38]. A reflector is mounted on the transducer and a camera or cameras (often of the infra-red type) records its motion. Optical systems are resistant to electromagnetic interference. However, they suffer from line-of-sight problems: if the reflector is not directly visible by the camera, the position of the transducer cannot be recorded. Specialised multi-face optical tools can reduce this problem to some extent. Electromagnetic position sensors are the least expensive and least accurate of the most commonly used sensors in 3DUS research [39]. They can be highly susceptible to electromag-

netic noise, and manufacturers often recommend that for best results, large metallic objects and electrical machinery is placed outside the measurement volume. This is seldom possible while scanning with US, so errors from the proximity of the US scanner are unavoidable. However, electromagnetic position sensors can be used inside the body, an important advantage for the development of transoesophageal 3DUS systems [40]. For most extra-vascular US applications, using an optical position sensor provides the best compromise between price, accuracy, resistance to external interference and freedom of movement for the user. More recently Ali and Logeswaran [41] have developed an optical tracking system based around a video camera with a reflector mounted to the transducer. Assuming accuracies equivalent to the more expensive position sensors, this type of position measurement system may make 3DUS more widespread and accepted.

Freehand scanning has a limited ability to capture a 3DUS dataset with precisely controlled image positions. The spacing between images is non-uniform and depends entirely on the user. This gives very variable performance: as the user gets more tired, their hand may become less steady and image positioning becomes more variable. Some groups have developed parallelogram-linkage based robot systems to move the transducer over the patient [42] and stepper-motor driven transducer holders to translate the transducer over the skin surface [43]. The latter type of device has been used to measure carotid plaque volume [44, 45]. The primary disadvantage of mechanically-controlled systems is similar to that of 2D array transducers. The working volume of the device may be small, meaning that larger arteries require multiple acquisitions and some form of registration process to merge several datasets together, along with an additional external position sensor. Mechanically-controlled systems also cannot respond well to changes in patient anatomy. If a mechanical actuator has a straight-line movement, it will be more difficult to use on curved anatomy such as on the neck for scanning the carotid. This may require changes in the position of the patient to produce a flatter scanning surface or the application of excessive probe pressure to maintain contact with the skin/ultrasound gel surface all the way along the device. The additional cost of development and the additional training required for users of the system are further disadvantages of a mechanically-controlled approach to scanning.

For 3DUS scanning *in vitro*, for example with flow phantoms such as those developed by Ramnarine et al. [46], mechanically-controlled 3DUS scanning has many advantages. Flow phantoms do not move and they are usually made with a flat upper surface. These features mean that

a mechanically-scanned approach has been used with success for gathering large amounts of spectral Doppler and colour Doppler data from the entire flow regime of anatomical phantoms [47], enhancing the understanding of how blood flows through complex arterial geometries in a manner that is impossible *in vivo*.

In freehand 3DUS scanning, the treatment of recorded data varies between different acquisition software developed by different research groups [48]. Typically most 3DUS acquisition programs remap the incoming image data into a large voxel array using the position sensor data stream [e.g. 49, 50, 51]. This results in voxel remapping artefacts which affect the quality of the US image and can reduce the clarity of the artery wall for segmentation of vascular images. Sometimes the motivation for voxelating the data on capture is to allow the use of image analysis and display software that has already been developed for other 3D imaging modalities such as CT and MRI that produce voxelated data. Another motivation is to facilitate registration of intra-operative 3DUS data to pre-operative MR data [52]. Uniquely the Stradx/Stradwin system [53] does not remap the images on capture, but rather treats the US images as several independent planes spatially registered in 3D space according to the coordinate system of the position sensor. Image quality is therefore maintained throughout the dataset.

Regardless of whether 3DUS data is voxel-mapped or not, there are several issues that make comparison and assessment of 3DUS systems difficult. Different research groups have different methods of assessing the performance of their systems, making direct comparison to find the most accurate system difficult. The method used to calibrate the position of the tool mounted on the transducer casing to the position of the image affects the accuracy of the rest of the 3DUS system. US scanning changes the shape of the underlying anatomical structures due to the application of pressure on the transducer (known as probe pressure). Patient movement also affects the positions of anatomical structures (especially pulsating arteries) during scanning.

1.4.4 Summary

3DUS in research has been widely used in most fields where conventional US imaging is used. Some challenges to 3DUS, such as reducing patient movement effects on captured 3D images and maintaining the accuracy of captured data, still remain. These challenges have received little development for arterial 3DUS scanning.

1.5 The biomechanics of arterial disease

The initiation and growth of atherosclerosis is a complex interaction of biomechanical forces and cellular responses. Biomechanical factors such as wall shear stress on the lumen, flow recirculation and tissue stresses from pulsatile blood flow are responsible for the initiation of arterial disease. Complex cellular responses to these biomechanical stimuli encourage the growth of atherosclerotic plaque. High tissue stresses on vulnerable plaques cause its rupture and the release of lipid particles into the blood stream and thrombus formation.

Wall shear stress (WSS) is the effect of viscous shear forces from blood on the artery wall. It is calculated using the viscosity and the velocity gradient of blood flow at the wall. WSS (τ) is defined as

$$\tau = \mu \cdot \frac{du}{dr} \quad (1.5)$$

where μ is the dynamic viscosity ($\text{kg/m} \cdot \text{s}$); u is the axial velocity of blood flow; and r is the radial distance measured from the centreline of the artery. WSS is implicated in the initiation of atherosclerosis. Sections of arteries with time-varying WSS, such as the carotid, femoral and coronary arteries, are correlated with the formation of atherosclerotic plaque [3].

Wall shear rate (WSR) is the rate of change of the motion of the arterial wall under the influence of pulsatile blood flow. WSS may be related to WSR using the following equation:

$$\tau = WBV \cdot WSR \quad (1.6)$$

where WBV is the whole blood viscosity ($\text{Pa} \cdot \text{s}$) and WSR is measured in s^{-1} [54]. WSR may be measured using dual-beam Doppler US techniques [55]. These techniques cannot measure the flow in recirculatory regions responsible for producing fluctuating WSR . To accurately determine WSS, a more complex method of measurement and estimation of blood flow parameters is required. This is provided by using an image-guided modelling approach.

Time-varying WSS, especially areas of fluctuating low WSS, are correlated to locations predisposed to the formation of arterial disease [56]. Time-varying WSS is responsible for the remodelling of the endothelial layer of the lumen. This produces complex biochemical reactions which can result in focal thickening of the lumen and eventually form atherosclerotic plaques [57]. Time-varying WSS is associated with flow recirculation regions. It is believed that flow recirculation keeps the endothelium in contact with lipid cells and other cells which

encourage plaque activation, thus encouraging disease growth [3]. High WSS is associated with a *reduction* in atherosclerosis. It is believed to reduce areas of low WSS and encourage normal function of the endothelium. Conversely, if fragile atherosclerotic plaque is present in an artery, high WSS is responsible for plaque rupture [58]. Moderate exercise is a normal method of maintaining healthy high WSS in the arterial system, and it is often recommended by physicians as a method of reducing arterial disease. However, patients with vulnerable arterial plaque may be discouraged from exercise to prevent plaque rupture and subsequent stroke.

The development of AAA begins with the degradation of smooth muscle fibres found in the inner layers of the aorta (the media and adventitia) [59]. This degradation results in the expansion of the wall of the aorta, forming an aneurysm sac. When stresses on the wall exceed the strength of the degraded tissue, rupture occurs. Tissue degradation is caused by proteolytic enzymes, in particular matrix-mellano-proteinases (MMPs), a family of elastases and collagenases [60]. The details of the pathways leading to MMP activation are not well understood. However, the presence of inflammatory cells at the artery wall is a key factor, as these cells secrete MMPs and induce smooth muscle cells in the endothelium to secrete further MMPs. Inflammation, high levels of MMPs and the localised formation of new blood vessels (focal neovascularisation) are present at sites of AAA rupture [61].

1.5.1 Summary

Biomechanical factors such as WSS and regions of recirculating flow are correlated with regions of arteries where atherogenesis occurs. Imaging methods are currently unable to measure these biomechanical factors. A method of estimating biomechanical factors and their effect on arteries is required to give a fuller understanding of the development of atherosclerosis and assess vulnerable plaques.

1.6 Modelling arterial disease using image-guided modelling

Image-guided modelling is the process of taking anatomical images from some form of medical imaging modality (e.g. MRI, CT or 3DUS) and forming a patient-specific computational model of the anatomy of interest. This patient-specific model is used to create a computational simulation of a biomechanical value of interest such as blood velocity or pressure on the artery wall. The computational simulation may then be used to predict the future behaviour

of the anatomy, or allow the calculation of important biomechanical values that are otherwise unobtainable from the images alone. An image-guided modelling approach has been used to visualise abnormal blood flow in the carotid bifurcation using magnetic resonance angiography (MRA) images [62], visualise the flow patterns in a giant intracranial aneurysm from computed rotational angiography images [63], and evaluate the effect of the movement of the artery wall on flow in a CT-scanned patient-specific AAA [64]. Further methods of using image-guided modelling with computational fluid dynamics (CFD) were reviewed by Steinman [65].

3DUS has also been used to provide computational models and boundary conditions for image-guided modelling. The research group at Imperial College, London, UK, led by Yun Lu, has a long track record of using 3DUS with image-guided modelling. Augst et al. [66] used a Philips HDI5000 US system with a magnetic position sensor to record image sequences from healthy volunteers. Patient-specific artery models were created from 3DUS images by fitting a spline to several manually-defined key points on each US image. A three-dimensional computational model of the artery was created by filling the spaces between each spline-fitted image with a smoothed surface. This was carried out using a solid modelling package. Spectral Doppler US data was used to provide flow boundary conditions to the model, and the flow regime within the artery model was calculated using CFX, a commercially-available CFD solver (ANSYS Inc., Canonburg, PA, USA). This group also carried out a similar study on a patient with arterial plaque in the carotid artery [26]. They compared artery geometries created from MRI and 3DUS images on the same volunteers to quantify the differences in simulated results due to the use of differing modalities [67]. They also considered the accuracy and reproducibility of WSS results calculated from CFD software using models created from 3DUS images [68]. Only 3DUS studies of the carotid artery in healthy volunteers and patients with diagnosed plaques were reported by this group.

Image guided modelling of the coronary artery has also been attempted by Slager et al. [69]. This method uses anatomical images captured using an IVUS system to create a computational model of the coronary artery. IVUS systems have different acquisition artefacts to extravascular US systems, meaning that a direct comparison of the acquisition methods and the optimisation of each method is not possible.

1.6.1 Summary

Image-guided modelling uses anatomical data from an imaging modality and computational simulation to provide biomechanical information that is unobtainable from images alone. 3DUS has been used as part of an image-guided modelling approach. Few groups have researched the optimisation of 3DUS methods for image-guided modelling.

1.7 Critical analysis

From the above text, it is notable that there has been little work on the optimisation of 3DUS techniques for image-guided modelling of arteries. Studies have been published on the use of 3DUS as part of an image-guided modelling system [e.g. 26]. However, there has been little work on the optimisation of the 3DUS acquisition process. Issues such as removing the effect of patient movement on the creation of artery computational models, correcting probe pressure effects on arterial images, quickly and accurately segmenting 3DUS images, and integrating the process of artery model creation with computational modelling have received little attention in the literature.

1.8 Aim

The aim of this thesis is to develop a 3DUS-based image-guided modelling system for use in the assessment of arterial disease. It will optimise and validate where possible the chain of tasks from 3DUS image acquisition to computational modelling.

1.9 Thesis outline

This thesis describes the development of a 3DUS system used in image-guided flow modelling. The development of a mechanically-controlled 3DUS scanning system for *in vitro* flow models is described in Chapter 2.

Chapter 3 contains an assessment of the accuracy and precision of a freehand 3DUS system for *in vivo* scanning using standardised test phantoms.

A method of removing probe pressure artefacts present in artery models reconstructed from

3DUS data was applied to 3DUS data. This used a rigid registration algorithm. It is assessed by considering the reduction in artery centreline curvature in registered artery models compared to unregistered models (Chapter 4).

The retrospective gating method used with the freehand scanning system is compared to ECG gating. The similarity of retrospective gating to ECG, a standard method of recording US datasets free from movement artefacts caused by pulsatile blood flow, is assessed (Chapter 5).

In Chapter 6 a semi-automatic segmentation technique is assessed against manual segmentation on a variety of arterial 3DUS scans. The precision and accuracy of automatic segmentation is evaluated, and the suitability of the semi-automatic method for segmenting arterial 3DUS images is assessed.

A registration-based artery mesh modelling technique is applied to 3DUS data. The shape of artery mesh models for computational simulation is assessed, along with simulations of fluid flow created using artery mesh models generated by this technique (Chapter 7).

The use of arterial wall motion (AWM) software to provide wall motion boundary conditions for simulation is evaluated using a computer-controlled test phantom (Chapter 8).

In Chapter 9, the 3DUS acquisition system and tools for computational artery model creation presented in this thesis will be critically analysed in the light of other research done in the field.

Chapter 10 contains conclusions and recommendations for future work based on this research.

Chapter 2

Mechanical 3D ultrasound for *in-vitro* flow models

2.1 Introduction

US imaging is used to make measurements of vascular geometry using B-mode imaging and for a variety of haemodynamic measurements using Doppler US. Vascular phantoms provide realistic US images and signals for the understanding and development of US techniques. Vascular wall phantoms with moving walls have been described by Dineley [70] for use with TDI. Dabrowski [71] used a real-vessel phantom to better understand the appearance of carotid B-mode images. Many flow phantoms have been described to provide physiological flow waveforms for use with Doppler US [46, 47, 72, 73]. The transducer position and scan plane were adjusted to visualise the region of interest, usually an axial segment in a normal vessel or a stenosed vessel. The probe may be adjusted in a freehand manner similar to that used in clinical scanning, or with fixing of the probe in a retort stand and clamp to prevent transducer movement during a series of experiments. More complex adjustments were performed by Poepping [47] who used a 3-axis computer controlled positioner to acquire phantom data. The above systems are concerned with the acquisition of 2D data.

3DUS systems mostly involve acquisition of 2D slices by sweeping or rotation of a 2D transducer [36]. More recently high quality cardiac images have been obtained using a Philips 2D array system [74]. Vascular geometry 3D data may be acquired for use in image guided modelling [65] in which 3D imaging is combined with computational fluid dynamics for estimation of the 3D time varying flow field. Most studies to date have used MRI, however a few studies have also used US [26, 66, 67, 75]. 3D Doppler data is of interest in the development of new diagnostic methods which utilise the whole flow field on the basis that flow fields in disease are complex and there is likely to be more information in the whole field compared to a spot measurement at the location of maximum velocity.

This chapter is concerned with the development of a scanning system for acquisition of 3D data in vascular phantoms. The phantom scanner was designed with high positional accuracy

(< 100 μm) for high reproducibility, and sufficient flexibility to allow for acquisition regimes which involve scanning the data with the probe aligned at different angles, as may be required in vector Doppler studies [76].

2.2 Materials & methods

2.2.1 Phantom scanning system

The following factors were important in the choice of the design of the phantom scanner:

1. A scanning range of 250 by 150 mm to allow for phantoms of major vascular areas including carotid bifurcation and abdominal aorta
2. High resolution and accuracy allowing for reproducible 3D imaging. From manufacturers data (see below) the movement resolution was 150 μm and the accuracy 0.28 mm. This compares with positional accuracies of the order of $\pm 2\text{ mm}$ and resolutions of $< 0.5\text{ mm}$ for freehand 3D acquisition systems [38]
3. Adjustment of the probe angle over the range $\pm 45^\circ$ with respect to the vertical, hence encompassing the typical range of probe angles used in Doppler studies (45° to 80° with respect to the horizontal)
4. Appropriate phantom positioning to avoid disturbance to entry and exit flow conditions.

The phantom scanner was designed to fit a phantom with a maximum outer casing size of 320 by 100 mm. If scans at 45° to the surface of this phantom are made, a total linear travel of 250 by 150 mm is required. Linear motion of the transducer was provided by two Parker 404XR linear positioners (Parker Inc., USA. <http://www.parker.com>)(Figure 2.1(a)). A further linear movement was provided by a sliding clamp mounted to the transducer holder (b). This allows the transducer to be lowered into place in a trough filled with ultrasonic coupling gel on the upper surface of the phantom. The height of the transducer was set once manually at the beginning of the scanning session. The phantom (c) was held underneath the transducer, and the frame (d) rigidly maintains the position of all of the other components.

A manually-operated Parker M2535 rotary table and a custom-built transducer holder allow transducer movement about two different axes. The transducer holder permits adjustment of

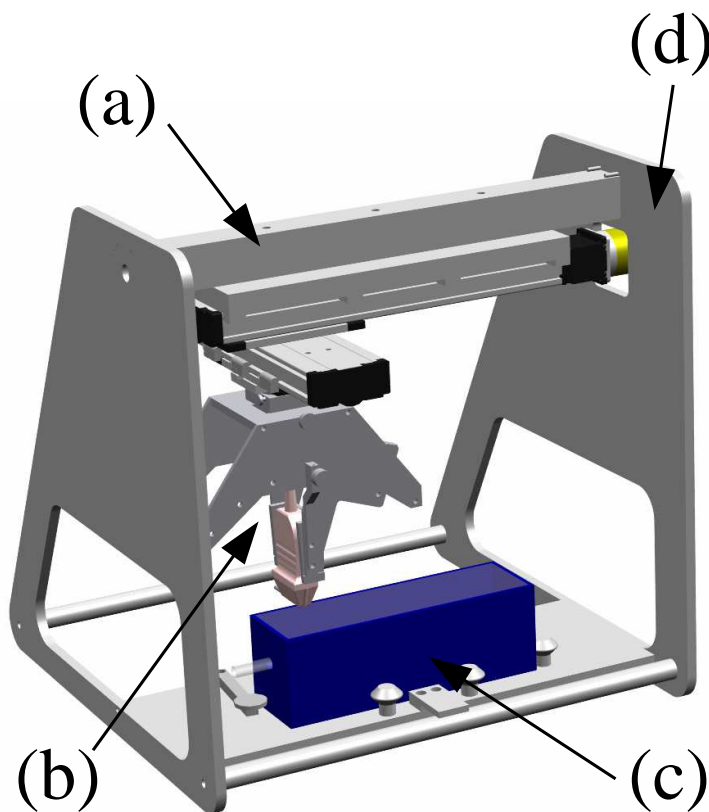


Figure 2.1: A rendered 3D CAD model of the phantom scanner. The linear positioners (a) were mounted above the phantom to lessen the risk of water damage from phantom leakage. The transducer holder (b) moves the transducer vertically and changes its angle to the surface of the flow phantom (c). The frame (d) holds everything in place.

the probe angle over the range -45° to $+45^\circ$ with respect to the vertical, encompassing the typical range of probe angles used in Doppler studies ($45 - 80^\circ$ with respect to the horizontal). While rotated, the transducer must still be in contact with the gel/water layer on the surface of the phantom. By positioning the centre of rotation of the transducer at the centre of the casing, where the array of piezoelectric elements is located, the transducer may be rotated without losing contact (see Figure 2.2).

Holding a US transducer in a plain clamp is difficult due to the curved shape of the casing, which was designed for comfortable manual operation. A mould made from aluminium putty (ITW Devcon, Rushden, UK. <http://www.itw-devcon.co.uk/>) was used to hold the transducer tightly in place.

This range of adjustment provides the flexibility for allowing transverse or axial scans to be acquired, and for changing the angle of the probe for Doppler studies. In addition this provides the facility for angling the orientation of the probe for vector Doppler studies.

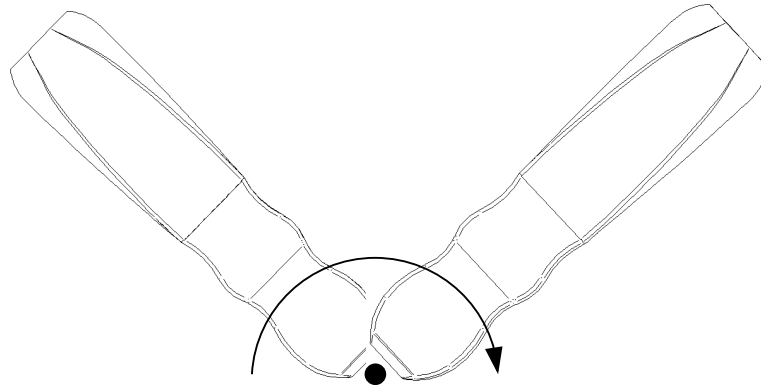


Figure 2.2: *Rotation of the US transducer around the curved surface covering the piezoelectric elements prevents displacement when it is rotated. This is a simple solution to providing a rotation of the transducer about its end axis.*

A clamping system was developed (see Figure 2.3) that could be modified to suit a standard size phantom of dimensions 200 mm long by 100 mm wide. These were positioned with their geometric centre collinear with the origin of the linear positioner coordinate system. Longer and wider phantoms can still be clamped in place by adjusting the rotating clamp arms at the side of the phantom.

Three clamping arms in total were required to hold the phantom in place. These push the phantom against three clamping studs mounted on the base of the phantom holder. This gives six contact points around the rectangular perimeter of the phantom, preventing the possibility of rotation of the phantom while blood mimicking fluid is being pumped through it.

Entry and exit flow conditions inside the phantom should not be altered by the phantom scanner. The phantom is held horizontally below the linear positioners to prevent alteration to the flow. The phantom is not moved at all during the scanning process to further prevent changes. During scanning, the US transducer does not touch the phantom surface directly. The phantom is imaged through a small trough of water or acoustic gel couplant built in to the top surface of the phantom.

Manufacturers tests of the mechanical positioners show a positional accuracy of 30 μm . Thus the main source of positional error is the tolerancing of the design of the rest of the components. The calculated positional error is 0.28 mm. Angular positional accuracy of the rotary table is

0.05°, and that of the transducer holder is 0.1°.

2.2.2 Ultrasound system

A Philips HDI5000 US scanner (Koninklijke Philips Electronics N.V., The Netherlands. <http://medical.phillips.com>) was used to capture 3D datasets. The L12-5 38mm and L7-4 linear array transducers were used with the system. Other transducers could be used with the system easily due to the modular nature of the transducer holder. US images were captured using the ResearchLink function of the scanner, and were downloaded to disk using the HDI Lab program.

2.2.3 Data capture and display

Scanning was performed automatically using the control software. Written using LabVIEW (National Instruments Inc., TX, USA. <http://www.ni.com>), the control software allowed the user to

- set start and end points for automatic scans
- set the distance between each scan
- control the HDI5000 US scanner
- move the transducer
- download scans from the US scanner
- save downloaded scans and their coordinates relative to the phantom scanner.

Automatic control of the scanning process reduces the repetitive task of collecting sequential data from flow phantoms.

Several LabVIEW Virtual Instruments for different operations were used, for example:

- Control of the stepper motor driver for the linear positioners, dealing with starting and stopping movement, changing step size, homing the positional actuators and running programmed moves
- Managing the download of HDI Lab files to disk and saving them in an orderly file structure

- Controlling the HDI5000 US scanner for freezing/unfreezing, downloading scans, changing scanning mode from B-mode to colour Doppler and changing the colour box orientation.

Control of all these different functions was available from the top-level user interface Virtual Instrument. This provides the user with a clear interface for setting up scanning tasks.

US data were captured in the HDI Lab file format, a format proprietary to Philips US machines. Unlike video capture of US data, it records the US image separate to the surrounding information typically seen on US scanner displays. It saves colour Doppler data as velocities and not blue/red colour values, making conversion to data files suitable for import into simulation software less difficult than converting a screen capture. However, to convert data from the HDI Lab image format to graphics files for display, it is necessary to use the HDI Lab program. This becomes problematic for large datasets. A 100 mm long phantom scanned with 0.25 mm between scan planes produces 400 images, which are time-consuming to convert manually using HDI Lab. Therefore software was developed to control the HDI Lab program and thus automate scan conversion. This saves B-mode data as bitmap files, colour Doppler data as an array of velocities and the ECG phase of each image if present.

2.2.4 ECG gating

Phantoms do not have any in-built flow phase signal for triggering acquisition. To provide gated data, the flow signal from the computer controlled pump providing the phantom flow waveform is used to provide an ECG signal. This uses a LabVIEW VI to send a trigger impulse to the phantom scanner control computer. The trigger tells the control software when the next flow waveform begins, allowing the US scanner to acquire over the whole flow waveform cycle. The ECG signal is automatically digitised by the HDI Lab software. With this software, ECG gated images can be downloaded for post processing.

2.2.5 Operation

The use of the phantom scanner can be divided into three different stages:

1. Pre-scan: Send the linear positioners to their home positions. Fit the flow phantom and its associated hardware into place. Clamp the phantom into place. Fit the US transducer

into the clamp.

2. Scan: Choose the step size and length of the phantom to be scanned. Orient the angle of the transducer as required. Choose the step size between scans. Choose the mode of the US scanner. Start scanning.
3. Post-scan: Convert the captured data from the HDI Lab file format to other graphics formats for reconstruction and conversion to data files for input into computational simulation software.

The phantom scanner includes software specific to the Philips HDI5000 for the control of scan settings and the download of data. The transducer holder is also specific to the design of the two linear array Philips HDI5000 transducers that were used. However, should it be required, the software and the hardware can be redesigned to suit other US scanners.

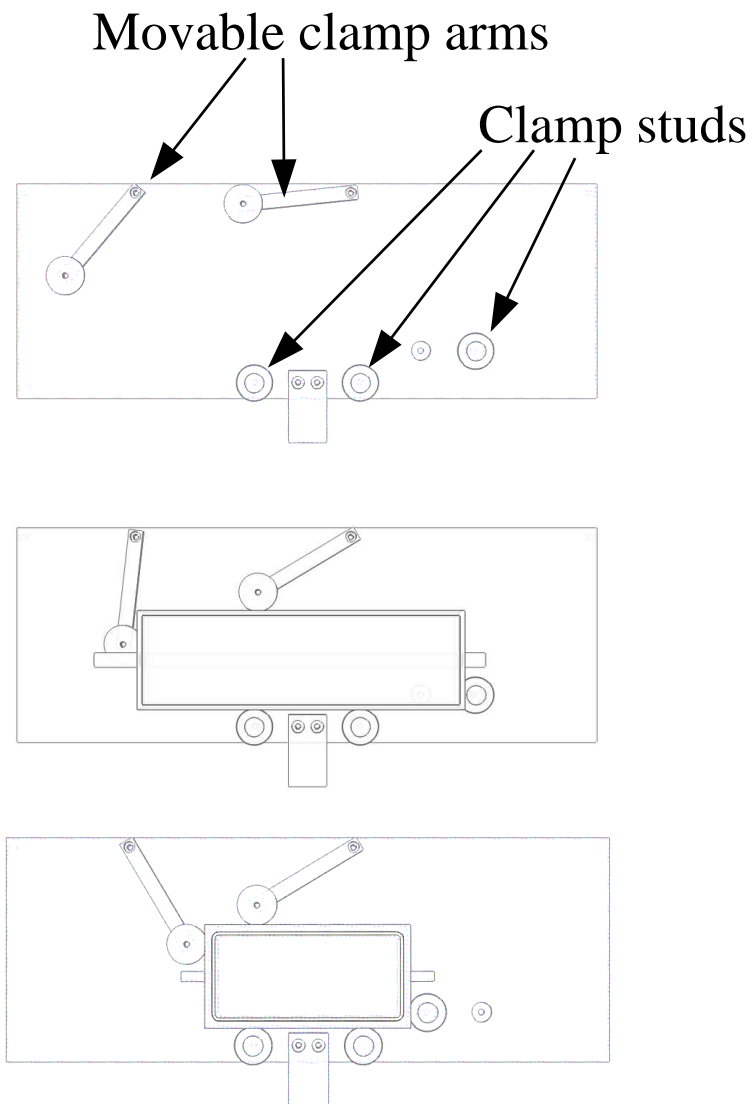
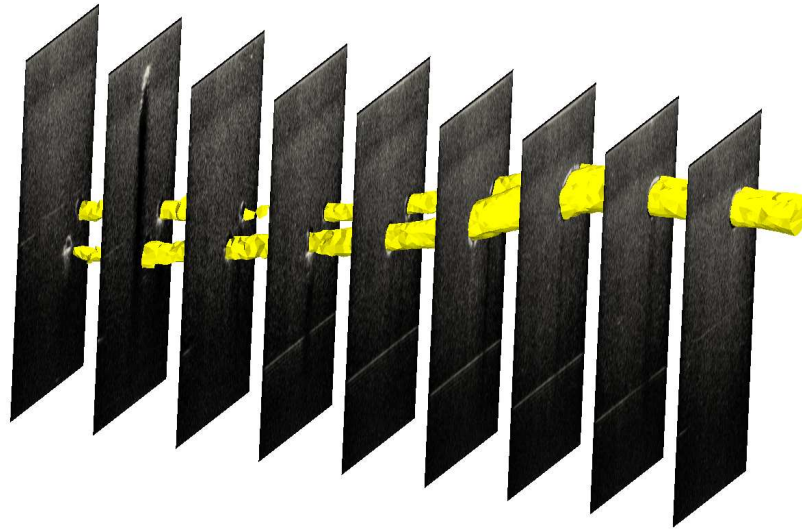


Figure 2.3: *The phantom holder. A clamp secures the phantom in place for scanning (top). The movable clamp arms force the edges of the phantom against the clamp studs. The clamp can easily be reconfigured for use with larger phantoms (centre) or smaller phantoms (bottom).*

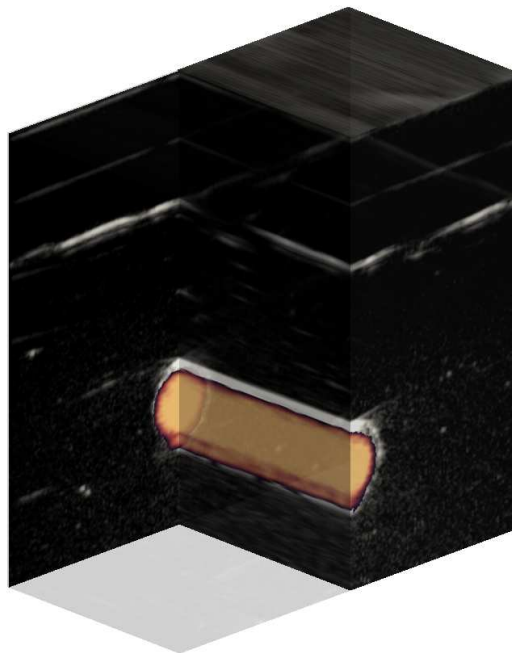
2.3 Results

Captured data comes in the form of regularly spaced US image planes. The image planes can be oriented at various angles to the top surface of the phantom and about the vertical axis of the transducer. Typically, parallel vertical image planes through the phantom were captured to provide phantom geometry images for segmentation. Angled scans were required to build up a 3D velocity map of the flow through the phantom.

3D data requires 3D methods of reconstruction and display. GE MicroView (GE Healthcare, Chalfont St. Giles, UK. <http://microview.sourceforge.net/>) was used to produce 3D volumes of B mode data. Images from HDI Lab files were saved as a sequentially numbered stack of images, then imported into GEM MicroView and converted to VTK format (KitWare Inc., NY, USA. <http://www.vtk.org>). Figure 2.4 shows two examples of reconstructed B mode scans. Figure 2.4a clearly shows the shape of an anatomical carotid phantom. The phantom shape was created by thresholding the greyscale values of each US image corresponding to the interior of the phantom. The thresholded values were then joined together and meshed using the tools in MicroView to create a 3D volume. Figure 2.4b shows images taken from a straight tube wall motion phantom. The power Doppler flow is visible inside the transparent phantom, and part of it has been cut away using MicroView to show internal detail.



(a) A scan of an anatomical phantom with the carotid geometry created from thresholded images and meshed using MicroView.



(b) Power Doppler flow through a straight tube wall motion phantom.

Figure 2.4: Two phantom datasets scanned using the phantom scanner and reconstructed using GEM MicroView.

2.4 Discussion

A phantom scanner suitable for acquiring sequential images from flow phantoms was developed. Flow phantoms are also best suited to mechanical scanning in this manner. Flow phantoms do not move involuntarily and do not experience discomfort during scanning. These are two factors that inherently limit the application of mechanical scanning methods for patients.

Mechanical scanning methods will always give the highest accuracy and most controllable image spacing. This is demonstrated in Table 2.1 where the mechanical systems have up to half the image spacing of most freehand scanning systems reported in the literature. Accuracy and image spacing are important features for developing anatomically accurate computer models of arteries. However, more important when applying 3D scanning methods to patients are comfort for the patient and controllability while scanning. Mechanical 3D scanning systems that have fixed positioners may be difficult to move into a comfortable position for scanning a patient. They may also have difficulty in accommodating obese patients, depending on the design of the positioners. A fixed, highly accurate positioner that moves in a straight line would be difficult to conform to the curved deformable anatomy of a patient, especially in the abdomen where considerable pressure may have to be applied through the positioner to acquire good quality images.

It would be highly desirable to attain the level of accuracy and fine control over image spacing possible with a mechanical scanning system like the phantom scanner. However, the development required to create a flexible scanning system able to scan carotids and femorals (like that developed by Fenster [43]) and also the abdominal aorta makes a more flexible though less accurate freehand scanning system more attractive for *in-vivo* scanning.

Group	Type of system	Image spacing (mm)	Notes
[28]	Mechanical	0.1	no gating
[77]	Magnetic freehand	0.03	no gating
[43]	Mechanical	0.5	ECG gated
[78]	Magnetic freehand	1.0	ECG gated

Table 2.1: Slice spacing recorded in the literature for various 3DUS systems designed for scanning patients.

2.5 Conclusion

A 3D US system for scanning flow phantoms was developed. The system uses mechanical positioners to give repeatable and accurate positioning of the US transducer on the flow phantoms. Angled scans at up to 45° to the surface of the phantoms can be made to provide full 3D Doppler flow data. Despite the high accuracy and controlled image spacing possible when scanning phantoms, it is more desirable to develop freehand methods of scanning patients due to the higher flexibility and control required.

Chapter 3

Characterisation of a 3D freehand ultrasound system

3.1 Introduction

Having discounted an adaptation of the mechanically-controlled 3DUS system described in Chapter 2, an alternative system has to be specified for creating patient-specific artery geometries from 3DUS data. A freehand system was chosen based around the Stradwin 3DUS program. Stradwin is a MicrosoftTMWindows-compatible variant of the Stradx 3DUS program [53]. It acts as a control and reconstruction program, recording position sensor data and a video stream (or raw radiofrequency (RF) data capture card datastream) and reconstructing the video images with the positions to create 3D visualisations of US data. Uniquely it does not remap the US data at capture into an array of voxels. This reduces loss of resolution and interpolation artefacts at capture. Figure 3.1 shows a screenshot of the Stradwin program showing reconstructed 3DUS data from a healthy volunteer abdominal aorta scan. Stradwin comes with several useful functions, including:

- A spatial calibration routine to determine the position of the US image relative to the position of the position sensor tool.
- Reconstruction routines to create arbitrary reslices (in a similar manner to voxel-based reconstructions of 3DUS data) through any part of the dataset post-acquisition.
- A routine to remap the Stradwin data file into a voxel-mapped 3D array for processing with other medical image processing software.
- Simple manual segmentation and mesh generation tools.
- Facilities to export images from the Stradwin data file to other 2D image formats (e. g. Windows bitmap format or Portable Network Graphics (PNG) format).

Stradwin is compatible with several different types of position sensor to suit the application and budget of a variety of research tasks. Published use of the Stradwin and Stradx software has considered its high accuracy [38], techniques for displaying 3DUS data [79], spatial calibration routines [80, 81] and some clinical applications [24].

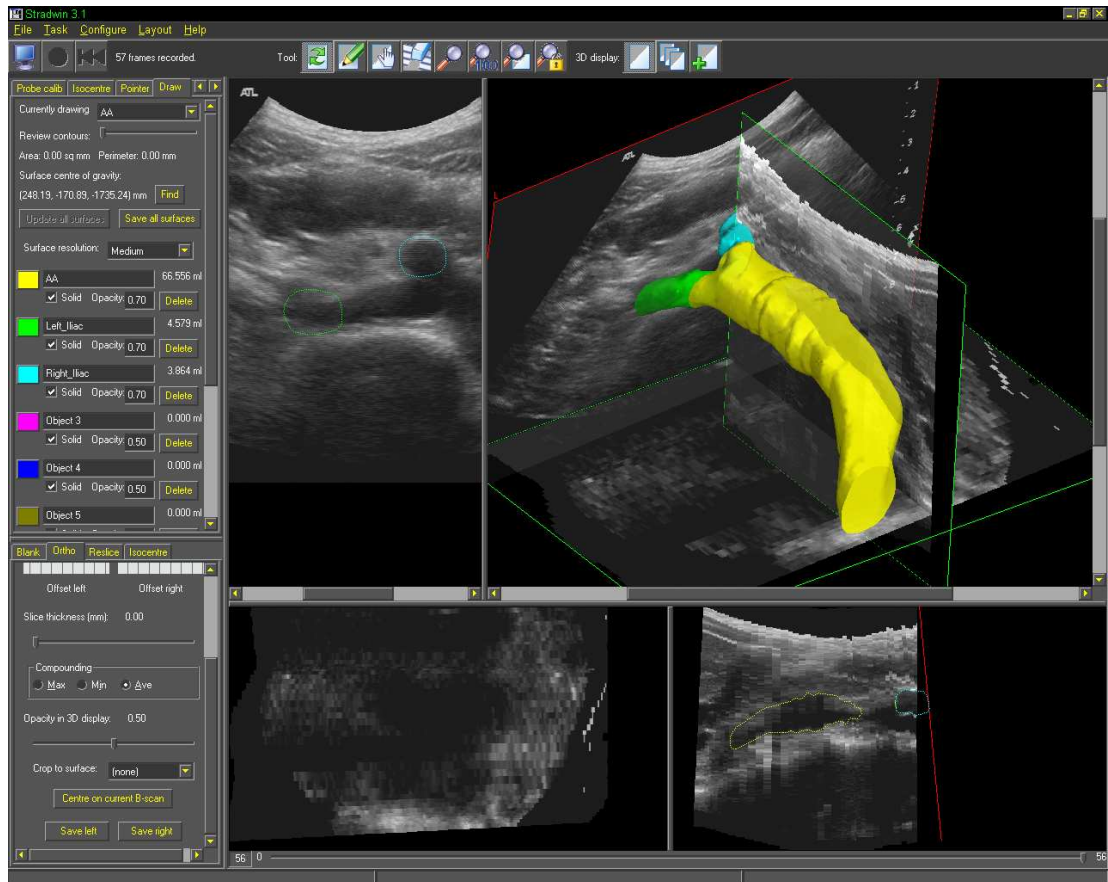


Figure 3.1: A screenshot from the Stradwin program. A hand-segmented abdominal aorta 3D model is visible in the top right-hand pane superimposed on the 3DUS data. Two arbitrary reslices through the data are also visible in the lower two panes. The left-hand pane shows the position of two segmented contours of the iliac arteries superimposed on an individual US image.

The performance of any 3DUS system in clinical practice is influenced by many different sources of error. In the assessment of the Stradwin system, it is important to recognise which sources of error can be controlled and quantified. The following errors are intrinsic to most 3DUS systems:

- US image errors

- Beam width, which can cause over-estimations of length in transversely scanned anatomy [82]
 - Image resolution, which varies across the image with the transducer depth setting and the position of the focal zones
 - Directionality of the US beam, which causes shadowing artefacts which are especially important in examining plaque in diseased patients. SonoCT compounding can reduce this artefact [23] but does not remove it completely.
 - Sensitivity to settings. If TGC or overall gain controls are not correctly set, some areas of the image may appear saturated or shadowed on the scanner display.
- Position sensor errors
 - Position sensor accuracy varies within the visible volume of the sensor [83, 84] and cannot be calculated if the position sensor tool is moved outside of the visible volume.
 - Other acquisition system errors
 - Calibration of the position of the US image to the measured position from the position sensor tool
 - Artefacts from the conversion of analogue video to digital images.

It is important to distinguish between sources of error that can be controlled, and sources of error that cannot be controlled. Sources of error associated with the patient are most difficult to control and likely to be most significant. Motion of the arteries due to pulsatile blood flow, motion of the abdominal aorta due to breathing, and patient movement due to discomfort affect acquisition of data. Errors associated with the US scanner often cannot be changed — there is limited control available over the quality of the image and the artefacts generated in scanning. It is up to the user of the machine to correctly set up the presets and focal zones of the machine for each specific acquisition. Beyond this, little can be done to improve sources of error associated with image quality. Some errors are inherent limitations of the technique chosen to capture images - for example the video data stream has a fixed low frame rate (25 Hz) relative to the refresh rate of the US machine (around 50 Hz, dependent on transducer frequency, depth setting and the number of focal zones). This mismatch in refresh rates can affect the spatial resolution of the captured 3D data [85].

An additional source of error is generated when the position sensor tool is removed from the transducer holder, or when the transducer holder is removed from the transducer. This renders the calibration useless and should require a recalibration of the system after each removal/replacement of the position sensor tool. Best practice would ensure that the transducer holder and position sensor tools are never removed from the transducer once calibration has been carried out. However, when more than one transducer is to be used, or where an US machine is to be shared with other users, removal of the tool and transducer holders is often necessary. It is possible to calculate the reduction in calibration precision as a result of removing either of these devices from the transducer.

This chapter will assess the reconstruction accuracy of the Stradwin 3DUS system using two test phantoms. The calibration precision and the effect of removal and replacement of the position sensor tool and the transducer holder will be considered. Some recommendations for best practice in 3D freehand scanning based on these results will be given.

3.2 Methods

3.2.1 3D US system

The main hardware components used with the Stradwin freehand 3D US program are as follows:

- Philips Medical Systems HDI5000 US machine
- NDI Polaris optical position sensor system (Northern Digital Inc., ON, Canada. <http://www.ndigital.com>)
- Traxtal Adaptrax multi-angle position sensor tool (Traxtal Inc., ON, Canada. <http://www.traxtaltech.com>)
- PC with a video capture card (Hauppauge Computer Works Inc., NY, USA. <http://www.hauppauge.com>).

The system is shown as set up in Figure 3.2. The HDI5000 US machine is a high-end clinical system, widely used for many types of US examination. An optical position sensor was used because of its superior positional accuracy compared to magnetic position sensors [85]. The

optical system can suffer from line-of-sight issues —if the position sensor tool is covered or rotated away from the cameras, the position sensor cannot record the position of the transducer. To minimise this problem, a Traxtal Adaptrax multi-angle tool was used. This allows a wider range of orientations of the transducer without it disappearing from view. A Hauppauge PCI-FM WinTV video capture card was used. This is compatible with the Microsoft™DirectCapture interface used by Stradwin to record images from the S-video connector of the US machine.

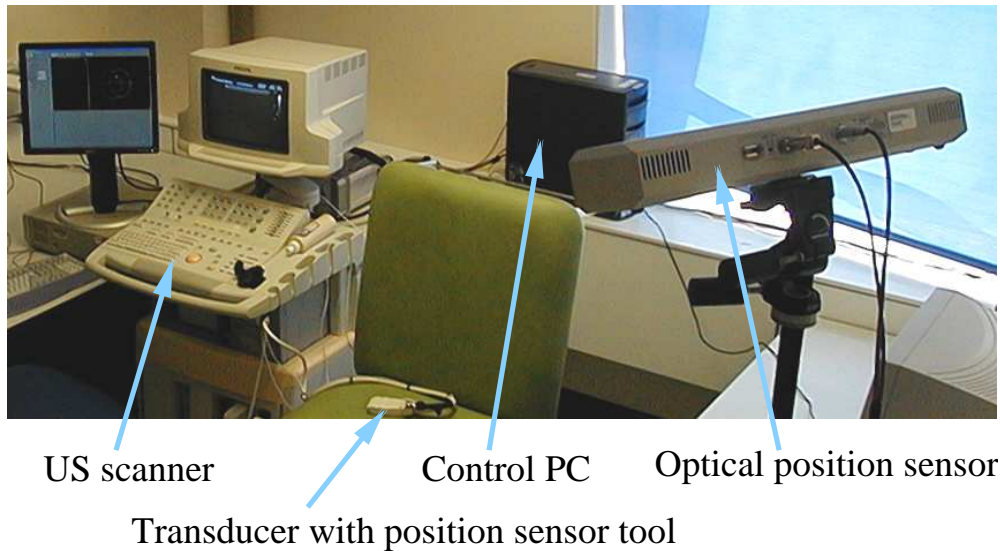


Figure 3.2: *The 3D US system*

3.2.2 Assessing whole system accuracy (3D reconstruction accuracy) using a test phantom

Two different phantoms constructed by CIRS (Computerized Imaging Reference Systems Inc., VA, USA. <http://www.cirsinc.com>) were used to assess whole system accuracy. The two phantoms were designed to assess point precision accuracy (or *3D reconstruction accuracy*) and *volume reconstruction accuracy* of a 3DUS system. The CIRS 055 phantom consists of two egg-shaped volumes mounted in a block of Zerdine™ tissue mimicking material [86] (Figure 3.8). The acoustic impedance of each egg-shaped volume is different to that of the surrounding material, giving a difference in contrast between the eggs and the background when imaged with an US scanner. To provide a calibrated reference, during manufacture the volume of each egg is measured before insertion into the tissue mimic. A US scan of the eggs allows the user to calculate the volume of the eggs using the measurement tools provided with most clinical US scanners. Alternatively, the reconstruction tools of the Stradwin program can be used to

measure the volumes.

The CIRS 055A phantom consists of a set of 0.1 mm diameter wire filaments arranged as shown in Figure 3.3. A panoramic scan, where the transducer is moved sideways along the top surface of the phantom, produces a set of images which allows the point precision accuracy to be measured. A raised ledge along the top surface of the phantom allows the user to move the transducer in a straight line along the phantom surface. An individual image showing the orientation of the filaments is shown in Figure 3.4. A panoramic reconstruction of a sweep along the length of the surface of the phantom is shown in Figure 3.5. Using the “Landmark” tool in Stradwin, the distances between filaments may be measured from individual images in the US dataset and compared with the specification of the phantom. It is important that the filament positions should not be measured from the panoramic reconstruction of the 3DUS scan of the CIRS 055A phantom. Overlapping images of the same filament often result in a broadened image of the filament as shown in Figure 3.6a. Instead, an image at the start of the sweep, one centred over the middle triangular arrangement of filaments, and one at the end of the sweep were used to measure filament position. The position of each filament in these images was measured from the centroid of the bright spot marking each filament (Figure 3.6b).

Scans of both phantoms were performed using the L12-5 38mm linear array and the C5-2 curvilinear array transducers. The settings and presets for each transducer are listed in Table 3.1.

Frequency	7 MHz (L12-5) or 3.5 MHz (C5-2)
SonoCT	On, set at Target using the FR RATE optimisation control
Depth setting	3.9 cm or 7.0 cm depending on the depth of the egg or row of filaments to be measured (L12-5) or 8.7 cm (C5-2)
Focal zones	One focal zone set close to the centre of each egg phantom (CIRS055). One focal zone set to close to the height of the row of filaments to be measured (CIRS055A)
TGC controls	set to the centre of their sliders
2D gain	Sufficient to produce adequate contrast to enable thresholding of egg shapes (CIRS 055). Low enough to distinguish the filament reflection from the background speckle (CIRS 055A).
Preset	Cardiovascular/Carotid (L12-5) or Abdominal/Aorta (C5-2)

Table 3.1: *US scanner settings used in scanning the CIRS phantoms.*

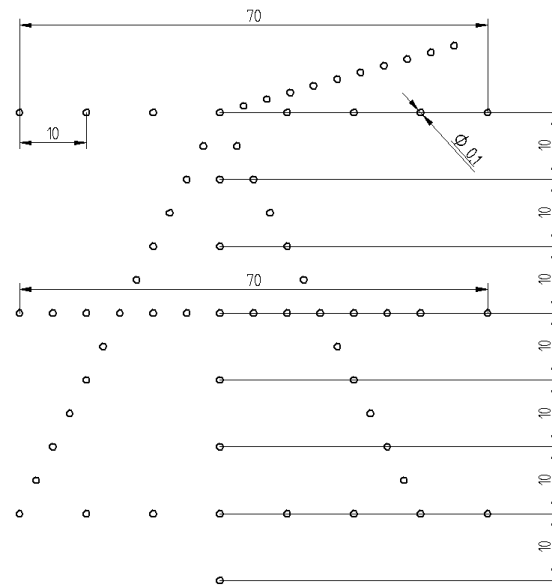


Figure 3.3: Dimensions of the filaments in the CIRS 055A phantom.

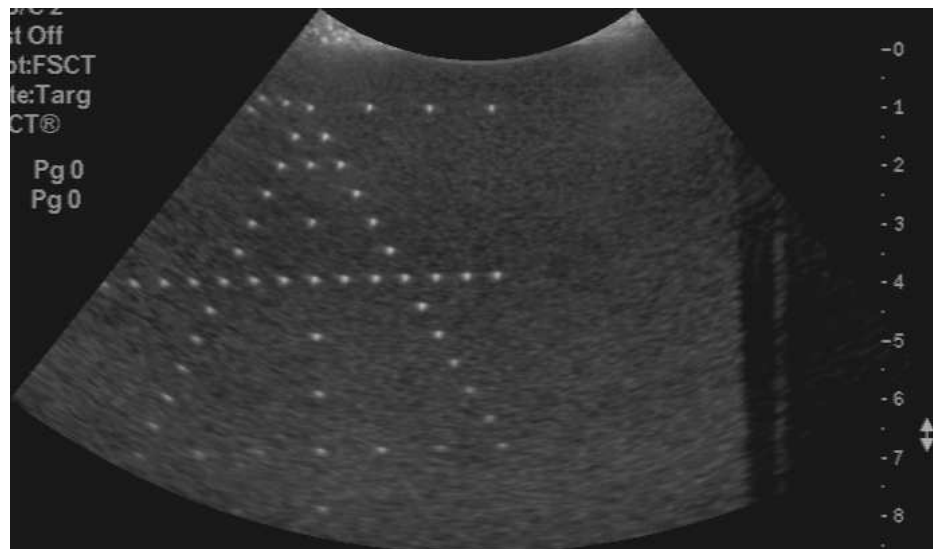


Figure 3.4: An image of the CIRS055A phantom showing the arrangement of filaments.

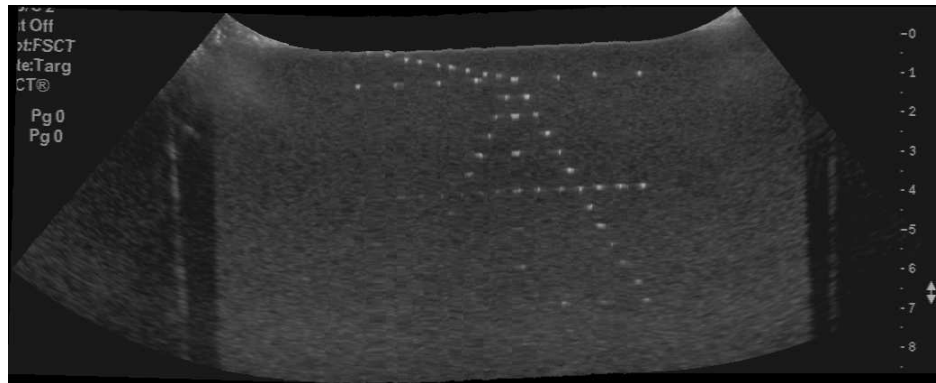
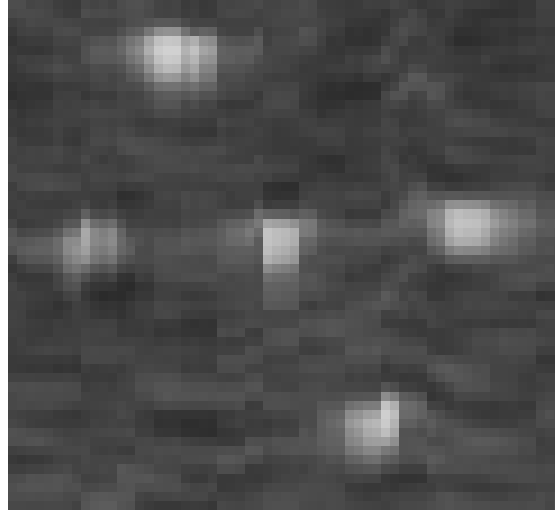
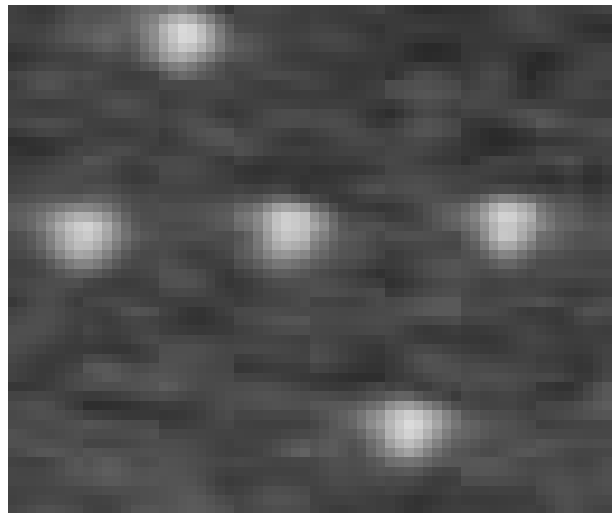


Figure 3.5: A reconstructed panorama from a 3DUS scan of the CIRS 055A filament phantom.



(a) A closeup of a panoramic 3DUS scan of the CIRS055A filament phantom. The panorama reconstruction uses data from several different image planes each with slightly different positions and orientations, resulting in blurred and extended cross-sections of the filaments.



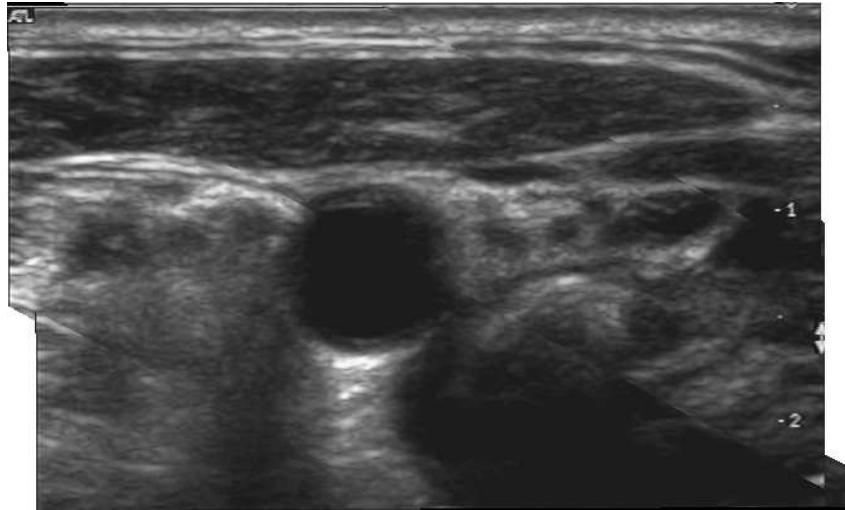
(b) A closeup of a single image in a panoramic scan of the CIRS055A filament phantom. The filament shapes are more defined and uniform than in the reconstructed panorama image.

Figure 3.6: A comparison of images of the CIRS055A filament phantom from a panoramic reconstruction of a 3DUS scan and a single image of the filament phantom.

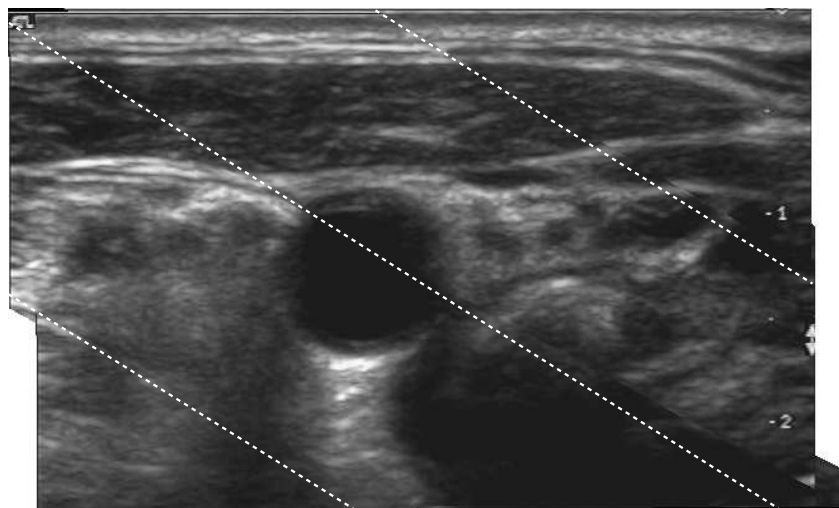
3.2.2.1 3D reconstruction accuracy

3D Reconstruction accuracy is defined as the ability of the whole 3DUS system to correctly reconstruct a given 3D object [22, 38, 85]. It assesses every part of the system used in normal scanning, and encompasses all errors generated by the US machine, the position sensor and the acquisition software. Conventionally it is calculated by scanning a phantom of known geometry, generating a 3D reconstruction of the phantom, and comparing the position of key objects in the reconstruction (e.g. wire filaments, well-defined features of an object) with the specification of the phantom. Reconstruction accuracy is often used to refer to the accuracy of a voxel-mapped dataset created from the individual US images and the position sensor data [53]. However, voxel mapping was not used in this case because it reduces resolution and adds interpolation artefacts between individual slices of the volume (see Figure 3.7). 3D reconstruction accuracy as used here shall refer to the ability of the system to position US images in three-dimensional space as measured by the reconstruction functions of the Stradwin program. It is calculated by measuring the position of two wire filaments on a single US image from a 3DUS dataset, then calculating the distance between them. This distance is related to the specification of the wire filament phantom which gives the actual distance between those two elements. The difference between the measured distance and the actual distance from the phantom specification is the reconstruction accuracy. For a set of measures of reconstruction accuracy, the reconstruction precision can also be calculated. This is the 95% confidence interval of the set of precisions calculated from the same two filament positions. This gives an indication of the variation in 3D reconstruction accuracy which is usually related to image resolution and therefore US transducer frequency and depth setting.

It is important to note that with a wire filament phantom, measures of reconstruction accuracy can be made both horizontally and vertically with respect to the US image. Vertical accuracy measures depend mainly on the settings used during acquisition (e.g. number of focus zones, gain settings, angle of the transducer relative to the plane defined by the wire elements). Using only a vertical measure to assess accuracy only allows the contribution of image acquisition settings to overall system accuracy to be measured. Using a horizontal measure allows the contribution of reconstruction errors from the whole 3DUS system (US scanner, position sensor, calibration and reconstruction technique) to be measured.



(a) A voxel mapped image from a carotid artery 3DUS scan.



(b) The voxel mapped image with lines added showing the position of banding artefacts due to interpolation.

Figure 3.7: *Banding artefacts due to interpolation from remapping 3DUS images to a voxel dataset. The 3DUS dataset was remapped to a voxel grid using Stradwin. An image was extracted from part of the voxelised dataset (Figure (a)). The image has several diagonal bands that are added from an interpolation routine to fill in the gaps between freehand 3DUS images (see Figure (b)). The artefacts have created a jagged effect on the outline of the lumen at each side.*

3.2.2.2 Volume reconstruction accuracy

Volume reconstruction accuracy is defined as the ability of a 3DUS system to measure the volume of a known test object. Carson [22] gives a suggested phantom layout which is that found in the CIRS 055 volume phantom. This phantom consists of two egg shaped volumes encased in ZerdineTM, as described above. The two volumes were measured before being placed in the tissue mimic, giving accurately known volumes (see Table 3.2). The phantom was scanned using the C5-2 abdominal US transducer at the 8.7 cm depth setting. It was then segmented using Stradwin to produce rendered images of the egg-shaped volumes and calculate their volume (see Figure 3.8). Volume calculations for the volume reconstruction phantom could only be carried out for the C5-2 transducer. The acoustic attenuation of the phantom was too high for the L12-5 transducer to produce an image clear enough for thresholding (see Figure 3.9).

Large egg volume (ml)	Small egg volume (ml)
72.4	7.2

Table 3.2: *Volumes of the two egg shaped objects in the CIRS 055 volume reconstruction phantom. Each egg was measured at manufacture before being set in Zerdine.*

Measurement of the volume of the eggs is carried out using either the measurement tools on the US scanner console, or by using the reconstruction tools of the Stradwin 3DUS system. If the US scanner console measurement tools (to measure the length or diameter of an egg) are used, a formula that calculates the volume of the egg given the maximum diameter or length of the egg is used. However, using the measurement tools on the US scanner console is subject to the skill of the user: if the egg-shaped volume is not measured at the position where the full length of the egg can be seen, the volume estimation is incorrect. In addition, using only the US scanner measurement tools does not measure the volume reconstruction accuracy of the Stradwin 3DUS system, but only the imaging capabilities of the US scanner. Both measurement methods are sensitive to US system settings, especially the gain setting used during acquisition. For scanning the egg phantoms, gain should be set so that the eggs are clearly visible against the background of the rest of the phantom. If the gain settings are too high, the outline of the egg/background interface is made brighter, and the apparent egg area on that image is reduced. The gain settings in each acquisition used to calculate volume reconstruction accuracy were set at a level sufficient to image the shape of the cross-section of the egg volume without overfilling or underfilling the egg cross-section. The same gain settings were used for each acquisition.

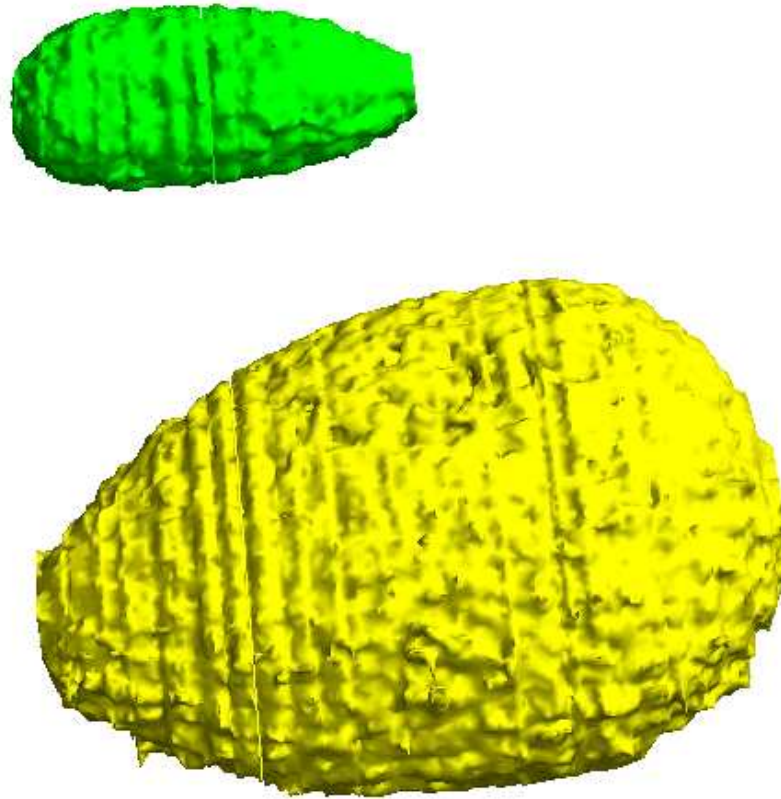


Figure 3.8: A view of the two egg-shaped volumes of the CIRS 055 volume reconstruction phantom created using the segmentation tools of Stradwin.

If a simple thresholding technique is used to measure the area of the egg on each image and thus the volume of the whole egg, areas inside the egg may not be included in the thresholded area. This reduces the estimated area of the egg. In order to counter this effect, a semi-automatic threshold-based segmentation technique was used with a custom designed LabVIEW Virtual Instrument (VI) (see Appendix F, section F.2.3). Each image was thresholded: greyscale levels from 0 to 99 (out of a possible 256 levels of grey) were selected from each image. To prevent other structures and noise from affecting the volume calculation, a region of interest (ROI) tool was used to select only the area of the US image containing the egg. The segmented area was then filled using the “IMAQ Fill Holes” function in LabVIEW. An image of one of the eggs before thresholding, after thresholding and after filling the segmented area using the “IMAQ Fill Holes” function is shown in Figure 3.10. The segmented images were saved as a Stradwin file and imported into Stradwin. The images were semi-automatically drawn around using the Stradwin drawing tools, then the volume of a surface fitted through all the segments (again

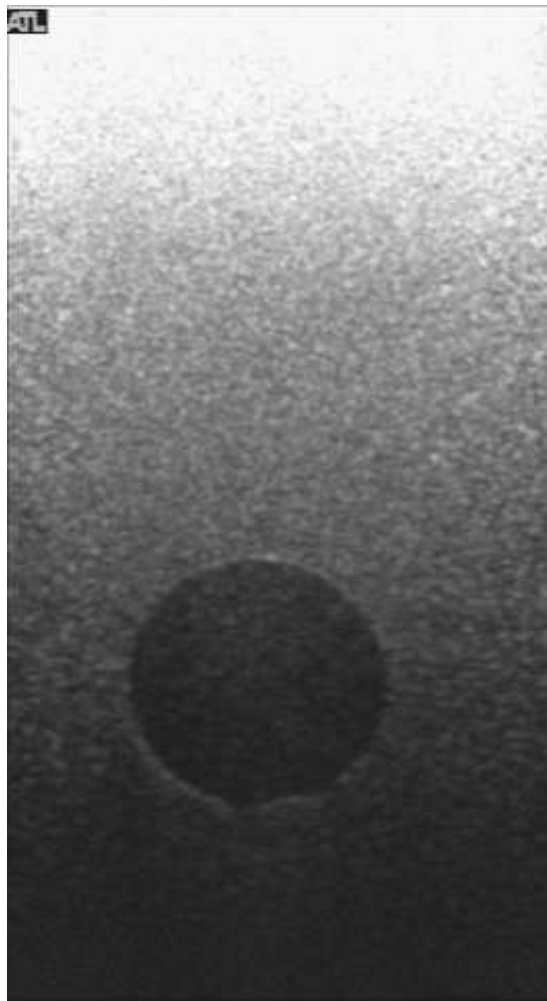


Figure 3.9: A highly attenuated image of the smaller egg-shaped volume of the CIRS 055 volume reconstruction phantom. The egg-shaped volume could not be thresholded clearly enough to calculate its volume.

using the Stradwin drawing tools) was measured. A measurement of egg volume from five separate 3DUS scans for each egg was made to establish the precision of volume estimation.

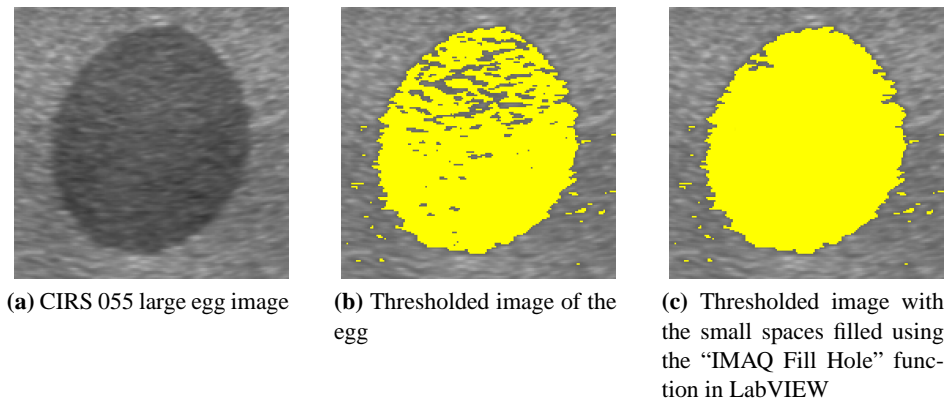


Figure 3.10: *Filling in small spaces in the thresholded image of the CIRS 055 olume reconstruction phantom.*

3.2.3 Assessing calibration precision

Calibration precision measures the limit of calibration accuracy to influence the reconstruction accuracy of the entire system. It is dependent on the following factors:

- Calibration method [80, 85]
- US settings (beam width, transducer frequency, focal zones, depth setting)
- Position sensor accuracy
- Rigidity of the mounting of the position sensor tool to the transducer.

The calibration method has an effect on the calibration accuracy. The two transducers used in this study were calibrated using two different methods. The L12-5 transducer was calibrated using a bar phantom developed by Prager et al. [80] and modified for use with the two Philips transducers. A calibration was carried out for every depth setting. The C5-2 transducer was calibrated using a flat surface mounted in a water bath, using a set of prescribed motions described in [80]. A flat sheet of acoustic absorber was used. This gives an image of a clear flat line without the reverberation artefacts that may be seen when scanning a flat aluminium plate. The depth and large field of view of the C5-2 transducer made the bar phantom unsuitable for use as a calibration device with this transducer. The bar was mounted too close to the piezoelectric elements (see Figure 3.11) which made it difficult for the Stradwin calibration routine to recognise the position of the surface of the bar.

In normal use, where freehand scanning is used in the calibration process, the calibration *accuracy* cannot be calculated. Calibration in this case is a set of translations and rotations that are derived from images of an assumed shape (a flat surface or a flat bar) and position sensor data. No attempt at directly measuring the calibration parameters is attempted. To do so would require a specially designed test rig like that developed by Gee et al. [81]. This rigidly mounted the transducer and transducer holder with the optical position sensor tool in a specially designed jig, and moved three wedge-shaped reflectors into the centre of the beam, coincident with the plane of the US image. The accurately-constructed jig on which the reflectors were mounted, combined with the transducer holder, allowed the position of the image relative to the transducer holder to be measured directly. The expense and complexity of this system puts it beyond the reach of most research groups.

To calculate the calibration precision, five calibrations were carried out at one depth setting for each transducer. The 95% confidence interval was calculated for each of the eight calibration resources shown in Table 3.3. The settings used in the Stradwin calibration function are recorded in Table 3.4.

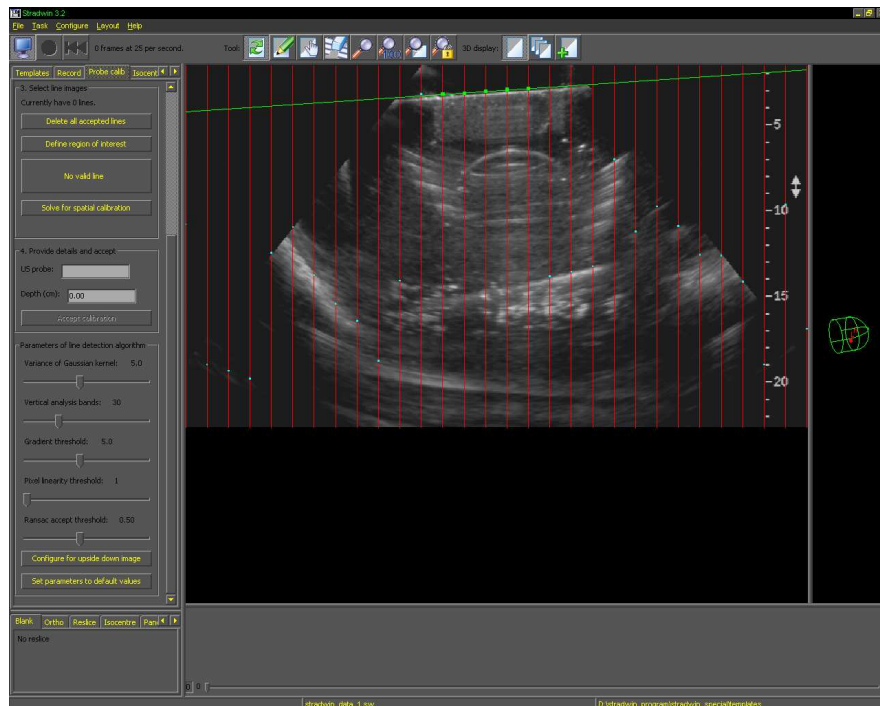


Figure 3.11: Using the larger depth settings of the C5-2 transducer, the Stradwin calibration facility cannot clearly image the top surface of the bar.

RES_XTRANS	Translation in x axis (cm)
RES_YTRANS	Translation in y axis (cm)
RES_ZTRANS	Translation in z axis (cm)
RES_AZIMUTH	Rotation about x axis (degrees)
RES_ELEVATION	Rotation about y axis (degrees)
RES_ROLL	Rotation about z axis (degrees)
RES_XSCALE	Pixel scaling in x axis (cm/pixel)
RES_YSCALE	Pixel scaling in y axis (cm/pixel)

Table 3.3: Parameters calculated from calibrations performed with Stradwin. These resources are saved in the .swt template file created for each calibration.

Setting	L12-5 38mm	C5-2
Variance of Gaussian kernel	5.0	5.0
Vertical analysis bands	30.0	60.0
Gradient Threshold	5.0	5.0
Pixel Linearity Threshold	1.0	1.0
Ransac Accept Threshold	0.70	0.2

Table 3.4: Calibration settings used for the Stradwin calibration procedure for the L12-5 38mm and C5-2 transducers.

3.2.4 Assessing precision of optical tool and transducer holder replacement

When a US machine is shared among several different users, it is often necessary to remove the optical sensor tool and the transducer holder from the US transducer. Also, where only one optical sensor tool is available due to their expense, it is often necessary to swap the tool between scanheads. If a volunteer in a research study requires both a superficial artery and the abdominal aorta to be scanned, it is not desirable to add extra time to the volunteer's appointment while a full recalibration is carried out. Therefore it is important to assess the significance and effect of removal and replacement of the transducer holder and the optical position sensor tool.

An assessment of the replacement precision of the transducer holder and the optical tool was made by removing:

1. The transducer holder and optical tool as a connected unit from the transducers
2. The optical position sensor tool from the transducer holder.

To test replacement precision of the transducer holder, the transducer assembly was clamped onto a workbench and the transducer holder and tool were removed from the transducer (see Figure 3.12). For assessment of the repeatability of the mounting of the optical tool, the rod for the tool was mounted to a sheet of aluminium plate which was clamped to a workbench (see Figure 3.13). The optical tool was then removed and replaced from the rod. Ten measurements of the position of the tool were made using the NDI Polaris optical position sensor. This process was repeated ten times for both operations. The precision of the location of the position sensor tool was then calculated.

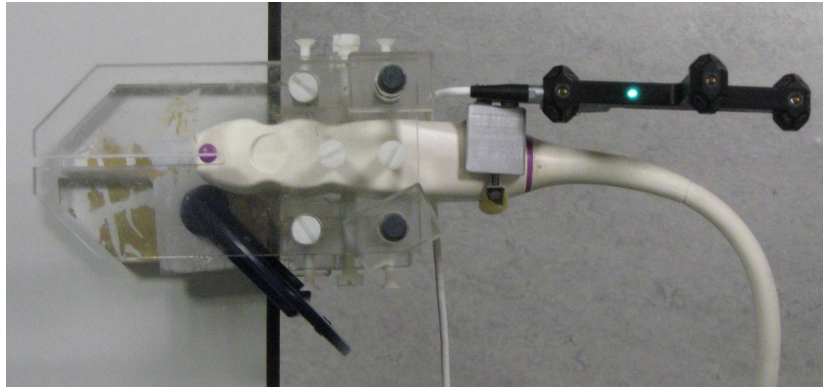


Figure 3.12: *The L12-5 transducer clamped to a workbench to assess replacement precision of the transducer holder.*

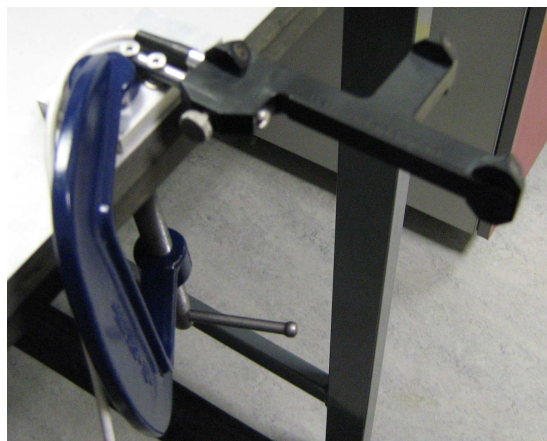


Figure 3.13: *The Traxtal Adaptrax optical position sensor tool clamped to a workbench to assess tool replacement precision.*

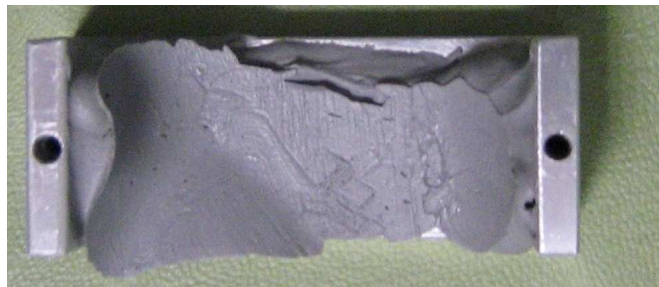
The design of a transducer holder is dependent on the shape of the transducer. Transducers with rectangular or uniformly shaped casings lend themselves to the type of transducer holder design used by Treece et al. [38]. However, many transducers feature ergonomically shaped asymmetric casings with compound curves and few planar surfaces (see Figure 3.14a). The

C5-2 transducer has an especially irregular casing design with an indent in the rear for the sonographer's fingers. To enable an optical tool to be mounted to this transducer an aluminium channel was used which was sized to the largest dimension on the upper part of the transducer casing. An impression was made of the rear of the transducer using aluminium putty. The putty was laid into the channel and the transducer was covered with a thin smearing of petroleum jelly. The transducer was then pressed into the putty until an impression of the transducer was clearly made (see Figure 3.14b). It was then left to harden. Once hardened, the transducer was removed and the transducer holder was ready for use.

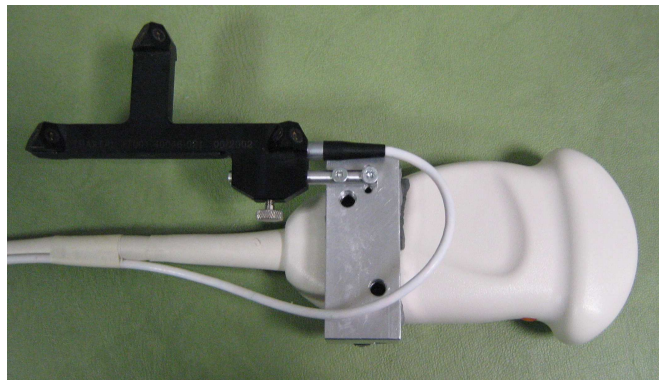
The L12-5 transducer has a symmetrical design with a conical upper end (Figure 3.15). A CAD model was made of this transducer developed from measurements made using a vernier caliper. Using this model, a tapered channel was designed with a spring steel bar to hold the transducer in place. The blunt edged bar was covered with rubber tubing to prevent scratching the transducer.



(a) C5-2 transducer



(b) C5-2 transducer holder



(c) C5-2 with Adaptrax

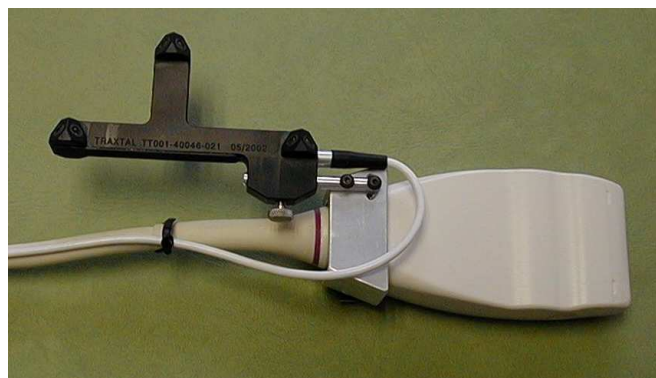
Figure 3.14: *The C5-2 curvilinear array transducer and the transducer holder designed to hold the Traxtal Adaptrax optical tool.*



(a) L12-5 transducer



(b) L12-5 transducer holder



(c) L12-5 with Adaptrax

Figure 3.15: The L12-5 38mm linear array transducer and the transducer holder designed to hold the Traxtal Adaptrax optical tool.

3.3 Results

3.3.1 Reconstruction accuracy

The reconstruction accuracy for the two transducers are listed in Table 3.5. Reconstruction precision is shown in Table 3.6. Volume reconstruction error using the egg phantom is recorded in Table 3.7 for the C5-2 transducer.

Transducer	Depth setting (cm)	Horizontal accuracy (mm)	Vertical accuracy (mm)
C5-2	8.7	0.18	1.84
L12-5	7.0	0.58	0.91
L12-5	3.9	0.17	0.68

Table 3.5: *Reconstruction accuracy of filament position for the two transducers.*

Transducer	Depth setting (cm)	Horizontal precision (mm)	Vertical precision (mm)
C5-2	8.7	± 0.37	± 0.23
L12-5	7.0	± 0.47	± 0.06
L12-5	3.9	± 0.35	± 0.08

Table 3.6: *Reconstruction precision of filament position for the two transducers.*

	Large egg volume (ml)	Small egg volume (ml)
Volume from automatic thresholding	69.30 ± 0.26	6.27 ± 0.11
Actual egg volumes	72.40	7.20
Reconstruction error	3.10	0.93

Table 3.7: *Volume reconstruction error of the 3D US system using the C5-2 transducer.*

3.3.2 Calibration Precision

Calibration precision for the L12-5 transducer at the 3.9 cm depth setting using the Cambridge phantom is shown in Table 3.8. The same results for the C5-2 transducer appear in Table 3.9.

Parameter	Mean	95% Confidence limit	Unit
RES_XTRANS	135.31	1.20	mm
RES_YTRANS	-53.51	0.27	mm
RES_ZTRANS	-23.86	0.57	mm
RES_AZIMUTH	89.46	0.08	degree
RES_ELEVATION	0.07	0.05	degree
RES_ROLL	180.91	0.72	degree
RES_XSCALE	0.008136	0.000007	cm/pixel
RES_YSCALE	0.008136	0.000007	cm/pixel
Reported RMS error	0.047842		cm
No. of calibration lines	163.6		

Table 3.8: Analysis of five calibrations of the L12-5 transducer at the 3.9 cm depth setting, showing mean calibration parameters and the 95% confidence limit for each parameter.

Parameter	Mean	95% Confidence limit	Unit
RES_XTRANS	118.32	1.30	mm
RES_YTRANS	-116.99	0.11	mm
RES_ZTRANS	-23.45	0.50	mm
RES_AZIMUTH	91.30	0.06	degree
RES_ELEVATION	3.47	0.15	degree
RES_ROLL	-179.52	0.55	degree
RES_XSCALE	0.023002	0.000035	cm/pixel
RES_YSCALE	0.023002	0.000035	cm/pixel
Reported RMS error	0.079392		cm
No. of calibration lines	168.0		

Table 3.9: Analysis of five calibrations of the C5-2 transducer at the 8.7 cm depth setting, showing mean calibration parameters and the 95% confidence limit for each parameter.

3.3.3 Optical tool and transducer holder replacement precision

Table 3.10 presents the replacement precision values for the four different sets of experiments to calculate replacement precision.

Replacement precision value	x (mm)	y (mm)	z (mm)	α ($^{\circ}$)	β ($^{\circ}$)	γ ($^{\circ}$)
Adaptrax rod on transducer holder	± 0.13	± 0.15	± 0.18	± 0.11	± 0.06	± 0.11
Adaptrax on rod	± 0.03	± 0.01	± 0.13	± 0.02	± 0.02	± 0.02
L12-5 transducer holder	± 0.20	± 0.08	± 0.20	± 0.11	± 0.15	± 0.04
C5-2 transducer holder	± 0.05	± 0.08	± 0.29	± 0.03	± 0.03	± 0.03

Table 3.10: Values of replacement precision measured for four different methods with the two US transducers.

3.4 Discussion

3.4.1 Assessment of whole system reconstruction accuracy

From the three accuracy values in Table 3.5, the L12-5 transducer at the 3.9 cm depth setting has the highest accuracy of the two scanheads. This increase in accuracy is caused by the higher frequency and hence spatial resolution of the linear array transducer.

Volume reconstruction accuracy measures 3D accuracy, and is dependent on the accuracy of the position sensor and the US image. From the volumes scanned using the C5-2 transducer presented in Table 3.7, volume reconstruction accuracy is 12.92% for the small egg and 4.28% for the small egg. A volume reconstruction error of 13.46% for a Stradx system using a Philips HDI5000 with the L12-5 scanhead and a magnetic position sensor (Ascension Technology PC-Bird) was found by Rousseau et al. [87]. The reconstruction accuracy presented here is therefore comparable with the findings of other groups in this field.

3.4.2 Assessment of calibration precision

Treece et al. [38] report 3D calibration precision values of up to ± 0.60 mm from their tests using the calibration phantom described by [80]. This value is the largest 95% confidence interval for calibrations carried out with a 10 – 22 MHz probe at 2 cm depth setting. The best calibration precision for the Stradx program is reported by Gee et al. [81] using their semi-automatic calibration device. This provided a 3D mean calibration precision of 0.28 mm.

However, this is the most expensive method of calibration currently described in the literature, requiring a precision-machined mechanism as discussed above.

Calibration precision varies from this previously published result due to the difference in transducer frequencies and depth settings. A maximum calibration precision result for this system could be calculated by using the minimum depth setting of 2.4 cm. However, few US scans of the arterial system *in-vivo* are carried out at this depth — the 3.9 cm depth is more commonly used, so ± 1.20 mm is typical for normal use of the system.

3.4.3 Replacement precision

Replacement precision is an important factor in any practical situation where a dedicated 3DUS research machine or many optical position sensor tools for each transducer are not available. The replacement precision of ± 0.29 mm is comparable to the effect that replacement of the optical position sensor tool had on the calibration process reported by Gee et al. [81].

3.4.4 Whole system characterisation

The effect of calibration precision and whole system accuracy should be considered in the context of scanning patients. Movement of the patient is likely to be greater than the reported errors measured using a phantom. It is vital to consider issues such as patient comfort and positioning as much as methods of improving calibration and whole system accuracy. Ideally, as Gee et al. [81] report, the position sensor tool and the transducer holder should remain on the transducer at all times once calibration has been carried out. This should guarantee the maximum accuracy of the acquisition system.

3.5 Conclusion

A freehand 3DUS system using the Stradwin program, a Philips HDI5000 US scanner and an NDI Polaris optical position sensor was characterised by calculating the calibration precision, reconstruction accuracy and replacement precision of the transducer holder and position sensor tool. Whole system accuracy was found to be ± 0.17 mm (L12-5 transducer, 3.9 cm depth setting), comparable with systems reviewed by Mercier et al. [85]. Calibration precision was ± 1.20 mm (L12-5 transducer, 3.9 cm depth setting), which is similar to the results of Treece

et al. [38] using the Stradx program. Volume reconstruction accuracy was 12.92% for the C5-2 transducer, which is comparable to the results of Rousseau et al. [87] using the Stradx program. Replacement precision of the transducer holder was ± 0.20 mm for the L12-5 transducer and ± 0.29 mm for the C5-2. Replacement precision of the optical position sensor tool on the transducer holder was ± 0.13 mm. For best calibration precision, appropriate design of the transducer holder is required. Highest accuracy is guaranteed by maintaining the transducer holder and optical position sensor tool on the transducer once calibration is complete.

Chapter 4

The effect of rigid registration on artery mesh curvature: an analysis of probe pressure correction using Stradwin

4.1 Introduction

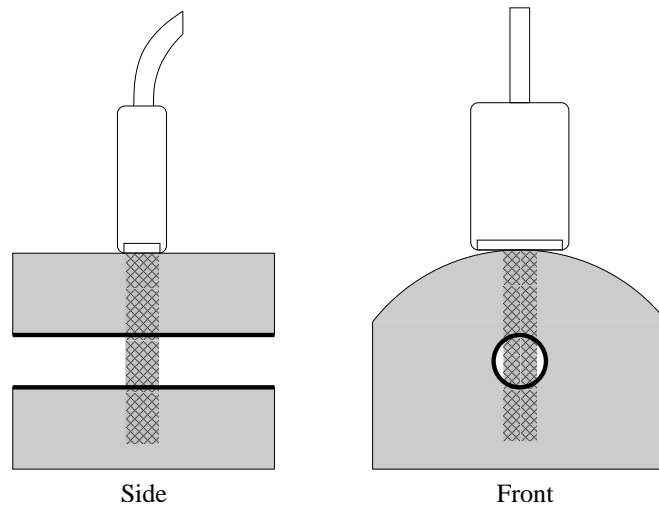
The process of scanning arteries with US changes the shape of the artery and the blood flow patterns within the artery. The pressure applied to the transducer casing to maintain contact between the piezoelectric elements and the skin surface can change the curvature and position of the artery within the patient (see Figure 4.1). Arteries are typically smoothly curved when at rest. It is this at rest position that is required for computational simulation of the blood flow patterns within the artery. To generate an at-rest geometry, gating is used (as described in Chapter 5). However gating only removes artery movement as a result of pulsatile flow: probe pressure effects remain.

To recover the shape of the artery without probe pressure effects, two US image registration techniques are included with Stradwin. These are both described by Treece et al. [88]. The first is a rigid registration technique which translates the acquired US images in the plane of each image until the whole dataset is aligned. This does not make any assumptions about the content of the US image, but only considers the alignment of each image in 3D space relative to each other. The second registration technique is a non-rigid method which changes the image according to the change in transducer position over the whole 3DUS dataset.

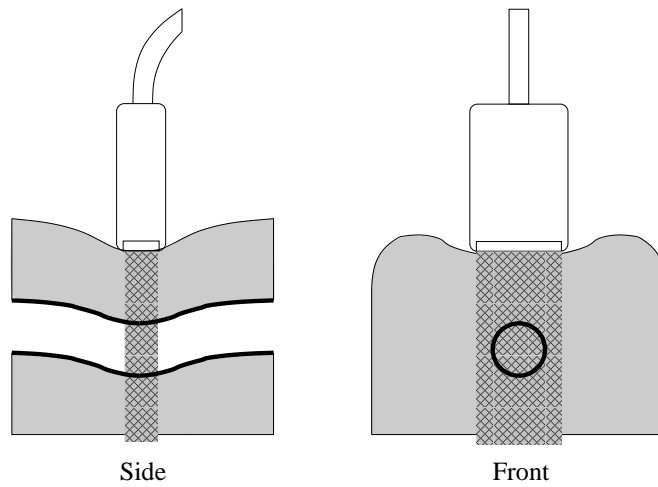
The non-rigid method assumes uniform elasticity of the tissue in the US image. This assumption may be valid in (for example) breast scanning or prostate scanning where the tissue has relatively uniform elasticity. However, due to the different types of tissue present around an artery (such as smooth muscles, veins, fat) and the way in which an artery changes shape during scanning, this assumption is not valid in arterial scanning. The large arteries are very rigid

structures due to the high pressure of the blood flow travelling through them. An artery, when pressure is applied, will tend to move downwards and sideways in the US image, rather than compressing and changing shape as an assumption of uniform elasticity in the image would suggest.

The effectiveness of the rigid registration technique included with Stradwin can be assessed by measuring the change in curvature of the artery. If the curvature of the unregistered artery decreases once registration is applied, the rigid registration technique removes the effect of probe pressure. If curvature of the registered artery increases, then rigid registration enhances the probe pressure effect and changes the artery away from the at-rest position required for computational simulation. If rigid registration is proven to reduce artery curvature, it should be used in the creation of patient-specific artery models for fluid flow simulation. This chapter will measure whether rigid registration reduces probe pressure effects on the centreline curvature of 3D artery models, and discuss whether it should be used in the creation of artery models for computational flow simulation.



(a) No probe pressure is applied to an area of the body with noticeable surface curvature (such as the neck). Only one part of the transducer is in contact with the skin/ultrasound gel layer, producing an incomplete image of the artery (the hatched area shows the portion of the US beam that is transmitted into the body.)



(b) Probe pressure is now applied to the curved area. Probe pressure is necessary here to produce contact between the transducer and the skin/gel surface, but it has the unwanted effect of changing the anatomical structure of interest. Artery curvature will be increased at this point.

Figure 4.1: The effect of probe pressure during scanning on a straight artery. Probe pressure needs to be applied to provide contact all along the array of piezoelectric elements in the transducer. Without this contact, the artery will be incompletely imaged (Figure (a)). Applying pressure to the transducer maintains contact with the skin surface but deforms the underlying anatomy (Figure (b)), locally increasing the curvature of the artery.

4.2 Methods

To assess the effect of rigid registration on the curvature of arterial scans, 3DUS scans were acquired from healthy volunteers and patients with diagnosed arterial disease. Scans from an abdominal aorta (AA); four carotid arteries (CA), consisting of the common carotid, the carotid bifurcation and sections of the internal and external carotid arteries; and four superficial femoral arteries (FE) were acquired using the Stradwin freehand 3DUS system as described in Chapter 3. The Analyze medical image analysis package (AnalyzeDirect, Inc., Overland Park, KS, USA. <http://www.analyzedirect.com>) was used to manually define the shape of the lumen on each acquired image for each dataset. More details of this technique are found in appendix B.

Segmented artery contours were extracted from the Stradwin program using a LabVIEW Virtual Instrument (VI) described in section F.3.3 of Appendix F. This VI extracts the positions of the points representing the outline of the segmented contour and saves them as a file that can be imported into the Rhino solid modelling package (McNeel Associates Inc., USA. <http://www.rhino3d.com>). The VI also calculates the position of the centroid of each segmented contour and saves its 3D position into an ASCII text file. The data acquisition and image processing path used in creating each geometry is summarised in Figure 4.2.

A surface model of the segmented contours was created using Rhino, using the procedure described in appendix D. The curvature of the centreline of the arterial geometries was calculated before and after applying the rigid registration technique, and curvature before and after was compared using a statistical test.

4.2.1 Lofting registered and unregistered surfaces in Rhino

Registered and unregistered artery contours were lofted using the Rhino solid modelling package. The “normal” lofting style option was used in each case. This produces a surface that closely reflects the underlying contours. If the contours are not smoothly curved, a lumpy surface model will result. Comparing lofted models of registered and unregistered artery contours allows immediate qualitative assessment of the effect of registration on curvature.

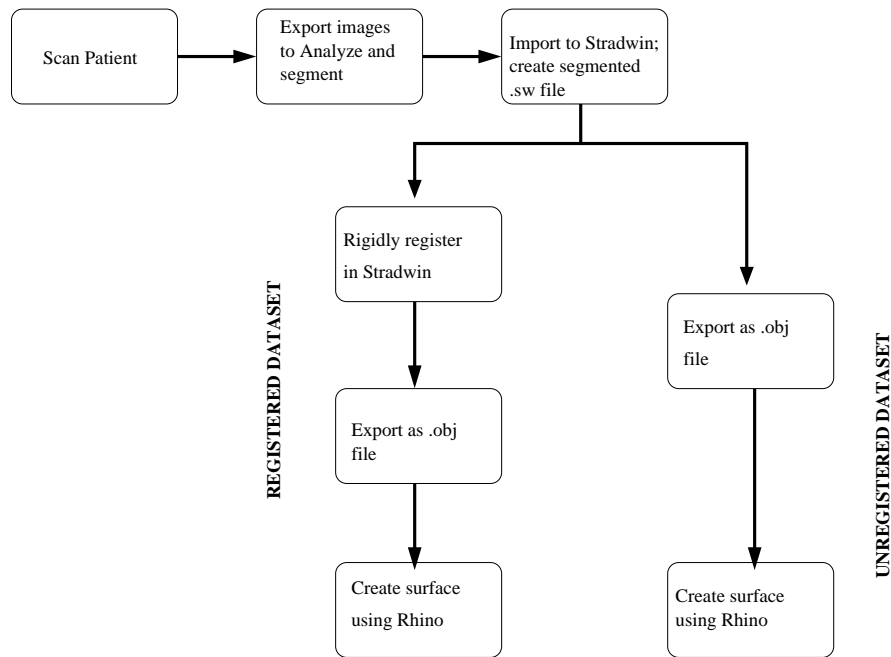


Figure 4.2: The steps taken to produce a registered (or unregistered) artery geometry for curvature measurement. The patient or healthy volunteer is firstly scanned using Stradwin. The images from each scan are exported to Analyze for manual segmentation. The outlines of the segmented artery shape found in each image are imported back into Stradwin to create a spatially-registered set of artery outlines. These are then exported as a .obj containing the spatially-registered segmented contours. A LabVIEW VI (see Appendix F, Section F.3.3 for more details) is used to produce this file. Rhino is then used to create a surface model of the artery using the contours defined in the .obj file. A similar procedure is followed for the registered artery datasets, except that each dataset is rigidly registered using Stradwin before export to Rhino.

4.2.2 Measuring arterial curvature

To measure the curvature of each artery geometry, the text file containing the positions of the centroid of each segmented contour in 3D space was used.¹ The radius of the circle joining three contiguous centroids was calculated at every position along the centreline [89]. This is known as an osculating circle. It is a circle that is uniquely defined by these three points. Figure 4.3 shows the osculating circle joining three contiguous points along the centreline of a 3D artery model.

The points $A(x_1, y_1, z_1)$, $B(x_2, y_2, z_2)$, and $C(x_3, y_3, z_3)$, respectively signify the n th, $(n + 1)$ th and $(n + 2)$ th points along the centreline. To find the radius of the osculating circle

¹This algorithm was developed by William T. Lee.

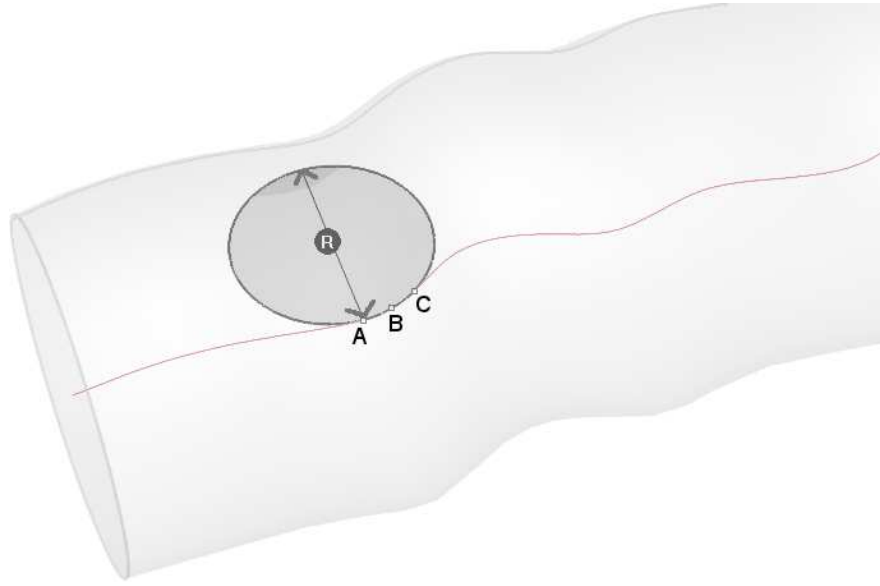


Figure 4.3: An osculating circle connecting three contiguous points along the centreline of a 3D artery model.

through these three points, the following distances are calculated:

$$|\vec{BA}|^2 = (z_2 - z_1)^2 + (y_2 - y_1)^2 + (x_2 - x_1)^2 \quad (4.1)$$

$$|\vec{CB}|^2 = (z_3 - z_2)^2 + (y_3 - y_2)^2 + (x_3 - x_2)^2 \quad (4.2)$$

$$|\vec{AC}|^2 = (z_1 - z_3)^2 + (y_1 - y_3)^2 + (x_1 - x_3)^2. \quad (4.3)$$

The radius of the osculating circle is then found using

$$R = \sqrt{\frac{|\vec{BA}|^2 \cdot |\vec{CB}|^2 \cdot |\vec{AC}|^2}{4 X^2}} \quad (4.4)$$

where

$$X^2 = (u_x \cdot v_y - u_y \cdot v_x)^2 + (u_z \cdot v_x - v_z \cdot u_x)^2 + (u_y \cdot v_z - v_y \cdot u_z)^2, \quad (4.5)$$

$u_x = x_3 - x_2$, $u_y = y_3 - y_2$, $u_z = z_3 - z_2$, $v_x = x_1 - x_3$, $v_y = y_1 - y_3$ and $v_z = z_1 - z_3$.

The curvature κ of the artery centreline is then calculated using

$$|\kappa| = \frac{1}{R}. \quad (4.6)$$

4.2.3 Assessing the effect of registration using a statistical test

To determine whether curvature with rigid registration is greater than that without, a Wilcoxon test for two paired samples [90] was applied to the difference between each set of curvature results. This test was used because the curvature data before and after registration were not normally distributed. The null hypothesis in each case was: the median of the difference between the curvature of the registered and unregistered artery centrelines was zero.

4.3 Results

4.3.1 Graphically assessing the effect of registration on lofted artery surface models

To get an immediate understanding of the effect of rigid registration, images of lofted surface models for each artery dataset are shown in Figures 4.4 to 4.12. The registered and unregistered surfaces are shown in two separate images, with a third image showing the unregistered geometry superimposed on the registered geometry. The codes attached to each dataset name mean:

- AA - abdominal aorta
- CA - carotid artery
- FE - superficial femoral artery

and a number is attached to each code to distinguish different datasets (e.g. CA1, FE2 etc.). The images with the unregistered and registered geometries overlapping allow a qualitative estimate of the effect of registration to be made. Regions where registration has had a noticeable effect on the shape of the original geometry are made clear by comparing the two geometries in this way. A good example is shown in Figure 4.11 where the removal of an obvious discontinuity in the shape of the artery by applying registration can be seen.

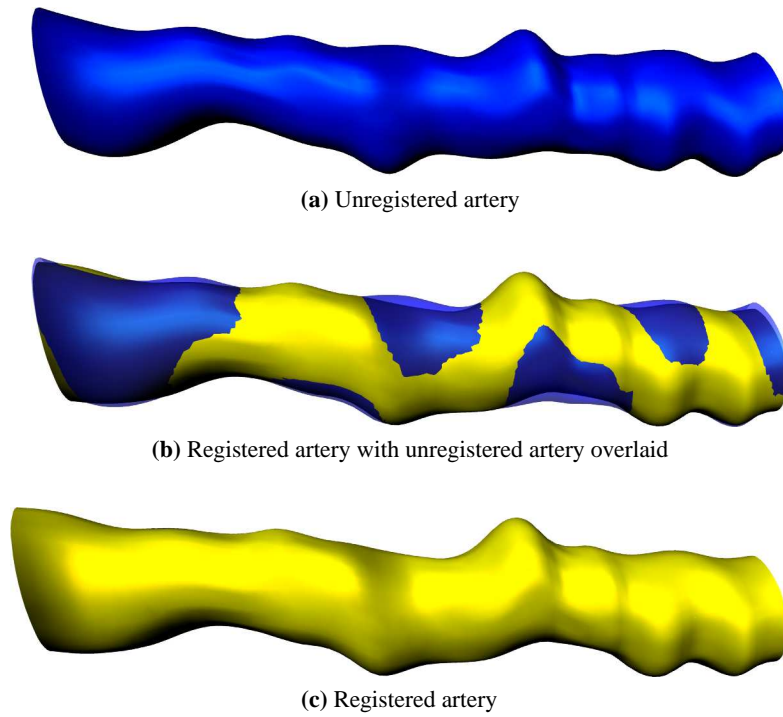


Figure 4.4: A comparison of registered and unregistered datasets for AA1

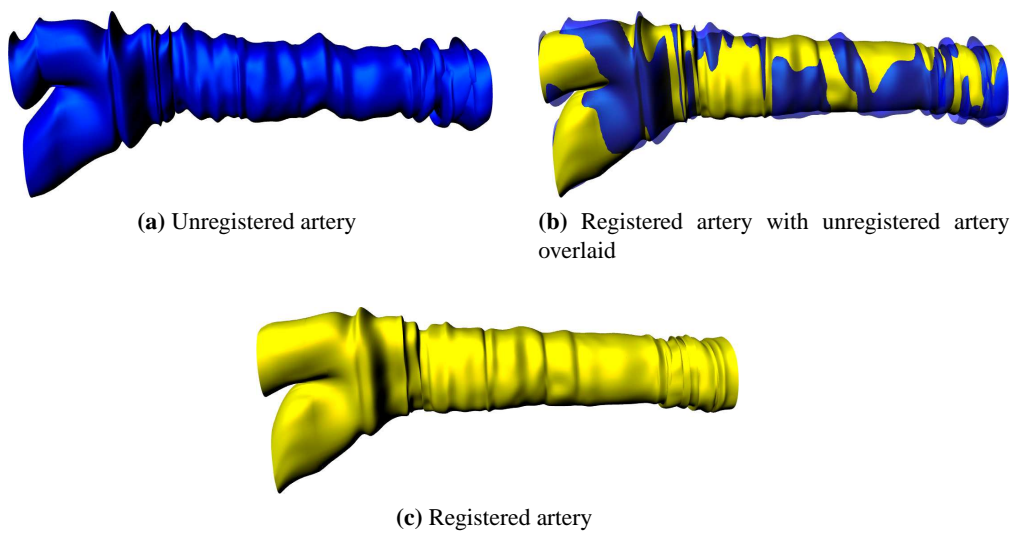


Figure 4.5: A comparison of registered and unregistered datasets for CA1

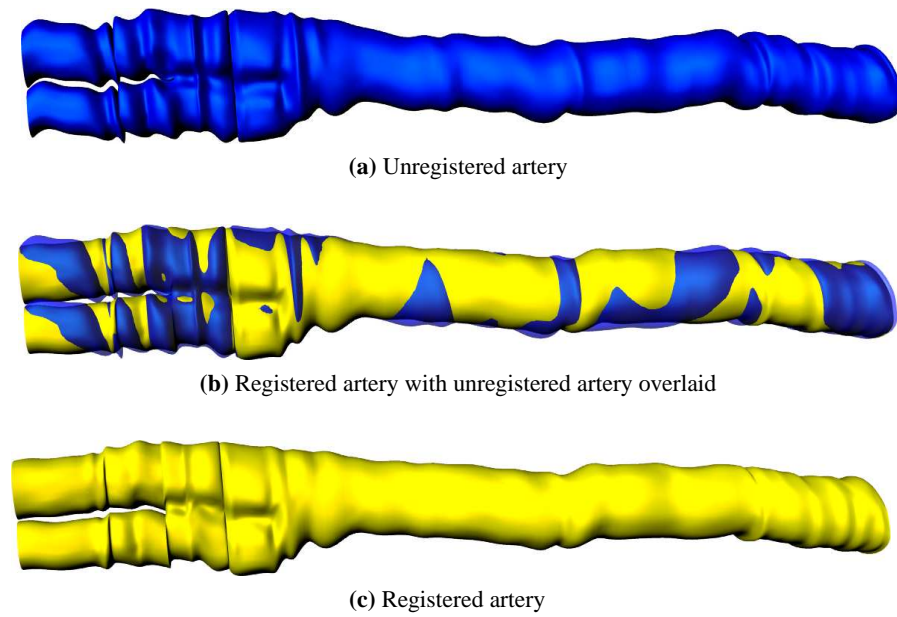


Figure 4.6: A comparison of registered and unregistered datasets for CA2

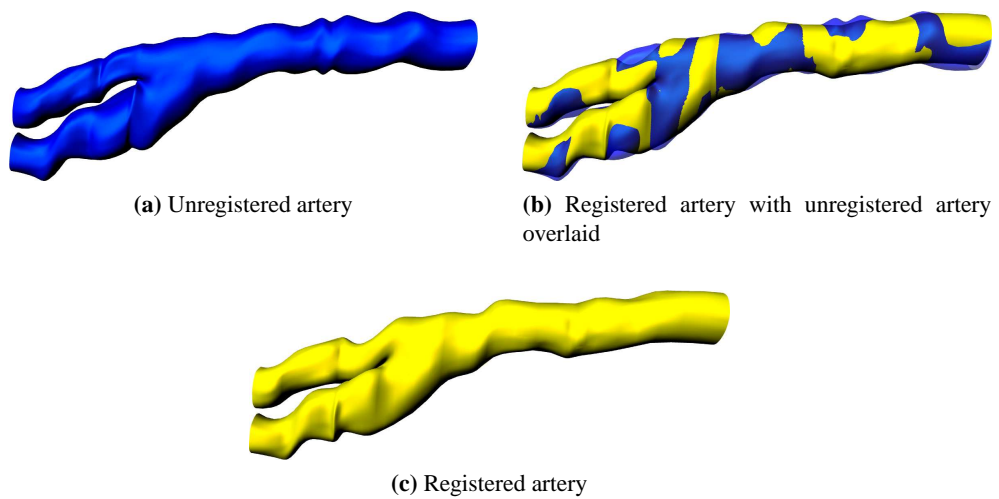


Figure 4.7: A comparison of registered and unregistered datasets for CA3

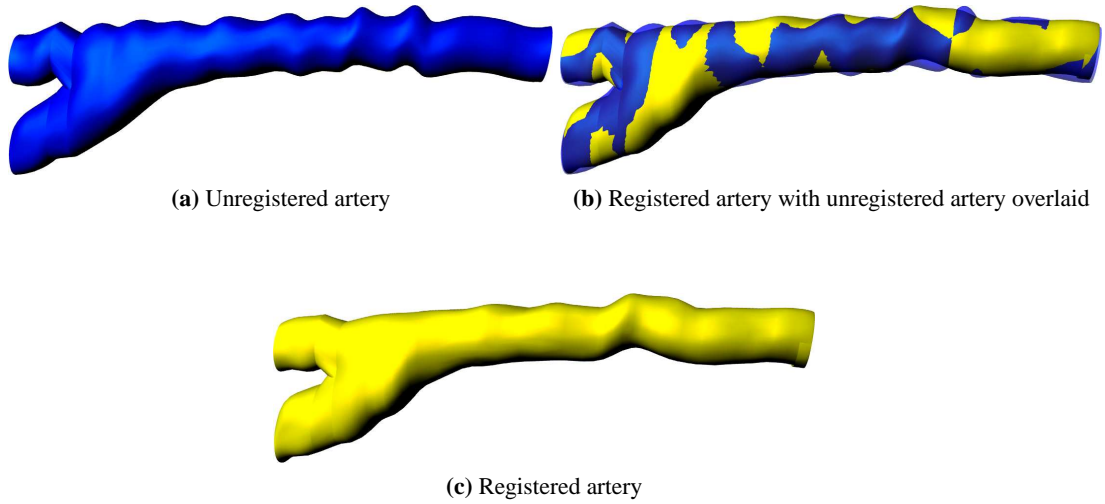


Figure 4.8: A comparison of registered and unregistered datasets for CA4

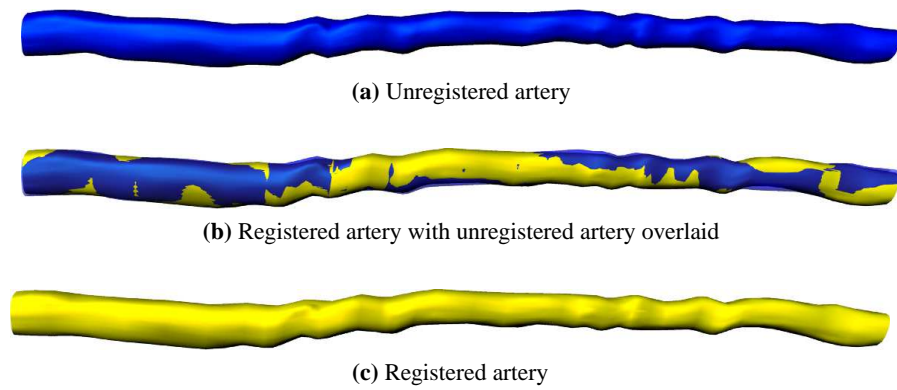


Figure 4.9: A comparison of registered and unregistered datasets for FE1

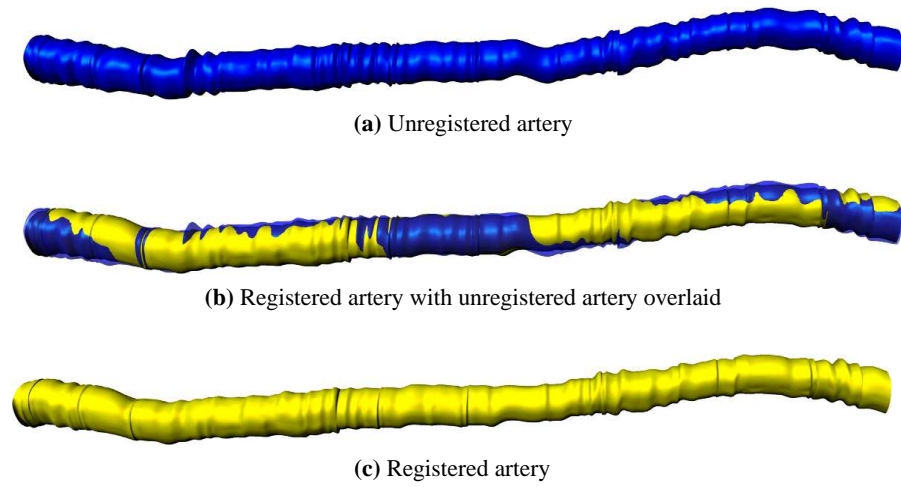


Figure 4.10: A comparison of registered and unregistered datasets for FE2

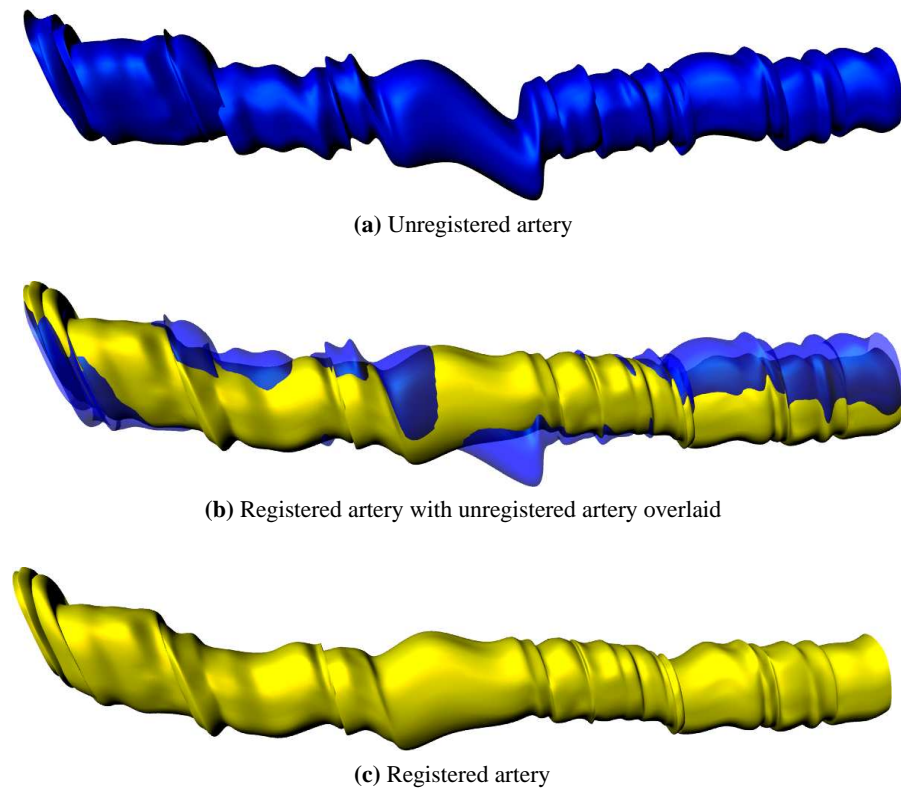


Figure 4.11: A comparison of registered and unregistered datasets for FE3

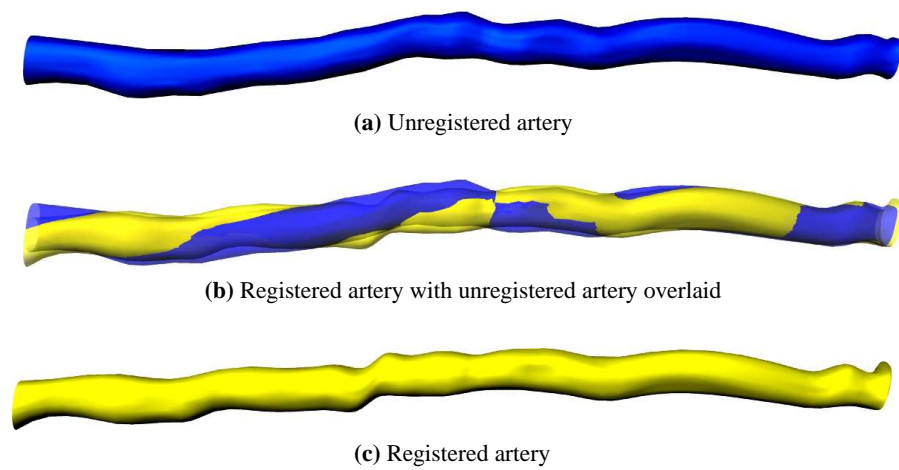


Figure 4.12: A comparison of registered and unregistered datasets for FE4

4.3.2 Summary of changes in curvature

Mean curvature \pm the 95% confidence interval for each artery is shown in Table 4.1.

Artery	Unregistered κ	Registered κ
AA1	0.074 \pm 0.031	0.073 \pm 0.029
CA1	1.336 \pm 0.210	1.510 \pm 0.303
CA2	0.599 \pm 0.118	0.479 \pm 0.111
CA3	1.187 \pm 0.215	1.564 \pm 0.311
CA4	0.188 \pm 0.046	0.144 \pm 0.034
FE1	0.052 \pm 0.020	0.050 \pm 0.017
FE2	0.690 \pm 0.085	0.642 \pm 0.097
FE3	1.322 \pm 0.225	1.262 \pm 0.248
FE4	0.148 \pm 0.082	0.186 \pm 0.142

Table 4.1: A summary of the changes in artery curvature κ due to rigid registration. Mean curvature \pm the 95% confidence interval is shown for each artery.

4.3.3 Statistical test results

The results from applying the Wilcoxon test for two paired samples are presented in Table 4.2. The estimated median of the difference between registered and unregistered curvature values, along with the confidence intervals, are presented. The null hypothesis in each case was that the median of the differences between the centreline curvature of registered and unregistered arteries is zero. Where the upper and lower confidence intervals contained a value of zero, the null hypothesis was not rejected (i.e. rigid registration was found to have no effect on artery curvature) and a “0” appears in the “Effect” column. Where the confidence interval bounds were both less than zero, the null hypothesis was rejected; rigid registration was considered to decrease curvature; and a “-” appears in the “Effect” column. Where the confidence interval bounds were both greater than zero, the null hypothesis was rejected; rigid registration was considered to increase curvature; and a “+” appears in the “Effect” column.

Artery	N	Median	Upper confidence interval	Lower confidence interval	Effect
AA1	19	-0.001	-0.012	0.009	0
CA1	161	-0.059	-0.112	-0.002	-
CA2	81	-0.104	-0.175	-0.046	-
CA3	84	-0.243	0.058	0.469	+
CA4	23	-0.052	-0.100	-0.006	-
FE1	36	0.000	-0.007	0.004	0
FE2	154	-0.062	-0.098	-0.024	-
FE3	74	-0.063	-0.185	0.064	0
FE4	29	-0.001	-0.180	0.020	0

Table 4.2: Wilcoxon Test Results. Here, N is the number of measurements of localised curvature κ made in each geometry. The “Effect” column interprets the results of the upper and lower confidence interval columns. If the confidence intervals are both less than 0, curvature was reduced. If the confidence intervals incorporate 0, there was no significant effect on curvature. If the confidence intervals are both greater than 0, curvature was increased.

4.4 Discussion

4.4.1 Corrugated surface models

Despite the use of rigid registration with a subsequent decrease in artery curvature κ , some surfaces show heavy corrugations such as CA1 (Figure 4.5a) and FE2 (Figure 4.10a). These are non-physiological results which will produce spurious flow patterns when used for CFD simulation. This is caused mainly by poor delineation of the lumen boundary, which gives abrupt changes in area between images. The geometries where surface corrugations are most apparent (CA1, Figure 4.5 and FE3, Figure 4.11), which also have two of the highest mean curvatures (Table 4.1), are from a patient with poorly defined lumen boundaries. The geometries that show least corrugation (CA4, Figure 4.8 and FE1, Figure 4.9), which also have the lowest mean curvatures (Table 4.1), are from young healthy volunteers with clearly defined lumen boundaries. The abdominal aorta dataset (AA1, Figure 4.4) also has some breathing movement and movement from surrounding tissue which further affect centreline curvature.

One method of reducing these effects, which are not eliminated by rigid registration, is to change the way in which the surface is created. There are several options for producing a lofted surface in Rhino. Normal lofting is the default setting. This produces curved lofted sections between each contour. Straight section lofting draws straight sections between each contour and produces a very corrugated effect. Tight lofting follows the curves used to create the lofted surface more closely than the Normal setting. Loose lofting allows the surface to move away

from the original curves to increase the smoothness of the lofted surface. The effect of each of these lofting styles is shown in Figure 4.13. Applying loose lofting with smoothing to the CA1 and FE2 datasets gives a reduction in corrugations at the expense of less respect of the underlying US data (Figure 4.14).

4.4.2 Statistical test results

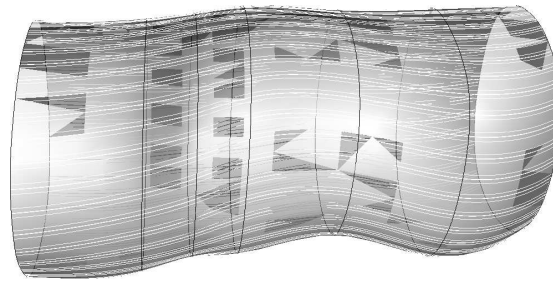
From the results of the Wilcoxon test in Table 4.2, it is clear that

- For 4 out of 9 arteries (44%) registration decreased focal curvature
- For 1 out of 9 arteries (12%) registration increased focal curvature
- For 4 out of 9 arteries (44%) registration had no significant effect on curvature.

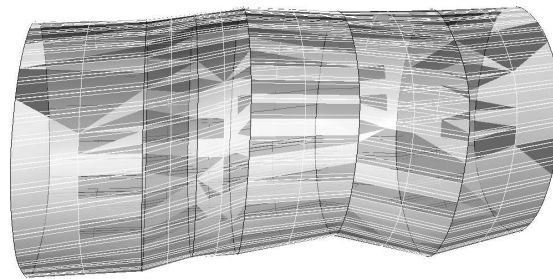
Out of these arteries,

- 3× carotid arteries and 1× femoral arteries had decreased curvature
- 1× carotid artery had increased curvature
- 1× abdominal aorta and 3× femoral arteries had unaffected curvature.

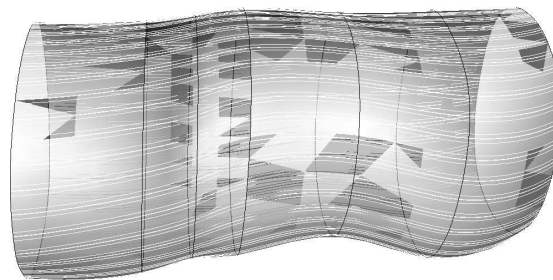
On the basis of these results, it is apparent that rigid registration has most effect on the curvature of the carotid artery, and least effect on the femoral artery. In most cases for the carotid artery, rigid registration had the desired effect of decreasing focal curvature, thus removing some of the effects of patient movement and probe pressure.



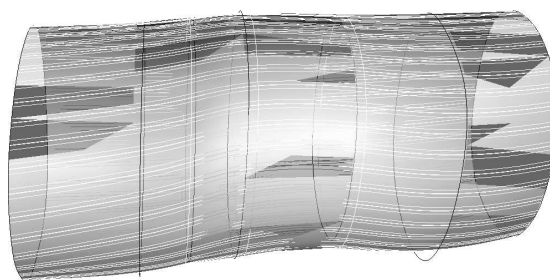
(a) Normal lofting



(b) Straight section lofting

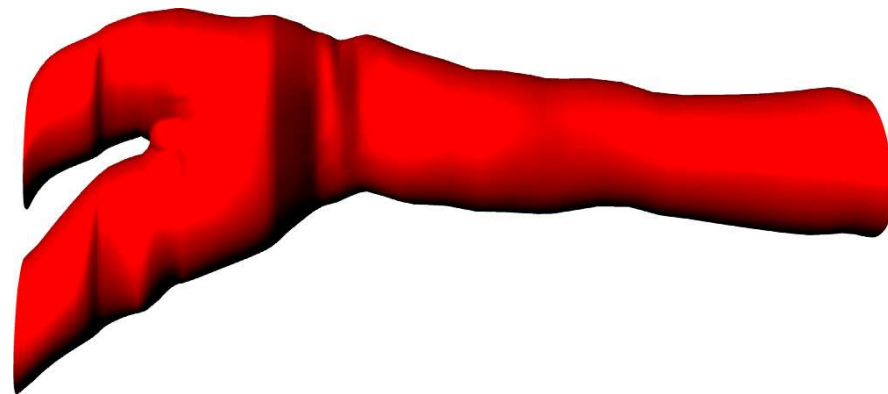
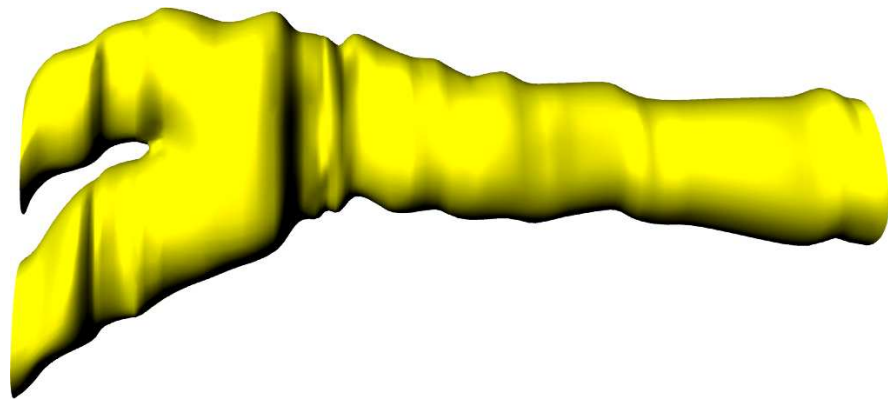


(c) Tight lofting

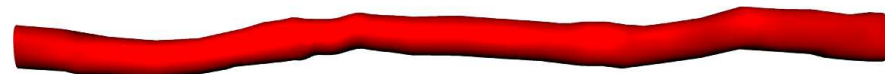
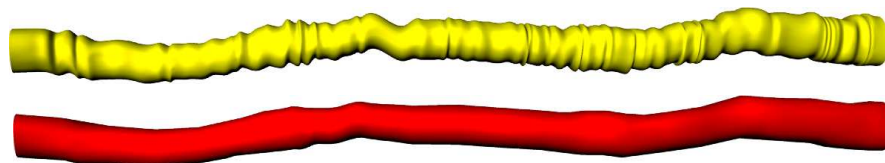


(d) Loose lofting

Figure 4.13: A comparison of different styles of lofting using Rhino. (a) Normal lofting is the default setting. (b) Straight section lofting draws straight sections between each contour. (c) Tight lofting follows the curves used to create the lofted surface more closely than the Normal setting. (d) Loose lofting allows the surface to move away from the original curves to increase smoothness.



(a) CA1



(b) FE2

Figure 4.14: Loose-lofted surfaces for CA1 and FE2. The upper image in each pair shows the surface created with “normal” lofting. The lower image in each pair shows the same contours with “loose” lofting with a smoothing factor of 1.5. Loose lofting with smoothing respects the underlying data less, but reduces corrugations in the surface.

4.5 Conclusion

Rigid registration may reduce patient movement and probe pressure artefacts, especially in the carotid artery. Variation in the area of manually segmented lumen boundaries and arterial movement are responsible for the corrugated effect that remains in many registered artery models. When a solid modelling package is used to create artery models, the use of loose lofting and smoothing is recommended to reduce this effect.

Chapter 5

Gating ultrasound data using Stradx: is retrospective gating equivalent to ECG gating?

5.1 Introduction

Retrospective gating of US data finds wide use where gating using the electrocardiogram (ECG) signal from the heart cannot be used. One application of retrospective gating is found in IVUS where the implantation of the US catheter can interfere with the surrounding tissue [91]. It is also useful when 3D freehand US is used with a magnetic position sensor. Using retrospective gating cuts down on the presence of metal cables and electrodes which can cause interference with magnetic position sensors [92]. Retrospective gating can also be used when imaging mode settings do not allow the use of ECG gated data acquisition. This is the case with the HDI5000 US scanner used in this study. Use of the SonoCT compounding mode [23] does not allow use of ECG gating. This is due to the complexity of synchronisation of the compounded images received from each movement of the steered US beam (see Figure 5.1). SonoCT compounding improves resolution, reduces edge shadowing artefacts [23, 28] and enhances the visibility of the artery wall. These are highly desirable qualities which can enhance US data for use with manual and automatic segmentation techniques.

Gated data is required for the creation of artery geometries for computational fluid dynamics (CFD) simulation [66]. Therefore the use of a retrospective gating technique to find data from one consistent timepoint throughout a US dataset to enable the generation of an artery model is required.

The Stradx 3DUS program [53], a predecessor to the Stradwin program, features a retrospective gating function. Considering the backward compatibility of Stradwin data as used throughout this thesis, a modification of the Stradx retrospective gating method was used. The Stradx retrospective gating method was used with modification due to its inability to correctly calculate the ECG phase angle from *in-vivo* datasets

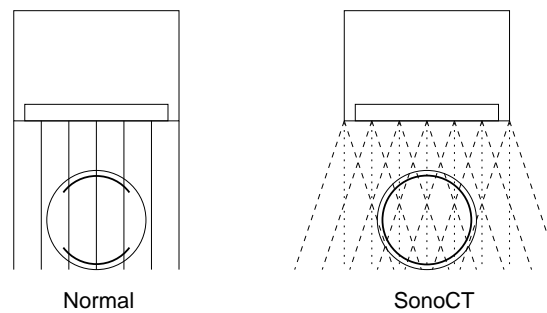


Figure 5.1: *Steering of the US beam in SonoCT to produce a compound image. In normal US scanning, the US beam is directed vertically into the patient, and produces directional effects such as the bright outlines at the top and bottom of the circular vessel shown. With SonoCT, the US beam is steered back and forth and the steered images are compounded to produce a bright outline all the way round the vessel wall.*

The use of a retrospective technique should lead one to question its validity: are retrospectively gated datasets the same as ECG gated datasets? The use of SonoCT compounding should also lead one to question how similar images recorded with this imaging mode are to images recorded without compounding. This chapter will describe the use of a straight tube flow phantom to study these two issues.

5.2 Methods

5.2.1 Scanning straight phantoms to assess variation in gating methods and scanning mode

Considering that patients and healthy volunteers were scanned, it would seem reasonable to use *in-vivo* data to assess the variability of gating methods and scanning modes. However several factors prevent the use of freehand 3DUS data from being used to make meaningful comparisons between datasets:

- No control over the angle of the transducer is available. Different scans will contain artery images with different diameters.
- No control of the position of acquisition of each image can be attempted. Start and end points of scans for comparison will not be the same.
- The spacing of individual images along the artery cannot be controlled. Multiple scans of the same artery therefore may not be spaced at the same distance.

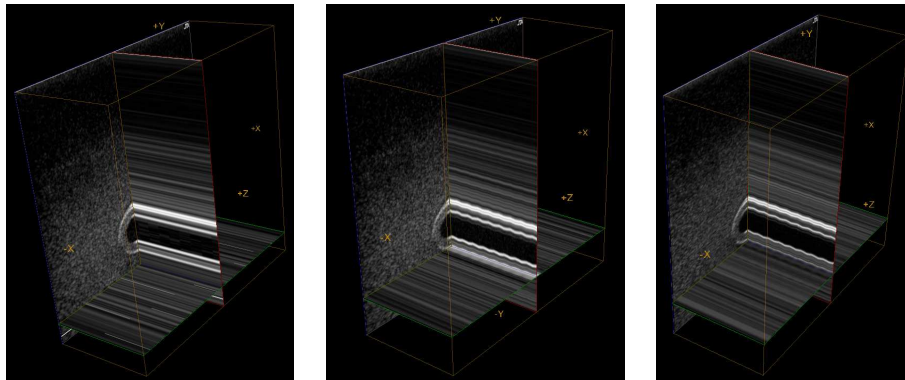


Figure 5.2: *Straight phantom datasets (L to R: ECG gated, B-mode, B-mode with SonoCT). These false 3D reconstructed datasets are shown with data shown in the x and y axes from the US images in each dataset, and the z axis showing image number (time) in each dataset. The ECG gated dataset shows minimal variation in cross-section, whereas the ungated datasets show changes in cross-section due to pulsatile flow.*

- Anatomical variation (e.g. a gradual increase in artery diameter over a section of artery) cannot be controlled. Variation in area caused by acquisition settings may be masked by anatomical variation.

Because of these issues, a straight tube flow phantom was used to assess variation in gating methods and scanning mode (see Figure 5.2). The wall-less flow phantom was constructed from tissue mimicking material according to the method described by Ramnarine et al. [46]. A sinusoidal input velocity profile was sent into the flow phantom using a computer-controlled pump. Blood-mimicking fluid was pumped through the phantom which was made to the recipe of Teirlinck et al. [93]. To avoid variation in measured phantom area from different transducer angles, the transducer was clamped in one position using a clamp stand. The L12-5 38mm transducer was used with the “Cerebrovascular/Carotid” preset. Nine datasets were captured in total: three each of ECG gated data, ungated data and ungated data with SonoCT compounding. The depth setting was fixed at 3.9 cm and the TGC sliders were set to the mid position for each acquisition.

5.2.2 Measuring phantom area using thresholding

To simplify the task of measuring phantom area, a LabVIEW Virtual Instrument (VI) was created (see Appendix F section F.2.3). This VI reads in the straight phantom data from the

captured Stradwin file and allows the user to define a region of interest (ROI) on every image corresponding to the position of the inside of the phantom tube. A threshold is applied to the image and the area of the thresholded pixels is calculated and saved as a text file. Consistent thresholds (from grey levels of 27 to 58) were used for every dataset to allow direct comparison between results. The threshold was defined to fill only the section of the image that corresponded to the fluid-filled region of the flow phantom. If a grey level higher than the upper bound of these values were used, the fluid-filled region of the phantom would be overfilled and any variation in phantom shape due to pulsatile flow would not be detected. Similarly, if a grey level lower than the lower bound of the threshold values were used, the fluid-filled region would be underfilled and variation in phantom shape would not be detected. The calculation of these grey values is specific to the US scanner and the phantom used for this analysis and may vary with other US scanners and phantoms.

5.2.3 Retrospective gating using Stradx

To retrospectively gate a 3D scan of an artery the user needs to define where the artery is on each image. The Stradx program allows the user to set a ROI over the artery in every image, and then threshold the image. Thresholded pixels covered by the ROI are counted and the result from every image is used to develop a cardiac activity (CA) waveform (see Figure 5.3).

An ECG phase angle value for each image is then calculated on the basis of the CA waveform. The dominant periodic component of the whole CA waveform is found by Stradx to create the ECG phase plots. CA waveforms from a straight flow phantom with pulsatile flow, a healthy volunteer, and a diseased patient are given in Figure 5.4. Note that in all cases, CA has arbitrary units. The phase angle plot created for the straight tube phantom (5.4a) shows a clearly periodic waveform that is in phase with the CA waveform, as would be expected. However, the phase angle plot for the healthy volunteer (5.4b) is out of phase with the periodic CA waveform. For the patient with arterial disease, the CA plot is clearly periodic, but the ECG phase angle plot is again out of phase (5.4c).

Instead of using the calculated ECG phase angle to gate *in-vivo* data, the peaks of the periodic CA trace were used. A LabVIEW VI was developed to read the CA trace from the Stradx datafile and find the peaks (Appendix F, section F.4.3). User intervention was then required to move through the selected peaks and ensure that they corresponded to the largest area of the artery at each point (see Figure 5.5). Peaks that were erroneously identified were manu-

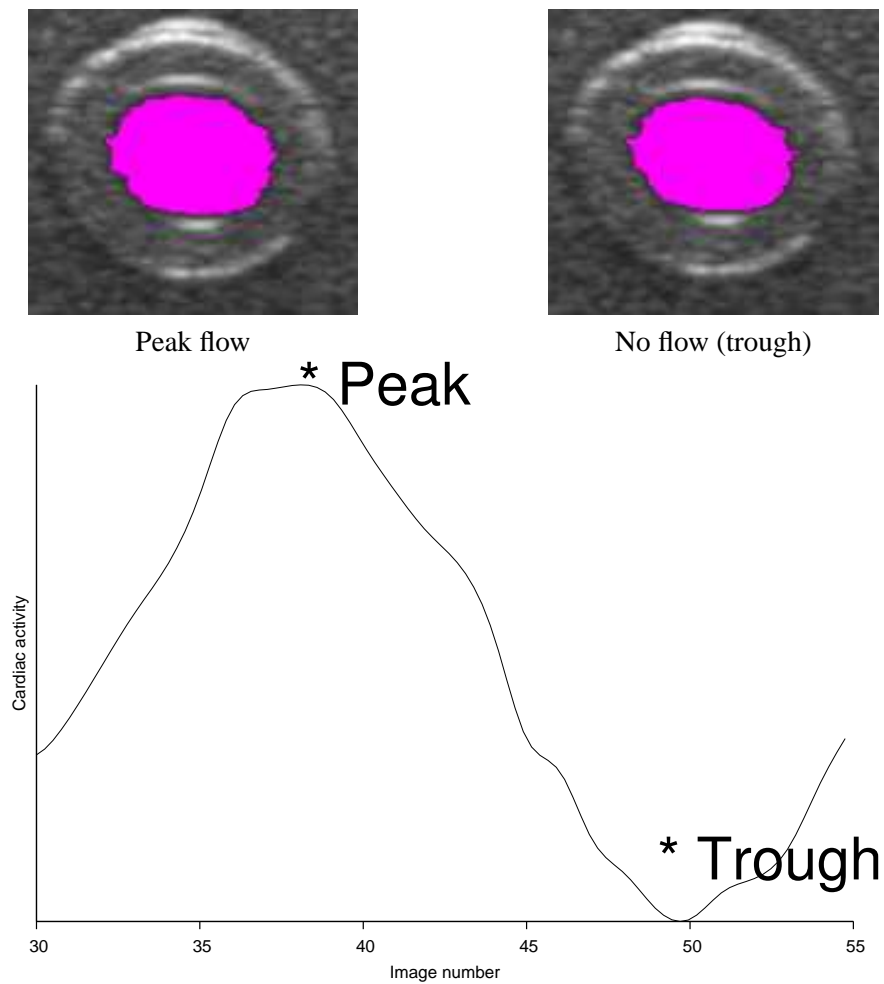
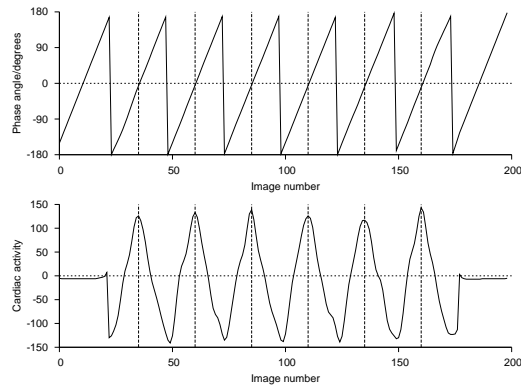
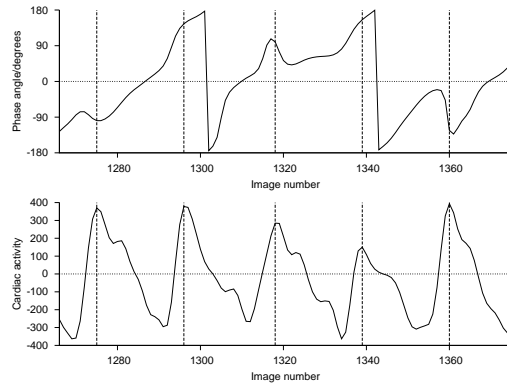


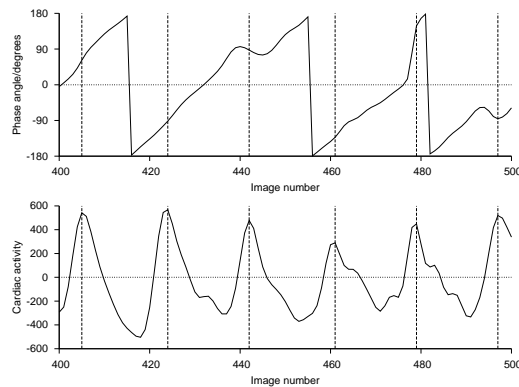
Figure 5.3: Calculating the cardiac activity waveform. The flow images are taken from a straight tube phantom with a sinusoidal flow profile. The size of the thresholded ROI on each US image (shown in pink) is measured. Cardiac activity is related to segmented area in pixels, but is calculated with arbitrary units. In this case, a sinusoidal cardiac activity trace is produced in phase with the sinusoidal flow profile.



(a) Cardiac activity and phase angle for a straight tube phantom. The peak cardiac activity is consistently aligned with zero phase angle.



(b) Cardiac activity and phase angle for a healthy carotid. The periodic nature of the cardiac activity waveform can be clearly seen. The phase angle trace is unaligned to the cardiac activity waveform.



(c) Cardiac activity and phase angle for a carotid with stenosis in the common carotid.

Figure 5.4: Cardiac activity (arbitrary units) and phase angle (degrees) compared for three different US scans, one in-vitro on a straight tube phantom and two in-vivo from a healthy volunteer and a patient. Vertical dashed lines show the position of the images with peak cardiac activity. The horizontal dashed lines show zero phase angle or cardiac activity.

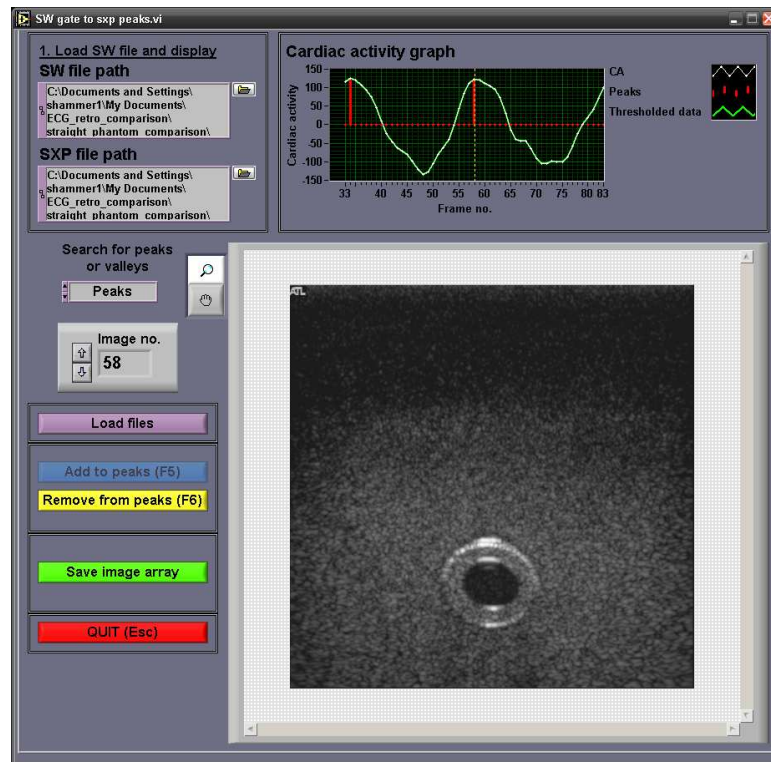


Figure 5.5: The LabVIEW VI used to gate a Stradwin dataset using a .sxp file. The program finds the peaks (or troughs) of the CA waveform automatically. The user can scroll through the peaks and add or remove other images to the list of peaks. The list can be saved as a text file.

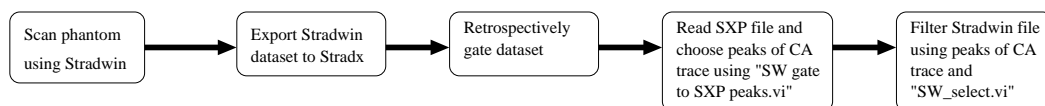


Figure 5.6: The image processing path used to create retrospectively-gated datasets. Explanations of the function of the two VIs used here are given in Appendix F, sections F.4.3 and F.5.3 for “SW gate to SXP peaks.vi” and “SW_select.vi” respectively.

ally removed, and peaks that were erroneously ignored could be added manually. The image numbers corresponding to the edited peaks were saved as a text file. Another VI (Appendix F, section F.5.3) was developed to create a gated Stradwin datafile by filtering it using the text file of peak CA image numbers. The full processing path from image acquisition to generation of a retrospectively-gated dataset is shown in Figure 5.6.

Retrospective gating produces unsatisfactory results for unclear images, especially from patients with severe disease. More manual intervention is required in this case to produce a correctly-gated data file. Despite this shortcoming, using ungated data has the advantage of being able to measure arterial wall motion over the whole artery, given an automatic segmentation

technique capable of using US images. Also, in patients who suffer from cardiac arrhythmia, it may be impossible to use ECG gating. This leaves retrospective gating as the only option available to produce gated data from such patients.

5.2.4 Statistical Analysis

Two statistical tests were carried out on thresholded phantom areas using MINITAB (Minitab Inc., State College PA, USA. <http://www.minitab.com>). Data were treated as unpaired in both cases because although all measurements were made on the same phantom, different imaging modes or gating methods were used each time. Areas from each of the three datasets for each type of acquisition were concatenated into one file for analysis.

5.2.4.1 Comparing SonoCT and non-SonoCT data

SonoCT and non-SonoCT data were compared to find out if there was any difference in the thresholded area of the phantom due to imaging mode. The SonoCT data were not normally distributed (see Figure 5.8b), so a Mann-Whitney U-test was used to compare SonoCT and non-SonoCT data [90]. The null hypothesis was: areas measured using SonoCT are equal to areas measured without SonoCT.

5.2.4.2 Comparing retrospectively gated data to ECG gated data

Retrospectively gated datasets captured without SonoCT were compared to ECG gated datasets to find out if there was any difference in the area of the phantom due to gating method. Retrospective gated data without SonoCT was compared to ECG gated data because (as will be shown later) images captured with SonoCT gave larger thresholded areas than without SonoCT. Therefore retrospective gating was applied to images captured without SonoCT for this comparison. A Mann-Whitney U-test was used to test gated data due to the small sample size of the retrospectively gated dataset (No. of samples (N) = 18 compared to N = 594 for ECG gated data). The null hypothesis was: areas of retrospectively gated images are equal to areas of ECG gated images.

5.3 Results

5.3.1 Straight phantom areas

Figure 5.7 shows a comparison between phantom areas measured with ECG gating and with and without SonoCT compounding. This figure shows that areas measured with SonoCT are consistently up to 10% larger than areas measured without it. Low variation of up to 2% in phantom area measured with ECG can also be seen.

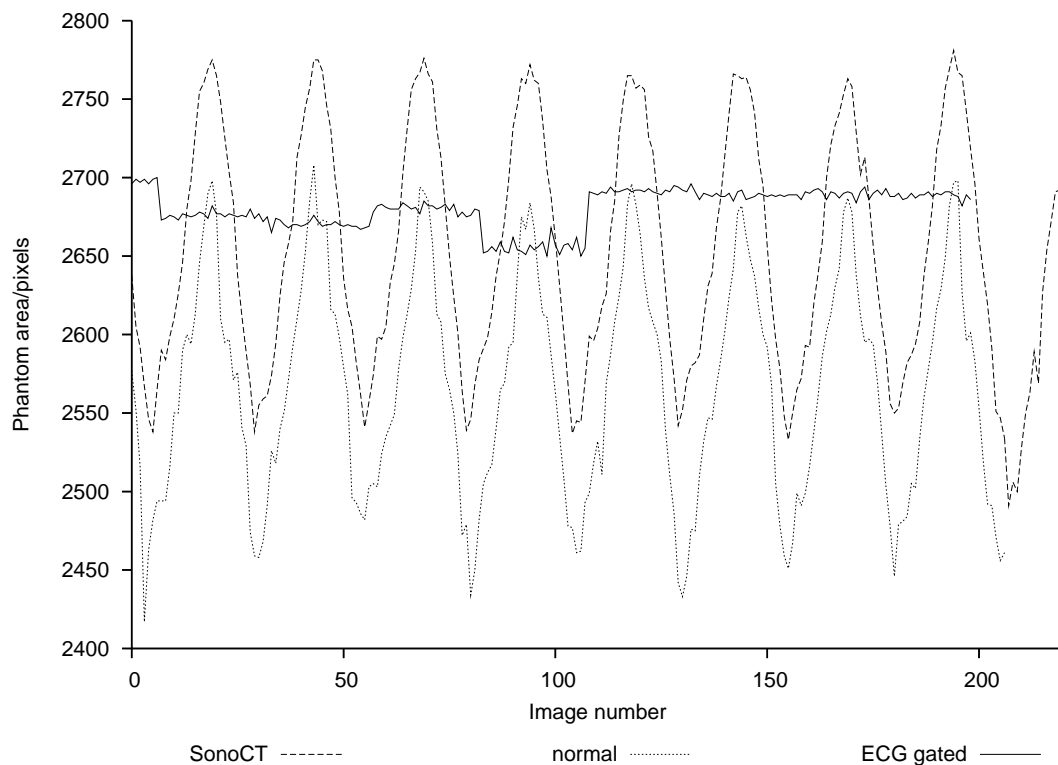
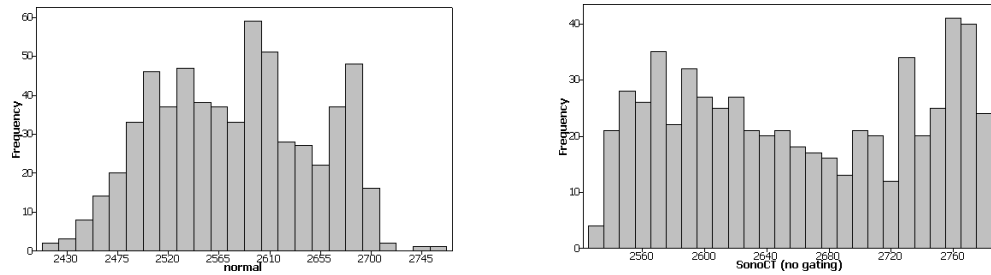


Figure 5.7: Thresholded areas of the flow phantom measured from a scan without SonoCT (labelled as “normal” on the chart), a scan with SonoCT, and an ECG gated scan. SonoCT areas are consistently larger than areas measured without SonoCT. The image resolution (pixels/mm) is the same for each of the three scans, so the different numbers of pixels correspond to different measured areas.

5.3.2 Summaries of the data

Figure 5.8 shows histograms of ungated phantom areas with and without SonoCT compounding. Figure 5.9 shows box-whisker plots of these datasets. Figure 5.10 shows histograms of gated phantom areas using retrospective gating and ECG gating. Figure 5.11 shows box-



(a) A histogram of ungated phantom areas measured from an ungated phantom 3DUS dataset imaged without SonoCT compounding. The data appear to be normally distributed.

(b) A histogram of ungated phantom areas measured from an ungated phantom 3DUS dataset imaged with SonoCT compounding. The data do not appear to be normally distributed.

Figure 5.8: Histograms of ungated phantom areas. The fact that both the datasets are not normally distributed implies that a statistical test that assumes normal distribution of the data (such as a *T*-test) may not be used to compare them.

whisker plots of these datasets. The box-whisker plots summarise all of the areas measured from each dataset. Whiskers (the horizontal lines extended above and below the boxes) show the maximum and minimum areas respectively measured in each dataset. The upper and lower bounds of the box indicate the 3rd quartile and 1st quartile of the dataset respectively, while the central horizontal line in each box indicates the median value of the dataset.

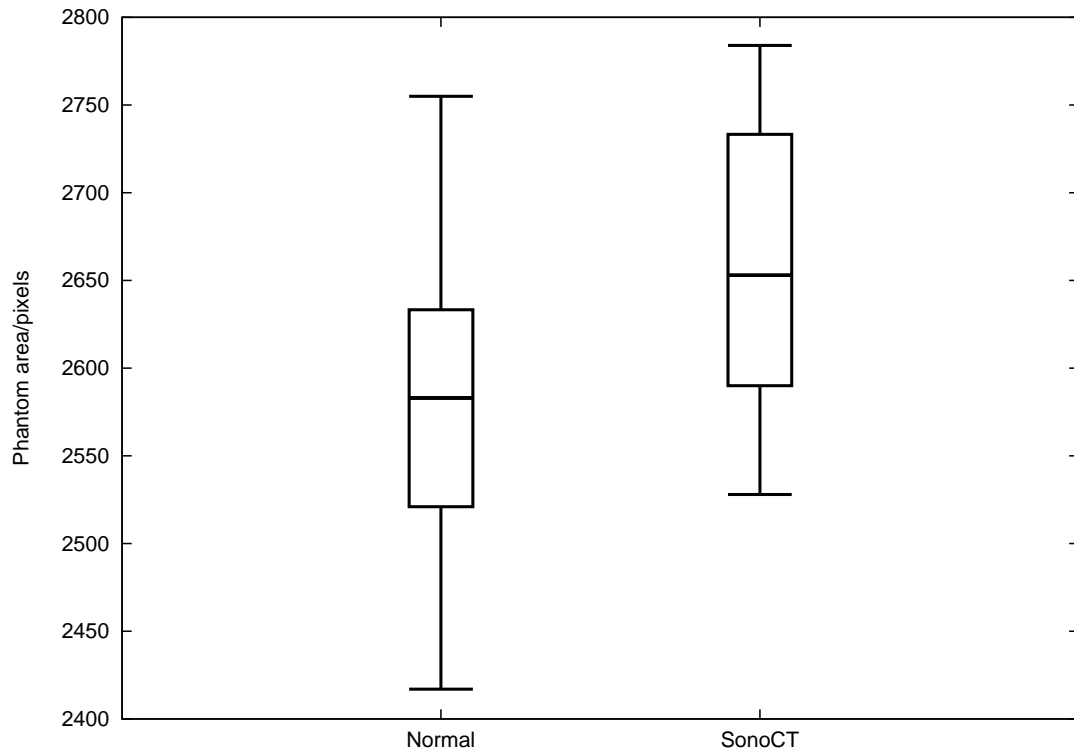
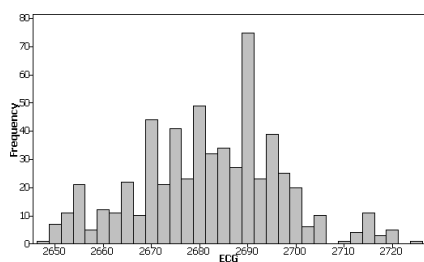
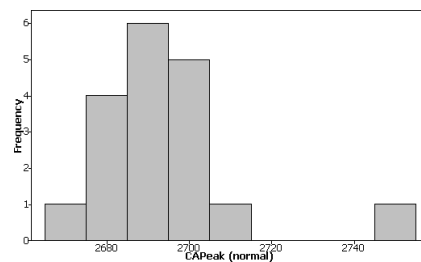


Figure 5.9: Box-whisker plots of phantom area measured without SonoCT (labelled “normal”) and with SonoCT image compounding. Measured phantom areas using SonoCT are usually larger than those measured without SonoCT, as shown by the higher median value of the SonoCT dataset.



(a) A histogram of gated phantom areas measured from an ECG gated phantom 3DUS dataset. Number of images (N) = 594.



(b) A histogram of phantom areas measured from a retrospectively gated 3DUS dataset without SonoCT. Number of images (N) = 18.

Figure 5.10: Histograms of gated phantom areas. The large difference in sample sizes of the two datasets implies that a statistical test that assumes similar sample size (such as the T-test) may not be used to compare them.

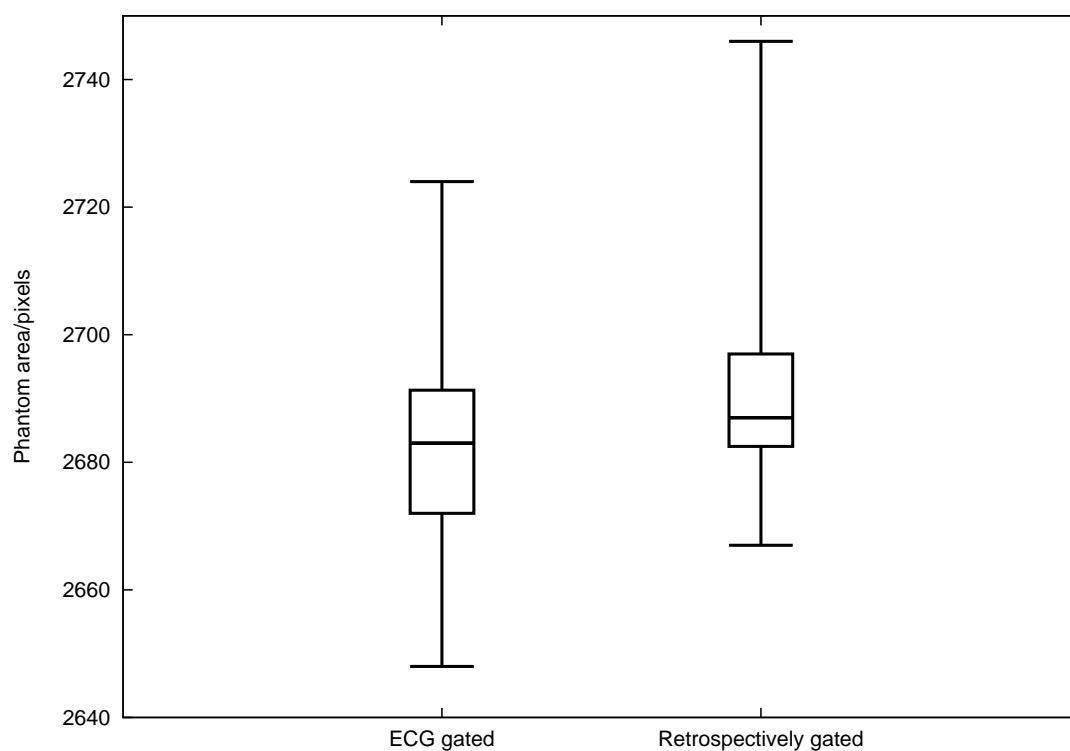


Figure 5.11: Box-whisker plots of phantom area measured from a retrospectively gated 3DUS dataset with SonoCT and an ECG gated dataset. Both datasets have similar ranges and similar median values. The retrospectively-gated dataset has a lower interquartile range, implying that this method suffers from less variation in measured area than ECG gating.

5.3.3 Statistical test results

Summaries of the Mann-Whitney U-test with unequal variances for the data comparing phantom areas with and without SonoCT compounding are shown in Table 5.1. The results of the Mann-Whitney U-test for the gated data are shown in Table 5.2.

Dataset	N	Median
Normal	610	2583
SonoCT	610	2653
Probability (adjusted for ties)	p < 0.05	

Table 5.1: Mann-Whitney U-test results for the ungated datasets

Dataset	N	Median
Retro gated	18	2687
ECG gated	594	2683
Probability (adjusted for ties)	p = 0.04	

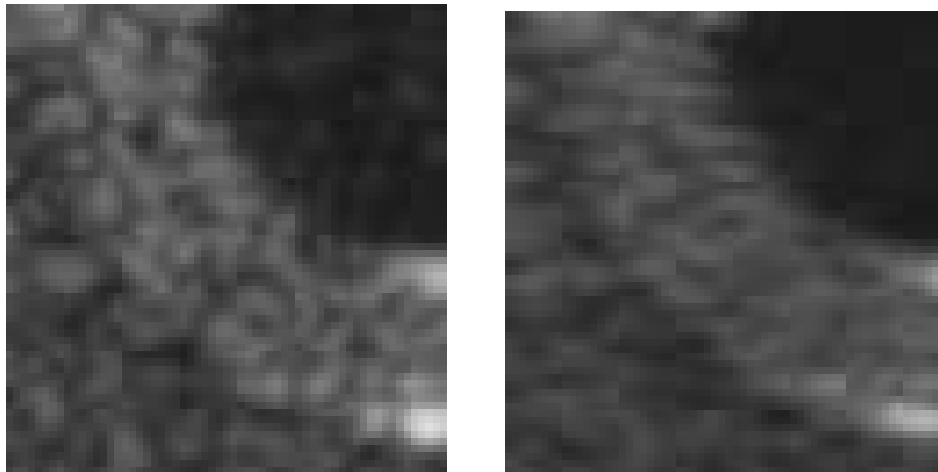
Table 5.2: Mann-Whitney U-test results for the gated datasets

5.4 Discussion

5.4.1 Statistical analysis of area with and without SonoCT compounding

As can be seen from Table 5.1, the difference between areas with and without SonoCT is statistically significant ($p < 0.05$). Therefore the null hypothesis, that areas measured using SonoCT are equal to areas measured without SonoCT, was rejected. By inspection of Figure 5.7, areas measured with SonoCT are consistently larger than areas measured without it. This is most likely due to the increased resolution of images recorded with SonoCT.

Before the US image is captured using Stradwin, it is resampled and converted to an analogue video format. For images captured with and without SonoCT, the size of the captured video frame is the same, but the display resolution on the US machine screen is different. The clearer outline of the walls of the straight phantom on SonoCT images is suggestive of this increase in resolution which is masked by the process of video conversion. A closeup of the same section of the straight phantom (Figure 5.12) shows this effect. This effect is only of significance when comparing images captured with SonoCT to images captured without SonoCT.



(a) A closeup of the straight tube phantom imaged without SonoCT.

(b) A closeup of the straight tube phantom imaged with SonoCT.

Figure 5.12: Comparing closeups of video captured images from the straight tube phantom imaged with and without SonoCT compounding. Figure (a) shows more speckle noise and a less smooth outline of the side of the phantom. The increased smoothness of Figure (b) is indicative of the higher resolution of the SonoCT scan before video conversion.

5.4.2 Statistical analysis of retrospective and ECG gating

From Table 5.2 the difference between retrospective and ECG gated datasets is statistically significant ($p < 0.05$). Therefore there is some evidence to reject the null hypothesis that the areas of images gated retrospectively are the same as the areas of images gated using ECG. This difference points to two factors for the difference in areas measured using each gating method: the acquisition parameters used in capturing ECG gated data, and the lag between measured phantom area and cardiac activity for the same dataset.

ECG gating cannot be set automatically: the user must select the position of the points on the ECG trace using the US machine console. This requires a degree of skill to set up, and the point of peak flow (for example) on the ECG trace can easily be missed by a few milliseconds. Figure 5.7 demonstrates this. Area measurements from three scans of the same dataset (two without gating and one with ECG gating at peak flow) show that for 6 out of 8 flow waveforms, the ECG gated area is smaller than the ungated peak areas without SonoCT. Retrospective gating gives a more robust and repeatable measure of the point of peak flow in an artery dataset because it can be applied semi-automatically post-capture, giving a better likelihood of recording true peak flow.

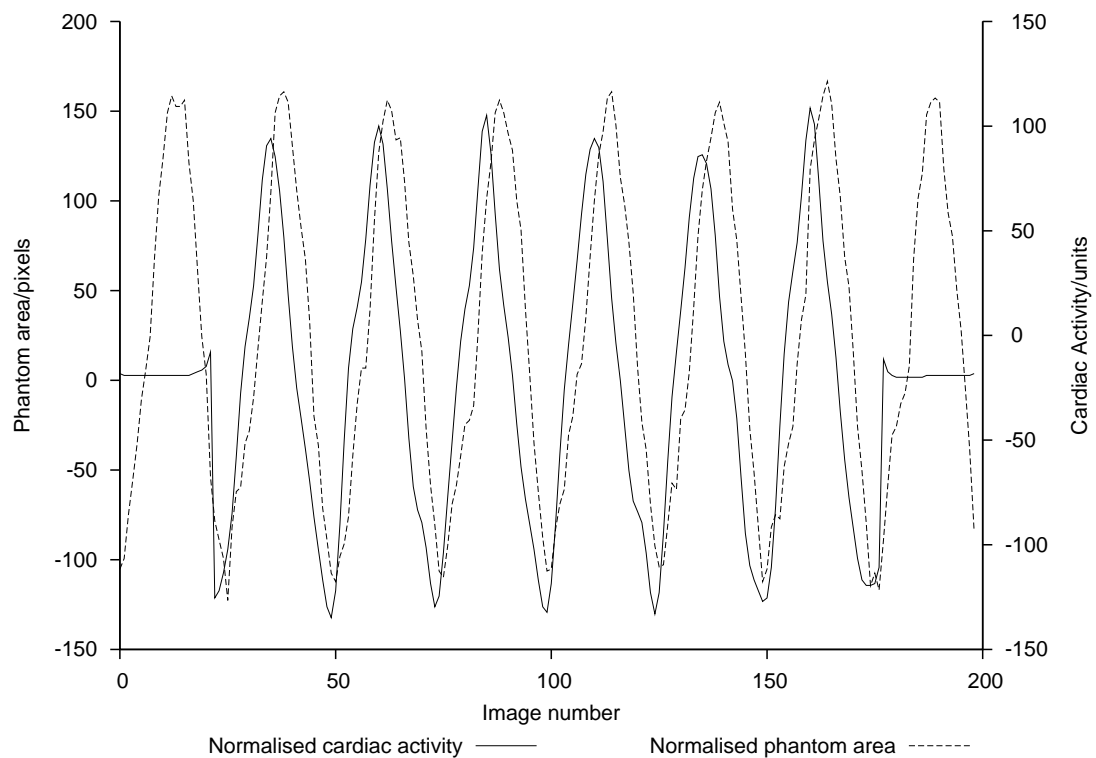


Figure 5.13: A comparison of cardiac activity to thresholded phantom area. Cardiac activity consistently leads phantom area.

A factor that may contribute to the observed difference between gating methods is the delay between the change in phantom area and the change in the CA waveform (see Figure 5.13). The CA waveform is based on the change in thresholded area, so it should change at the same time as the thresholded area. However, the CA trace precedes the change in phantom area. This difference may further explain differences in gating methods. To guarantee correct retrospective gating, the user can manually check the position of each peak of the CA waveform using the LabVIEW VI discussed in section 5.5.

5.5 Conclusion

Comparing the area of a straight tube flow phantom measured with and without SonoCT compounding showed that area measured with SonoCT was larger than when measured without SonoCT. This was due to the enhanced resolution of SonoCT imaging, producing more smaller pixels around the borders of the thresholded phantom area. A comparison of retrospectively gated and ECG gated US images from a straight flow phantom revealed that areas of the flow

phantom measured using retrospective gating were different to areas measured using ECG gating. This was due to the cardiac activity waveform generated by the retrospective gating algorithm in Stradx lagging behind the true area of the phantom, and the variability inherent in setting up and recording ECG gated data with the HDI5000 US scanner. Careful selection of the gated peaks using the described software ensures that a retrospectively gated dataset is produced that is equivalent to an ECG gated dataset.

Chapter 6

Segmentation of 3D ultrasound data: a comparison of automatic methods with manual methods

6.1 Introduction

Segmentation of 3DUS data is an important step in the creation of patient-specific artery models. Segmentation is the process of defining anatomical boundaries on a medical image. Many segmentation methods exist that vary depending on the anatomical structure of interest and the type of data used for segmentation. Recent advances in the field are reviewed by Noble and Boukerroui [27]. In most cases manual segmentation (also known as manual planimetry) is considered a “gold standard” technique. An outline drawn by an experienced expert observer (in most cases a radiologist or sonographer) is considered to represent the best available segmentation in any particular case. Expert observer time is expensive, and manual segmentation is a difficult and time-consuming manual task and vulnerable to variation. This is especially so for large studies with many thousands of images. The drive towards developing semi-automatic techniques that rely on little manual input is therefore based on reducing the time to segment and increasing the repeatability of segmentation.

To create a patient-specific artery model from a 3DUS scan, the lumen (the area inside the artery that carries blood) needs to be identified. Due to the directional nature of US scanning, the sides of the lumen as seen in arterial US images are often less well defined than the top and bottom of the lumen. The US beam is transmitted into the body from one direction (typically from above the artery in arterial scanning) resulting in increased resolution of the top of the artery but reduced resolution of the sides (see Figure 6.1). The absence of data at the sides of arterial US scans is a fundamental limitation of US imaging, and is an important challenge for both manual and semi-automatic segmentation techniques: if there is no clear outline at the sides of the lumen, how can the “true” lumen boundary be defined in these regions? SonoCT compounding [23] can reduce this artefact but does not eliminate it completely in most scans.

Three-dimensional compounding of several scans taken at different angles around the artery of interest is another method which may reduce this artefact [94]. However for some arteries it is impossible to move the transducer far enough around to completely reduce this artefact. Performing multiple scans at different angles also increases the time required to scan a patient.

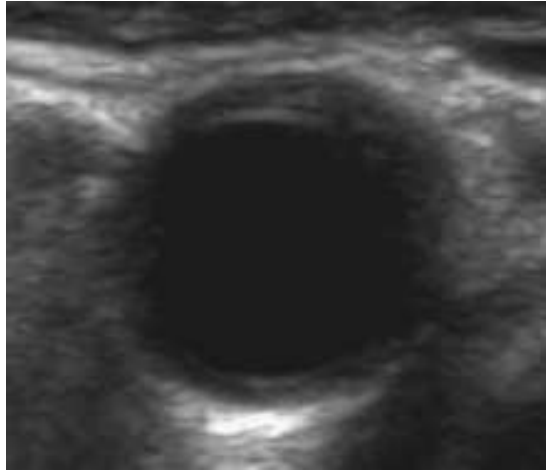


Figure 6.1: *An example of how the directionality of US imaging affects the clarity of the lumen outline. The top and bottom edges of the lumen reflect more of the US beam back to the transducer, and are clearly seen. The edges of the lumen are less well defined.*

A semi-automatic registration-based segmentation method was used to segment arterial datasets. The segmentations produced by this method were analysed by calculating the accuracy of the method compared to manual segmentation and by calculating the precision of the method from repeated segmentations performed on three test datasets.

6.2 Methods

The Sheffield Image Registration Toolkit (ShIRT) is a registration-based semi-automatic segmentation method [95]. This was developed initially for the segmentation of MRI and CT images. This represents the first time this toolkit has been used on US data. The toolkit is available as a compiled program which can be used with Matlab (The MathWorks, Inc., Natick, MA, USA. <http://www.mathworks.com>). It is a registration-based segmentation technique: the images are registered before segmentation. A schematic of how ShIRT is used is shown in Figure 6.2, and another example using real US data is shown in Figure 6.3. The user defines a registration region on a single image near the centre of the dataset, showing the major features of the images which will be registered. In this case, a region defined around the outside of the

artery is used as the registration region. ShIRT then registers the images, aligning the defined features in the other images to the image with the registration region. A segmentation outline is then defined on an image in the dataset with good contrast and clear lumen boundaries. This segmented outline is then morphed to suit the other images in the dataset. To create a set of segmented contours which corresponds to the original set of images, the segmented contours are unregistered and exported to Stradwin where they can be superimposed on the original US images to confirm the accuracy of the segmentation.

Gold standard manual segmentation was carried out using Analyze (AnalyzeDirect, Inc., Overland Park, KS, USA. <http://www.analyzedirect.com>). Images from the Stradwin 3DUS datafile were imported and segmented individually using a spline-based drawing method. The spline from image $n - 1$ may be imported to image n to provide continuity between the shape of the segmented contour on different images. A more comprehensive description of its use is found in Appendix B. A diagram of the image processing route used with manual and semi-automatic segmentation methods is shown in figure 6.4.

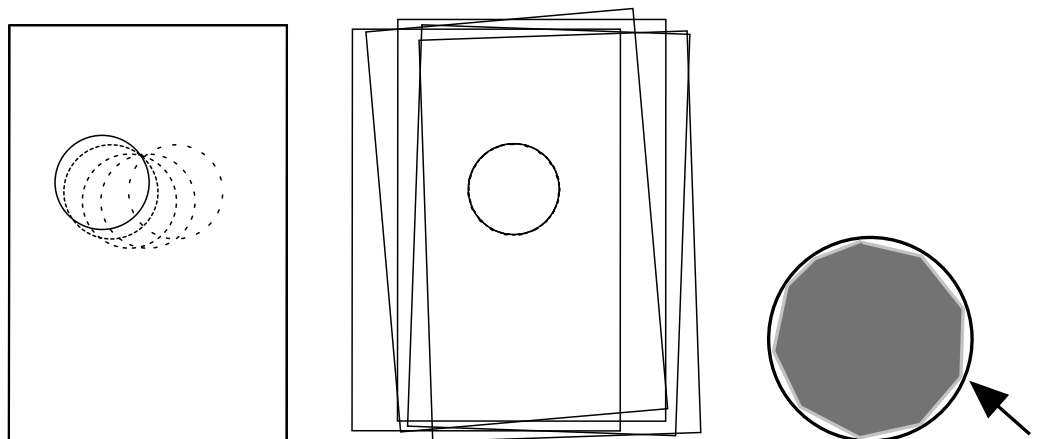
6.2.1 Methods to measure the accuracy and precision of segmentation techniques

There are almost as many methods of assessing the performance of segmentation techniques as there are segmentation techniques. Some groups consider a single important factor that is measured by a segmentation routine such as heart chamber volume [25] or the diameter of a foetal head measured from one image [96]. Other factors could be considered such as the position of the centroid of the automatically-segmented contour compared to that of the gold standard contour. However, as Hammoude [96] points out

A meaningful indication of border accuracy is provided only if the error measure is a mathematical metric. A metric generates a real-valued, non-negative quantification of contour error which is zero only when the two contours are truly identical...Relatively few investigators implement metrical error measures. Other investigators, therefore, base system evaluation on misleading error criteria.

It is therefore important to define a valid metric for assessing the performance of a segmentation technique. Rules to define a valid metric are given by Chalana and Kim [97].

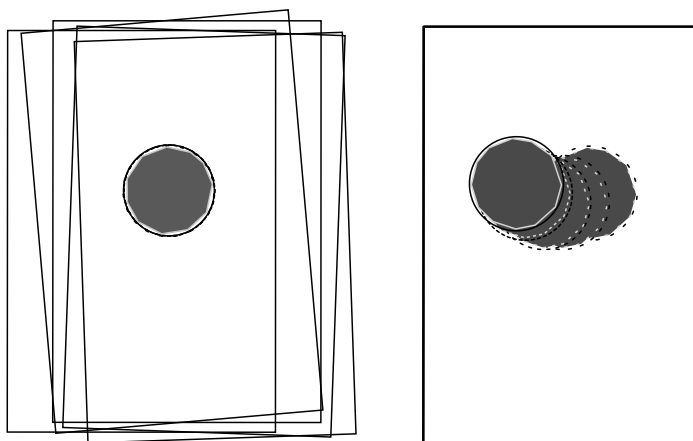
Many metrics only assess one aspect of the performance of a segmentation technique. They



(a) US images are read from the Stradwin file. The registration of each image to the position sensor is discarded and the images are treated as a sequence of non-spatially registered images.

(b) The US images are rigidly registered. In a centrally located image in the sequence, a region of interest (ROI) is defined that covers the artery. ShIRT rigidly registers the other images in the sequence to the features in the ROI by rotating and translating them until the portion of the artery shown in each image overlaps.

(c) The user defines an initial segmentation using the mouse, clearly outlining the shape of the lumen.



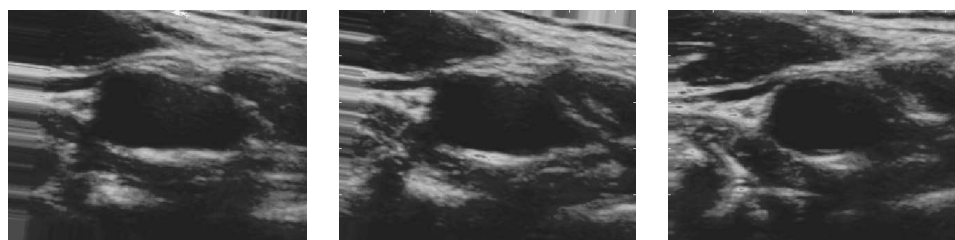
(d) The initial segmentation is morphed to match the shape of the artery in the other images in the sequence.

(e) To create a segmented version of the original US images, the registered image sequence with the overlaid segmented contours is unregistered.

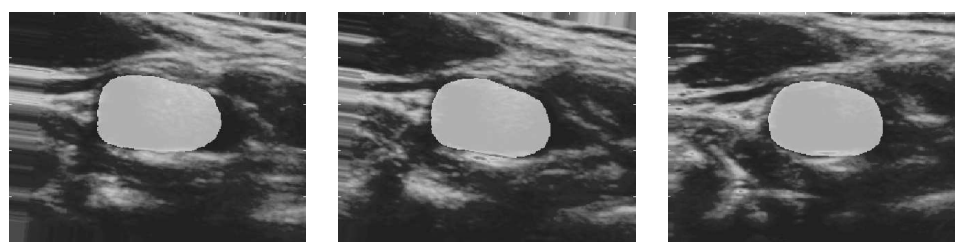
Figure 6.2: A schematic showing how ShIRT is used to register and segment 3DUS images.



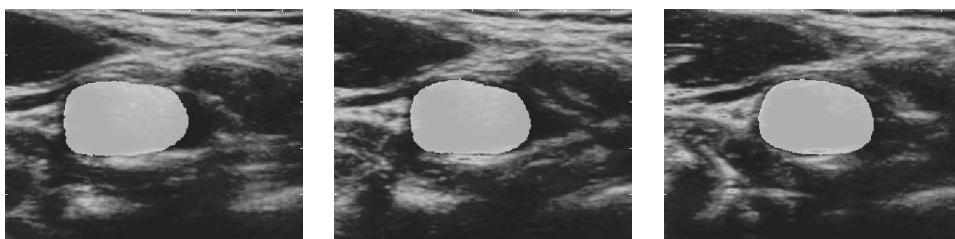
(a) Cropped portions of the original US images. Using a cropped image reduces memory use and processing time for registration and segmentation.



(b) Registered US images. The left-hand and middle images have been translated and rotated to match the right-hand image, which is at the centre of the image sequence. The image smearing at the left-hand border of the registered images shows where some movement has taken place.



(c) Segmented registered US images. A manually-defined contour was drawn on one of the images and then morphed to match the shape of the artery in the other images.



(d) Unregistered and segmented US images. To recover the original images with an overlaid segmented contour, the images are unregistered. These images may then be imported back into Stradwin and used to create a 3D segmented artery outline.

Figure 6.3: Using *ShIRT* to segment US images (following the example in Figure 6.2). Figure (a) shows some cropped images from a section of a common carotid. In Figure (b), the images have been rigidly registered to an image at the centre of the dataset. Figure (c) shows the registered images with a segmented outline applied to each. The final step, shown in Figure (d), involves unregistering the segmented dataset using the mapping previously defined in the registration step. The segmentation now corresponds to the original image data.

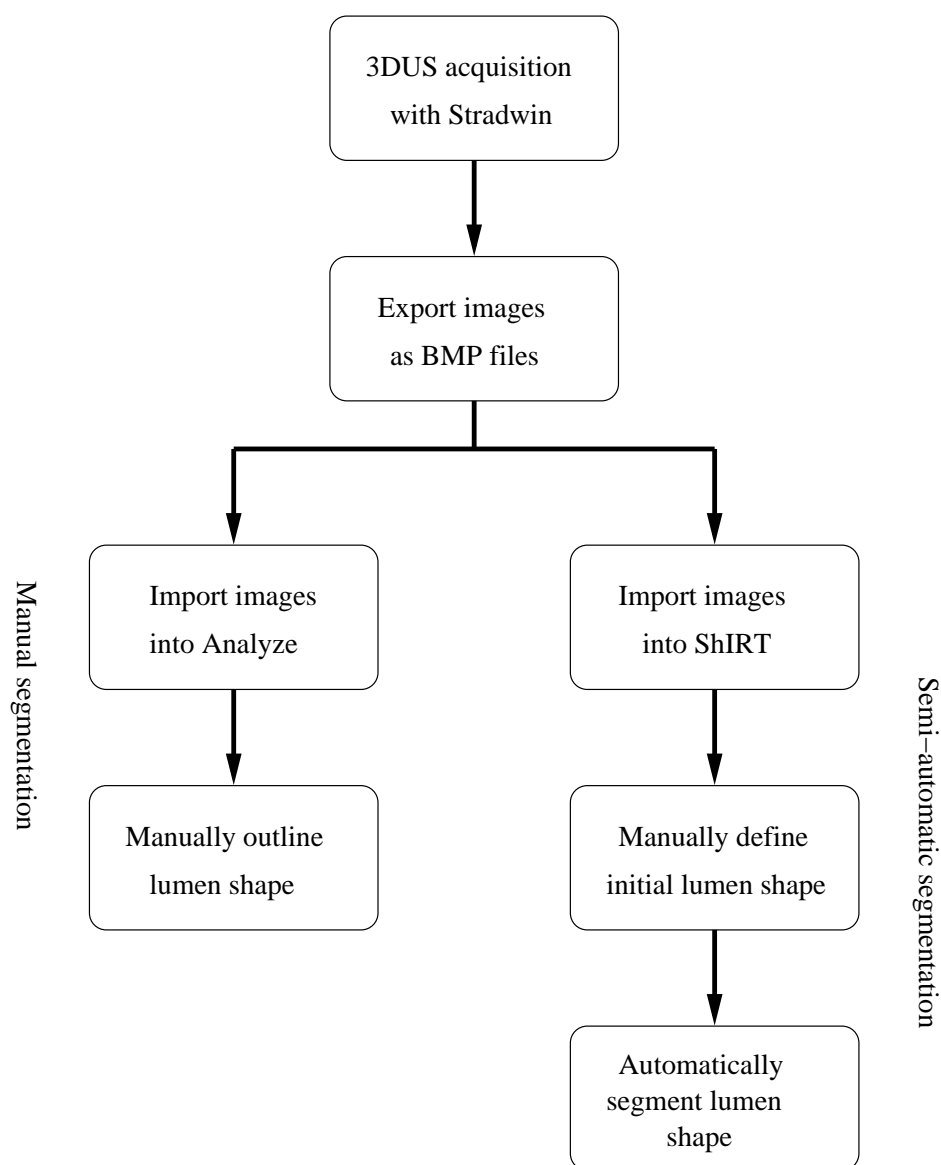


Figure 6.4: The image processing path used to create segmented 3DUS images. The patient or volunteer is scanned using the Stradwin 3DUS system. The images captured in this 3DUS dataset are exported to bitmap (BMP) format. For manual segmentation, the images are imported into Analyze and the lumen shape is manually outlined on each image. For semi-automatic segmentation, the images are imported into the ShIRT segmentation and registration program. An initial lumen shape is manually defined on the first image in the dataset. The initial shape is then morphed to match the shape of the lumen on subsequent images.

usually calculate how different a contour created using a partially automated segmentation technique is to a manually-outlined gold standard segmentation. The metrics proposed by Udupa et al. [98] allows a more comprehensive assessment. They can measure how much the automatically segmented contour was inside and how much it was outside of the gold standard contour. This set of metrics was intended originally for a 3D volumetric dataset. These were modified to be applicable to 2D image space, since segmentation of Stradwin 3DUS data was done on an image-by-image basis without reference to the 3D coordinate system provided by the position sensor. The applicable metrics are defined in the following sections. Before describing these metrics, some definitions are required.

- \mathcal{O} is the physical object of interest. In the context of this study, this is the lumen of the artery of interest.
- \mathcal{U}_d is the scene containing the objects to be segmented. This is equivalent to the whole image in a 2D case.
- \mathcal{C}_{td} is the true delineation (td), considered in this case to be the pixels on the image corresponding to the manually-defined gold standard segmentation.
- \mathcal{C}_d^M is the automatically-segmented delineation defined using method M , where method M in this case is the ShIRT segmentation method.

Several quantities can be derived from these basic definitions. These are the false negative scene \mathcal{C}_{FN}

$$\mathcal{C}_{FN} = \mathcal{C}_{td} - \mathcal{C}_d^M, \quad (6.1)$$

the false positive scene \mathcal{C}_{FP}

$$\mathcal{C}_{FP} = \mathcal{C}_d^M - \mathcal{C}_{td}, \quad (6.2)$$

the true negative scene \mathcal{C}_{TN}

$$\mathcal{C}_{TN} = \mathcal{U}_d - \mathcal{C}_d^M - \mathcal{C}_{td} \quad (6.3)$$

and the true positive scene \mathcal{C}_{TP}

$$\mathcal{C}_{TP} = \mathcal{C}_d^M \cap \mathcal{C}_{td}. \quad (6.4)$$

These scenes are illustrated in Figure 6.5.

Two important measures of segmentation performance are derived from [98] to suit a 2D image. The true negative area fraction ($TNAF$) expresses the fraction of the image in the gold standard

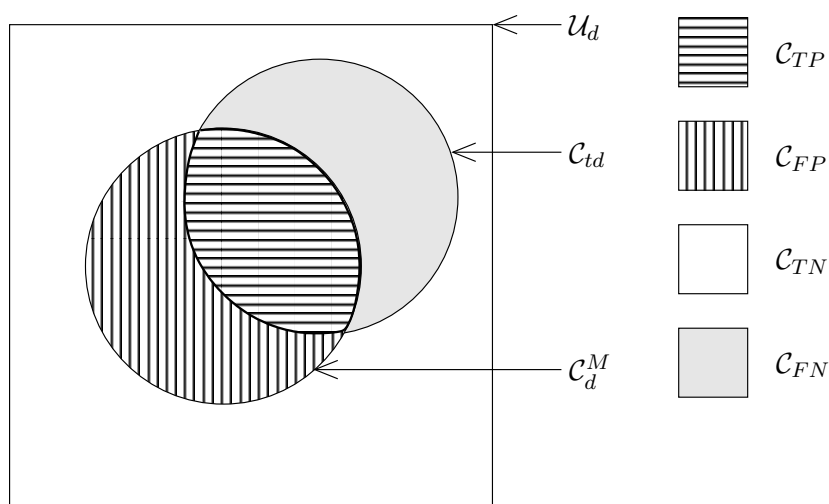


Figure 6.5: An illustration of the different scenes used to define a set of segmentation error metrics. \mathcal{U}_d is the US image. \mathcal{C}_{td} is the manually segmented outline (the true delineation). \mathcal{C}_d^M is the outline created using ShIRT. \mathcal{C}_{TP} is the True Positive scene, the portion inside the manually segmented outline correctly identified by ShIRT (shown with horizontal lines). \mathcal{C}_{TN} is the True Negative scene, the portion of the image that is not inside the manually segmented outline (shown in white). \mathcal{C}_{FP} , the False Positive scene, is the portion of the image identified by ShIRT that is outside the manually segmented outline (shown in vertical lines). \mathcal{C}_{FN} , the False Negative scene, is the portion of the manually segmented outline that was not identified by ShIRT (shown in grey).

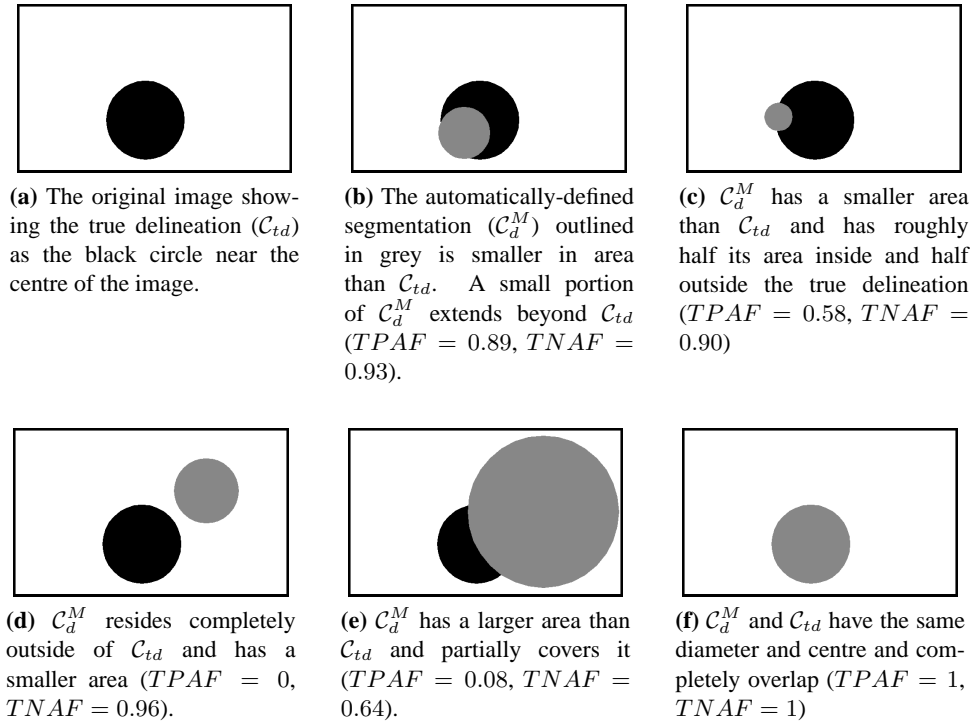


Figure 6.6: The effect of changes in the automatically-defined segmentation \mathcal{C}_d^M on the value of the $TNAF$ and $TPAF$ metrics. In each case the true delineation \mathcal{C}_{td} is outlined in black and the automatic segmentation \mathcal{C}_d^M is in grey.

segmentation that was missed by the automatic method.

$$TNAF_d^M(\mathcal{O}) = 1 - \frac{|\mathcal{C}_{FP}|}{|\mathcal{U}_d - \mathcal{C}_{td}|} \quad (6.5)$$

The true positive area fraction ($TPAF$) expresses the fraction of the image falsely identified by method M as a fraction of the amount of the image in \mathcal{U}_d that is truly not in the object.

$$TPAF_d^M(\mathcal{O}) = \frac{|\mathcal{C}_{TP}|}{|\mathcal{C}_{td}|} \quad (6.6)$$

To illustrate the effect of different segmentation results on these two metrics, Figure 6.6 shows a simulated image with the true delineation (\mathcal{C}_{td}) in black. The automatically-defined segmentation \mathcal{C}_d^M is outlined in grey on each image. Values of $TNAF$ and $TPAF$ are given for each image to show the effect of variations in the position and shape of \mathcal{C}_d^M on the value of each performance metric.

By using these two fractions we can measure the *delineation sensitivity* using $TPAF_d^M(\mathcal{O})$ and the *delineation specificity* using $TNAF_d^M(\mathcal{O})$. The closer these two measures are to 1, the more closely the ShIRT segmentation matches the gold standard manual segmentation. These two measures were used to evaluate the accuracy of ShIRT compared to manual segmentation.

6.2.2 Assessing the precision of ShIRT

Precision is another important feature of segmentation. The precision (PR) of the same image segmented twice using a single technique M is defined by

$$PR_{T_1}^M(\mathcal{O}) = \frac{|\mathcal{C}_{0_1} \cap \mathcal{C}_{0_2}|}{|\mathcal{C}_{0_1} \cup \mathcal{C}_{0_2}|}. \quad (6.7)$$

This is the intraobserver precision. It represents the total area of the image that is common to both \mathcal{C}_{0_1} and \mathcal{C}_{0_2} as a fraction of the total area of the image in the union of \mathcal{C}_{0_1} and \mathcal{C}_{0_2} .

To calculate the inter-operator precision, three 3DUS datasets representative of the three different arteries considered in this thesis (the abdominal aorta, the carotid artery, and the superficial femoral artery) were segmented (see Figure 6.7).

Each dataset consisted of up to 11 images taken from three healthy volunteer 3DUS scans. These were segmented five times manually and five times using ShIRT. The settings used in each ShIRT segmentation are listed in Table 6.1.

The intraobserver precision for both segmentation methods was calculated using the method

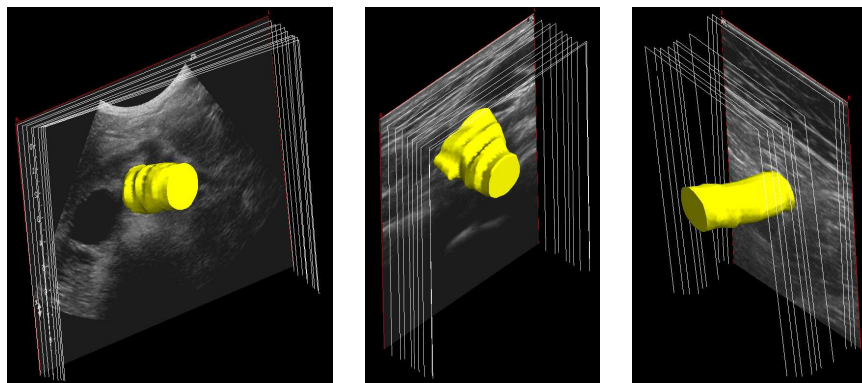


Figure 6.7: Three segmented arteries (L to R: abdominal aorta, carotid artery, femoral artery).

Image cropping	Sufficient to include the artery on all images plus 50 pixels
Registration node spacing	8
Registration method	Rigid.
Segmented image	The first image in the series was used for initial manual segmentation
Initial segmentation method	By hand. A new initial segmentation was used each time.
Segmentation node spacing	16

Table 6.1: *Settings used with ShIRT to register and segment US data. Registration node spacing refers to the number of nodes in the alignment grid used to perform the initial image registration. Higher values of node spacing produce a higher resolution registration at the expense of increased computing time. Segmentation node spacing refers to the number of nodes in the grid used to map the segmented shape. A higher node spacing will produce a higher resolution segmentation, again at the expense of increased computing time.*

described by equation 6.7. To assess whether ShIRT is as precise as manual segmentation, a Mann-Whitney U-test [90] was used. This statistical test was used because the precision values for the ShIRT segmentations were not normally distributed. The null hypothesis (H_0) was: the sample of precision values for the ShIRT-segmented dataset comes from the same population as the sample of precision values for the manually-segmented dataset. This hypothesis was tested against three alternative hypotheses for each dataset. The alternative hypotheses considered the median (η) of values of PR for the ShIRT segmented datasets (η_S) and the manually segmented datasets (η_m). They were:

- $\eta_S < \eta_m$
- $\eta_S \neq \eta_m$
- $\eta_S > \eta_m$.

Testing these alternative hypotheses showed which of the two segmentation techniques had the highest precision for the three 3DUS datasets considered here.

6.2.3 Comparing ShIRT to a set of intraobserver segmentations

A quick and simple method of assessing whether ShIRT is as good as manual segmentation is reported in Chalana and Kim [97] with modifications suggested by Alberola-Lopez et al. [99]. The percent statistic test computes the percentage of images where the ShIRT-generated segmentation lies within the range of segmentations created by a human observer. This was originally designed to compare an automatic method with the *interobserver* error. However

here ShIRT is compared to the *intraobserver* error which is a much more stringent test: one observer is more precise than several observers. The percent statistic test checks whether the maximum ShIRT-to-observer error is less than or equal to the maximum intraobserver error i.e.

$$\max_i \{e(C, O_i)\} \leq \max_{i,j} \{e(O_i, O_j)\} \quad (6.8)$$

where C is the computer-defined segmented contour and O_i is a manually defined contour where $i \neq j$. This test is carried out on a per-image basis, deciding whether the ShIRT segmentation on image N is as good as the manual segmentations on image N . To determine whether a set of ShIRT segmentations on the images in a given 3DUS dataset is as good as the sets of manual segmentations, the percentage of times that the ShIRT segmentations lie within the intraobserver range is compared to the expected probability that the ShIRT segmentations should lie in the intraobserver range.

Given the hypothesis that the expected probability that the ShIRT segmented contour and the manually-segmented contours are samples from the same distribution, the expected percentage of times that the ShIRT-segmented boundaries lie within the intraobserver range is given by

$$p = P(C_0 \in IR) = \frac{n-1}{n+1}. \quad (6.9)$$

where n = number of observers. To test whether the percent statistic calculated from the ShIRT segmented boundaries is part of this population, a threshold test is used. The threshold is given by

$$\epsilon = z_{1-\alpha} \sqrt{\frac{pq}{N}} \quad (6.10)$$

where N = number of images, p is defined in equation 6.9, $q = 1 - p$, $z_{1-\alpha}$ is the value for which $G(z_{1-\alpha}) = 1 - \alpha$ and $G(\cdot)$ is the distribution function of a normal standard variable. Here, $z_{1-\alpha} = 1.6449$ for $\alpha = 0.05$. When $Z > p - \epsilon$ (where Z = the mean percent statistic calculated from the ShIRT segmented boundaries using equation 6.8) the ShIRT segmented dataset is considered to be part of the population of manually-segmented datasets.

The percent statistic test was carried out using both the $FNAF$ and $FPAF$ metrics. These are defined as

$$FNAF_d^M(O) = \frac{|C_{FN}|}{|C_{td}|} \quad (6.11)$$

which measures the fraction of the image in the true delineation C_{td} that was missed by seg-

mentation method M , and

$$FPAF_d^M(\mathcal{O}) = \frac{|C_{FP}|}{|\mathcal{U}_d - \mathcal{C}_{td}|} \quad (6.12)$$

which measures the area of the image falsely identified by segmentation method M as a fraction of the area of the image \mathcal{U}_d that is truly not in the object. These two metrics were used instead of the $TNAF$ and $TPAF$ metrics used earlier because lower values of $FNAF$ and $FPAF$ imply better performance of the ShIRT segmentation technique, in the same way that a lower value of error implies better performance.

Values of the $FPAF$ and $FNAF$ metrics were calculated for the set of three datasets representing a healthy example of an abdominal aorta, a carotid artery and a superficial femoral artery. Each human-segmented image was tested against every other human-segmented image using these two metrics, and the highest value of each metric was found. Similarly, ShIRT segmentations were tested against the human segmentations and the maximum value of each metric was found. The percent statistic test was used to determine whether the highest value of each metric for the ShIRT vs. observer tests was greater than or equal to the highest value of each metric for the intraobserver tests on each image. The percentage of times that the ShIRT vs. observer tests met this condition was tested using equations 6.9 and 6.10, giving an indication of whether ShIRT was as accurate as the observer at segmenting each 3DUS artery dataset.

6.2.4 Assessing the accuracy of ShIRT on full artery scans

Using ShIRT to segment small sections of healthy arteries is useful for defining precision and comparing its results to those of manual segmentation. The use of ShIRT on a full dataset with all the variation in image quality, artery position and edge definition found in typical *in-vivo* scanning for healthy volunteers and patients with disease was used to provide a realistic test. Six full datasets from healthy volunteers and patients were segmented manually using Analyze. These were then segmented using ShIRT and the $TNAF$ and $TPAF$ metrics were calculated for each image. The six datasets are described in the following sections.

6.2.4.1 An abdominal aorta from a healthy volunteer

A young healthy volunteer was scanned using the C5-2 abdominal probe. The abdominal aorta is clearly visible among the other vessels in the abdomen (see Figure 6.8). The scan begins at

the point where the AA ascends from above the spinal column and ends as the two iliac arteries branch off into the pelvis. Some respiratory movement is visible, although the volunteer was scanned with their breath held.

6.2.4.2 A carotid from a healthy volunteer

The right carotid artery and internal and external carotid arteries of a young healthy volunteer were scanned. This is a very good quality scan, with the intima-media layer clearly visible on many images (see Figure 6.9), especially in the common carotid before the bulb.

6.2.4.3 A carotid from a patient with a large plaque near the carotid bulb

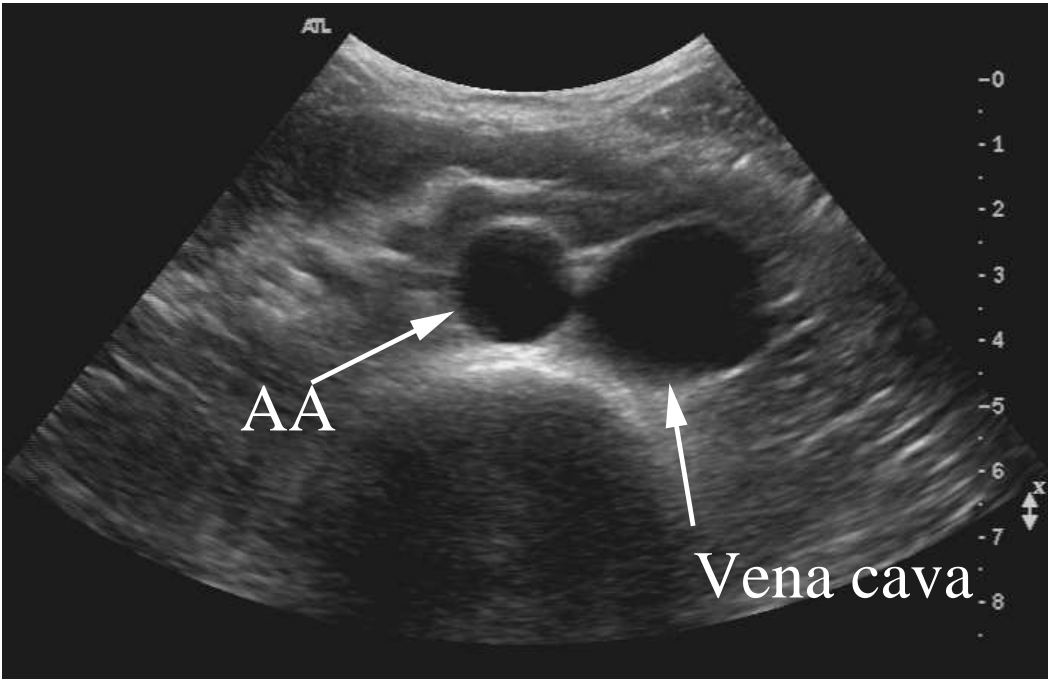
A thin patient with no reported carotid artery disease was scanned. The patient was found to have a large plaque located downstream of the bulb in the common carotid (see Figure 6.10). Very complex plaque geometry was clearly visible here. Although the patient was thin, and in many places in the scan intimal-medial thickening is visible, the intima-media layer was not well defined on many of the images in the dataset. The lumen boundary was also very poorly defined at and beyond the bulb, resulting in poorly defined outlines of the internal carotid artery in particular.

6.2.4.4 A femoral artery from a healthy volunteer

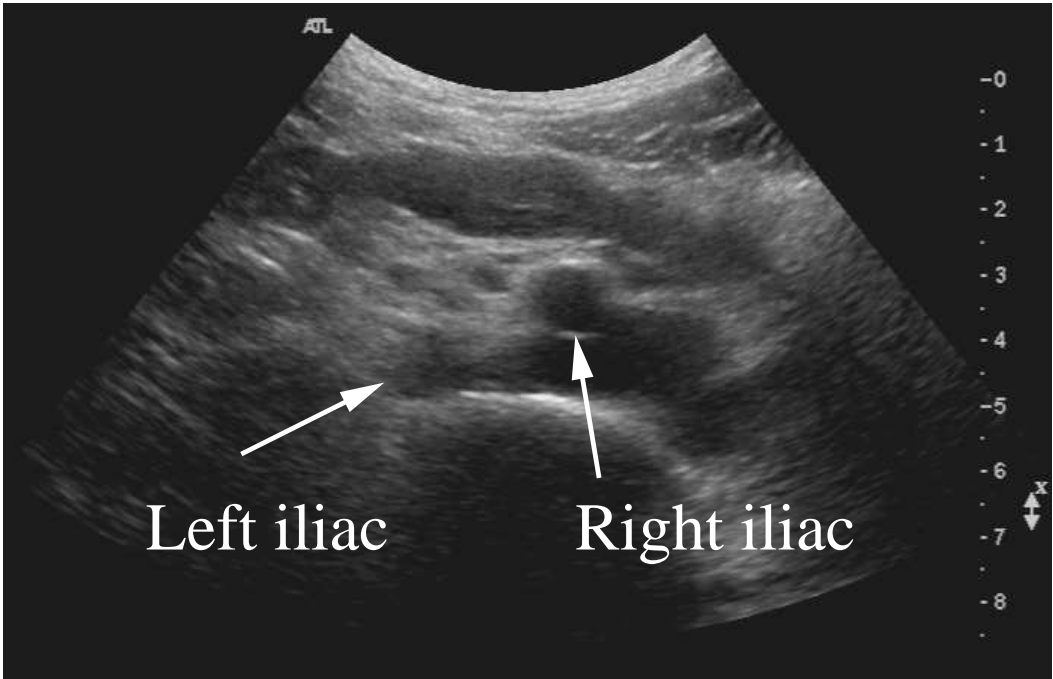
This scan was from a healthy volunteer (see Figure 6.11). The scan extends from above the inguinal ligament to where the superficial femoral descends behind the knee. The lumen outline is poorly defined at the start (near the groin) and the end (near the knee) of this scan, but more clearly defined in the middle.

6.2.4.5 A femoral artery from a patient

The superficial femoral artery of a patient with no reported femoral artery disease was scanned (see Figure 6.12). No disease is visible in this scan, although image quality is very poor, especially where the artery descends into the thigh. A large intima-media layer is visible in many images.

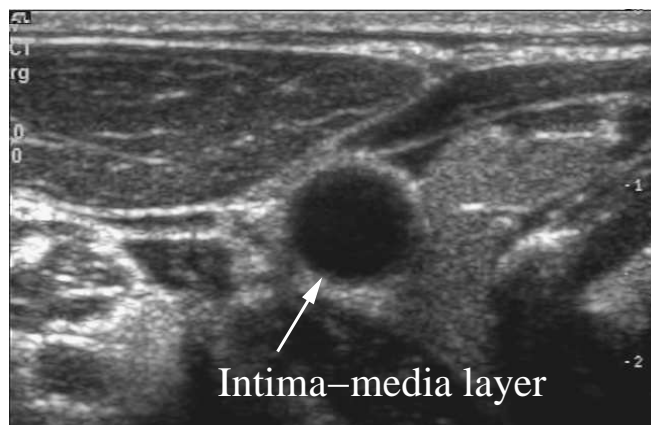


(a) A typical image of the abdominal aorta (centre of image), with the inferior vena cava to the right of the vessel

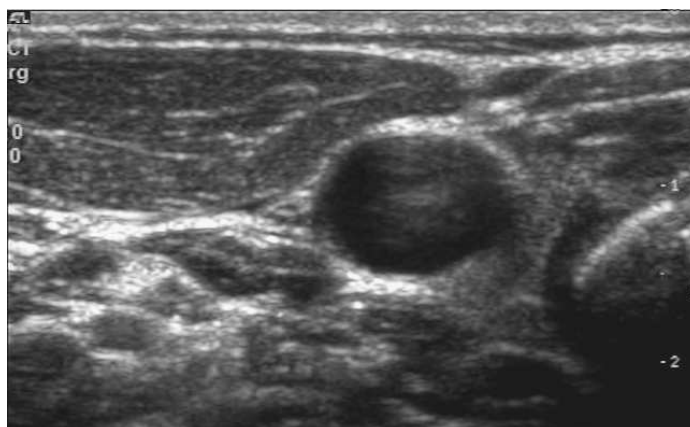


(b) The iliac branches, showing the reduced clarity of the artery outline at this position.

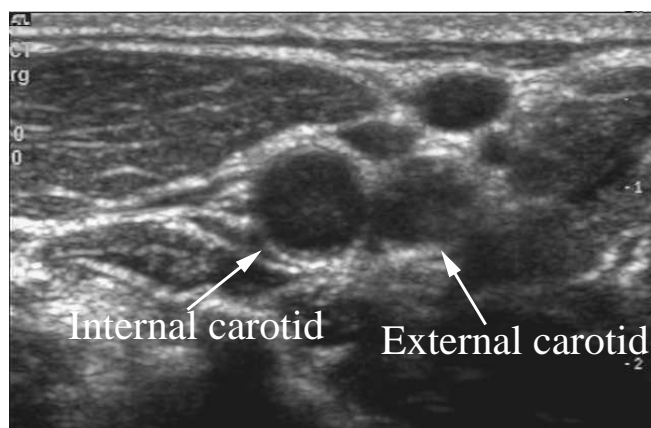
Figure 6.8: Some images from the abdominal aorta of a healthy volunteer.



(a) A very clear image of the common carotid showing the intima-media layer.

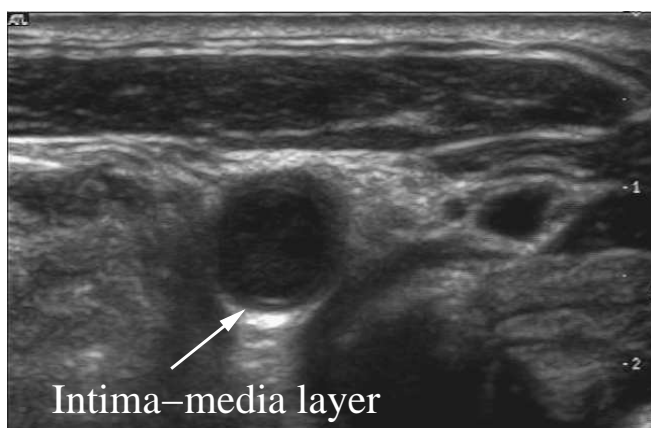


(b) The carotid bulb.

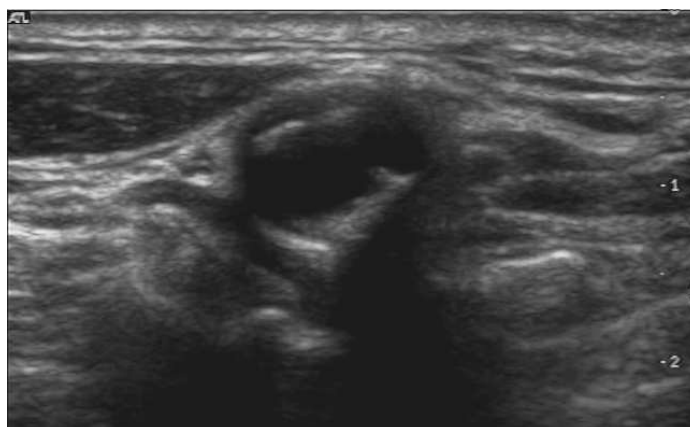


(c) The carotid artery above the bulb showing the internal and external carotid artery branches.

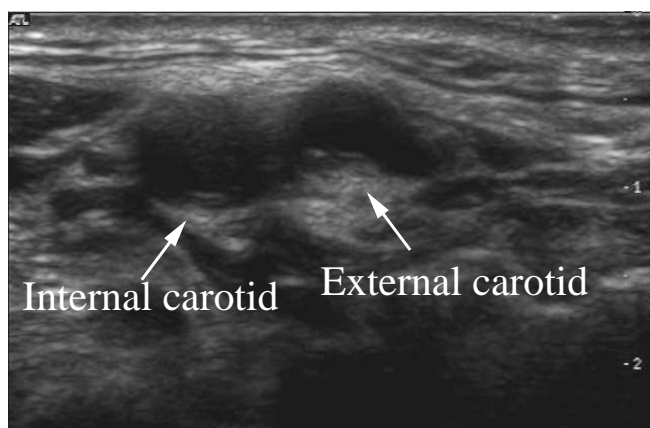
Figure 6.9: Some images from the common carotid of a healthy volunteer.



(a) The intima-media layer is clearly defined in this image.

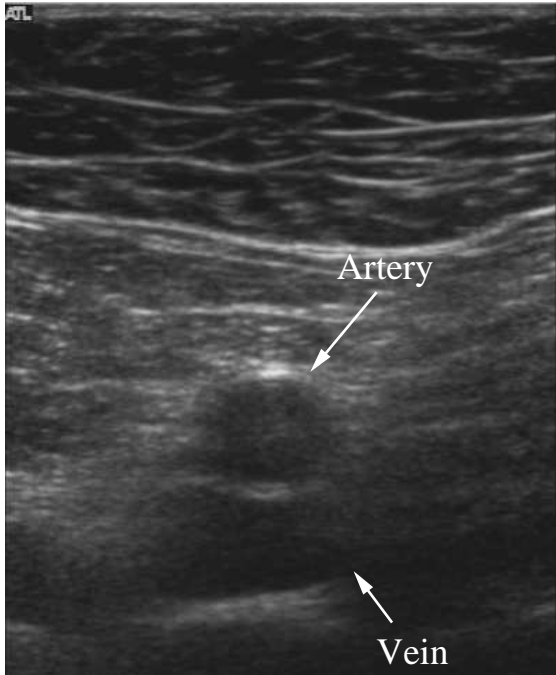


(b) The complex plaque encountered just downstream of the carotid bulb.



(c) Poorly defined internal and external carotid arteries.

Figure 6.10: Some images from the common carotid of a patient with a complex plaque near the bulb.

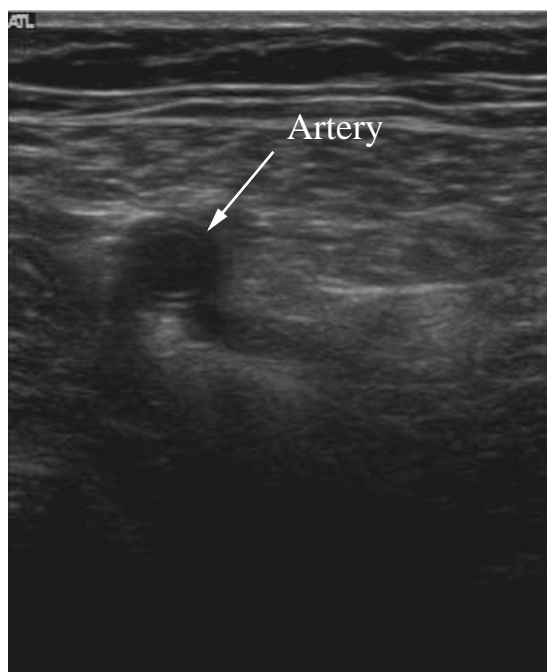


(a) A good quality image of the superficial femoral artery with a clearly defined lumen boundary. Note the larger femoral vein beneath the artery.

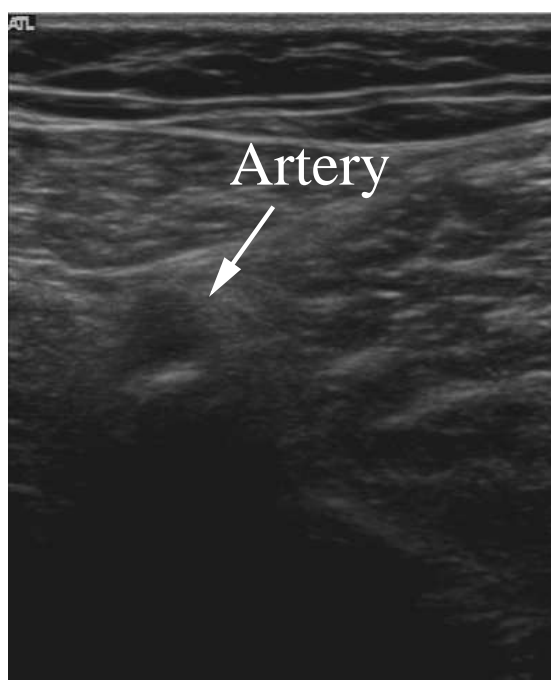


(b) Further downstream, the image quality reduces as the artery descends into the thigh.

Figure 6.11: Some images from the superficial femoral artery of a healthy volunteer.



(a) A typical image showing the thick artery wall.



(b) Downstream, as the femoral artery descends into the leg, the image quality is degraded making accurate identification of the location and shape of the lumen difficult.

Figure 6.12: *Some images from the superficial femoral artery of a patient.*

6.3 Results

6.3.1 Assessing the precision of ShIRT

Figure 6.13 shows a summary of the precision values calculated for the three manually-segmented datasets. This can be compared with the summary data for the datasets segmented using ShIRT shown in Figure 6.14. Median values of $PR \pm 95\%$ confidence interval for the three 3DUS datasets are found in Table 6.2. Mann-Whitney U-test results to evaluate whether ShIRT is as precise as intraobserver manual segmentations are given in Table 6.3.

Artery	Manual PR	ShIRT PR
AA	0.94±0.00	0.93±0.00
CA	0.94±0.00	0.92±0.01
FE	0.91±0.01	0.93±0.00

Table 6.2: Median precision (PR) \pm 95% confidence interval for ShIRT and manual segmentations of the three arteries.

Artery	H_0	H_1	P	Result
AA	$\eta_S = \eta_m$	$\eta_S < \eta_m$	cannot reject H_0	$PR_m > PR_S$
	$\eta_S = \eta_m$	$\eta_S \neq \eta_m$	< 0.001	
	$\eta_S = \eta_m$	$\eta_S > \eta_m$	< 0.001	
CA	$\eta_S = \eta_m$	$\eta_S < \eta_m$	cannot reject H_0	$PR_m > PR_S$
	$\eta_S = \eta_m$	$\eta_S \neq \eta_m$	< 0.001	
	$\eta_S = \eta_m$	$\eta_S > \eta_m$	< 0.001	
FE	$\eta_S = \eta_m$	$\eta_S < \eta_m$	< 0.001	$PR_m < PR_S$
	$\eta_S = \eta_m$	$\eta_S \neq \eta_m$	< 0.001	
	$\eta_S = \eta_m$	$\eta_S > \eta_m$	cannot reject H_0	

Table 6.3: Mann-Whitney U-test results for comparing the precision (PR) of ShIRT segmentations to the precision of manually-segmented segmentations for the three arteries. PR_m denotes manual segmentation precision; PR_S is the ShIRT segmentation precision; H_0 is the null hypothesis that is tested by the U-test; H_1 is the alternative hypothesis; η_S is the median value of ShIRT segmentation precision; and η_m is the median value of manual segmentation precision.

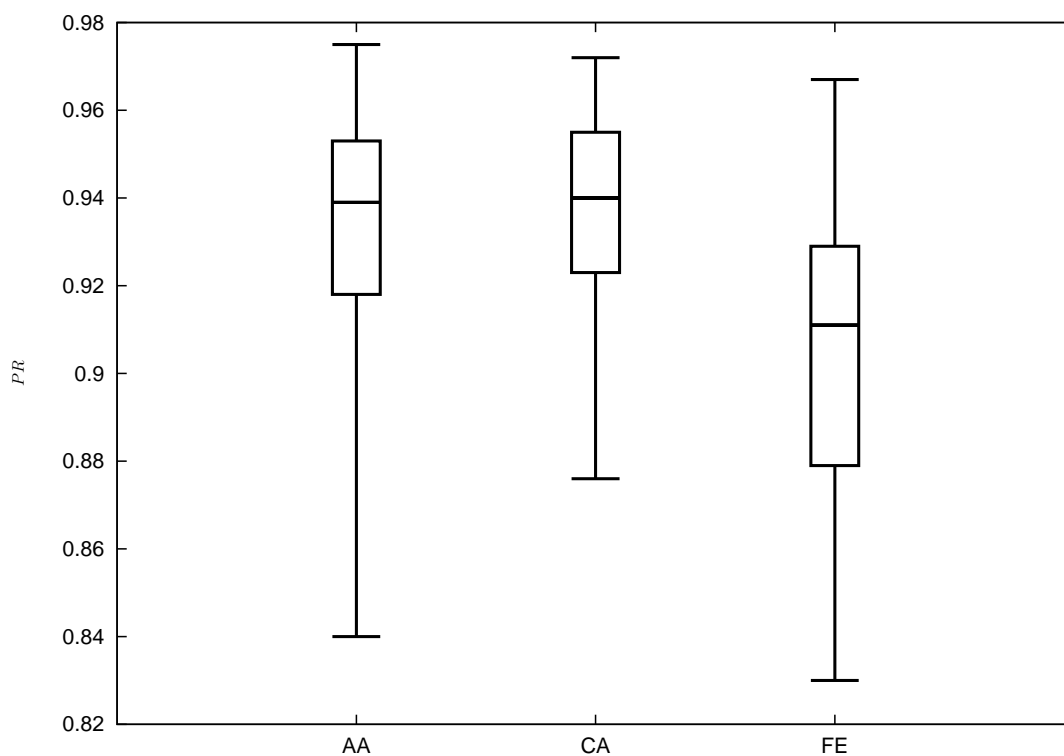


Figure 6.13: Box-whisker plots of precision (PR) for the three manually segmented datasets.

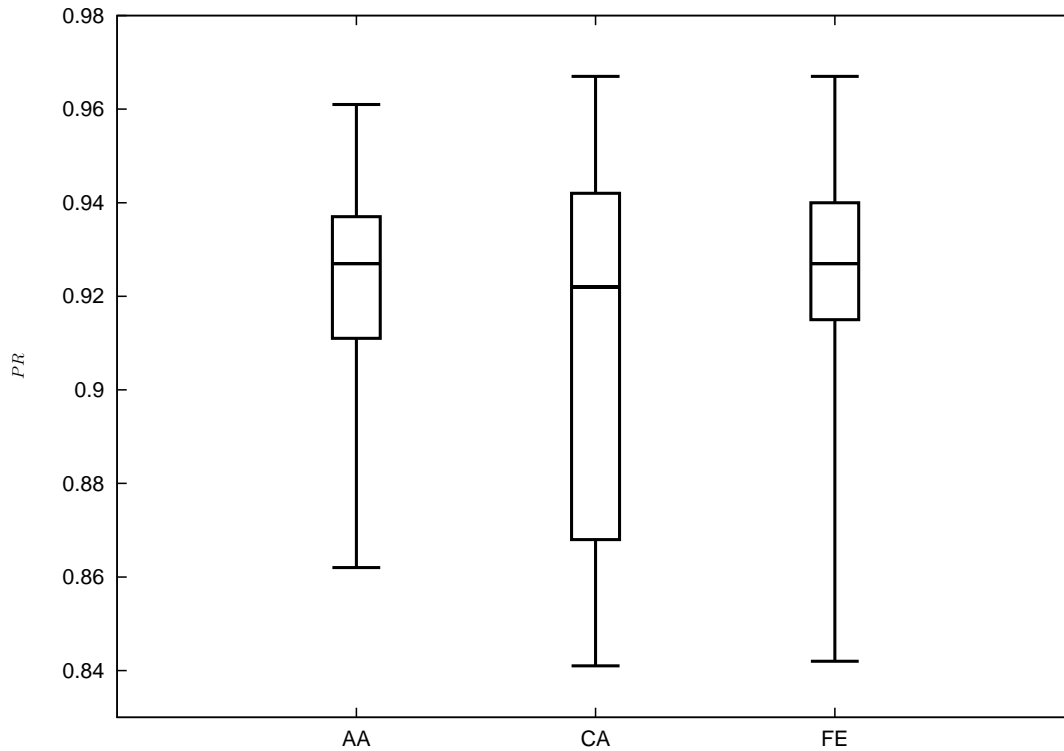


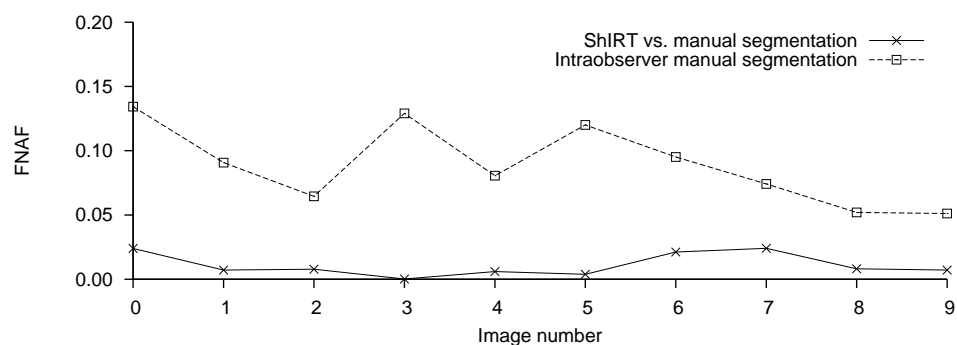
Figure 6.14: Box-whisker plots of precision (PR) for the three datasets segmented using ShIRT.

6.3.2 Comparing ShIRT to a set of intraobserver segmentations

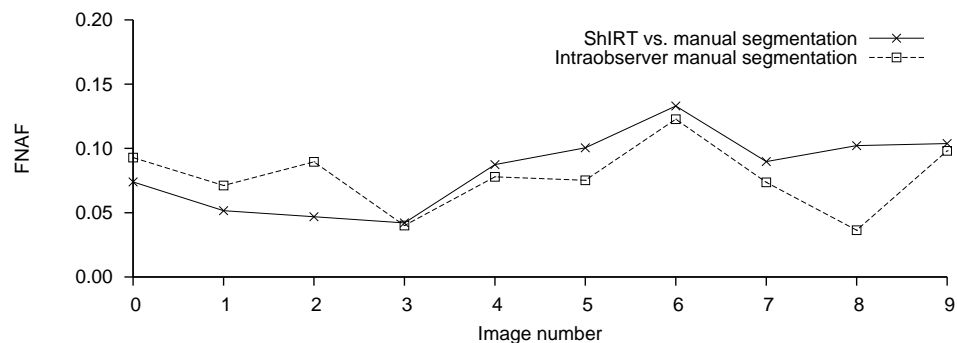
Values of $FNAF$ and $FPAF$ were calculated for a ShIRT-segmented dataset *versus* the intraobserver manually segmented datasets (figures 6.15 and 6.16). $FNAF$ and $FPAF$ are calculated for every image in each artery dataset; this shows variation in each metric in each part of the dataset. Values for ShIRT vs. manual segmentation and intraobserver manual segmentation are plotted together on each Figure to directly compare their performance. If values of the ShIRT segmentation metric are below the intraobserver segmentation metric then ShIRT is as accurate as manual segmentation at that point. The percent statistic (PS) was also calculated for these datasets and pass/fail results for each value for each artery are shown in Table 6.4.

Artery	Metric	p	$p - e$	Z	$Z > p - e$	Result
Abdominal aorta	$FPAF$	0.667	0.319	1	True	Pass
	$FNAF$	0.667	0.319	0	False	Fail
Common carotid	$FPAF$	0.667	0.319	0.400	True	Pass
	$FNAF$	0.667	0.319	0.300	False	Fail
Superficial femoral	$FPAF$	0.667	0.319	0.273	False	Fail
	$FNAF$	0.667	0.319	1	True	Pass

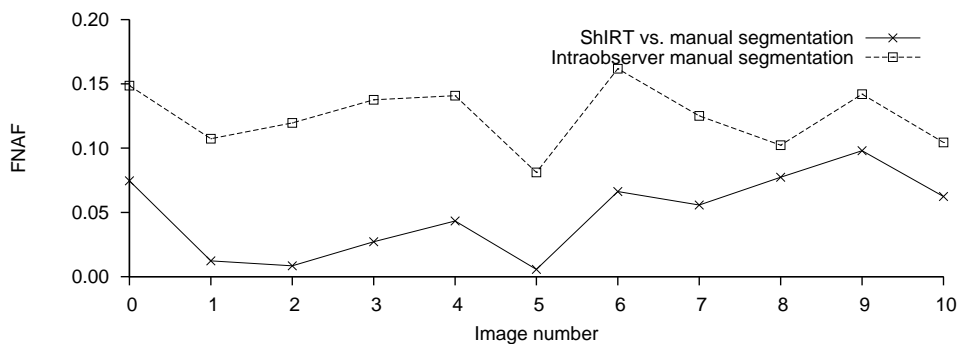
Table 6.4: Percent statistic (PS) results, testing whether a segmentation of each artery using ShIRT was as good as five manual segmentations. p is the expected probability that the value of the error metric calculated for the ShIRT segmentation compared to the manual segmentations will be within the range of error metric values for each manual segmentation tested against each other. $p - e$ is the critical value of the error metric. Z is the mean probability of the value of the metric calculated for the ShIRT segmentation lying within the range of intraobserver metric values. The column with $Z > p - e$ tests this condition, and the Result column confirms whether the ShIRT segmentation for each artery dataset is as accurate as a set of intraobserver segmentations.



(a) FNAF for the abdominal aorta

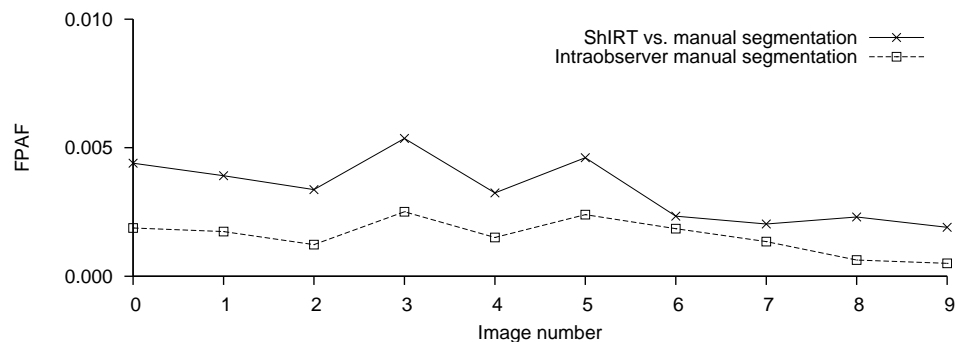


(b) FNAF for the common carotid

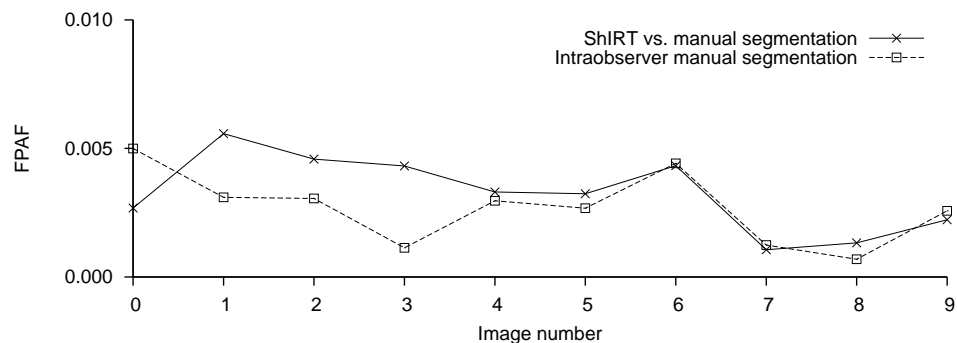


(c) FNAF for the superficial femoral artery

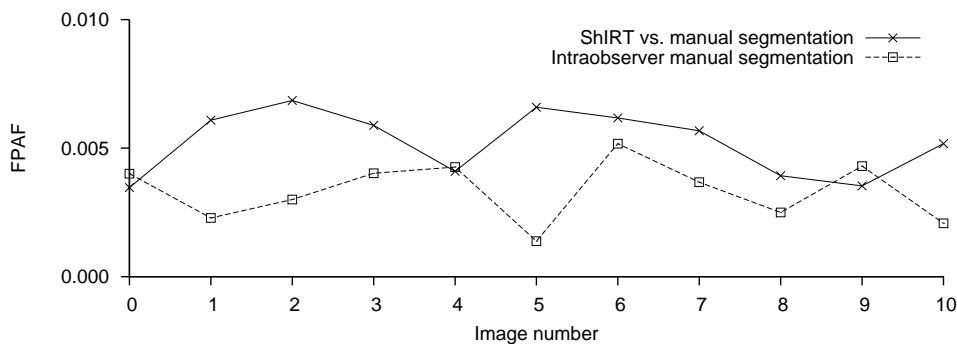
Figure 6.15: False Negative Area Fraction (FNAF) calculated for the five repeatedly segmented scans from three healthy arteries.



(a) *FPAF* for the abdominal aorta



(b) *FPAF* for the common carotid



(c) *FPAF* for the superficial femoral artery

Figure 6.16: False Positive Area Fraction (*FPAF*) calculated for the five repeatedly segmented scans from three healthy arteries.

6.3.3 Assessing the accuracy of ShIRT on full artery scans

Figures 6.17 to 6.26 show graphs of $TNAF$ and $TPAF$ for the five 3DUS arterial scans described in section 6.2.4. For every image of every scan it is possible to compare the performance of ShIRT with the gold standard manual segmentation. Values of each metric could not be calculated for some images. These are shown with dark grey filled bars. These occur when the US image is not clear enough to be segmented manually. Table 6.5 summarises these figures, giving the mean \pm 95% confidence interval of $TNAF$ and $TPAF$ for each 3DUS scan.

For the abdominal aorta, $TPAF$ is lowest at the beginning of the abdominal aorta scan (Figure 6.17), reaching a minimum of 0.78. This corresponds to an area of poorer image quality at this point in the scan. Values of $TPAF$ in the right iliac were lowest of all (down to a minimum of 0.6). $TNAF$ was typically higher than $TPAF$ for the AA, and varies in a similar way to $TPAF$ (Figure 6.18).

The image numbers in Figures 6.17 and 6.18 increase as the transducer moves down the body. This scan was begun with the transducer placed below the sternum where the aorta was clearly visible. Image 0 is at the beginning of the abdominal aorta. Image 70 is at the root of the iliac bifurcation, and from images 71 onwards the iliac branches are segmented separately.

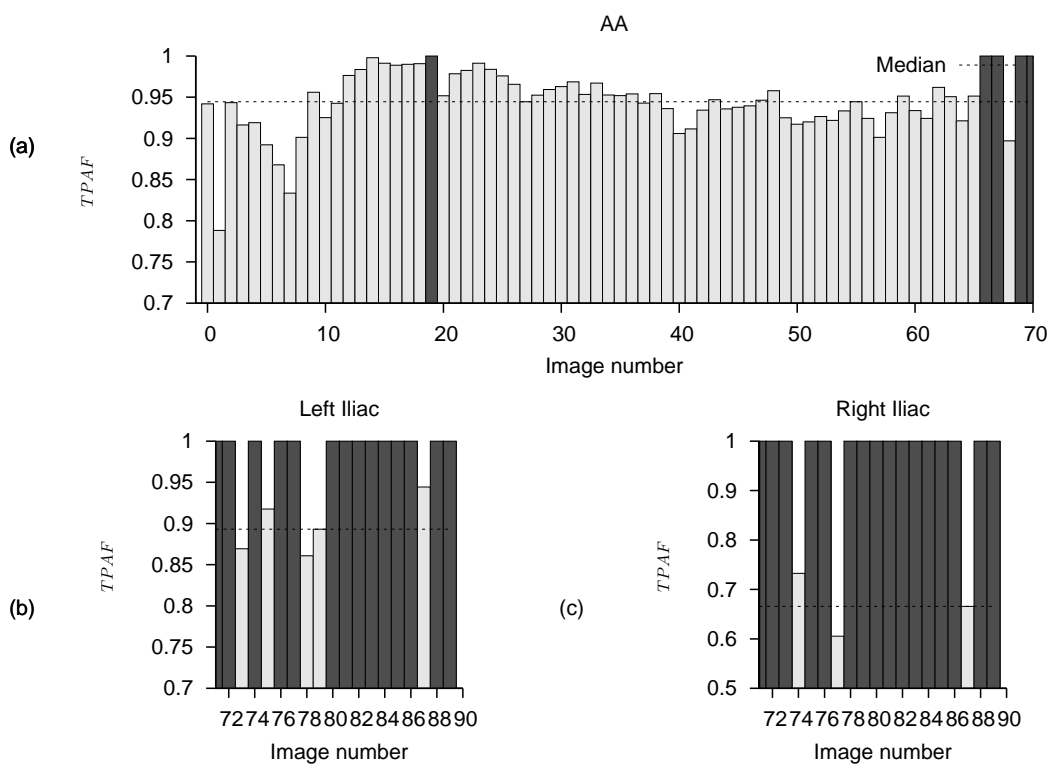


Figure 6.17: $TPAF$ for the healthy AA.

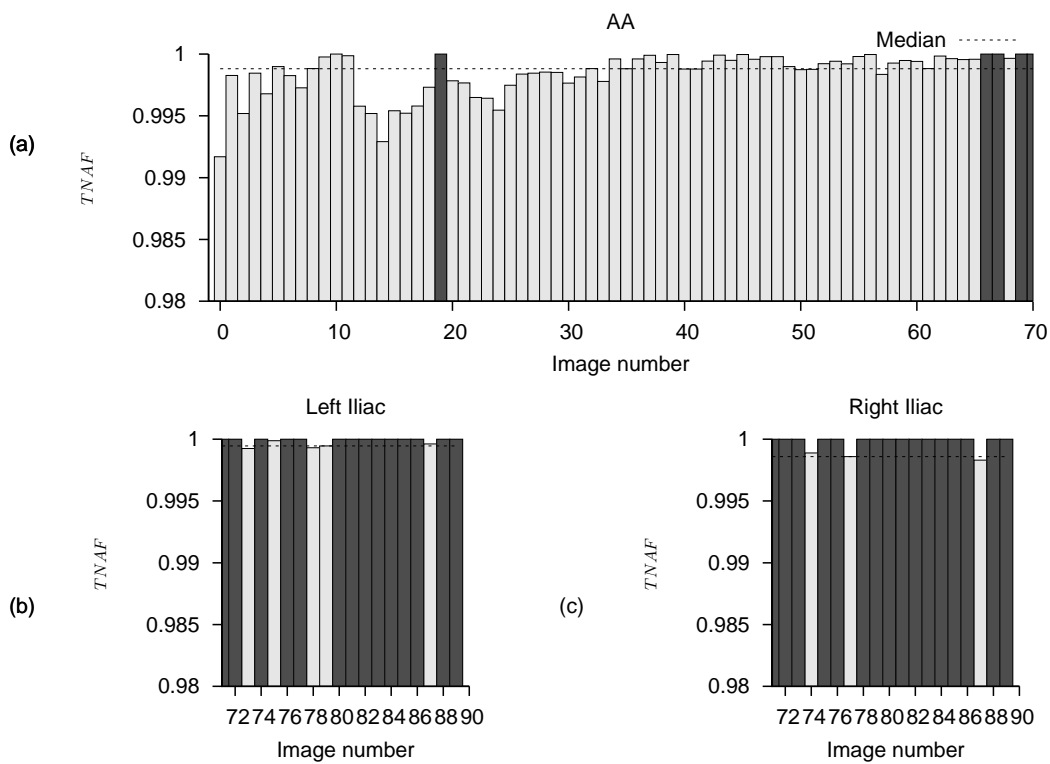


Figure 6.18: $TNAF$ for the healthy AA.

In the healthy carotid artery, variation in image quality with changing anatomy also affects $TPAF$. In the images taken in the common carotid artery (images 0 to 38 in Figure 6.19), there are two main minima, at images 6 and 47. The minimum at image 47 is related to reduced image quality in the carotid bulb, and is confirmed by the lack of a manually segmented contour nearby. $TPAF$ is smaller in the more clearly defined internal and external carotid arteries. In the external carotid artery, $TPAF$ increases distally to the carotid bulb, which is related to the improved image quality in this area. $TNAF$ shows similar trends (Figure 6.20).

The image numbers in Figures 6.19 and 6.20 begin on the neck above the collar bone where the common carotid is visible. Image number increases as the transducer heads towards the mandible. Images 0 to 54 contain the common carotid artery and the carotid bulb. From image 55 onwards the internal and external carotids are segmented separately. The scan ends near the mandible.

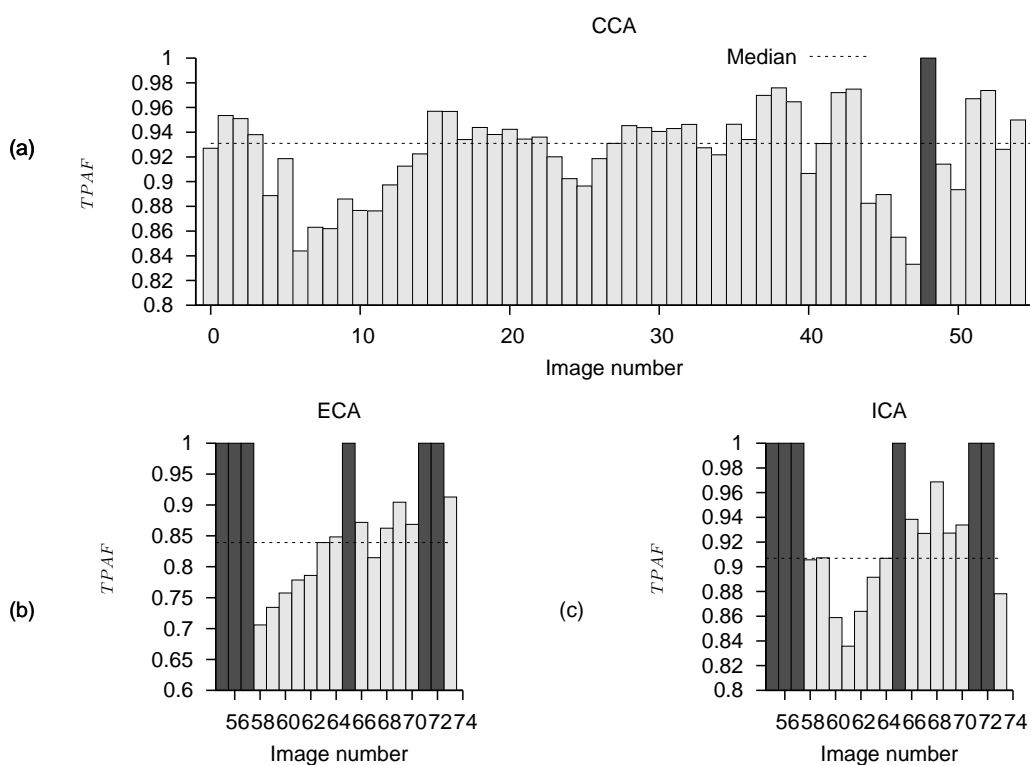


Figure 6.19: $TPAF$ for the healthy CA.

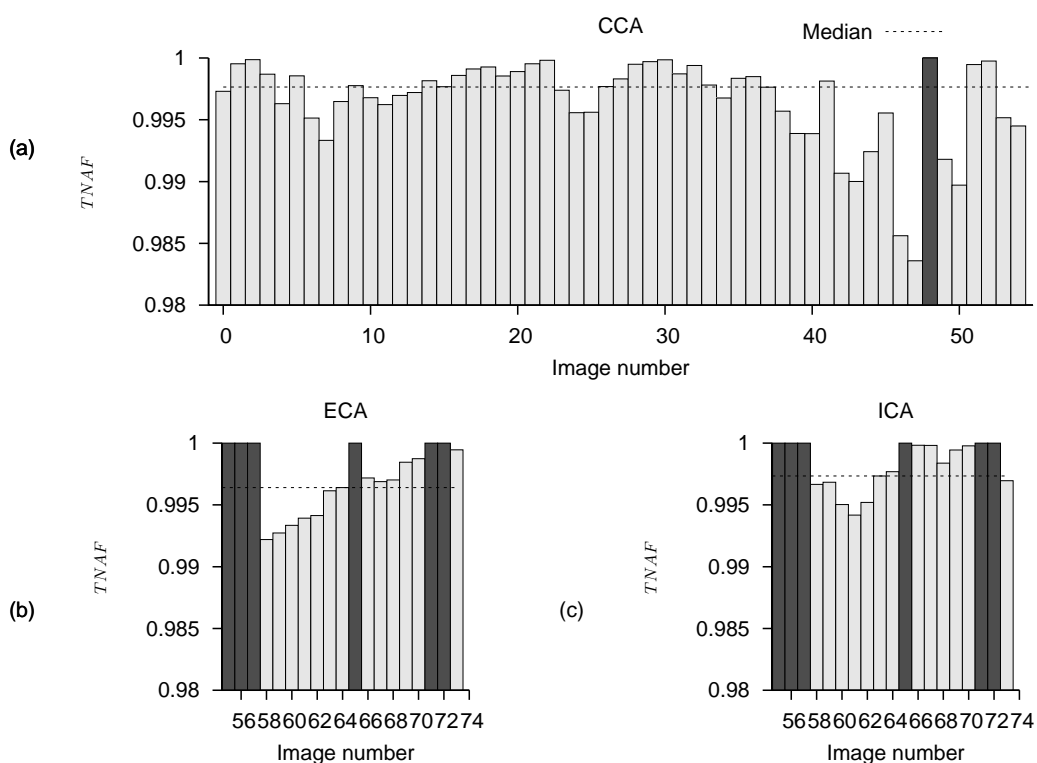


Figure 6.20: $TNAF$ for the healthy CA.

The majority of the images in the healthy femoral artery show high $TPAF$, but have notable troughs at the beginning and end of the scan (Figure 6.21). Image quality is reduced at these two areas, and especially near the knee where the superficial femoral artery descends into the thigh (image 0 is taken near to the top of the thigh; image 160 is from ≈ 5 cm above the knee). Here it reaches a minimum of 0.1. The graph of $TNAF$ (Figure 6.22) shows a similar trend near the knee (e.g. at image 140) but has a less pronounced trough than $TPAF$ at the top of the thigh.

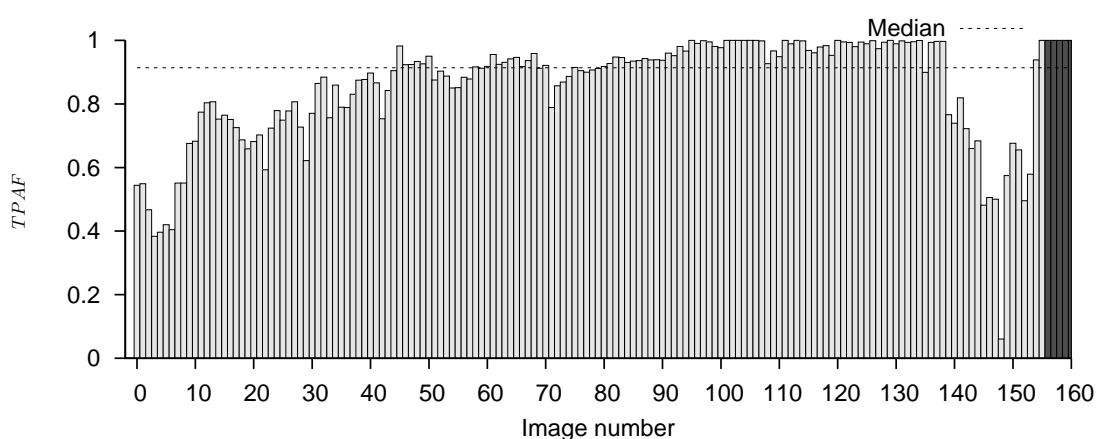


Figure 6.21: $TPAF$ for the healthy FE.

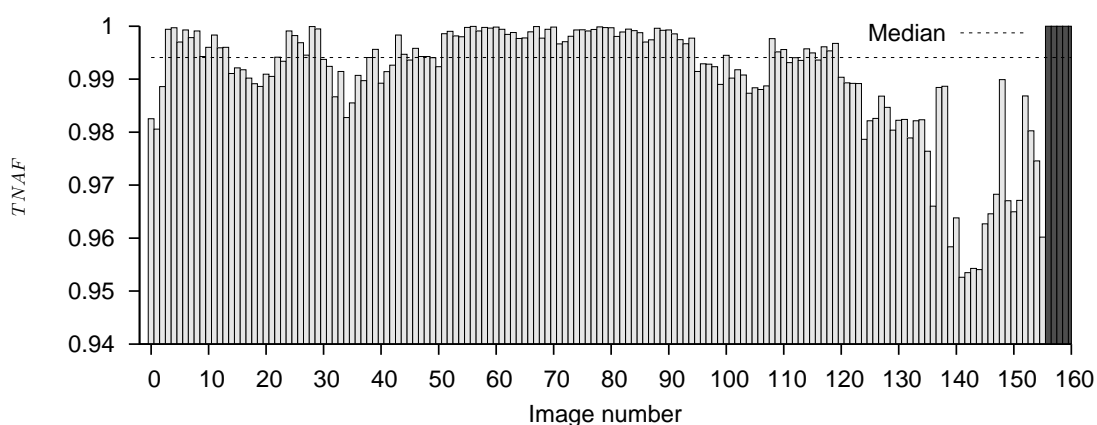


Figure 6.22: $TNAF$ for the healthy FE.

The diseased carotid artery shows no clear trend in $TPAF$ (Figure 6.23). In the internal and external carotid arteries, $TPAF$ is lower than in the carotid artery. $TNAF$ once again shows no clear trend (Figure 6.24), but is again higher in the common carotid than in the less poorly defined external and internal carotid arteries.

The image numbers in Figures 6.23 and 6.24 begin on the neck above the collar bone where the common carotid is visible. Image number increases as the transducer heads towards the mandible. Images 0 to 71 contain the common carotid artery and the carotid bulb. Images 50 to 62 contain complex atherosclerotic plaque. Next to the plaque, image quality is reduced in the carotid bulb, and manual segmentation was not able to determine the lumen outline (images 64, 65, 69 and 70). From image 72 onwards the internal and external carotids are segmented separately. The scan ends near the mandible.

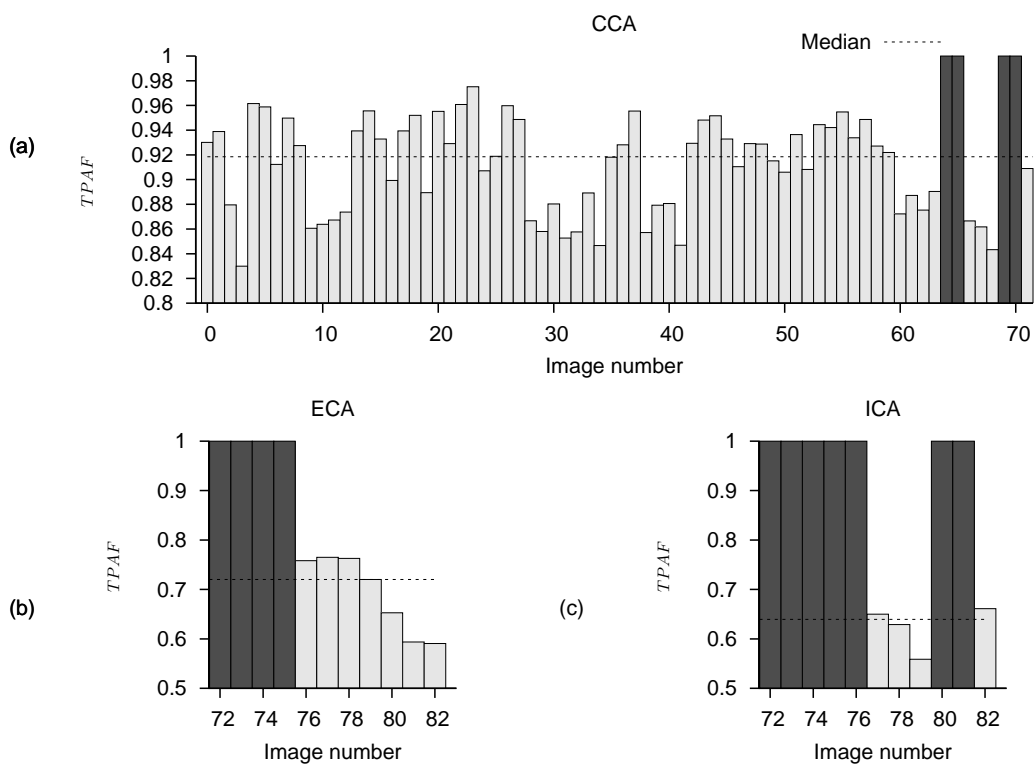


Figure 6.23: $TPAF$ for the diseased CA.

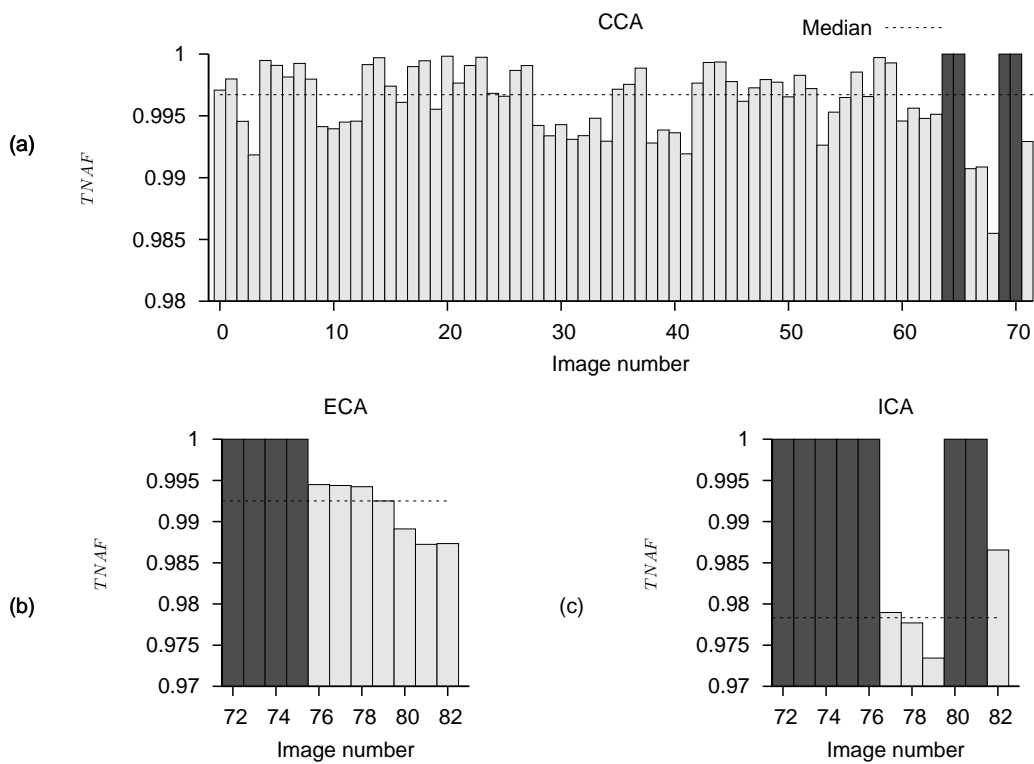


Figure 6.24: $TNAF$ for the diseased CA.

The scan of the patient femoral artery has a higher $TPAF$ than the scan of the healthy volunteer (Figure 6.25). The thickened intima-media layer may have helped with improving the segmentation here. $TPAF$ showed large variations at the centre of the vessel (images 19 to 42), while $TNAF$ showed no clear trend (Figure 6.26). The difference in image quality at the start and end of the vessel is less apparent here than in the healthy volunteer scan.

Image 0 corresponds to the start of the common femoral artery, near to the femoral bifurcation at the top of the leg. At image 80, the femoral artery has begun to descend into the leg to become the popliteal artery.

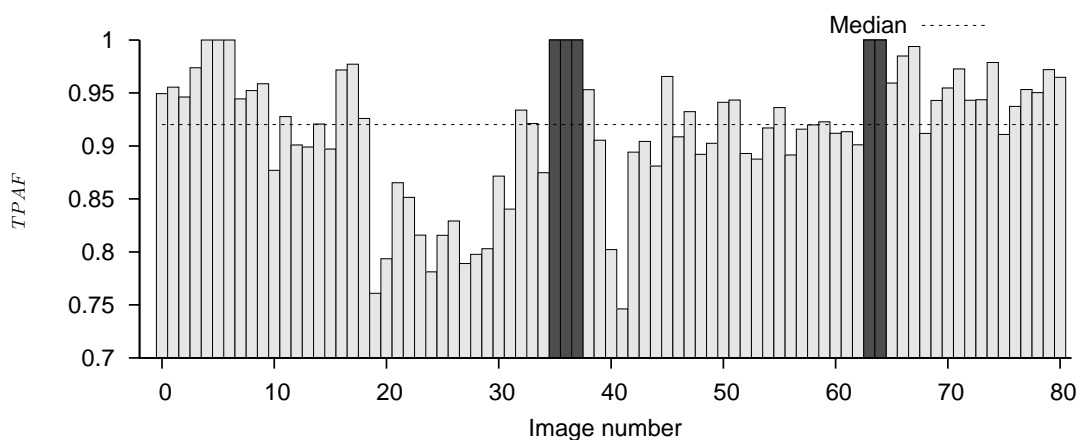


Figure 6.25: $TPAF$ for the patient FE.

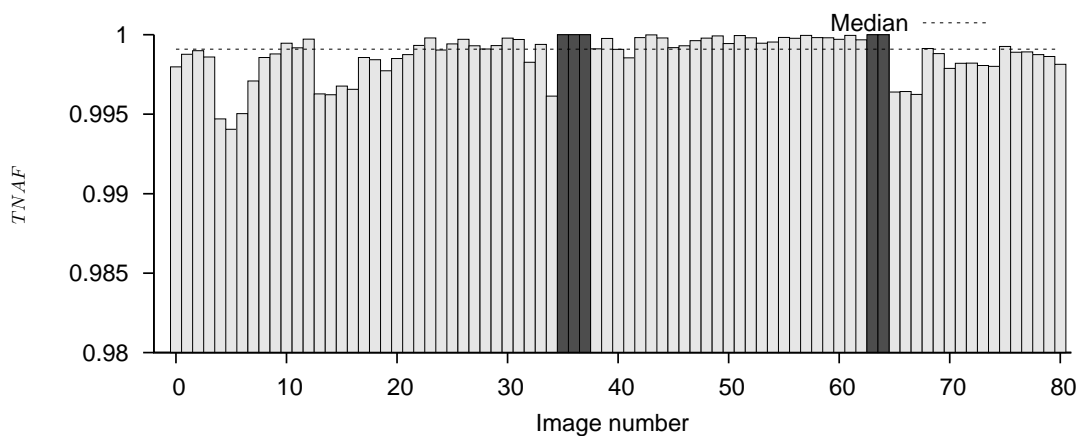


Figure 6.26: $TNAF$ for the patient FE.

Artery	TNAF	TPAF
Healthy AA	0.99±0.00	0.92±0.02
Healthy CA	0.99±0.00	0.90±0.01
Healthy FE	0.85±0.03	0.99±0.00
Diseased CA	0.99±0.00	0.87±0.02
Patient FE	0.99±0.06	0.85±0.03

Table 6.5: Mean *TNAF* and *TPAF* for the five full artery segmentations, comparing *ShIRT* segmentation to manual segmentation using *Analyze*. The data presented above represents the mean value of the metric used \pm the 95% confidence interval.

6.4 Discussion

6.4.1 Assessing the precision of *ShIRT*

ShIRT was less precise than manual segmentation for the carotid artery and abdominal aorta datasets, but more precise for the femoral artery dataset (Table 6.3). The difference in median precision was not significant for all three arteries, at around 1% for the AA dataset and 2% for the CA and FE datasets (Table 6.2). This difference can be attributed to the slightly differing manually-defined initial segmentations and ROI used for each *ShIRT* segmentation. In practice, this slight variation in precision implies that *ShIRT* segmentation can be considered as precise as manual segmentation.

It is noteworthy that the range of precision values for the carotid artery dataset segmented with *ShIRT* (see Figure 6.14) is wider than for the other two arteries. The images from the carotid artery scan used here are close to the carotid bulb, where the diameter of the vessel increases and the shape changes. This is indicative of how *ShIRT* is not as good as manual segmentation at responding to changes in vessel size or shape.

6.4.2 Comparing *ShIRT* to a set of intraobserver segmentations

ShIRT passes the percent statistic test for one metric for all of the three arteries (Table 6.4). For the CA and AA datasets *ShIRT* passed the *FPAF* test but failed the *FNAF* test. Conversely, for the FE dataset, *ShIRT* passed the *FNAF* test but failed the *FPAF* test. This can be interpreted as

- For the AA and CA *ShIRT* consistently identified a shape that is wholly enclosed by the manually segmented boundary.

- For the FE ShIRT consistently identified a shape that extended outside the manually segmented boundary.

This may reflect the quality of the US images found in each artery. AA and CA images tend to have more clearly defined artery walls, whereas in the FE the wall is less clear.

6.4.3 Assessing the accuracy of ShIRT on full artery scans

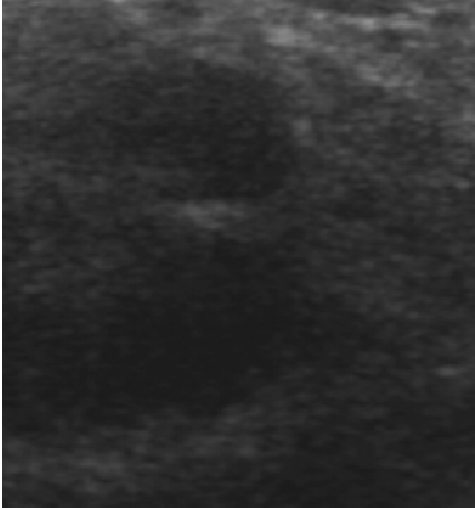
From inspection of figures 6.17 to 6.26, the $TPAF$ metric for ShIRT varies according to change in image quality, which is related to anatomical changes of the scanned arteries. $TPAF$ is generally lowest in the internal and external carotid arteries and the iliac arteries. $TNAF$ showed similar correlation for most datasets, and in most cases had a higher value than $TPAF$.

6.4.4 How appropriate is ShIRT for use with ultrasound data?

Certain characteristics of 3DUS arterial scans caused increases in the values of $TNAF$ and $TPAF$ for comparing ShIRT with manual segmentation. On images where there is a poor outline of the artery wall ShIRT was often as good as manual segmentation (see Figure 6.27). Due to the three-dimensional nature of the ShIRT segmentation algorithm, good quality images placed before and after poor-quality images in the sequence of images in a 3DUS scan can affect the segmentation generated on the poor-quality images, allowing greater continuity of the shape of the segmented contour.

In general, to maximise the quality of the output from ShIRT, it is best to split up the artery where there is significant change in lumen shape or at bifurcations. This includes sections that contain disease, which may require great care and multiple segmented sections for complex plaque. Each section should be segmented individually, then combined afterwards to produce a whole artery. The results for $TPAF$ from comparing manual segmentation to ShIRT segmentation on a patient with carotid artery disease confirms this (Figure 6.23) where $TPAF$ is maintained in the diseased portion of the vessel (images 53 to 66) due to the new ShIRT segmentation initialised at this point. However this may increase the processing time to be greater than or equal to the time taken to produce a manual segmentation.

Given that ShIRT was originally designed for use with MRI and CT scanned data, it can be confirmed from the above analysis that ShIRT is also suitable for use with 3DUS data. It is as



(a) The original US image



(b) US image plus manually segmented contour. It is difficult to tell whether the manually segmented lumen is in the correct place.



(c) US image plus ShIRT segmented contour. The ShIRT contour was attracted by the more clearly defined structure beneath the lumen.

Figure 6.27: Segmentation of a poor quality image, comparing manual segmentation and *ShIRT*.

precise as manual segmentation (Table 6.2), and the percent statistic confirms that in most cases it is as accurate as manual segmentation (Table 6.4). High values of the $TNAF$ and $TPAF$ metrics across most whole artery datasets also confirm this conclusion (figures 6.17 to 6.26).

6.5 Conclusion

From tests comparing ShIRT to manual segmentation it was found that ShIRT is suitable for use as a semi-automatic segmentation technique for 3DUS images of the abdominal aorta and the carotid and femoral arteries. ShIRT segmentations were as precise and as accurate as several manual segmentations made on the same 3DUS arterial datasets. Comparing ShIRT to arterial scans from various patients and healthy volunteers confirmed high values of the $TPAF$ and $TNAF$ metrics for all arteries. The performance of ShIRT was reduced in poorer quality images where it was difficult to identify the lumen.

Chapter 7

Image-guided flow modelling of patient-specific artery geometries

7.1 Introduction

In previous chapters, the initial steps of creating an image-guided modelling system using 3DUS were described. The development of an image acquisition system (Chapter 3), image processing to identify the artery lumen (Chapter 6) and methods to reduce patient movement artefacts (Chapter 4) were described. The final stage in image-guided modelling, that of simulation using a computer model of an artery, is described in this chapter. The method used to create the artery model from 3DUS data is described, and results of flow simulations using artery geometries created with this method are given. The artery geometry is compared to the original segmented 3DUS images to assess its realism, and flow simulations are compared to *in vivo* measurements of flow patterns and wall shear stress (WSS).

Every image-guided modelling system requires some method of creating an artery model from image data. To this end, several methods have been developed to create a computational mesh from serially scanned medical images [100]. Some methods use a “two-dimensional serial reconstruction” technique [101]. This typically includes the following steps:

1. The lumen is segmented from each image in the 3DUS dataset. This is essentially a two-dimensional operation: only the features present in the image are segmented, without considering features in other images.
2. A three-dimensional surface mesh is constructed from the segmented lumen outlines.
3. A volume mesh is created from the surface mesh. The volume mesh defines the locations of the finite elements used to simulate the flow domain in the lumen.

The method described by Augst et al. [66] is an example of this technique. Segmented contours are created manually by fitting an ellipse to the shape of the lumen. Smoothed splines

are fitted to the control points of each ellipse on each image, and are then used to create a smoothed surface mesh. A volume mesh is then created manually from the surface mesh using a commercially-available meshing package.

Alternative methods of mesh creation that may speed up this process and require less skilled user input are available. An example of these is the registration-based mesh generation method developed by Barber et al. [102]. In this chapter, this method is applied to segmented 3DUS data as described in Chapter 6 for healthy and diseased carotid artery scans. The artery models created using this method are compared to the original segmented 3DUS data to assess the realism of the models. Computational fluid dynamics (CFD) results using these models are presented. WSS and flow recirculation patterns are compared to expected results from *in vivo* studies of flow and WSS in diseased arteries [3, 58, 103].

7.2 Methods

7.2.1 Artery geometry creation

The method of creating artery models using the package developed by Barber et al.[102] is described in this section. Before doing so, the term “computational mesh” is clarified in the context of image-guided modelling, and the challenges facing mesh creation from 3DUS images are evaluated.

7.2.1.1 Types of computational mesh

Artery geometries for flow simulation are defined using a computational mesh model of the shape of the artery. In this context, a computational mesh is a set of irregularly spaced points that represent the shape of a patient artery. There are two types of mesh mentioned in this chapter: a surface mesh, and a finite element mesh. A surface mesh represents only the boundary of the artery. Typically, this is saved as a triangulated mesh file in STL (Stereolithography) format. This format is widely used to define three-dimensional surfaces in the fields of computer-aided design (CAD) and rapid prototyping. It provides a compact and complete representation of complex shapes. The surface mesh is defined as a set of triangles, where the three corner points and a normal to the three points defines the shape and orientation of each triangle. Some lines from an STL file, showing how points and normals are defined for each triangular surface

element are shown in Figure 7.1.

A finite element mesh represents the volume that defines the interior of the artery. It is filled with finite elements, each of which defines a portion of the internal volume of the artery. Each finite element may be one of several three-dimensional forms, such as prisms and tetrahedrons. The location of each finite element is necessary as an input into CFD simulation software. Figure 7.2 compares a finite element mesh to a surface mesh, showing the difference in their scope.

```
solid
facet normal 0.021137 -0.756586 0.653552
outer loop

vertex 426.450000 113.647000 -1778.234000
vertex 425.549200 113.066400 -1778.877000
vertex 426.450000 113.081200 -1778.889000
endloop

endfacet
facet normal 0.021137 -0.757079 0.652981
outer loop

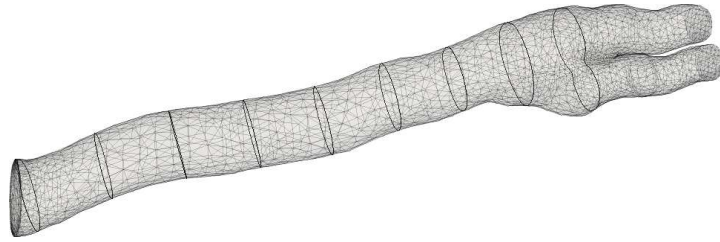
vertex 426.450000 112.515400 -1779.545000
vertex 426.450000 113.081200 -1778.889000
vertex 425.549200 113.066400 -1778.877000
endloop

endfacet
facet normal 0.021862 -0.756575 0.653542
outer loop

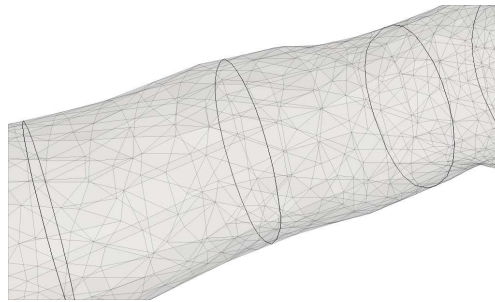
vertex 426.450000 112.515400 -1779.545000
vertex 425.549200 113.066400 -1778.877000
vertex 425.549200 112.500600 -1779.532000
endloop

endfacet
```

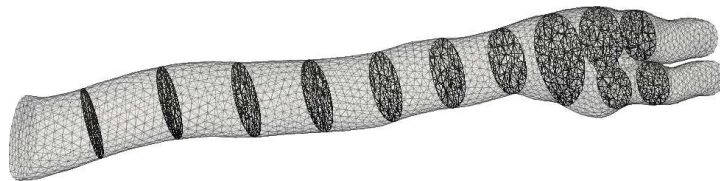
Figure 7.1: An excerpt from an STL file, showing how triangular elements are defined using three corner points (each labelled “vertex”) and the normal to the three points.



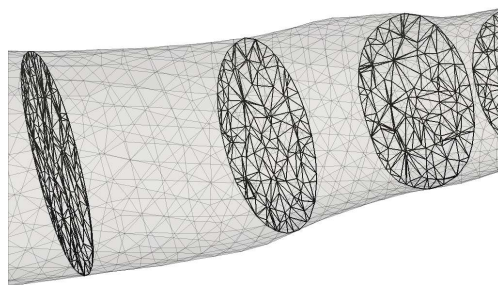
(a) A surface mesh created from spatially-registered and segmented lumen outlines from a healthy volunteer. The black outlines show slices taken through the mesh, spaced evenly along the artery.



(b) A closeup of sliced sections taken through the surface mesh. The slices show that only the outer surface of the mesh is defined in a surface mesh. There is no internal detail.



(c) A volume mesh created from the surface mesh in Figure (a). Slices through the mesh are shown outlined in black.



(d) A closeup of sliced sections taken through the volume mesh. The internal definition of elements is shown clearly inside each slice.

Figure 7.2: Comparing a surface mesh to a volume mesh. The volume mesh in Figure (c) was created using the surface mesh in Figure (a).

7.2.1.2 Challenges to mesh creation using 3DUS images

Important challenges to the creation of realistic artery models from any imaging modality are patient movement and image misregistration. Surface mesh smoothing is often used to reduce these effects. CFD simulations of arterial flow typically use data which is gated at one timestep on the cardiac cycle. At this instant in time the artery shape is assumed to be smooth and free from movement caused by pulsatile blood flow, breathing motion or other patient movement. This reflects the shape of arteries cast and measured *ex vivo* from cadavers [104]. Techniques to reduce misregistration and smooth the position of segmented contours for a two-dimensional serial reconstruction technique include registering the centrelines of segmented contours [29] and applying a surface smoothing technique [105]. Chapters 4 and 5 also present post-processing steps to reduce patient movement artefacts from pulsatile flow and patient movement. In most cases these were found to reduce but not eliminate motion artefacts, necessitating a further smoothing stage after registration and gating to improve the shape of a surface mesh. In most cases the degree of smoothing to apply to an artery mesh requires the judgement of a skilled user [26, 105]. In addition, if a single smoothing is applied to the whole of an artery, physiologically significant details such as the shape of complex atherosclerotic plaque may be removed. One approach that has been suggested to reduce this effect is to apply a global smoothing factor to all of the model, but allow for a different local smoothing factor to be applied to regions with plaque [29].

Modelling bifurcations from sequentially-scanned medical images is a large field of research [100]. The shape of a bifurcating vessel is dependent on its location in the arterial tree [106] and can also vary with age [107] and with head position in the carotid artery [108]. The bifurcation of the carotid in particular is a site of significant plaque development, so changes in the shape of the artery mesh here (especially at the flow divider, the curved area at the intersection of the two branching arteries) could lead to an incorrect understanding of the location of sections of the patient artery most at risk from disease development or plaque rupture. Studies on the effect of small changes in geometry in models of the abdominal aorta confirm that changes in flow divider curvature [109] and branching angle [110] have significant effects on WSS.

An important limitation of using sequentially-scanned images (such as those from the 3DUS system used here) to reconstruct bifurcating vessels is that insufficient information on the shape of the artery bifurcation is given using one set of sequential scans from one direction. When modelling bifurcating arteries, if images are not closely enough spaced at the flow divider, the

shape of the bifurcation cannot be imaged accurately. This is due to the low elevational resolution of US scanning, and the fact that during freehand 3DUS scanning, images are often captured before or after the flow divider, but not precisely at the flow divider [29]. Several methods have been used to overcome this problem. Barratt et al. [29] fitted smoothing splines to the region of the flow divider to improve modelling of this area as part of their two-dimensional serial reconstruction technique. Yim et al. [106] manually adjusted overlapping semi-automatically created vessel surfaces to create a bifurcation free from discontinuities. Barber et al. [102] registered an assumed geometry to segmented two-dimensional lumen contours. These methods vary in complexity and the time required to produce a smooth artery model free from the effects of image misregistration and patient movement.

7.2.1.3 Artery mesh creation

Patient-specific artery geometries are created by firstly segmenting the 3DUS dataset using a semi-automatic segmentation technique. Chapter 6 explains this process. The segmented images are loaded into the Stradwin 3DUS program using the code described in Appendix F, section F.2 and saved as a Stradwin (.sw and .sxi) file (Figure 7.3a). The segmentation process is done without reference to the original position of each image in the 3DUS dataset, so this step is required to spatially re-register the segmented US images.

The segmented 3DUS dataset is mapped onto a voxel grid using the “Export voxels” function of Stradwin (Figure 7.3b). The voxel mapping function of the Stradwin program uses a linear interpolation scheme to fill in the spaces between each US image in the 3DUS dataset. This introduces some interpolation artefacts into the data (as discussed previously in Chapter 3). However, a voxel dataset is the only type that can be used with the mesh creation method developed by Barber et al. [102]. Voxels are the standard method of representing 3D image data in most other 3D medical imaging modalities, and their method was originally designed for use with these.

An idealised geometry is then created that approximates to the shape of the artery geometry in the voxel-mapped 3DUS dataset. Each idealised geometry is made up of solid model primitives such as cylinders and planes (Figure 7.3c). A different idealised geometry is required for each 3DUS dataset. However, if a large library of idealised geometries were created (perhaps once

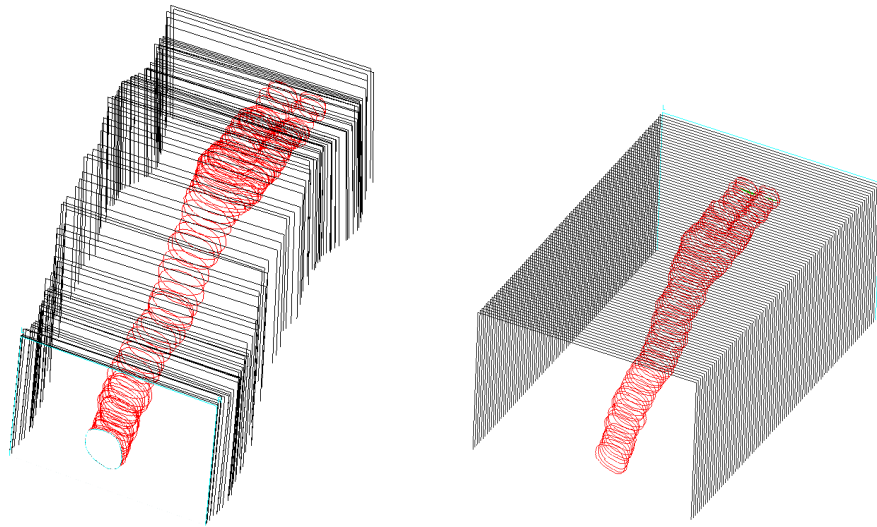
this method is mature and available more widely) this step may not be required.¹

Once the idealised geometry has been created, it is reshaped to closely match the shape of the artery in the voxel-mapped 3DUS dataset. This 3D mesh registration technique is implemented in a MATLAB-compatible executable file and a MATLAB toolbox (The MathWorks Inc., US. <http://www.themathworks.com>)². The reshaped geometry is created in a volume mesh format, eliminating the need for further volume mesh creation steps. The reshaped geometry is saved as an ANSYS-compatible mesh file format (ANSYS Inc., US. <http://www.ansys.com>) for import into the Fluent CFD package (ANSYS Inc., as above)³. The stages used in this process are summarised in Figure 7.4.

¹Idealised geometries and technical help with the creation of reshaped geometries were provided by Adam Jeays of the University of Sheffield.

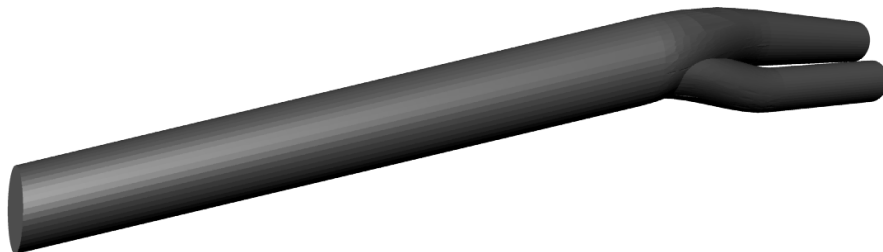
²The executable file and MATLAB toolbox were developed by D. C. Barber and D. R. Hose at the University of Sheffield.

³In practice, the ANSYS mesh file could not be imported into Fluent. To work around this problem, a surface mesh was created from the volume mesh using the ANSYS finite element solver. This was imported into GAMBIT, the Fluent preprocessor, and used to create a volume mesh

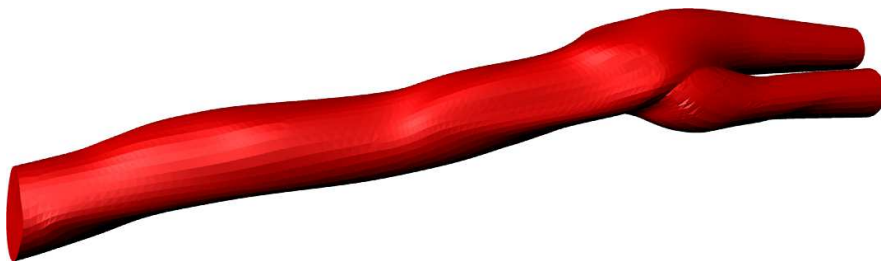


(a) 3DUS images segmented using the automatic method described in Chapter 6. This image shows the segmented contours of the lumen on each image of the dataset. All images are spatially registered using position data from the position sensor.

(b) Voxelised segmented 3DUS data. The dataset in Figure (a) is remapped to a regular voxel grid.



(c) An idealised mesh is created which roughly corresponds to the dimensions and shape of the artery imaged in the 3DUS dataset.



(d) The idealised mesh in Figure (c) is automatically reshaped to match the segmented lumen contours in the voxelised 3DUS dataset.

Figure 7.3: *Creating a patient-specific artery mesh from 3D US data.*

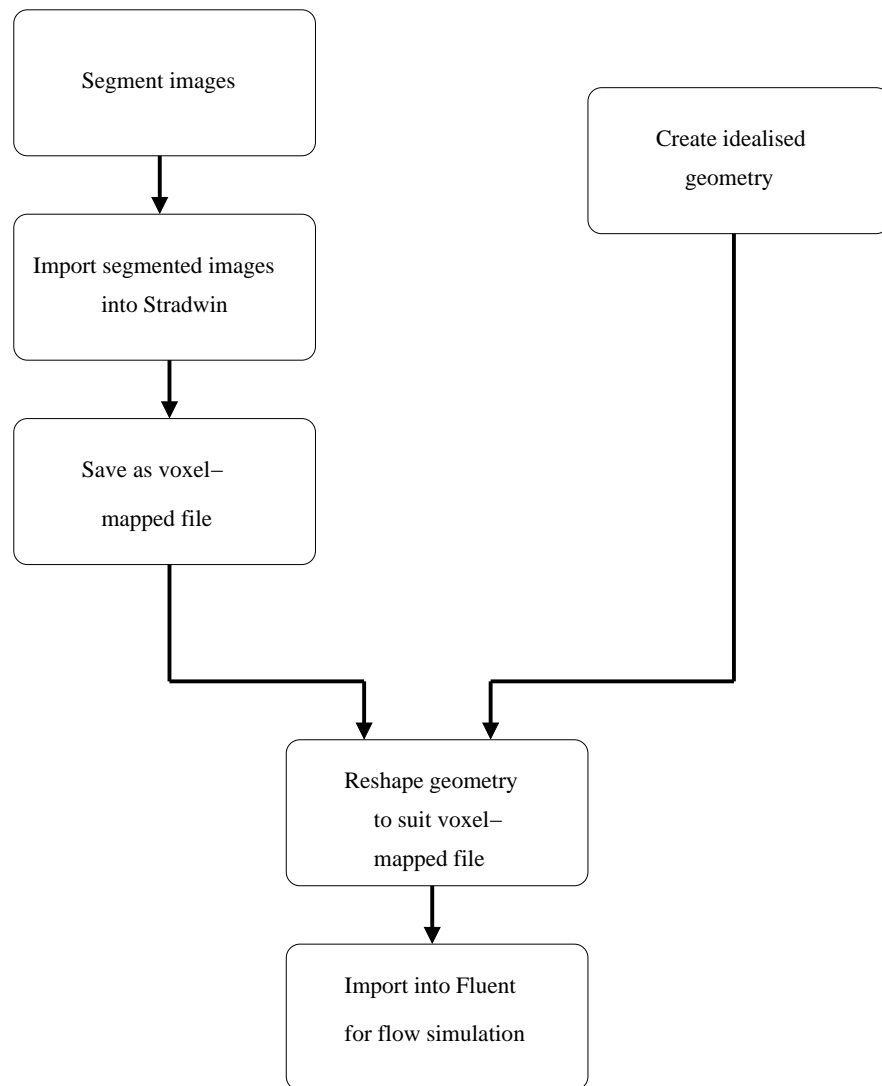


Figure 7.4: A schematic diagram showing the processes used in creating a 3D artery model.

7.2.1.4 Assessing the realism of artery models

Assessing the accuracy of an artery geometry creation method could be made by comparing the original segmented contours to the geometry. However, this may not be the most important consideration in assessing an artery geometry. The original segmented contours incorporate variability from the segmentation process. Patient movement may still influence the location and shape of the segmented contours. US imaging artefacts, though reduced by compounding, may still affect the shape of the segmented contours in different areas.

Comparison with the original contours is made more complex when assessing meshes created using the registration-based mesh generation method. The artery mesh creation package used displaces the created artery geometry from the position of the voxelised segmented contours. No accurate direct comparison is therefore possible.

An additional method of assessing the realism of a computational mesh is to compare meshes generated using this method to 3D scanned meshes of excised carotid arteries from cadavers. A study [104] excised and measured the carotid arteries from cadavers of patients who had a history of arterial disease. The shape of the bifurcation created using the registration-based mesh generation method can be compared to these *ex vivo* measurements. This shows the realism of mesh geometries created from 3DUS images using the registration-based method.

Overall, these factors imply that in the absence of a coherent and rigorous framework of assessing the accuracy of a patient-specific artery mesh creation method, only a qualitative approach can be used to decide whether a physiologically accurate artery mesh was created. To qualitatively assess the realism of artery models, cross-section slices of the artery mesh are compared side-by-side with the original segmented 3DUS data to identify areas where the cross-sectional shape of the mesh deviates from the shape of the segmented images. Segmented images registered in 3D are overlaid onto the artery model to assess where the shape of the mesh in 3D space differs from the shape of the segmented contours. In addition, the shape of the bifurcation is compared to bifurcations measured from cadavers to assess the realism of the bifurcation shape.

7.2.2 Simulating flow patterns and wall shear stress

The topic of how to simulate blood flow in a computational model of an artery has received wide coverage in the literature [e.g. 62, 100, 111]. However, in-depth consideration of the merits of different strategies for flow simulation is beyond the scope of this chapter. The flow

simulation featured here serves to demonstrate the feasibility of using a 3DUS-based approach to image-guided modelling.

Simulations of a diseased carotid artery from a patient and a healthy carotid artery from an asymptomatic volunteer were created. The carotid artery was simulated in both cases because this is one of the most critical sites for the development of arterial disease. Disease that develops here is most likely to cause a fatal or disabling stroke than that found in other arteries. The carotid also bifurcates, leading to more complex flow patterns than straight arteries. This also demonstrates the ability of the mesh generation technique reported here to reconstruct the complex shapes found in a bifurcation. The two carotid simulations are based on the same datasets used for segmentation in Chapter 6. The healthy carotid dataset and the diseased carotid dataset are the same as those displayed in Figures 6.9 and 6.10 respectively in section 6.2.4 of Chapter 6.

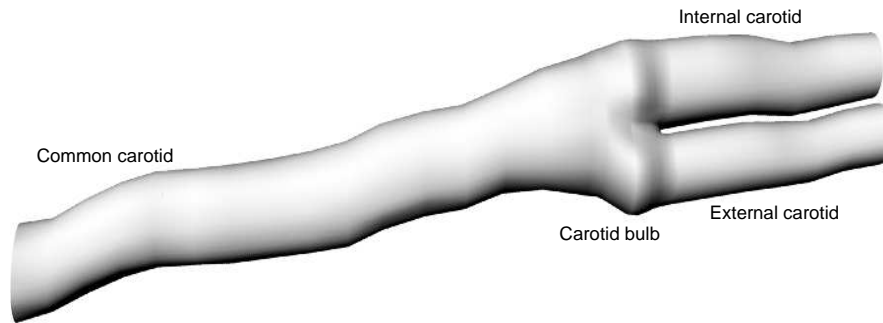
The blood flow field in each artery mesh was simulated using the Fluent CFD package. A turbulent $k - \omega$ flow model was used to model the flow. Second-order simulations of blood flow were carried out for the diseased artery geometry to calculate blood velocities and WSS in the artery model. Womersley profiles [112] were calculated at the inlet to create a 3D velocity inlet boundary condition. Womersley profiles assume a circular inlet cross-section and create parabolic flow profiles. These profiles were calculated using an angle-corrected spectral Doppler US flow measurement from the centreline of the patient artery. Spectral Doppler waveforms were downloaded from the Phillips HDI5000 US scanner using the HDI Lab program and converted to a velocity waveform. The Doppler acquisition window was placed at the centreline of the artery to measure peak velocity. Each spectral Doppler scan was taken from the volunteer during the same scanning session as 3DUS image acquisition. Once the flow field was simulated, visualisations of WSS contours and velocity streamlines were created using ParaView (Kitware Inc., NY, USA. <http://www.paraview.org>).

7.2.2.1 Comparing CFD simulations to *in vivo* flow measurement

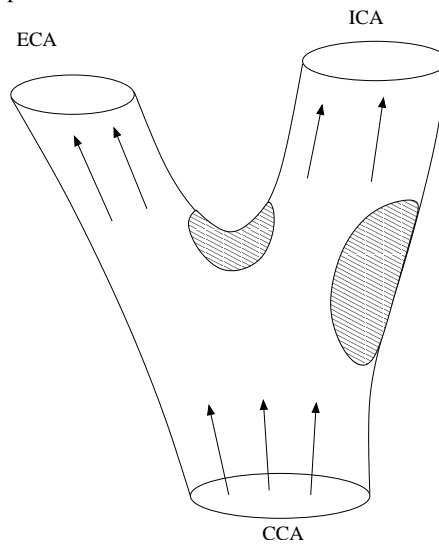
The expected flow patterns and distributions of WSS in an artery have been extensively measured using accurate models of geometries found *in vivo* [103]. Using these results, the realism of flow patterns and WSS locations in simulations made using an artery geometry may be assessed. The exact WSS values and velocity values within a specific artery are patient-specific and geometry-specific, making a like-for-like comparison between flow simulations and results

reported in the literature impossible. However good qualitative comparisons of the location of recirculation zones and areas of high WSS may be made.

To assess the accuracy of artery mesh reconstruction, positions of recirculation and peak WSS are compared with expected positions from typical *in vivo* results [104] and simulations from other groups [66]. These studies show that in a healthy carotid artery, areas of recirculation are expected to be found in the carotid bulb during peak systole (see Figure 7.5). Disease can add significant turbulent flow to this area, dependent on the shape of the plaque. WSS would be expected to peak at the centre of the flow divider, and may also peak at areas of vulnerable plaque.



(a) The main features of the carotid artery at the bifurcation. The common carotid (left) ascends from the aortic arch and supplies blood to the head. At the carotid bulb the common carotid enlarges and bifurcates into the internal and external carotid arteries. The internal carotid artery usually has a slightly larger diameter than the external carotid artery. The internal carotid supplies the brain, forehead, eyes, nose and the inner ear. The external carotid supplies the neck, scalp and face.



(b) Areas of flow recirculation in the carotid artery. The arrows show the direction of flow. The shaded areas show where recirculation zones occur, and by implication where atherosclerotic disease and oscillating WSS is most often found.

Figure 7.5: The main features of the carotid artery and areas of flow recirculation.

7.3 Results

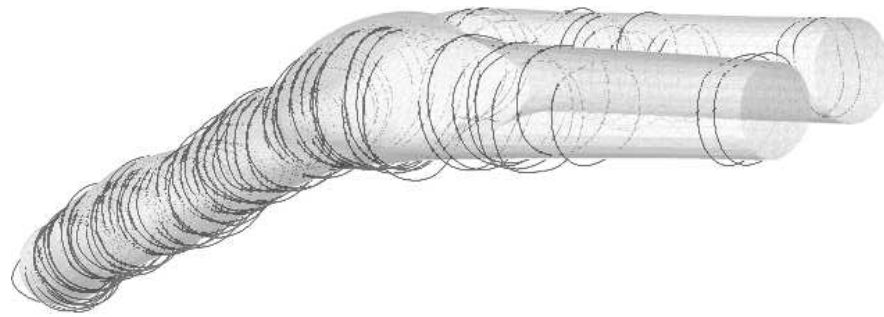
7.3.1 Assessing the realism of artery models

The healthy and diseased carotid artery geometries are considered in turn. To best assess the realism of an artery mesh, meshes are displayed with the original segmented contours from the 3DUS dataset overlaid. Plan, side and isometric views of the mesh with overlaid contours are given to review how faithfully the artery mesh resembles the original segmented data. The shape of the bifurcation of each artery mesh is also displayed in detail to assess the realism of the bifurcation shape.

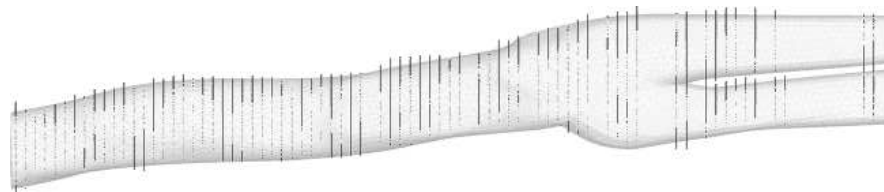
7.3.1.1 Assessing the healthy artery mesh

Images of the healthy artery mesh with overlaid segmented contours are displayed in Figure 7.6. These images show that there is some deviation between the shape of the outside of the segmented contours and the mesh shape. This deviation may be due to misregistration of the segmented contours. The artery mesh reduces the discontinuities present in the segmented data to produce a smoother mesh shape.

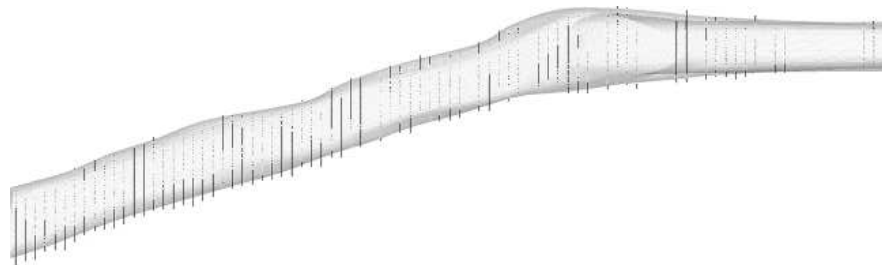
The bifurcation is shown in Figures 7.7b and 7.7c. The flow divider has a smoothed internal shape (Figure 7.7c) but the shape of the external carotid artery at the bifurcation (shown at the top of Figure 7.7b) does not develop smoothly from the rest of the artery. There is a sharp join visible in this image where the ICA is butted on to the rest of the artery.



(a) Isometric view



(b) Front view

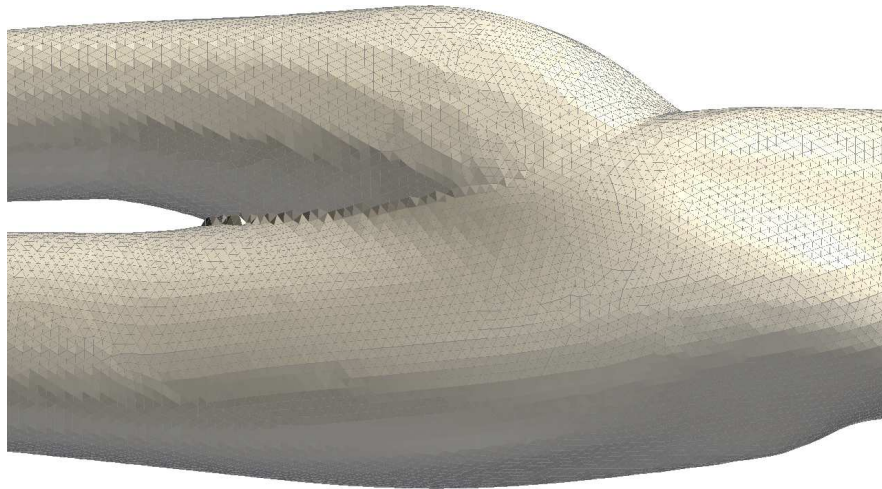


(c) Side view

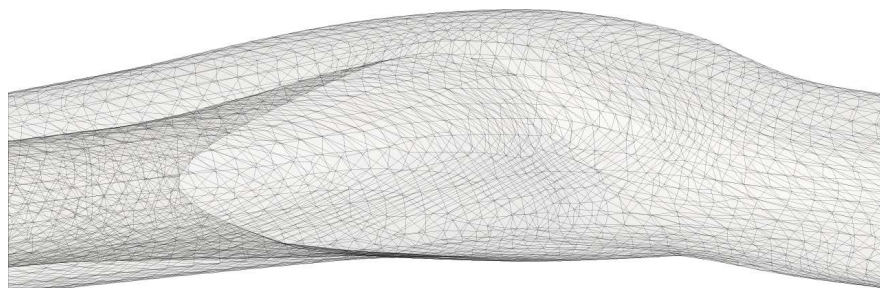
Figure 7.6: *The healthy carotid artery mesh compared to the original segmented contours. Comparing the mesh to the original segmented contours shows how the shape of the mesh is different to the original segmented dataset.*



(a) The whole of the surface mesh of the healthy carotid artery geometry.



(b) A closeup of the side of the bifurcation flow divider. The discontinuous join between the internal (lower branch) and external (upper branch) carotid arteries at the carotid bulb creates the hard line between the two sections of the artery.



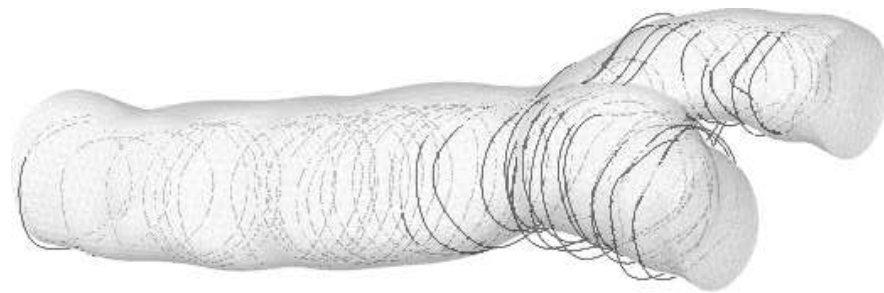
(c) The side of the bifurcation flow divider. The mesh is rendered semi-transparently to show the shape of the internal structure of the mesh. A smooth rounded internal shape is apparent at the bifurcation.

Figure 7.7: *The bifurcation region of the healthy carotid artery mesh.*

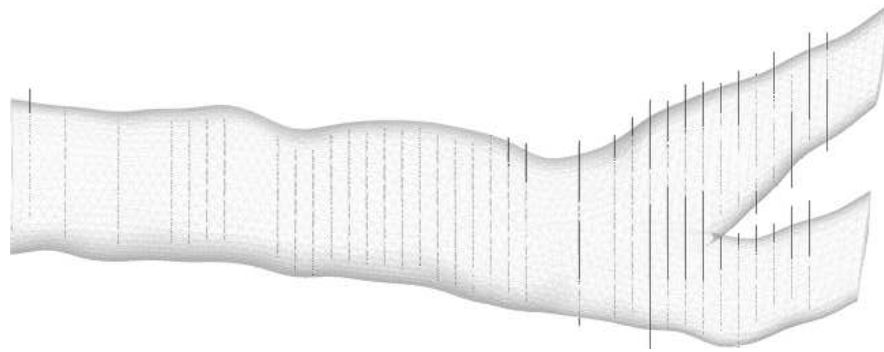
7.3.1.2 Assessing the diseased artery mesh

Images of the diseased artery mesh with overlaid segmented contours are displayed in Figure 7.8. For the majority of the mesh, especially in the common carotid, the segmented contours are wholly enclosed by the mesh rather than appearing on the surface as would be expected. The diseased mesh has a large section of diseased plaque near the bulb. Figure 7.9b shows US images of this section with segmented contours drawn on each image. Figure 7.9a shows these segmented contours registered in 3D space using the position information from the position sensor which was captured at the same time as the images. Comparing these images to the mesh shape at this point is made easier by drawing contours on to the surface of the mesh to show how its shape develops in 3D (Figure 7.10). This reveals that the diseased section is largely smoothed out by the mesh. For comparison, a mesh was created in a similar way to that used by Barratt et al. [29] using the method described in Appendix D. Contours drawn onto the surface of this mesh confirm that this method more faithfully models the shape of complex disease (Figure 7.11).

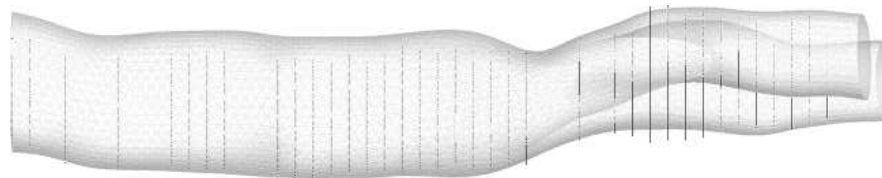
The bifurcation shape of the diseased artery mesh is shown in Figure 7.12. In the same way as the healthy carotid mesh, the bifurcation internal shape is smooth but the outer shape of the mesh shows discontinuities where the branching internal and external carotid arteries develop from the carotid bulb. A sharp dividing line is visible at the bifurcation (Figure 7.12b) which will have the effect of increasing WSS results in this region.



(a) Isometric view

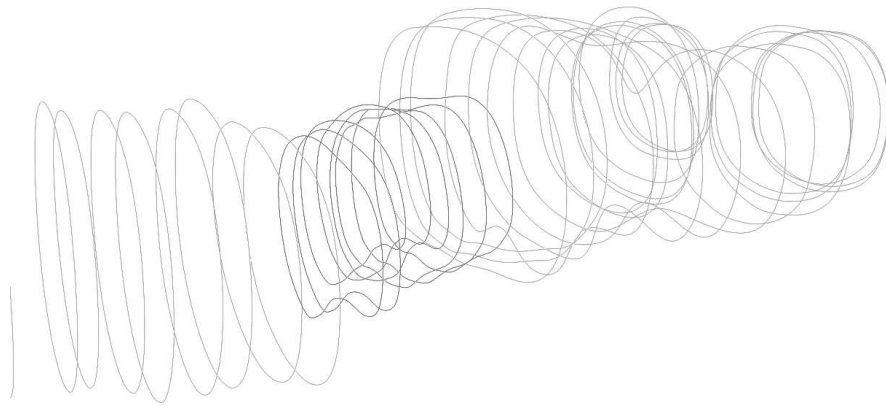


(b) Front view

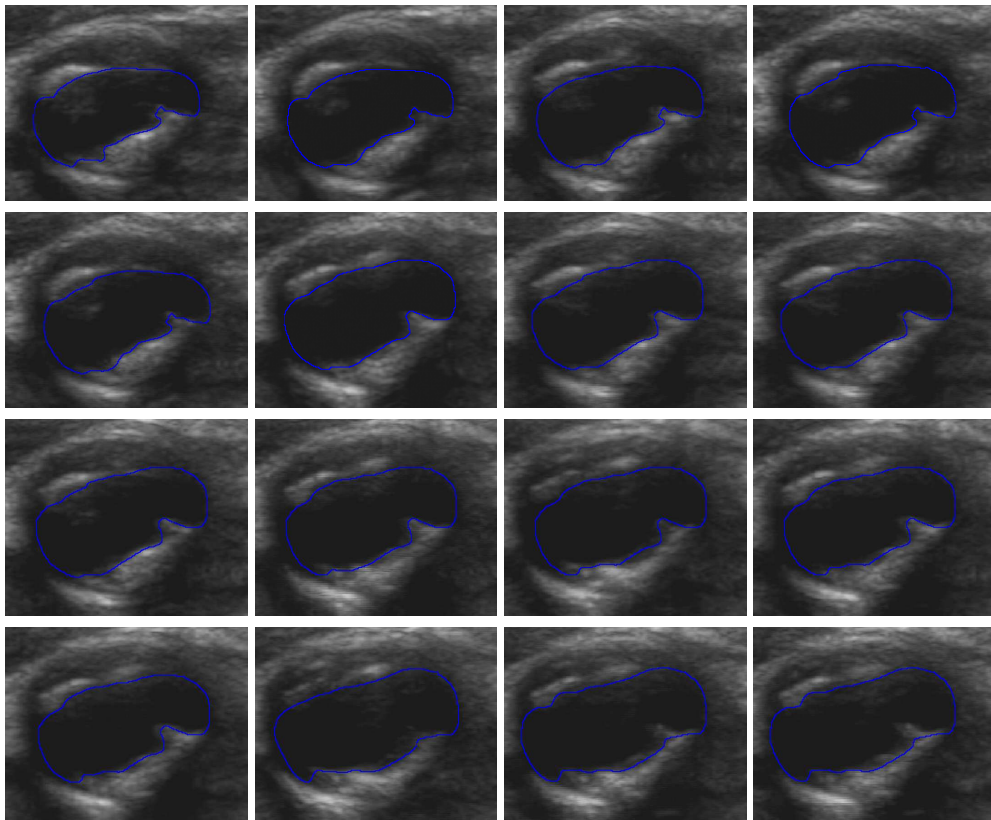


(c) Side view

Figure 7.8: *The diseased carotid artery mesh compared to the original segmented contours. Comparing the mesh to the original segmented contours shows how the shape of the mesh is different to the original segmented dataset.*



(a) The segmented contours at the diseased portion of the carotid artery reconstructed in 3D space. The black contours are at the throat of the stenosis. Grey contours are from the healthier sections of the vessel before and after the stenosis.



(b) US images of the diseased portion of the carotid artery.

Figure 7.9: Segmented contours of disease shown with US images for the diseased carotid artery.

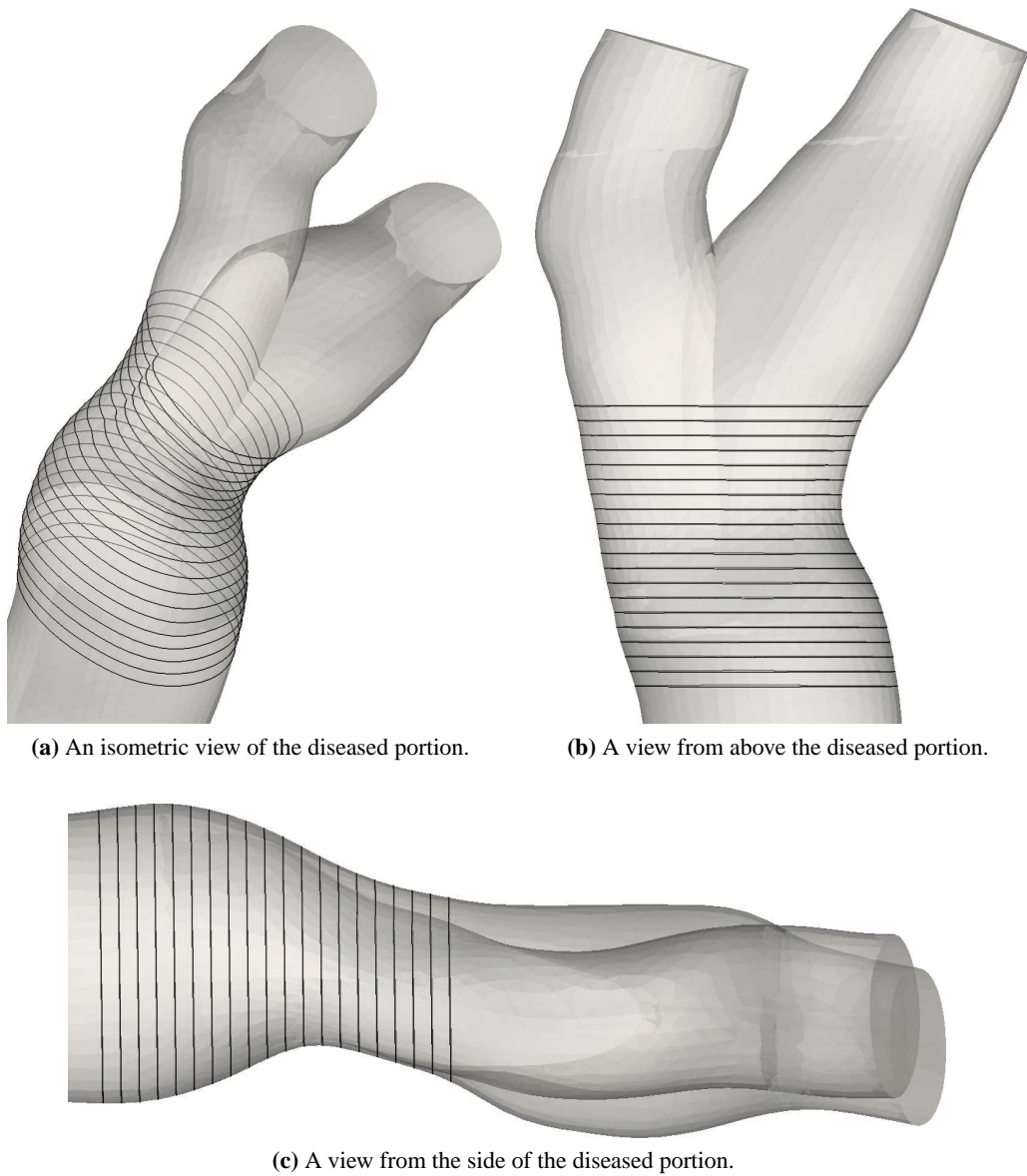
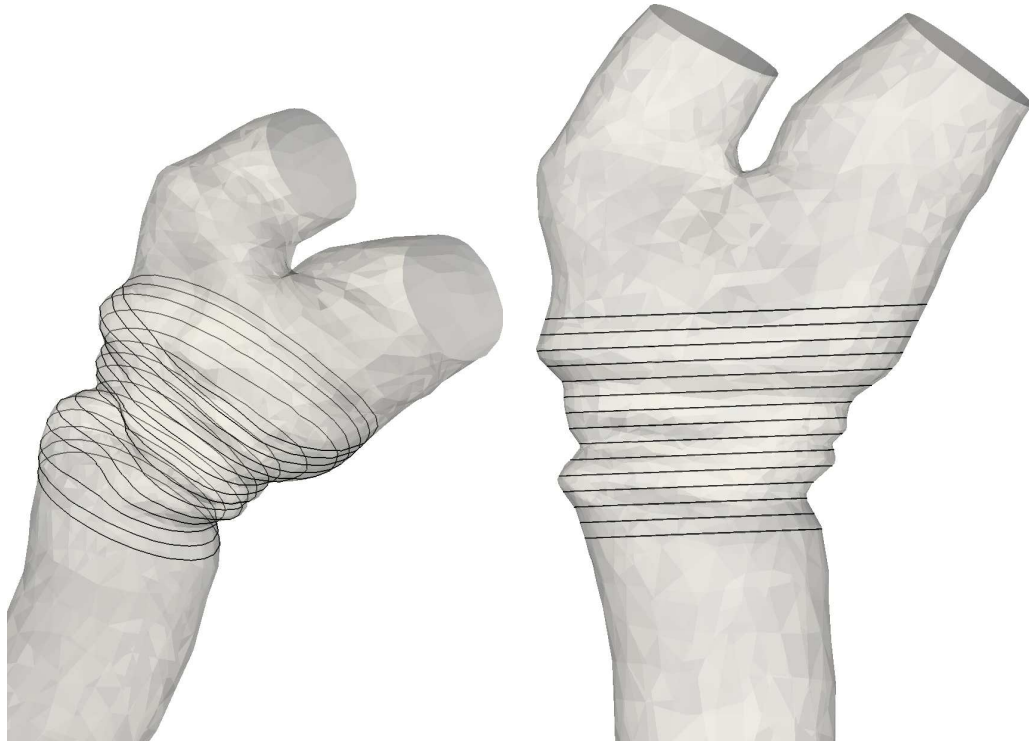
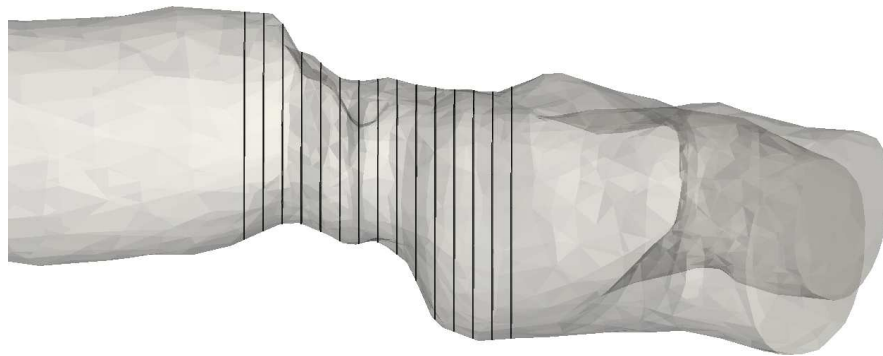


Figure 7.10: A closeup of the diseased portion of an artery geometry created using the 3D method. Contours are drawn on to the surface to demonstrate how the geometry changes through the diseased area.



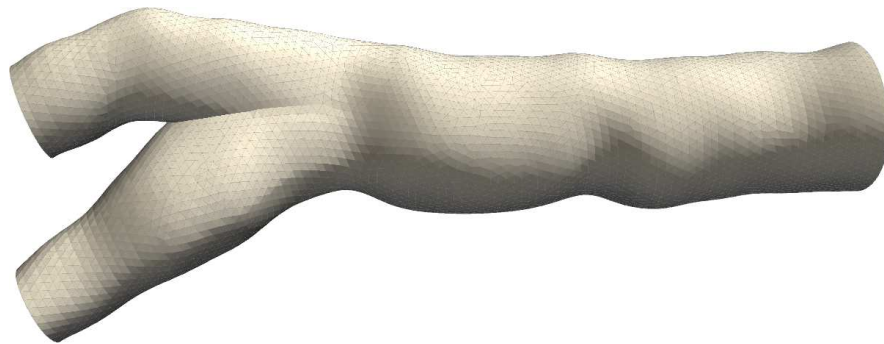
(a) An isometric view of the diseased portion.

(b) A view from above the diseased portion.

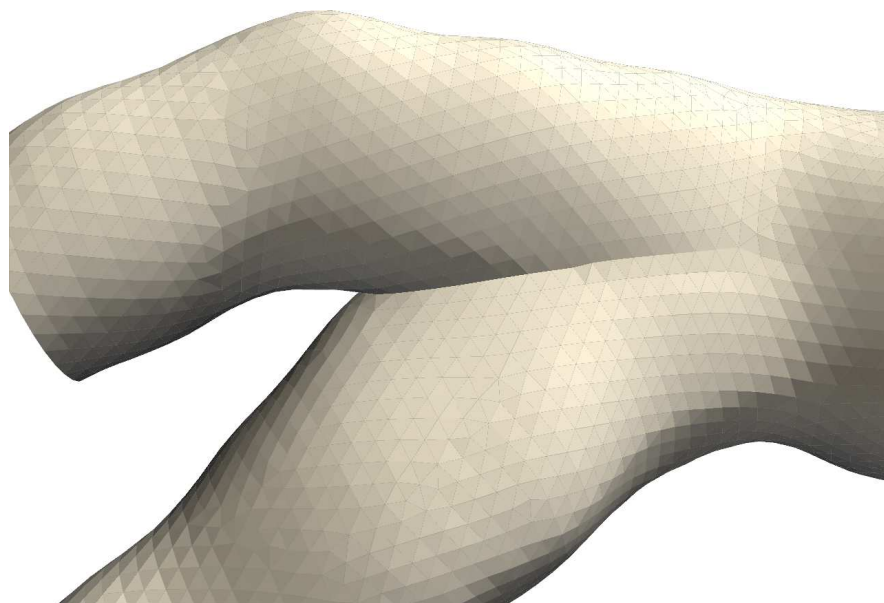


(c) A view from the side of the diseased portion.

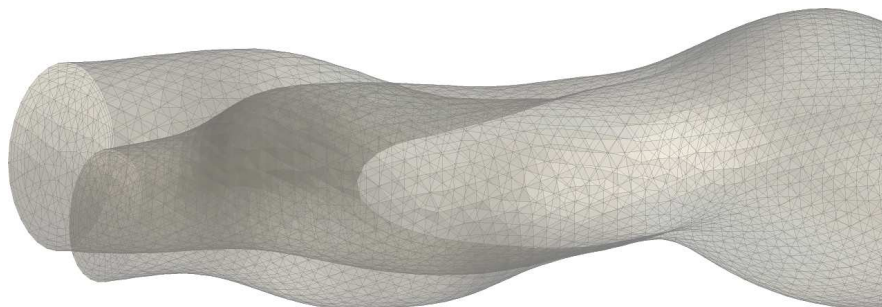
Figure 7.11: A closeup of the diseased portion of an artery geometry created using the 2D method. Contours are drawn on to the surface to demonstrate how the geometry changes through the diseased area.



(a) The whole of the surface mesh of the diseased carotid artery geometry.



(b) A closeup of the side of the bifurcation flow divider. A sharp dividing line is present between the two branches of the artery.



(c) A closeup of the side of the bifurcation flow divider.

Figure 7.12: *The bifurcation region of the diseased carotid artery mesh.*

7.3.2 Simulating flow patterns and wall shear stress

Flow simulations using Fluent⁴ can confirm whether flow patterns and WSS contours in the artery geometries resemble those found *in vivo*. For both arteries, simulation results are shown at peak systole where flow is fully developed and WSS is at its peak.

7.3.2.1 Healthy artery simulations

Figure 7.13 shows a closeup view of the carotid bulb of the healthy carotid artery simulation. Streamlines of flow are shown. The results are shown at peak systole, which occurred at $t = 0.07s$. Turbulent streamlines are shown to fill the carotid bulb region, with low velocity recirculation regions shown at either side coloured in varying shades of blue.

To show the development of flow along the whole artery geometry, velocity profiles along the artery are displayed in Figure 7.14. Peak velocities are shown along the centreline of the common carotid leading up to the bulb. At the bulb, the flow splits and recirculation causes the asymmetric plot found here. Higher velocities are then found in the internal carotid branch (on the left of the image) than in the external carotid.

A closeup of the carotid bulb, showing the location of peak WSS, is shown in Figure 7.15. WSS peaks at the flow divider, a result that is similar to that seen in other flow simulation studies and *in vivo*. The highly localised peak WSS value shown at this point is an effect of the sharp division between the internal and external carotid arteries found in the idealised geometry.

⁴CFD simulations using Fluent were performed by William J. Easson and William T. Lee and visualised by the author.

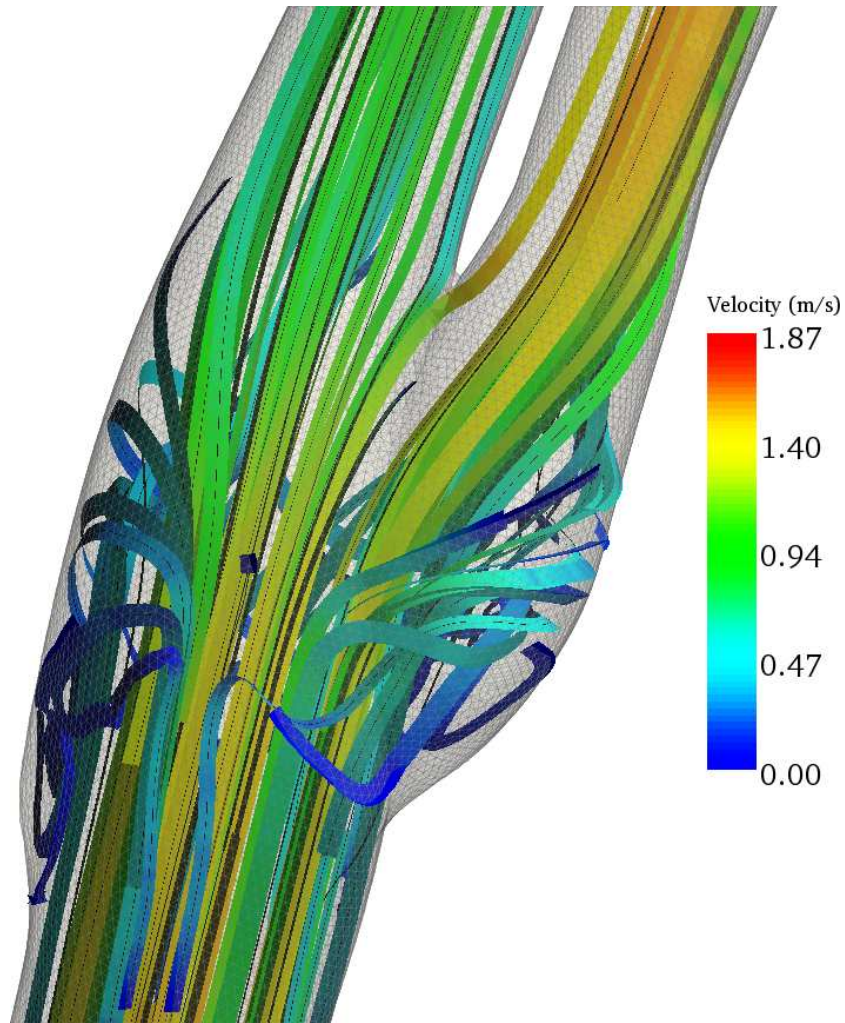


Figure 7.13: Flow streamlines in the healthy carotid artery mesh. Streamlines are coloured by velocity (m/s) and are shown at peak systole ($t = 0.07s$). The internal and external carotid arteries are at the top left and right of the image respectively.

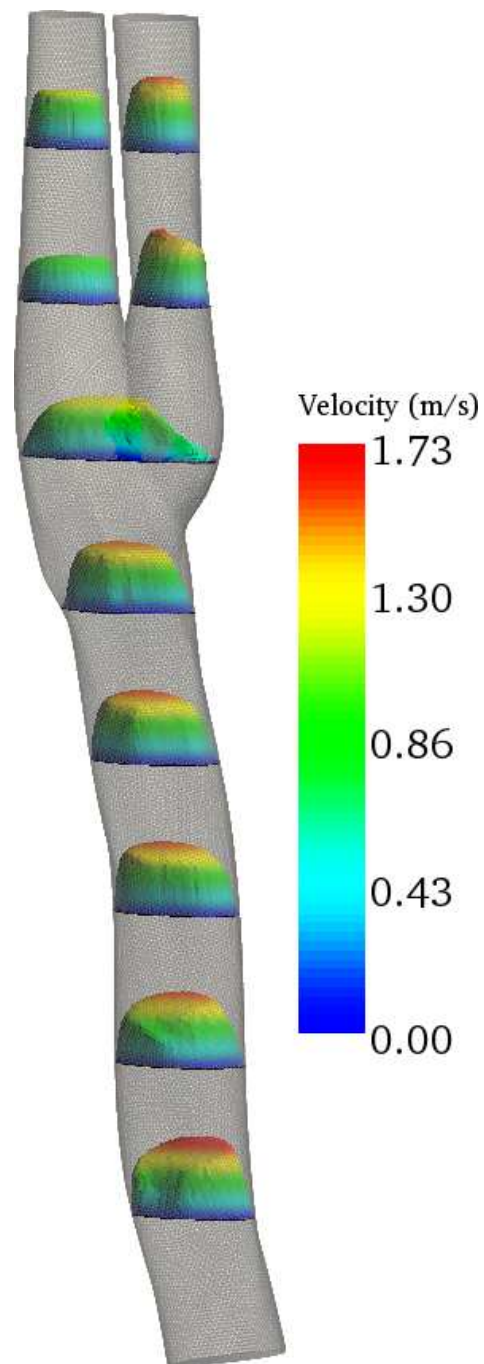


Figure 7.14: Velocity profiles in the healthy carotid artery mesh. Velocity profiles are coloured by velocity (m/s) as shown in the colour bar and are shown at peak systole ($t = 0.07s$). The internal and external carotid arteries are at the top left and right of the image respectively.

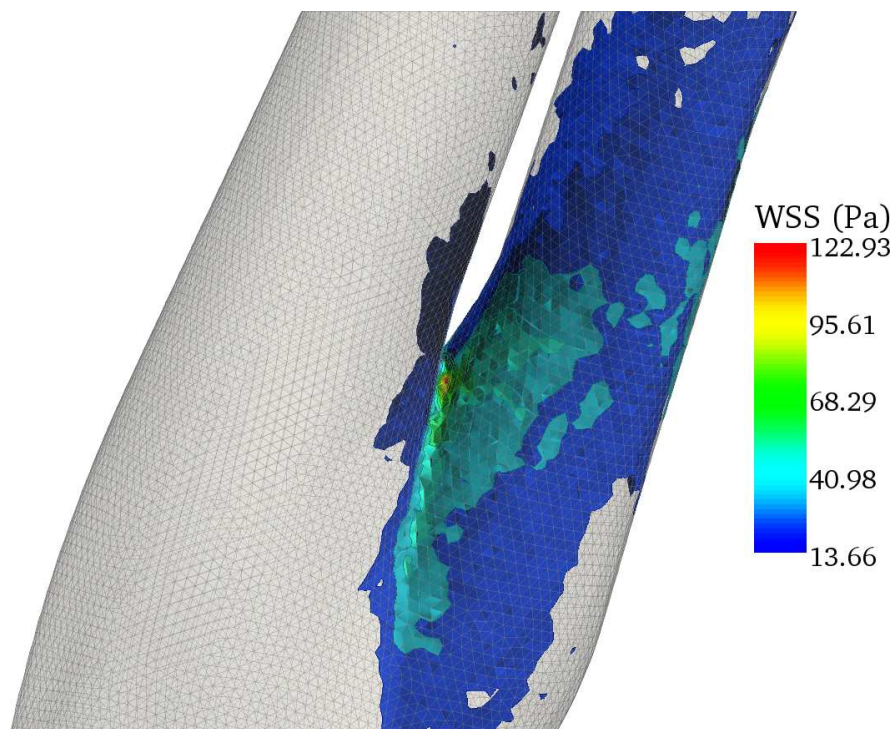


Figure 7.15: Contours of high WSS in the healthy carotid artery mesh. Peak values are found near the flow divider. WSS contours are shown at peak systole ($t = 0.07s$)

7.3.2.2 Diseased artery simulations

Figure 7.16 shows streamlines coloured by velocity in the bulb of the diseased carotid artery. A large recirculation zone is apparent on the left of the image at the beginning of the external carotid artery. Flow accelerates through the narrowed region distal to the diseased portion of the artery inferior to the bulb.

Recirculation in the diseased artery is also demonstrated by the velocity profile plot in Figure 7.17. The flow is most disturbed at the flow divider between the internal and external carotid arteries. However, the disease shown in Figure 7.9a has been smoothed out in this mesh, and has little effect on the flow other than to moderately increase the flow velocity here.

The smoothed diseased portion of the artery is shown to have little effect on WSS in Figure 7.18. WSS is increased slightly in the diseased portion, but appears no higher than in the internal and external carotid arteries (all shown shaded in blue, with values of WSS ranging from 12 to 15 Pa). WSS, in a similar way to the healthy artery, peaks at the flow divider. This corresponds to the sharp division between the two branching arteries at this point.

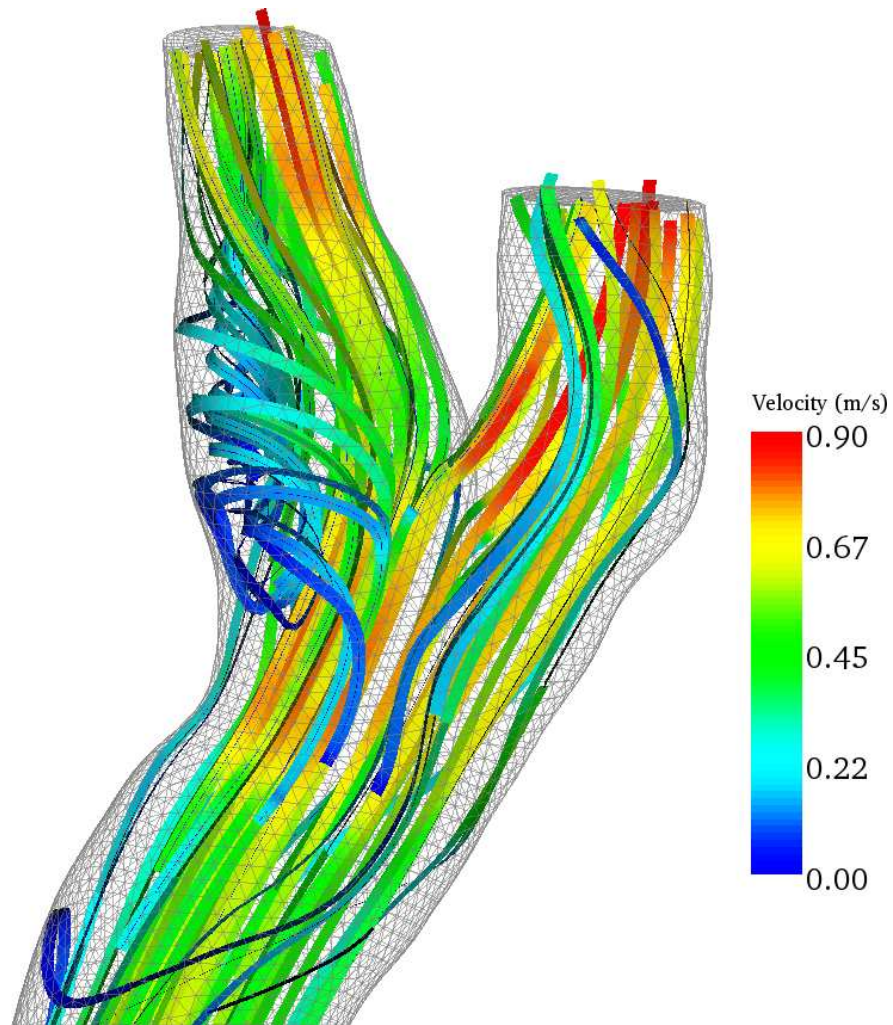


Figure 7.16: Flow streamlines in the diseased carotid artery mesh. The internal carotid artery is the branch at the left of the image. Streamlines are coloured by velocity (m/s) and are shown at peak systole ($t = 0.07s$). The internal and external carotid arteries are at the top right and left of the image respectively.

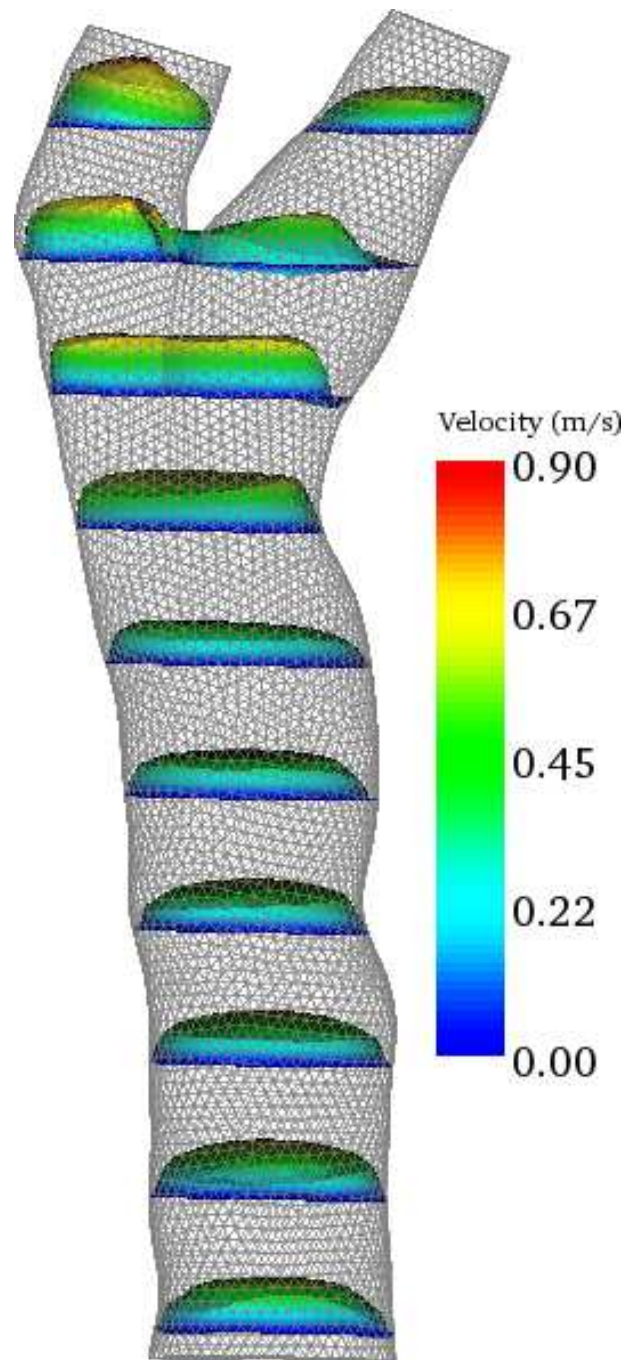


Figure 7.17: Velocity profiles in the diseased carotid artery mesh. The internal carotid artery branch appears at the top right and the external carotid at the top left of the image. Ten velocity profiles are mapped along the mesh. Velocity profiles are coloured by velocity (m/s) with values as shown in the colour bar and are shown at peak systole ($t = 0.07s$). The internal and external carotid arteries are at the top left and right of the image respectively.

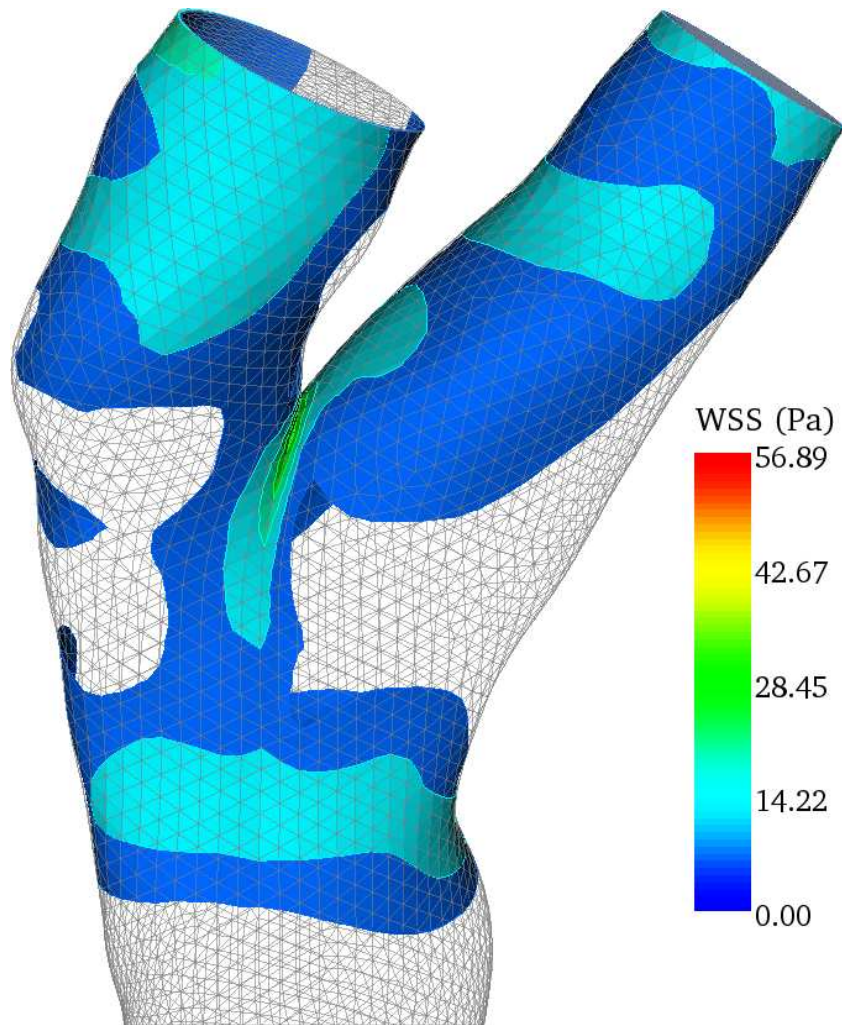


Figure 7.18: Contours of high WSS in the diseased carotid artery mesh. Peak values are found near the flow divider. WSS contours are shown at peak systole ($t = 0.07s$). The internal and external carotid arteries are at the top right and left of the image respectively.

7.4 Discussion

Simulations of flow in healthy and diseased carotid artery meshes using a registration-based mesh creation technique gave results for WSS and flow velocity in the expected range for healthy and diseased patients. However the distributions of WSS in each mesh were heavily dependent on the mesh creation process.

In both healthy and diseased meshes, WSS peaked at the flow divider. This is typically what happens *in vivo* [104]. However, these coincided with the sharp divisions between the external and internal carotid arteries on both geometries. A smooth transition, without sharp dividing lines, is more typically found in real arteries. To more accurately simulate WSS, the shape of the bifurcation at this point needs to be more physiologically realistic.

Recirculation zones were found in the carotid bulb in both arteries, another flow feature shown *in vivo*. However, in the diseased artery mesh, the large irregular plaque found proximal to the carotid bulb would be expected to have more effect on the flow entering the bulb. The registration-based method did not accurately simulate the shape of the plaque in this region, leading to unexpectedly smooth flow into the carotid bulb in the diseased region. A mesh created using the method described in appendix D created a diseased region with plaque that was more similar to the original segmented images, at the expense of requiring more time and expertise to create the mesh. The registration-based mesh generation method may be improved using a hybrid approach. This would use a two-dimensional serial reconstruction approach (like that described in Appendix D) to create regions of complex plaque, combined with registration of an assumed geometry for healthier regions of the artery. However, a hybrid approach would increase the complexity of the mesh generation process.

The registration-based technique was found to give acceptable flow simulation results for healthy arteries except at the flow divider. It did not model diseased portions correctly, smoothing out complex disease. This implies that, as a method of creating artery meshes from 3DUS data in diseased arteries, further development work is required. The registration-based method may decrease the time taken to create artery meshes given more accurate idealised models and a more sensitive method of modelling complex disease.

7.5 Conclusion

Artery meshes were created for CFD simulation using a registration-based segmentation and mesh generation method. The shape of bifurcating vessels and a diseased carotid artery were compared with the original 3DUS images and expected bifurcation flow dividers from arteries *in vivo*. Simulation results were compared with *in vivo* results of flow patterns and regions of peak wall shear stress. The shape of the flow divider in healthy and diseased artery meshes was found to have sharp discontinuities which affected the distributions of wall shear stress at this point. Complex plaque in a diseased artery mesh was smoothed out, giving a greatly reduced effect on flow recirculation in the carotid bulb. Further development of the registration-based mesh generation method is required to more accurately model bifurcating arteries and diseased plaques.

Chapter 8

Evaluation of arterial wall motion software as a validation tool for moving-wall arterial simulations

8.1 Introduction

Once a patient-specific artery mesh has been created from 3DUS data, a method of measuring the properties of blood flow and the arterial wall is required to develop moving wall artery simulations. For flow simulation, angle-corrected spectral Doppler US [100] is typically used to give a velocity profile on the centreline of the inlet and outlet(s) of an arterial segment. For moving wall simulations, a pressure boundary condition [111] is also required which can be measured using US tonometry, which uses a small US transducer to measure the pressure wave in an artery. Additional information on the stiffness of the artery wall can also be used to develop more realistic simulations with inhomogeneous wall properties. In diseased arteries the mechanical properties of diseased plaque and regions with intimal thickening are different to healthy arteries [113]. The mechanical properties of the artery wall in these regions may be estimated by measuring the motion of the arterial wall [114]. The measured motion of the artery wall may also be used to validate moving wall arterial simulations.

A variety of different methods of measuring arterial wall motion (AWM) using US are reported in the literature. These include M-mode imaging [115], video frame analysis of B-mode images [116], techniques using radio-frequency (RF) signal processing [117, 118], and Tissue Doppler Imaging (TDI) [114, 119]. In common with all *in-vivo* measurement techniques, it is common practice to assess the accuracy of a technique using an *in-vitro* approach. This is a vital step in the assessment of an AWM measurement method. Many of these techniques for flow phantoms are reviewed in [120].

Mechanically controlled methods of creating wall motion in a phantom are most useful for determining accuracy and precision of a wall motion measurement technique. A controlled

method creates well-defined wall movements free from the inherent uncertainty of using flow phantoms to produce a controlled wall displacement. Cylindrical flow phantoms are more similar to an artery than a single moving wall. However flow phantoms do not offer direct control of the motion of the wall. Only flow can be directly controlled. To establish the accuracy and precision of wall motion measurement, a wall motion phantom capable of simulating a transverse view through an artery was developed. Bonnefous et al.[16] used a similar technique for the assessment of a TDI-based method for estimating the wall distension waveform. They used a computer-controlled motor in a water bath to move a single flat plane. A physiologically realistic wall motion displacement waveform was used to move the plane. Their reported results covered only one physiological waveform and did not assess the effect of changes in wall velocity on the measurement accuracy of the TDI-based method. This chapter describes a more rigorous treatment of the TDI-based method, providing a fuller characterisation of its performance than previous published studies.

This chapter describes the design, construction and accuracy assessment of the wall motion phantom. An assessment of a TDI-based method for estimating the distension waveform [121] is presented, finding the minimum resolvable displacement of the method and the effect of changing velocity on its accuracy. The suitability of this TDI-based method for validating moving wall arterial simulations is discussed.

8.2 Wall motion phantom design

8.2.1 Wall motion phantom assembly

The wall motion phantom is designed to resemble a transverse view of a straight section of artery. Two flat tissue mimicking material (TMM) layers made from an agar solution [93] resting in a water bath simulate the top and bottom walls of an artery. The top wall is fixed just below the US transducer using two wire supports that rest on the top edge of the water bath (see Figure 8.1). The lower surface is precisely controlled using a stepper motor driven Unislide linear table (LG Motion Ltd., Hampshire, UK. <http://www.lg-motion.co.uk>).

While it is recognised that *in-vivo* both walls are moving and both may be used to obtain wall motion measurements, the design of a phantom in which both walls move would be more challenging and expensive. In this study a single-moving wall was used as this simplified both the complexity of the design and decreased cost to acceptable levels. It is noted that one moving

wall is the minimum required to provide a valid displacement signal for TDI-based wall motion measurements [16]. The linear table has two support arms that rest in the water bath and hold a sandwich of a rigid aluminium frame, a layer of TMM, a layer of acoustic absorbing foam, and a layer of aluminium plate. This assembly provides rigidity and a flat surface to the TMM layer. Using TMM layers provides a similar level of backscatter and texture to artery tissue, providing a realistic test of the TDI-based wall motion method. All motion experiments used a water plus 9% glycerol solution to set the speed of sound in the water bath to $1540 \text{ m} \cdot \text{s}^{-1}$. This is different to the speed of sound in blood ($1570 \text{ m} \cdot \text{s}^{-1}$) [122], giving a possible measurement error of 2 % in the reported results for the wall motion measurements reported here.

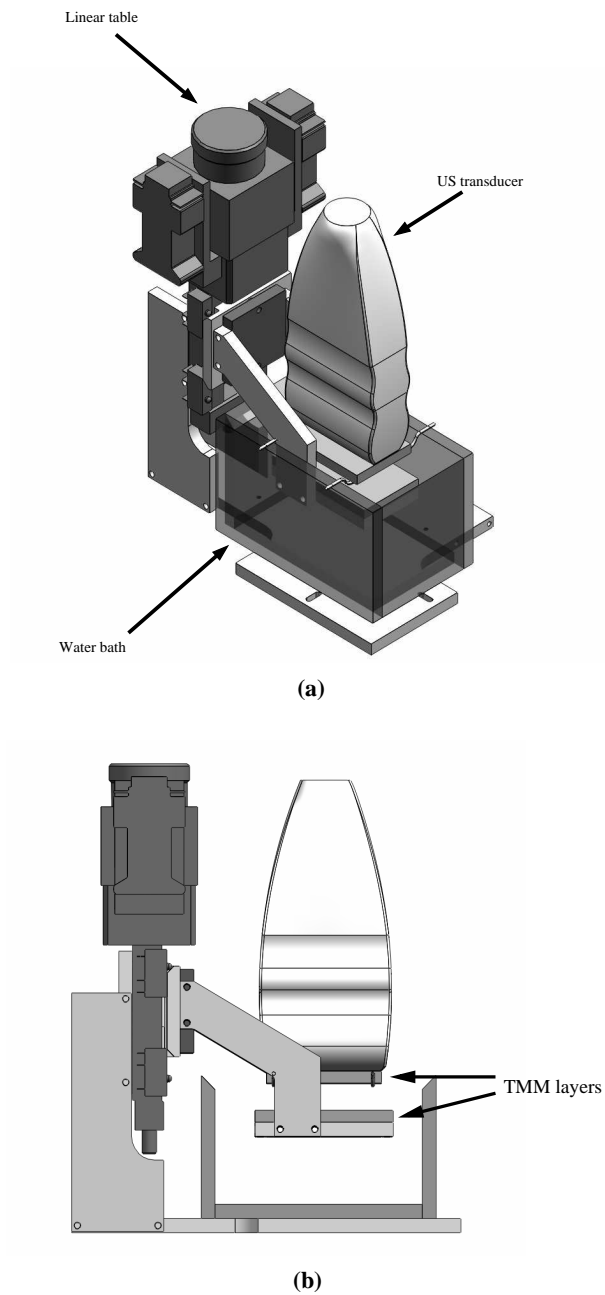


Figure 8.1: *The wall motion test phantom. Figure 8.1a shows the entire wall motion test tool assembly. The US transducer is held in place using a clamp stand. Both layers of TMM are shown in Figure 8.1b. The upper layer is fixed in place just below the transducer using a wire frame. The lower layer is held on to the moving paddle attached to the linear table using rubber bands.*

8.2.2 Wall position

The separation of the two artery walls was set to 6 mm. This is similar to that found in a healthy carotid artery. The upper wall was positioned 15 mm below the lower edge of the transducer. The depth of the artery could be increased by using a thicker upper layer of TMM and lowering it using the wire supports. Maximum lower wall displacement is limited by the 40 mm peak travel of the linear table. Due to the thickness of the lower wall assembly and the position of the upper TMM layer, peak usable displacement is limited to 32 mm. Maximum artery diameter is 12 mm, which allows the simulation of larger peripheral arteries. Figure 8.2 shows a typical image with the TDI colour box positioned over the two TMM layers.

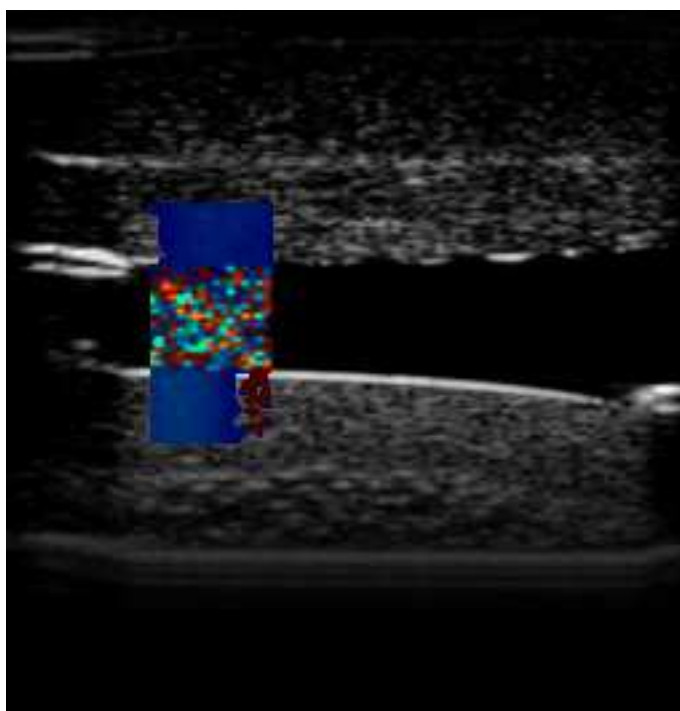


Figure 8.2: A US image of the test phantom walls. The colour box is placed over the straightest part of the lower wall.

8.2.3 Generating wall motion waveforms

The lower artery wall is controlled by a Parker (Parker Hannifin Corp., Ohio, USA) L25i Intelligent Stepper Motor Controller via a PC running EASITools, a terminal interface for the L25i controller. Displacement of the lower wall is defined using a custom-written LabVIEW (National Instruments Corp., Texas, USA) program (see Appendix F.6.3). Using this program, the user may choose from a variety of preset displacement waveforms or develop their own custom waveform. The program plots the predicted displacement of the lower wall and allows the user to download the EASITools program for that movement. The user can then load the EASITools program into the on-board memory of the L25i controller and move the lower wall. The physiological wall motion waveforms used for this work had a cycle length of 1.2 s, which is similar to that found in a healthy carotid artery. However the waveform generation program is not limited to this cycle length: the user can create shorter or longer waveforms to simulate the motion of whichever artery is desired. Permitted movement velocity of the lower wall can be between 0.05 and 250 mm/s with accelerations ranging from 0.5 to 5220 mm · s⁻².

8.2.4 Removal of stepper motor interference

There were three sources of noise that caused interference to wall motion measurements that were identified in our system:

- Noise from the switching of the coils in the stepper motor was transmitted to the lower wall.
- Vibrations from the movement of the motor were transmitted to the transducer casing.

Figure 8.3 shows how these sources of noise affected the recorded wall motion. These sources of noise were remedied using the following techniques:

- Acoustic absorbing foam was applied to the lower moving layer of the tool.
- The US transducer was isolated from the rest of the system by mounting it on a clamp stand resting on acoustic absorbing foam.
- The water bath was grounded to remove electrical interference from the stepper motor.

Figure 8.4 shows the effect of these noise suppression methods on the recorded wall motion.

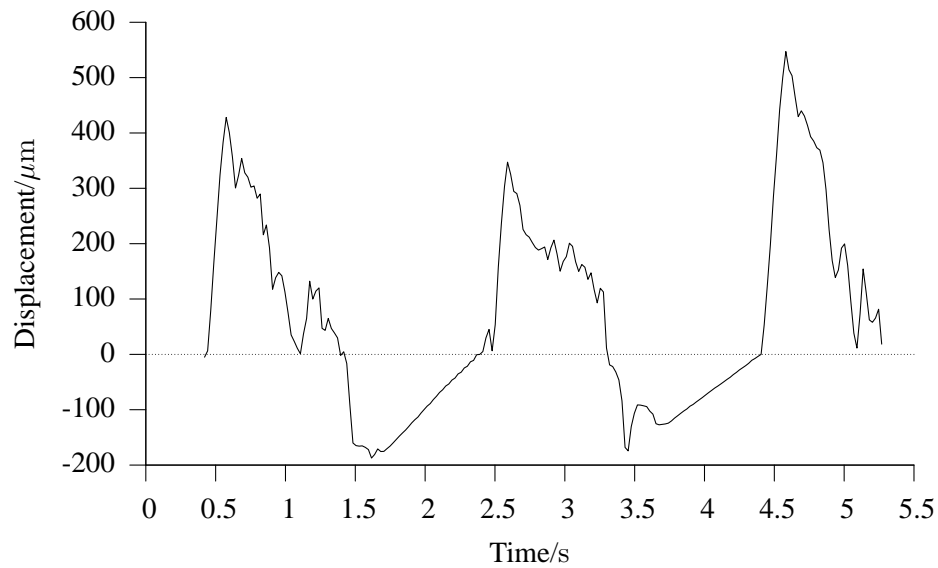
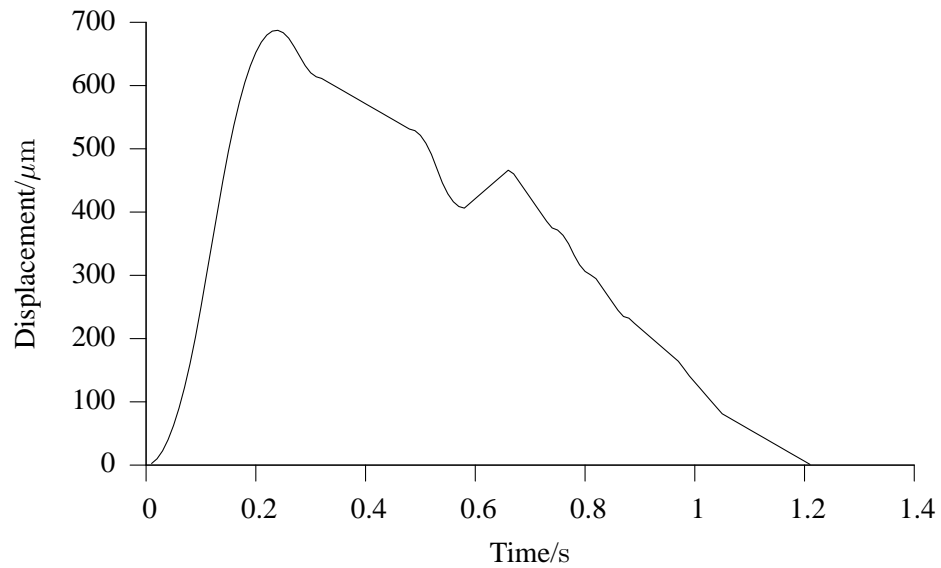
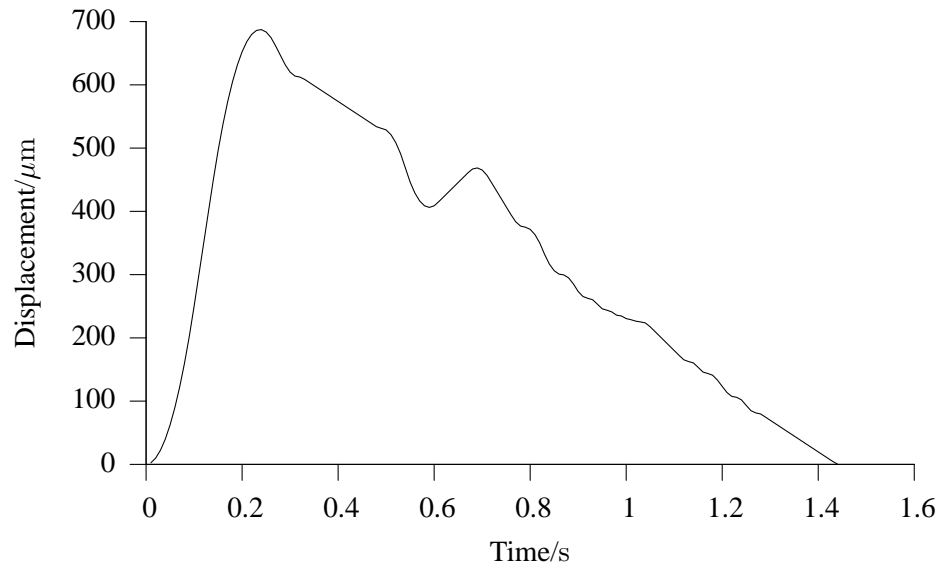
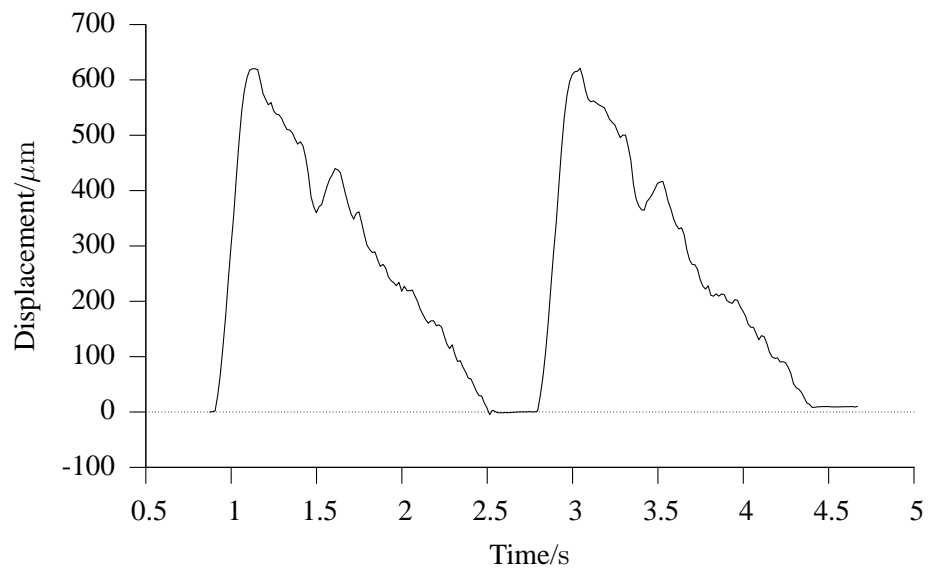


Figure 8.3: The effect of stepper motor noise on recorded AWM displacements. The waveform in Figure 8.3a is a 700 μm peak displacement physiological wall motion waveform. This was used to move the stepper motor repeatedly with a 1 sec gap between waveforms. Electrical grounding for the stepper motor was not used, and vibration reducing foam was not applied to the lower arm of the test phantom. The recorded results (Figure 8.3b) show the effect of mechanical and electrical noise. Peak recorded displacement was up to 50% less than the peak sent displacement; negative displacements were recorded; and the shape of the waveform is lost after the initial peak displacement.



(a)



(b)

Figure 8.4: Stepper motor noise has been removed from this set of results. The 700 μm peak displacement physiological wall motion waveform in Figure 8.4a was used to move the lower wall. The recorded displacements from the wall motion software (Figure 8.4b) show faithful reproduction of the shape of the waveform.

8.2.5 Assessment of wall motion phantom accuracy

A laser vibrometer (Polytec GmbH, Waldbronn, Germany) was used to assess the positional accuracy of the test phantom. The resolution of the laser was $0.32 \mu\text{m}$ and its positional accuracy was $0.0032 \mu\text{m}$. The resolution of the laser refers to the minimum measurable displacement of the laser vibrometry equipment. This means that movements of the wall motion test phantom as small as $0.32 \mu\text{m}$ could be measured using this equipment. The AWM test phantom was set up with no water in the water bath, no upper TMM layer and without the US transducer. The laser spot was directed onto the flat upper surface of the lower wall at an angle of 90° . Displacements from a $300 \mu\text{m}$ peak displacement physiological waveform and a $700 \mu\text{m}$ peak displacement waveform were measured and compared to calculate the accuracy of the system. Five measurements using each waveform were recorded and the peak displacement of the sent waveform was compared to the mean of the peak displacements of five sets of measured waveforms. The difference in the mean peak displacement of these waveforms compared to the sent waveform gives the positional accuracy of the test phantom.

8.2.6 TDI-based wall motion software assessment

To illustrate the use of the wall motion phantom, a TDI-based method for estimating arterial wall motion was analysed [16]. TDI is used in a similar way to Colour Doppler US for blood flow. The colour box is placed over the artery, encompassing a part of both upper and lower walls. Instead of displaying colour blood flow in the lumen, coloured pixels representing wall motion are superimposed on the artery wall. The TDI technique was used with a Philips HDI5000 US scanner and the L12-5 38mm linear array transducer. Cineloops of TDI data were recorded on the US scanner and downloaded to PC via an ethernet cable to arterial wall motion software for offline analysis. Each cineloop was captured with identical machine settings (see Table 8.1) save for velocity setting which was set to 0.4 or 0.6 cm/s depending on the peak velocity of the lower wall.

Displacement and strain rate can then be calculated and saved as a spreadsheet file for further analysis. The wall motion phantom was used to assess the following key parameters of the TDI-based technique:

- Measurement accuracy using a range of physiological wall motions
- Minimum resolvable displacement

Parameter	Setting
Probe	L12-5 38mm linear array
Frequency	7 MHz
Sensitivity	Medium
Line density	A
Dynamic Motion Differentiator (DMD)	Off
Colour gain	Saturated (>85 %)
Velocity Scale	Dependent on peak velocity of wall motion waveform
2D gain	Minimum for clear wall definition
Frame Rate Optimisation (FRO)	Maximum
Time Gain Control (TGC)	Mid Range
Colour box size	0.75 × 1.3 cm

Table 8.1: US machine settings for use with TDI. The same settings were used with each acquisition for consistency.

- Change in accuracy with change in wall velocity

8.2.6.1 Measurement accuracy using a range of physiological wall motions

To assess the accuracy of the TDI wall motion software, a series of scaled physiological wall motion waveforms were created (see Figure 8.5.) Peak displacements varied from 689 to 85 μm . The wall motion phantom was assembled, and the lower wall was moved using each waveform. Five measurements of each movement waveform were recorded, with each measurement covering three complete wall motion movements. This fills the US scanner buffer completely, and allows for the software misregistering some of the movements. The peak displacement was recorded from the recorded waveform which best resembled the actual movement waveform of the wall. This was then compared to the actual peak displacement of the lower wall. From the five peaks, the mean error and the 95% confidence interval of the error were calculated. The velocity setting of the US scanner was set to 0.4 cm/s for the 100 to 400 μm waveforms since the highest velocity in these movements was < 0.4 cm/s. The velocity setting for the 500 to 700 μm peak displacement waveforms was 0.6 cm/s

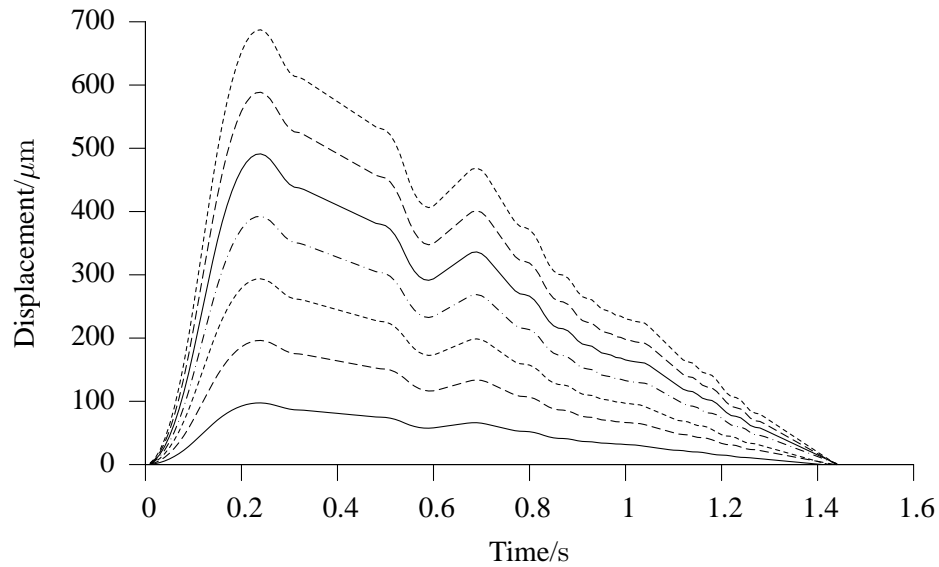


Figure 8.5: Seven physiological AWM displacement waveforms ranging from 100 to 700 μm peak displacement.

8.2.6.2 Minimum resolvable displacement

Determining the minimum resolvable displacement (d_{crit}) of the TDI wall motion software shows how useful the software is for measuring fine displacements. Two constant-velocity waveforms were created (Figure 8.6 and 8.7). Each waveform was used to move the wall motion phantom. The displacement of the wall was recorded in a similar way to the physiological waveform experiments. The height of each peak was measured from the best data provided by the TDI software. The velocity setting of the US scanner was set to 0.6 cm/s for both waveforms. Measured peak displacements were recorded and analysed as before. The minimum resolvable displacement was found to be at the point of lowest position measurement error.

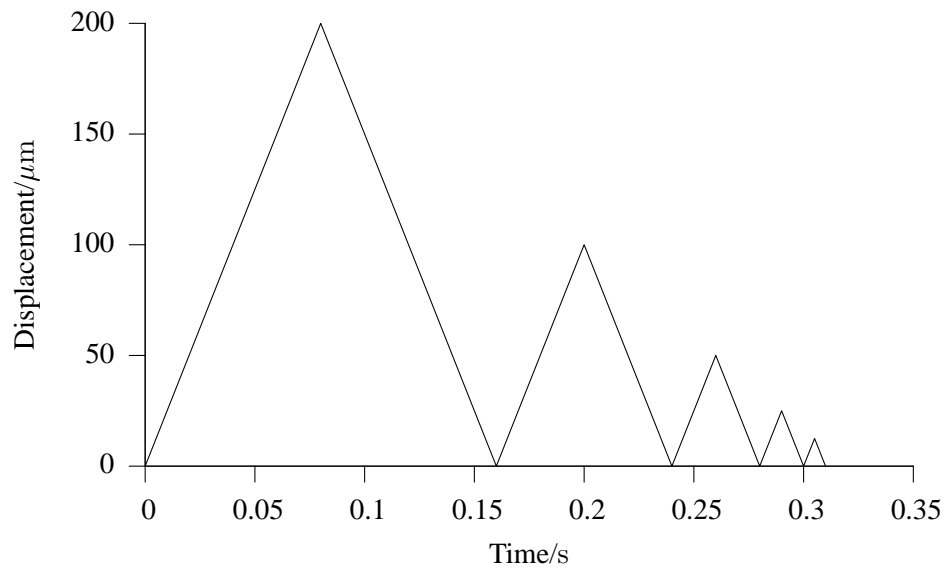


Figure 8.6: The first constant velocity and variable displacement waveform used to determine d_{crit} . Peak displacements are 200, 100, 50, 25 and 12.5 μm .

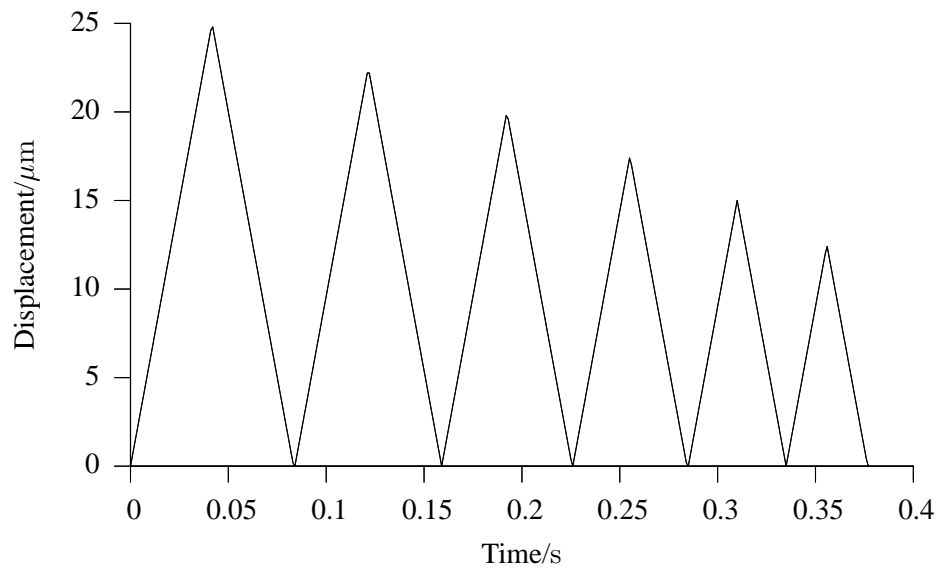


Figure 8.7: The second constant velocity and variable displacement waveform used to determine d_{crit} . Peak displacements are 25, 22.5, 20, 17.5, 15 and 12.5 μm .

8.2.6.3 Change in accuracy with change in wall velocity

The velocity of the artery wall can vary significantly within one cardiac cycle due to the pulsatile nature of blood flow. Wall motion software must therefore respond accurately to a large range of velocities. The effect of changing velocity on wall motion displacement error was calculated by using two variable velocity but constant displacement waveforms (figures 8.8 and 8.9). These were used to move the wall motion phantom in a similar way to the earlier constant velocity waveforms. Peak displacements were measured and error was calculated for each peak movement. The velocity setting of the US scanner was set to 0.6 cm/s for both waveforms.

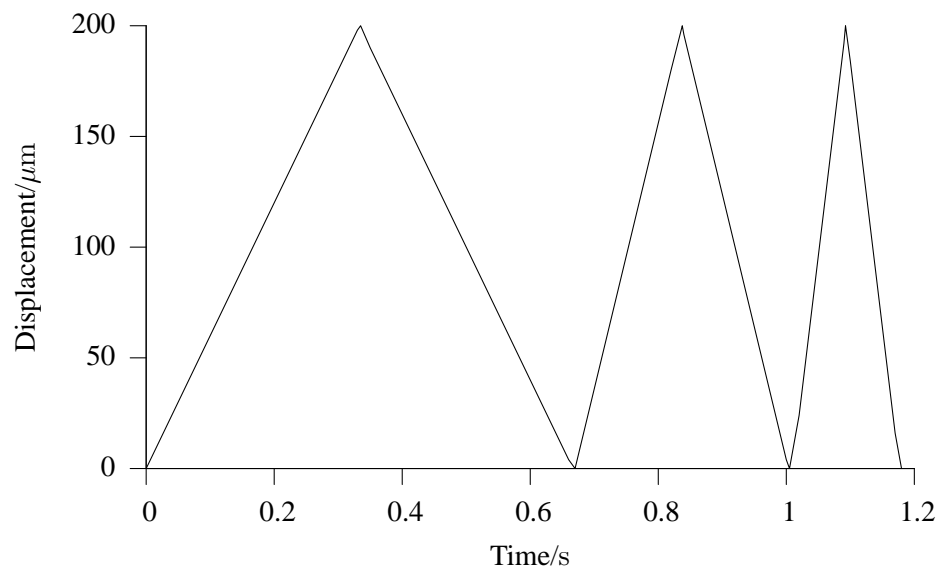


Figure 8.8: *The first constant displacement and variable velocity waveform used to find the effect of changing velocity on accuracy. The velocities of the four peaks are 0.6, 1.2 and 2.4 mm/s.*

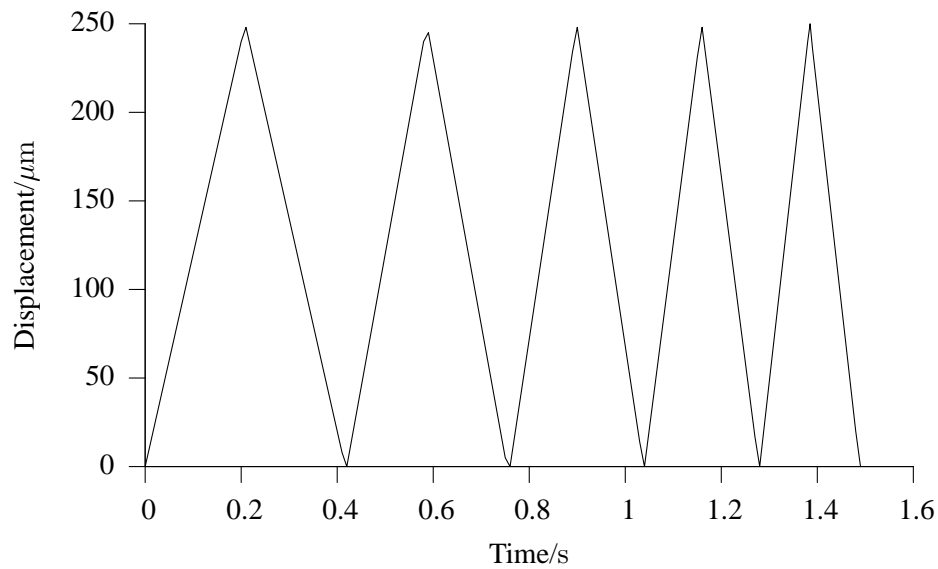


Figure 8.9: *The second constant displacement and variable velocity waveform used to find the effect of changing velocity on accuracy. The velocities of the four peaks are 1.2, 1.5, 1.8, 2.1 and 2.4 mm/s.*

8.3 Results

8.3.1 Wall motion phantom accuracy

Using the laser vibrometer as described above, positional accuracy was $(7 \pm 2) \mu\text{m}$ for the $300 \mu\text{m}$ peak waveform and $(36 \pm 2) \mu\text{m}$ for the $700 \mu\text{m}$ peak waveform. Positional accuracy refers to the ability of the wall motion phantom to reproduce a wall motion waveform. For example a positional accuracy of $36 \mu\text{m}$ means that the peak displacement of the phantom will be within $36 \mu\text{m}$ of the waveform used to control the movement.

8.3.2 Measurement accuracy using a range of physiological wall motions

Error in recorded wall motion from the TDI-based method is displayed in Figure 8.10. Error bars show the 95% confidence interval above and below the calculated error for each of the seven physiological waveforms. Error is consistently below 10% for the 300 to $700 \mu\text{m}$ peak displacement waveforms. These error values range from $(6 \pm 2)\%$ for the $300 \mu\text{m}$ waveform to $(8 \pm 2)\%$ for the $700 \mu\text{m}$ waveform. Measurement error increases from $(12 \pm 10)\%$ for the $200 \mu\text{m}$ waveform up to a peak of $(39 \pm 14)\%$ for the $100 \mu\text{m}$ waveform.

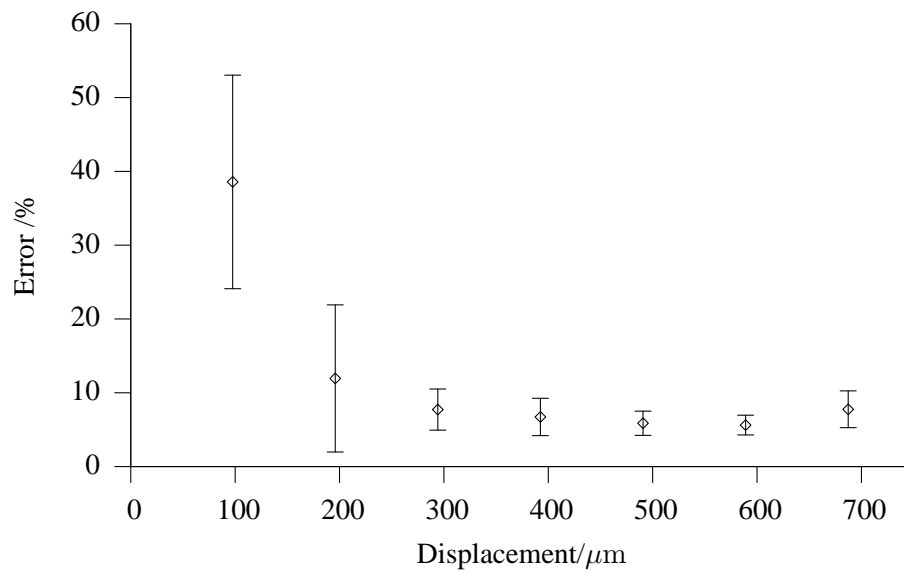


Figure 8.10: Error as a function of displacement for the seven physiological wall motion waveforms.

8.3.3 Minimum resolvable displacement

Figure 8.11 shows the error in the recorded constant velocity displacements. The waveforms with peak displacements of 25 and 22.5 μm both have errors of around 25%. Beyond 22.5 μm , error increases to a maximum of $(51 \pm 65)\%$ at 12.5 μm .

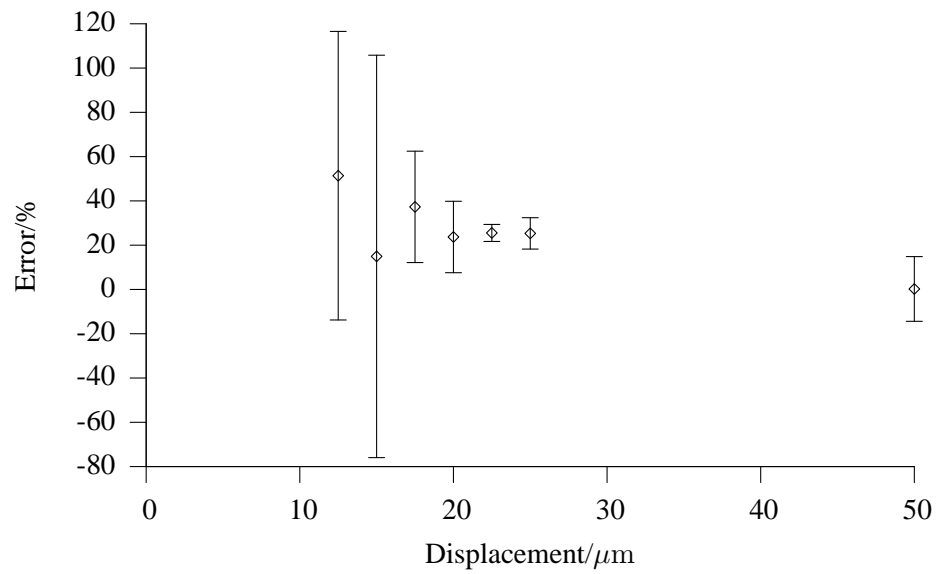


Figure 8.11: Accuracy of measured displacement from the two constant velocity and variable displacement waveforms shown in figures 8.6 and 8.7.

8.3.4 Change in accuracy with change in wall velocity

Changes in motion velocity induce changes in the accuracy of the recorded wall motion (see Figure 8.12.) For the $250\ \mu\text{m}$ waveforms measured at different velocities, measurement error was consistently around 20% for velocities from 1.2 to 2.1 mm/s, and increased to $(39 \pm 23)\%$ at 2.4 mm/s.

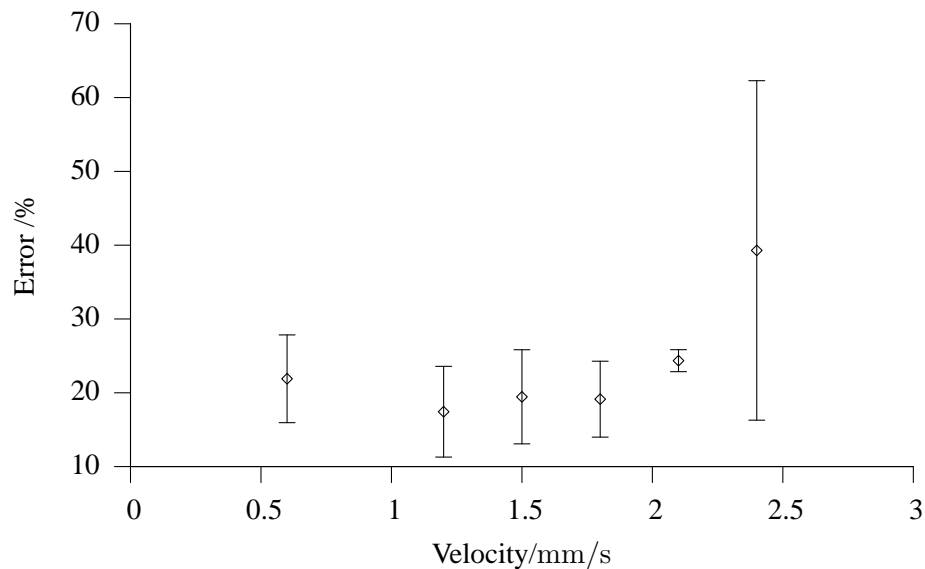


Figure 8.12: Accuracy of measured displacement from the two constant displacement and variable velocity waveforms shown in figures 8.8 and 8.9

8.4 Discussion

8.4.1 Assessment of wall motion test phantom

The arterial wall motion test phantom simulates a transverse slice through a straight artery when imaged with US. It has a positional accuracy of $36 \mu\text{m}$, which is less than 0.25 pixels at the 3.9 cm/s depth setting on the 12 MHz linear array used for these experiments. Since the phantom does not simulate a cross-sectional view of an artery, it is not suitable for arterial wall motion measurement methods that rely on measuring change in diameter of a cross-section of an artery. However, it is suitable for other techniques (like the TDI-based method described) that require two clearly defined walls. Controlling the test phantom requires some specialist knowledge of the terminal commands for the stepper motor controller. The test phantom uses layers of agar-based TMM created in our laboratory. However, off-the-shelf materials such as Zerdine (Computerized Imaging Reference Systems, Inc., Norfolk, Virginia, USA) could be used instead. Nonetheless, the test phantom is a useful tool for the accurate calibration of US arterial wall motion techniques that require two parallel lumen walls.

In principle a vessel phantom could be used as a calibration device provided that the motion of the wall was accurately known. Bergel [123] measured the Young's modulus of arteries by

distending the arteries under pressure and measuring the change in outer diameter. The change in inner diameter was calculated from the outer diameter and the known volume of the arterial wall. It was assumed that this did not change during the distension. The diameter variation was measured by illuminating the artery with a light source and using a photomultiplier positioned behind the vessel to monitor the light. Alterations in the detected light brightness were linearly related to diameter, though there is no indication of measurement accuracy in the paper. In principle a laser based technique could be used to monitor the position of the outer wall of the vessel. The wall motion phantom described in this chapter used a reflector positioned on the moving surface to reflect the laser light, so provided that a reflector was positioned on the wall of the vessel, the technique described in [123] might work. The wall motion phantom described in this chapter has the advantage over the use of a vessel phantom in that the position of the moving plate can be precisely controlled, something which is difficult to achieve in a vessel phantom [70].

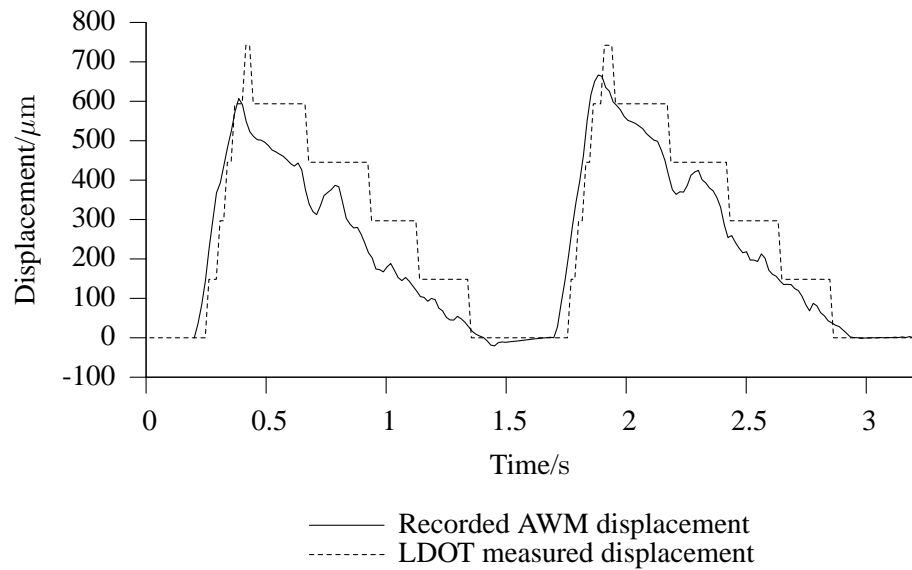
Forces experienced by the moving wall of the phantom and the two arms that support it will be different in the water and glycerol solution than in air. The laser vibrometer measurements were made in air because reflection from the solution/air surface, and scattering and diffraction effects in the solution would prevent accurate measurement of the moving wall. Larger drag forces on the moving wall, coupled to the additional weight of the TMM layer, would produce a larger bending force on the support arms and the moving wall than in air. A finite element simulation (ANSYS, Pennsylvania, USA.) confirmed that these effects produced a negligible deflection ($< 0.001\mu\text{m}$) of the support arms and the moving wall. The greater forces on the wall have no significant effect on the motion of the stepper motor. When the load on the motor is greater, the current is increased to compensate and the displacement remains the same.

8.4.2 Assessment of wall motion software

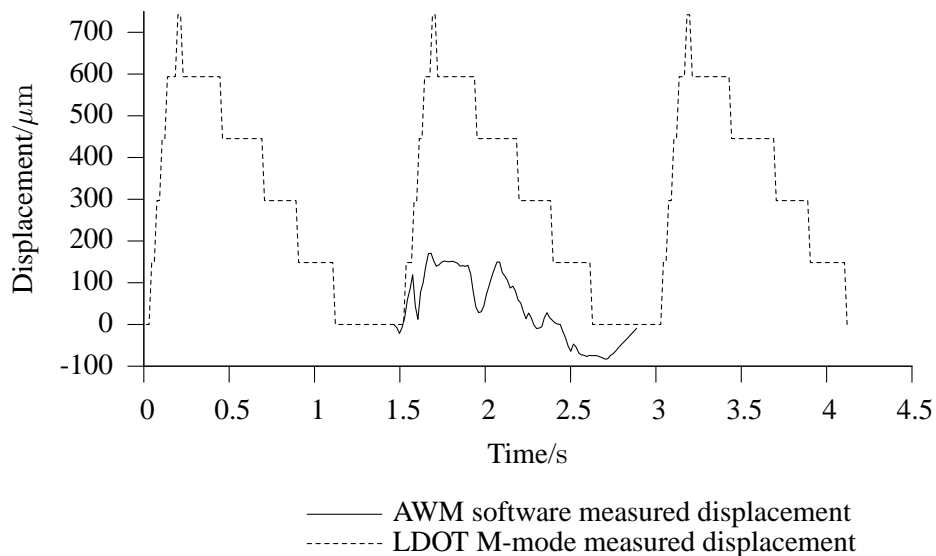
The TDI-based technique was compared to the lumen diameter over time (LDOT) function in the HDI Lab software [124, 125]. This technique creates a virtual M-mode image by choosing one scan line of data from each dataset and thresholding the scan line to isolate the artery wall. The relative height of the wall from each image is plotted and then compared to the measurement using the TDI-based technique (Figure 8.13). Effects similar to that shown occurred in approximately 10% of recorded datasets. The source of this variation is difficult to determine. It may be due to data transmission and encoding errors from the US scanner that cause errors in

wall motion data but not in B-mode data. It may also be caused by a programming error in the experimental wall motion software used in this study. Full investigation of this issue would be required by the developers of the wall motion software to find its source. In practice, it suggests that the wall motion waveforms recorded by this TDI-based wall motion technique require careful analysis to ensure their validity. This could most easily be done using a comparison with the LDOT function as reported here.

Using constant velocity waveforms to move the phantom and calculate d_{crit} , the minimum resolvable displacement (as in Figure 8.7), an error of $(25 \pm 4)\%$ was found for a $22.5 \mu\text{m}$ peak displacement. However, using a $100 \mu\text{m}$ physiological waveform to move the phantom resulted in an error of $(39 \pm 14)\%$. The TDI-based wall motion technique also demonstrated variability in error with changes in wall motion velocity. Wall motions with velocities greater than 1.8 mm/s experience errors greater than $(24 \pm 1)\%$. The large and variable positional error associated with AWM measurements using the TDI-based technique implies that it would not be suitable for validating moving wall arterial simulations. The suitability of other US-based techniques for AWM measurements may be easily assessed with the wall motion test phantom described here. For methods of AWM measurement developed in future this device can easily be used to provide an assessment of the accuracy and repeatability of the method. The use of this test phantom with some of the other methods mentioned in the literature such as an M-mode technique [115] or a technique based on signal processing of RF data [117, 118] would show the potential of these rival techniques for providing accurate validation of moving wall arterial simulations.



(a)



(b)

Figure 8.13: Figure 8.13a shows a normal recorded wall motion result using the TDI-based wall motion technique. The TDI displacement result (solid line) is compared with the displacement recorded using the HDI Lab Lumen Diameter Over Time (LDOT) tool. However up to 10 % of our recorded datasets delivered incorrectly read wall motion displacement results (see Figure 8.13b). This comparison with LDOT using the same data confirms that the variation was not due to uncontrolled motion of the test phantom moving wall.

8.4.3 Conclusion

The suitability of the use of arterial wall motion measurements from a TDI-based AWM measurement technique to validate moving wall arterial simulations was assessed using a wall motion test phantom. The test phantom has a positional accuracy of $(36 \pm 2) \mu\text{m}$. It simulates a transverse slice through a straight artery, and reproduces physiological displacements, velocities and accelerations. Typical displacement errors measured by this technique varied between 10 and 20%, and increased with decreasing wall displacement and increasing wall velocity. The TDI-based technique was rejected as a tool for validating moving-wall artery simulations due to its high variability and low accuracy.

Chapter 9

Critically evaluating the 3D ultrasound system for image-guided modelling

9.1 Introduction

In earlier chapters, the development of a system for image-guided modelling (IGM) using 3DUS was described. This system was developed to provide a diagnostic system for arterial disease in symptomatic patients. Other systems have also been developed that aim to accurately image and model diseased arteries.

This chapter assesses the IGM system developed in this thesis, comparing the performance of important system components with other IGM systems presented in the literature. It evaluates the ability of the 3DUS imaging system to image healthy and diseased arteries. The ability to create an accurate computational mesh model of healthy and diseased arteries is also evaluated. These evaluations will contribute to the understanding of 3DUS-based IGM systems, and will help to identify areas of development that hinder their adoption into routine clinical practice.

9.2 Comparisons with other IGM work

IGM in the literature has received considerable attention [65]. Principal groups that have used IGM techniques with 3DUS to simulate the arterial system include the group led by Xu at Imperial College in the UK [e.g. 111], the group at Robarts Research Institute, London, Ontario, Canada led by Fenster, Holdsworth and Steinman [e.g. 63] and the Thorax Center in Rotterdam, NL, led by Slager [69]. The group led by Slager has concentrated on IGM in the coronary artery using IVUS, which is not directly comparable to the *extravascular* US system described in this thesis. The process of capturing 3D coronary artery images using from IVUS has many different challenges to the extravascular 3DUS system developed in this thesis. Recent work by the group led by Fenster has concentrated on the use of 3DUS to study plaque morphology [45]; its IGM work has mainly been concerned with the use of MRI images to create patient-specific artery geometries.

This section evaluates the work of the two groups mentioned above that have used 3D extravascular US. The 3DUS acquisition system for IGM presented in this thesis is compared to similar systems used by the Fenster and Xu groups. Methods of creating patient-specific artery geometries and segmenting B-mode arterial US images will be compared. Finally, simulations using different CFD packages based on US data will be compared. To avoid confusion between the works cited from different groups, Table 9.1 lists the papers that are referenced in this chapter. Works published which refer to different methods used by each group often do not feature the group leader’s name in the author list. This table clarifies which works were produced by each group.

Group	Function	References
Xu (Imperial College, UK)	3DUS acquisition system	[39, 92]
	Segmentation and mesh generation	[26, 29, 66]
	CFD simulations	[66, 67, 78]
Fenster (Robarts, Canada)	3DUS acquisition system	[28, 45]
	Segmentation and mesh generation	[28, 126, 127]

Table 9.1: *Published works by the two image-guided modelling groups that have used extravascular 3D US.*

9.2.1 3DUS acquisition system

The specification of a 3DUS imaging system is partly dependent on the historical development of US machines and positioning systems. It is also dependent on the availability of equipment and budget constraints. The Philips HDI5000 US scanner used by Barratt et al.[92] is an older version of the scanner used in this thesis (see Chapter 3). The scanner used in the system described in this thesis features newer imaging technologies such as SonoCT and XRes. These features mean that the accuracy of 3DUS segmentation can be increased due to the improved image quality they provide. Landry et al. [45] also made use of these improved imaging technologies to clearly define plaque boundaries using their 3DUS system.

The position sensor used by a 3DUS system also governs the overall accuracy of the system. The magnetic tracking system developed by Barratt et al. [92] features a lower positional accuracy than the optical system used here. The magnetic system is also affected by metal objects in the tracking volume of the sensor, which was reduced (but not eliminated) by using a wooden bed for the patient. A more accurate system was used by Landry et al. [45]. Their mechanically-controlled system was used to image carotid plaque in diseased patients. This system has po-

tentially higher accuracy than the optical position sensor reported here (see Chapter 3), but only has a limited scanning range. Longer artery scans would require several acquisitions plus a registration step to provide a full-length scan. The freehand optical system presented here avoids this problem (see Chapter 1, section 1.4.3 for more on this issue).

The spacing between arterial images captured using a 3DUS system has an effect on the resolution of artery geometries. Large spacings between images will miss out important changes in vessel morphology; scanning with very close spacings increases the duration of the scan, with implications for patient comfort and clinical utility. Freehand systems (such as that presented in this thesis, and that developed by Barratt et al. [92]) have no absolute control over the spacing of images. The motorised system developed by Landry et al. [45] has the highest spatial resolution, with the associated disadvantage of a limited maximum scanning length. A method for specifying a theoretical optimal slice spacing was developed by Tong et al. [128]. This is only of practical significance for a motorised system. Freehand systems rely on the skill and endurance of the operator to minimise image spacing. Of the three systems discussed here, slice spacings of the two freehand systems are both around 1 mm for scans of the carotid arteries (see Figure 9.2) while the motorised system has spacings of up to 0.1 mm. The system described in this thesis therefore has as good image spacing as other freehand systems in the literature.

System origin	Type of system	Image spacing (mm)	Notes
[28]	Mechanical	0.1	no gating
[78]	Magnetic freehand	1.0	ECG gated
This thesis	Optical freehand	1.10 ^a	Retrospectively gated

^aMedian image spacing for 7 gated femoral and carotid scans using the L12-5 high-resolution transducer

Table 9.2: Image spacing for 3DUS systems developed by different groups.

The speed of 3D image reconstruction is an additional indicator of the usefulness of a system. The 3DUS system using Stradwin described in this thesis featured instantaneous 3D reconstruction of 3DUS data. This was at the expense of image quality: some artefacts and loss of resolution was inevitable from the process of converting US image data from the scanner into a video signal, then digitising it for storage with the video capture card. The system developed by Barratt et al. [39] used the HDILab program to download digital data direct from the scanner to a networked PC. Images from HDILab were reconstructed offline using simultaneously recorded position data from the magnetic position sensor. The long download times due to the

slow network card in the older-generation Philips HDI5000 US machine used would mean a lengthy wait post-scan for the backup of data. Images would then have to be converted post-capture to another image format for segmentation. No indication of how long this process took is given in the papers related to the development of their system. The HDILab program was also used by Ainsworth et al. [28] along with the same generation of HDI5000 US machine as used in this thesis. The faster download times available with this machine would speed up image capture and backup. Neither the systems reported in [28] nor [39] were able to reconstruct 3DUS data in real-time like the Stradwin-based system reported here.

9.2.2 Creating patient-specific artery geometries

Patient-specific artery meshes for CFD simulation used by the Xu group were created using a 2D serial reconstruction method. Individual US images were manually segmented. The 3D-registered segmented contours were imported into a solid modelling program. Centreline smoothing was applied to remove traces of patient movement and misregistration. Finally a solid modelling program was used to create a surface mesh, representing the 3D artery lumen. The Xu group reports carotid bifurcations created from patient-specific data [78] and a carotid model with plaque [26]. Reconstruction of the diseased lumen to compare it with the original artery wall shape were also carried out using this method [29]. In contrast to the work of this group, this thesis presents the effect of a rigid-registration based approach to reducing the effect of patient movement on artery mesh generation (see Chapter 4). As discussed in Chapter 7, this method may produce more anatomically realistic models of arterial disease and flow dividers than the registration-based reconstruction method used in this thesis. However, it should be noted that the diseased artery meshes created by this group had less complex plaque than that described in Chapter 7. A side-by-side comparison of both mesh generation methods on the same image data would confirm which is more accurate at modelling complex arterial disease.

No use of semi-automatic segmentation was reported by the Xu group. The group led by Fenster developed a semi-automatic method of segmenting artery lumens from 3DUS images [126]. This method also automatically generated a 3D patient-specific artery mesh from the segmented data without any additional solid modelling step. However for the more complex diseased artery geometries scanned in a 3DUS study quantifying plaque volume [28] manual segmentation (referred to in this paper as “manual planimetry”) was used to identify the diseased lumen. Perhaps due to the complexity of the plaque morphology found in more severely

diseased patients, their semi-automatic segmentation method was not able to identify the lumen. This would reinforce the findings presented in this thesis, comparing semi-automatic segmentation with manual segmentation for a variety of arterial US scans (see Chapter 6). It was found that reinitialisation of the ShIRT semi-automatic segmentation method was required in images of the artery where the lumen shape changes significantly. In addition, the automatic artery mesh generation method (also employing different features of the ShIRT package) was not sensitive enough to changes in segmented lumen shape, and smoothed out complex plaque geometries creating unrealistic flow patterns and WSS results.

Overall, the lumen segmentation and patient-specific artery mesh creation methods presented in this thesis are equivalent to those reported by the Fenster and Xu groups. Comparison of each method on the same image data would confirm which method produces the most accurate reconstructions of complex arterial disease and flow dividers.

9.2.3 CFD simulations based on 3DUS data

The main focus of this thesis has been concerned with the development of a 3DUS acquisition system and the creation of patient-specific arterial geometries based on 3DUS images. It is beyond the scope of this work to comment on the different flow models and CFD solvers used by the various groups considered here. However, a consideration of how artery geometry creation methods based on 3DUS affect the results of computational simulation will be made.

A primary factor that influences how 3DUS images are captured is the position of the patient. For carotid artery scans, the patient needs to be positioned comfortably, revealing enough of the neck to allow scanning of the common carotid and the internal and external branches. This inevitably produces an arched appearance to the neck, leading the carotid to bend sympathetically with the position of the rest of the neck. This has an effect on the flow patterns in the carotid. Glor et al. [78] considered this effect and how geometries based on 3DUS scans produce different wall shear stress patterns to geometries based on MRI scans of the same patient. In addition, some patients are not suitable for 3DUS examination because not enough of the branches of the carotid artery are visible using US. The carotid may begin to bifurcate above the jaw line in some patients. High bifurcations were reported in [66] and were also experienced while using the system described in Chapter 3. This represents a fundamental limitation of 3DUS scanning when performed in the extravascular method presented in this thesis and also that used by the Xu group. However, this problem is not encountered in all patients, meaning that 3DUS is still

considered beneficial in clinical examinations and in current IGM research.

Flow effects experienced from the misregistration of 3DUS images were dealt with in other groups mainly through the use of smoothing. The amount of smoothing applied in any particular case was determined empirically, relying on the expert judgement of the user of the system. This thesis has attempted to compare different methods of patient-specific artery geometry creation and its effect on flow simulation (see Chapter 7). Other groups (e.g. the Fenster group in [127]) have only considered different segmentation methods. Chapter 7 highlights how the smooth appearance of an artery geometry may hide its lack of physiological realism, especially in the case of complex disease.

Comparisons of CFD simulations also obviate the lack of a benchmark method for comparing simulations using different mesh generation methods. Peak values of WSS [67, 126] or the shape of flow patterns may be compared. Chapter 7 uses both of these comparisons. These two methods are qualitative and imprecise. They only compare one factor of the flow field simulation that can be conveniently measured. This type of comparison may attract a similar criticism as Hammoude [96] gave to the field of comparing the performance of different segmentation techniques (see Chapter 6). Further work on an objective standard for comparing simulations would be a constructive contribution to this field.

9.2.4 Summary

The 3DUS system for image-guided modelling presented in this thesis was compared to literature from other US and modelling groups. The freehand 3DUS system presented here is more accurate and faster than the freehand system developed by the Xu group. It was less accurate with larger image spacing than the mechanically controlled system developed by Fenster. Solid modelling to create artery mesh models was as good as that created by the Xu group for healthy arteries, with further work required to effectively arteries with regions of complex plaque.

9.3 Evaluating 3DUS imaging in healthy and diseased arteries

3DUS imaging builds on the advantages of conventional 2D US by providing a 3D representation of 3D arterial geometries. 2DUS provides real-time images of moving arterial anatomy, and gives high-resolution images of small arterial structures within the limitations of beam pen-

etration depth found with high frequency transducers. However, the performance of 3DUS is inherently limited by the disadvantages of 2DUS imaging.

US image quality is degraded due to bony structures obscuring the artery of interest; subcutaneous fat attenuating the US signal and preventing clear images of the lumen; and bowel gas causing shadowing of the abdominal vasculature. These effects on carotid artery, femoral artery and abdominal aorta scanning are considered in the following sections.

9.3.1 3DUS imaging of the carotid artery

The carotid artery is a superficial large artery which runs up either side of the neck, supplying the brain and the face with blood. It bifurcates into the internal and external carotid arteries. The carotid is typically found between 2 and 4 cm deep under the surface of the skin. Its superficial position allows the use of high frequency (7–12 MHz) transducers for imaging.

In most patients, few problems are encountered in producing a clear image of most of the carotid artery. However, in some, subcutaneous fat prevents clear US imaging. Some patients may have sufficient fat in the neck (Figure 9.1) to obscure the outline of the lumen. This prevents accurate segmentation of the lumen, limiting the length of the computational mesh model that is created for CFD simulation.

It is not possible to reliably image below bony structures since US is absorbed and scattered due to the high-density structures found in bone. This limits the number and type of patients that can receive a full 3DUS carotid examination: patients with a carotid bifurcation that is positioned superior to the mandible may not present a sufficient length of the internal and external carotid arteries or the carotid bulb to create a complete computer mesh model of the carotid [108]. This effect may also prevent Doppler measurement of peak flow in the carotid branches which reduces the number of boundary conditions available to correctly configure a flow simulation.

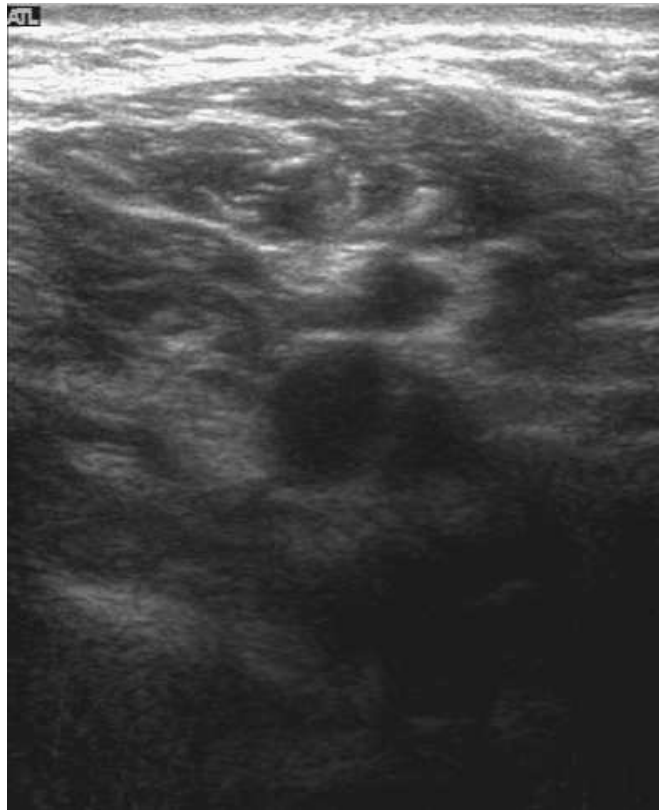
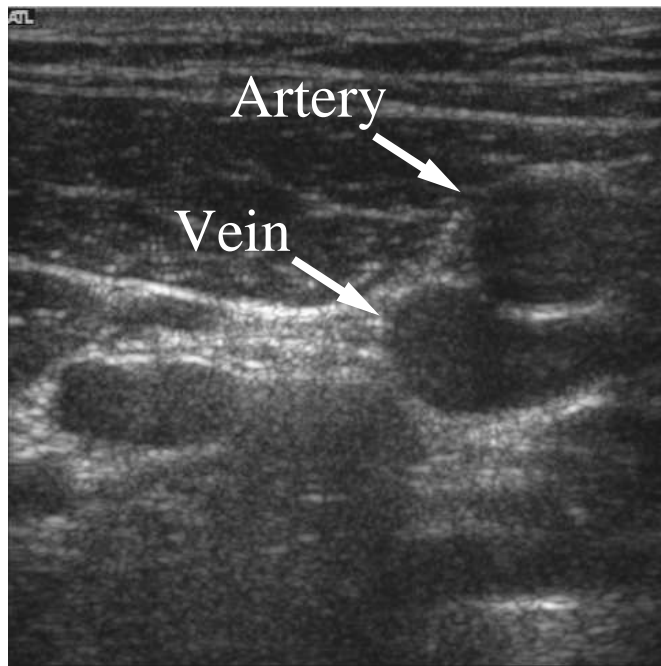


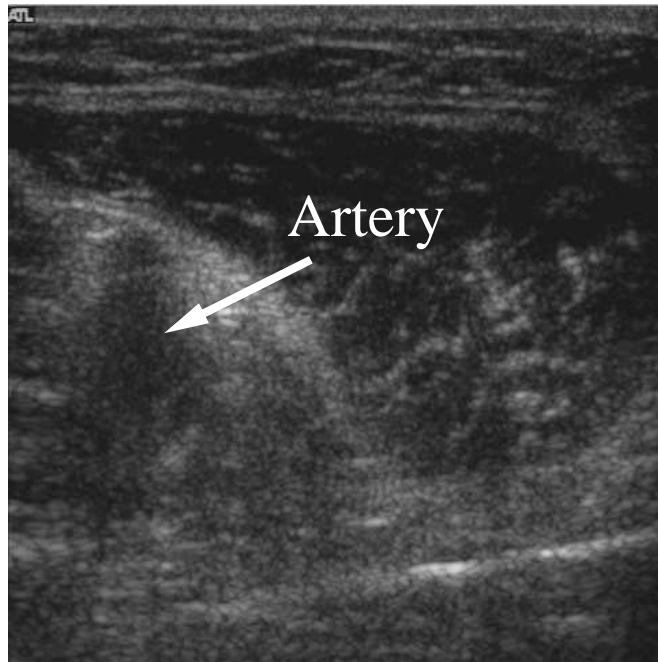
Figure 9.1: *Subcutaneous fat in this carotid image from a patient causes strong reflections at the top of the image, attenuating the signal and preventing clear imaging of the carotid artery. The carotid is only 2.5 cm deep at this point.*

9.3.2 3DUS imaging of the femoral artery

Femoral 3DUS imaging uses the same type of transducer as for the carotid. The femoral is located deeper than the carotid, lying 4–5 cm below the surface of the skin. The femoral artery gradually assumes a more profound position as it approaches the knee, and eventually becomes the popliteal artery as it runs behind the knee. The presence of more muscle tissue and subcutaneous fat above the femoral artery than above the carotid artery mean that the image quality of femoral scans is degraded compared to carotid scans. In most patients and volunteers, clear images of the femoral artery were captured. In some patients, as the femoral artery travels down the leg, a noticeable drop in image quality was found due to the increased depth of the artery (see Figure 9.2).



(a) The superficial femoral artery imaged near the groin. At this point it is 1.4 cm below the surface of the skin. The femoral vein is visible directly below it. The lumen is clearly outlined.



(b) The superficial femoral artery imaged near the knee. The depth is now 2 cm and the artery (pictured at the left) is indistinct compared to the texture of the surrounding muscle tissue.

Figure 9.2: Changes in image quality of US scans of the femoral artery as it approaches the knee.

9.3.3 3DUS imaging of the abdominal aorta

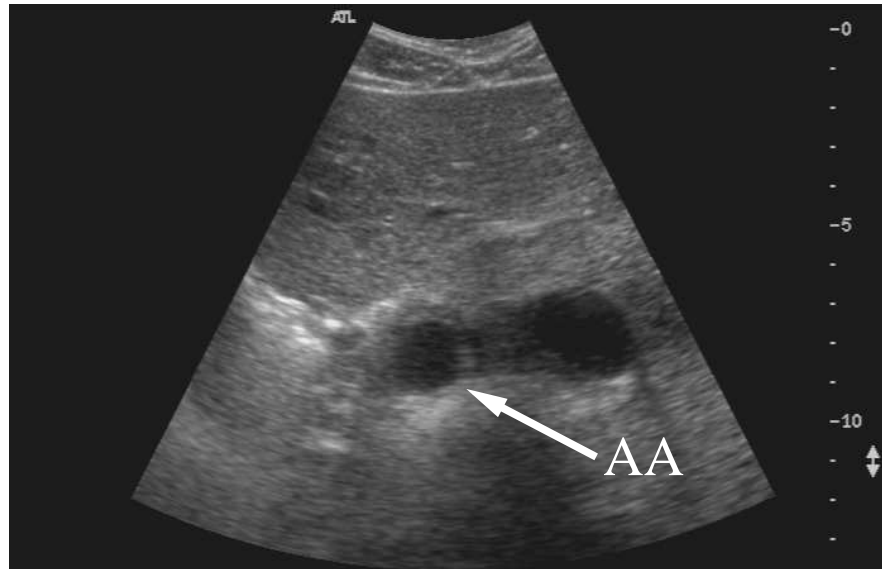
Abdominal imaging using US is particularly challenging due to factors such as bowel gas and subcutaneous fat. The large movements experienced in the abdomen due to respiration also affect 3DUS imaging. Respiratory gating is recommended to reduce misregistration artefacts in this region. The aorta is situated anterior to the spinal column in the abdominal cavity, so a transducer with high penetration depth and low resolution (in comparison to the transducers used for the carotid) is used. A curvilinear 5 MHz transducer was used for abdominal scanning.

In many cases, bowel gas prevents accurate imaging of the abdominal vasculature. Bowel gas scatters US signals, preventing imaging of structures below it. It is normal in abdominal scanning practice to ask the patient to fast before scanning to reduce the build-up of gas. However some patients still have bowel gas, making clear imaging impossible.

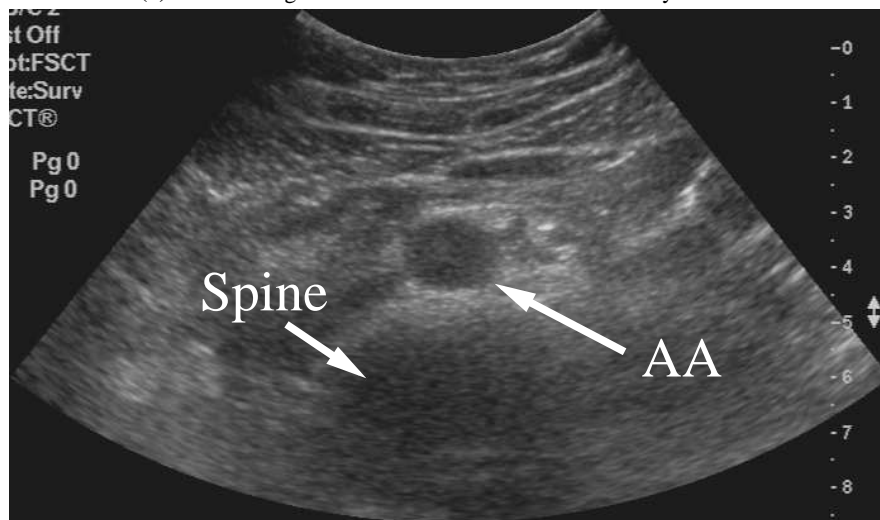
The location of bony structures over the aneurysm may also prevent clear imaging of an AAA. If the aneurysm is high up in the abdominal cavity, it may be partially obscured by the ribs, preventing a complete 3D scan of its geometry.

Subcutaneous fat may also be commonly found over the abdominal cavity. This has an adverse effect on scanning the abdominal aorta. The depth setting of the scanhead is usually increased to enable imaging of the more profoundly located vasculature. The increase in depth setting reduces the quality of imaging, an effect which is especially pronounced when using a curvilinear abdominal transducer.

The combination of bowel gas, aneurysms located high in the abdominal cavity, and subcutaneous fat meant that it was not possible to create a 3DUS scan of an abdominal aortic aneurysm (AAA). It was possible to image the aorta of some healthy volunteers (Figure 9.3). However the limited number of participants (3 in total) who were diagnosed with AAA does not enable a definitive conclusion on the suitability of 3DUS for AAA imaging to be made. An assessment of more patients diagnosed with AAA would help to determine the suitability of using 3DUS for imaging this type of arterial disease.



(a) A clear image of the abdominal aorta from a healthy volunteer.

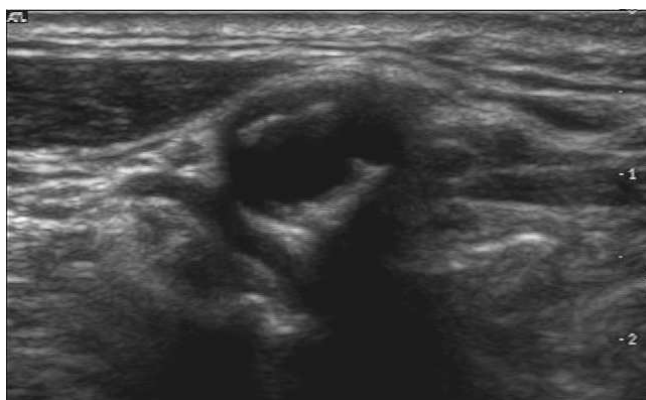


(b) Another image of the abdominal aorta, clearly showing the outline of the lumen as it runs above the spinal column.

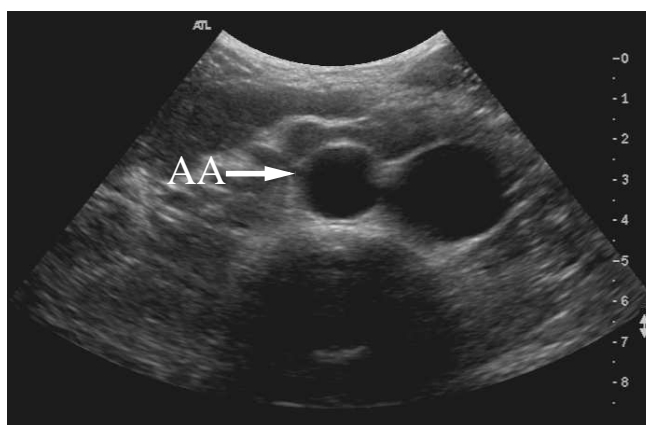
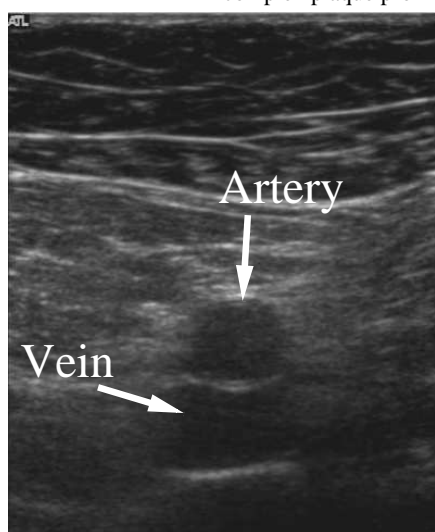
Figure 9.3: Some images of the abdominal aorta scanned from healthy volunteers.

9.3.4 Successful arterial 3DUS scanning

When the effects of bowel gas, significant subcutaneous fat and obstructing bony structures are not present, clear imaging of patient anatomy is possible. Figure 9.4 demonstrates where clear imaging in the carotid, femoral and abdominal aorta in patients and healthy volunteers has resulted in clear scans with sufficient images of the lumen to create a computational mesh model of the artery.



(a) The carotid artery of a diseased patient showing the shape of a complex plaque proximal to the carotid bulb.



(b) An image of the superficial femoral artery with the femoral vein positioned inferiorly. (c) An abdominal aorta US scan from a healthy volunteer showing a clearly defined lumen.

Figure 9.4: Various high-quality US images captured using the freehand 3DUS system.

9.4 Computational modelling of arteries

Segmentation of US images has relied mainly on manual segmentation by an expert trained in interpreting US images. The semi-automatic segmentation technique used in Chapter 6 was assessed against manual segmentation. This technique created similar lumen shapes to manual segmentation when measured using several performance metrics. This is the first time that this segmentation code has been applied to US images, demonstrating its accuracy and versatility. The task of segmentation still requires careful choice of manually-defined initial conditions, and care is also required to ensure that at areas where the shape of the lumen changes suddenly (e.g. at bifurcations and disease) the initial conditions have to be modified to prevent inaccurate segmentation.

A significant area for development is that of computational mesh generation. The registration-based mesh generation method described in chapter 7 represents the first attempts at using this method on 3DUS images. For healthy arteries, the shape of the mesh was realistic, except for the shape of the bifurcation. For diseased arteries, regions of complex plaque were smoothed out, and the bifurcation shape was not rendered realistically. This registration-based mesh generation method was shown to produce meshes feasibly from 3DUS images, but requires further development to realistically model the shape of arteries.

For the creation of diseased artery meshes, a more conventional (and more time-consuming) method using a solid modelling package is recommended. To develop the registration-based method further, more accurate idealised models of arteries are required, with development of a realistic carotid bifurcation shape a priority.

9.4.1 Summary

From the above analysis, the 3DUS based IGM system is able to produce 3D images of arterial anatomy from most patients and is limited mainly by the anatomical characteristics that prevent successful US imaging (e.g. bowel gas, excessive patient movement and bony structures obscuring arterial anatomy). The semi-automatic segmentation method used to identify the lumen shape does so successfully when compared to manual segmentation. Care should be taken to reinitialise the segmentation package at sites where arterial anatomy changes significantly such as at bifurcations or disease. 3D arterial mesh models were successfully created using a registration-based mesh generation method using the segmented 3DUS images. However this

method did not model the true shape of the carotid bifurcation or a complex atherosclerotic plaque from a patient. Improvements to mesh generation are recommended before this method is used on a larger study. The mesh models created using the mesh generation method were successfully used to simulate arterial flow in the carotid artery, producing physiological flow effects such as recirculation in the bulb and high WSS at the bifurcation flow divider and at areas of disease.

9.5 Conclusion

The 3DUS-based system for IGM was found to be as accurate as other systems in the literature. This is the only system reported that used a registration-based method of creating artery computational mesh models. The 3DUS system is limited by US imaging problems such as bowel gas, subcutaneous fat and certain types of patient anatomy which prevent imaging of some arteries. Modelling of patient-specific artery computational mesh models is feasible using the registration-based mesh generation method, but requires improvements to the shape of bifurcating artery models and the modelling of complex disease.

Chapter 10

Conclusions

This thesis contributes to the field of 3DUS imaging and image-guided modelling in the following ways:

- The first recorded application of the Stradwin 3DUS acquisition package to image-guided arterial flow modelling is described. The development work involved in characterising the Stradwin package and using 3DUS data for segmentation and flow modelling are documented.
- A method for evaluating the effectiveness of different 3DUS image registration algorithms was developed. This provides a realistic method of measuring the effect of registration by measuring the change in centreline curvature of a segmented artery geometry. This method may also be used to evaluate registration of other anatomy where probe pressure has an effect on the shape of 3D surface models created using segmented outlines of anatomical features.
- A set of metrics developed to evaluate segmentation performance [98] was applied for the first time to the segmentation of US images. This used two metrics which describe the delineation sensitivity and the delineation specificity as a means of assessing the accuracy of a segmentation. A semi-automatic segmentation technique was tested using these metrics against gold-standard manual segmentation. The precision and intra-observer variability of both segmentation techniques were also evaluated.
- The first application of a 3D computational mesh generation technique using a registered idealised geometry fitted to 3DUS data was described. The mesh generation technique was used on segmented lumen contours from bifurcating healthy and diseased arteries.
- A wall motion test phantom was developed to calculate the accuracy of a TDI-based AWM measurement technique. The wall motion test phantom is the most accurate currently described in the literature, and is capable of simulating physiological and idealised artery movement waveforms to rigorously test wall motion measurement techniques.

This thesis demonstrates the feasibility of using 3DUS-based IGM using alternative techniques to those discussed in the literature. Firstly, a different 3DUS acquisition system was used compared to other published 3DUS systems [28, 92], demonstrating that the Stradwin system can also be used for IGM applications. Secondly, a registration-based semi-automatic segmentation method was used to segment the lumen shape, which reduces the human interaction required and time taken to segment an artery geometry compared to the manual segmentation methods used elsewhere [29, 44]. Thirdly, a registration-based mesh generation technique was used to create patient-specific artery geometries in healthy and diseased arteries. This contrasts with other more time-consuming methods that require the use of a specialised surface modelling package and a user trained in surface modelling to create artery geometries [66].

Future work in this field should focus on developing mesh generation and registration for registration-based segmentation of 3DUS data. The registration-based mesh generation method did not realistically reproduce the flow patterns and WSS found *in vivo*. This was due to the shape of the idealised mesh at the point of bifurcation. The development of a more physiologically realistic method of modelling artery bifurcations would enhance the clinical utility of this IGM system. In addition, complex atherosclerotic plaques were smoothed in an unrealistic manner by the registration-based mesh generation technique. An improved method of adapting idealised mesh models to complex patient-specific artery geometries would improve the accuracy of IGM. This thesis also demonstrates the complexity of the development of an IGM system. Significant development was required to implement and evaluate a 3DUS system, perform image processing to develop a computational mesh model, and then simulate the flow field within the artery model. The research and diagnostic value of IGM would be increased by reducing the time taken and work required to move from the initial patient 3DUS scan to the creation of a patient-specific flow model.

Appendix A

Papers and conference presentations

A.1 Papers and published conference proceedings

Hammer, S. J., Jeays, A. D., Lee, W. T., Barber, D. C., Hose, D. R., Easson, W. J., Hoskins, P. R. (2008), '3D ultrasound image-guided modelling in the simulation of arterial disease', *Proceedings of the Institution of Mechanical Engineers. Part H: Journal of Medical Engineering*, in preparation.

Hammer, S. J., Jeays, A. D., Lee, W. T., Barber, D. C., Hose, D. R., Easson, W. J., Hoskins, P. R. (2007), 'A 3D ultrasound system for image guided modeling of patient-specific artery geometries', *IEEE Ultrasonics Symposium* 2469-2472.

Hammer, S. J., Dineley, J., Easson, W. J. & Hoskins, P. R. (2007), 'An arterial wall motion test phantom for the evaluation of wall motion software', *Ultrasound in Medicine & Biology* **33**(9), 1504–1511.¹

Hammer, S. J., MacGillivray, T. J., Lee, W. T., Beech-Brandt, J. J., Easson, W. J. & Hoskins, P. R. (2006), 'Issues in 3D ultrasound scanning affecting arterial CFD simulation', *Journal of Biomechanics* **39**(Supplement 1), S616.

Hammer, S. J., Beech-Brandt, J., Chen, C., Poepping, T. L., Easson, W. J. & Hoskins, P. R. (2003), Design and development of a 3D ultrasound phantom scanner, in '25th Annual Conference of the IEEE Engineering in Medicine and Biology Society' **2**, 1184–1187

A.2 Conference presentations and posters

Hammer, S. J., Lee, W. T., Easson, W. J., Hoskins, P. R. (2007), A 3D ultrasound system for image-guided modelling of arteries., in '39th Annual Scientific Meeting of the British Medical Ultrasound Society', Vol. 15, Maney Publishing, Manchester, UK.

¹This publication is based on Chapter 8 of this thesis and is available online at <http://dx.doi.org/10.1016/j.ultrasmedbio.2007.04.005>

Hammer, S. J., Jeays, A. D., Hose, D. R., Barber, D. C., Hoskins, P. R. (2007), Evaluation of Registration-Based Segmentation of 3D Arterial Ultrasound, *in* '39th Annual Scientific Meeting of the British Medical Ultrasound Society', Vol. 15, Maney Publishing, Manchester, UK.

Hammer, S. J., Lee, W. T., Macgillivray, T. J., Beech-Brandt, J. J., Easson, W. J. & Hoskins, P. (2006), Issues in 3D ultrasound scanning affecting arterial CFD simulation, *in* 'World Congress of Biomechanics', Vol. 39 Supplement 1, Elsevier, Munich, Germany, p. S616.

Hammer, S. J., Macgillivray, T. J., Beech-Brandt, J. J., Easson, W. J. & Hoskins, P. (2005), 3D ultrasound to 3D blood flow using image guided modelling., *in* '37th Annual Scientific Meeting of the British Medical Ultrasound Society', Vol. 13, Maney Publishing, Manchester, UK, p. 272.

Hammer, S. J., Easson, W. J. & Hoskins, P. (2005), Vascular imaging using 3D ultrasound, *in* S. Sherwin, ed., 'Second Physiological Flow Meeting: Cardiovascular haemodynamics and modelling', eScience Centre, Edinburgh, UK.

Hammer, S. J., Dineley, J., Easson, W. J. & Hoskins, P. (2004), Development of a tool for accuracy checking of arterial wall motion measurement., *in* '36th Annual Scientific Meeting of the British Medical Ultrasound Society', Vol. 12, Maney Publishing, Manchester, UK, p. 246.

Hammer, S. J., Dineley, J., Easson, W. J. & Hoskins, P. R. (2004), An arterial wall motion test tool to assess Philips wall motion software, *in* 'Third International Conference on the Ultrasonic Measurement and Imaging of Tissue Elasticity', Lake Windermere, Cumbria, UK.

Hammer, S. J., Beech-Brandt, J., Chen, C., Poepping, T. L., Easson, W. J. & Hoskins, P. R. (2003), Design of a 3D ultrasound scanner for image guided modelling of in-vitro flow models, *in* '35th Annual Scientific Meeting of the British Medical Ultrasound Society', Harrogate, UK.

Hammer, S. J., Beech-Brandt, J., Chen, C., Poepping, T. L., Easson, W. J. & Hoskins, P. R. (2003), Development of a 3D ultrasound phantom scanning system, *in* 'IPEM The Physics and Technology of Medical Ultrasound Biennial Meeting', York, UK.

Appendix B

Manually segmenting ultrasound data using Analyze

Analyze (AnalyzeDirect Inc., KS, USA. <http://www.analyzedirect.com>) is a fully-featured medical image processing and analysis package. It is designed to process many different types of medical image from most modalities. It features several useful manual segmentation tools that were used to create the “gold standard” manual segmentations used in chapter 6.

Manual segmentation using Analyze is more difficult than using the simple segmentation tools included with Stradwin. However, Analyze allows the user to copy the segmentation from the previous image to the current image, maintaining continuity with the rest of the segmented images in the dataset. The segmentation tools provided with Stradwin are more basic and cannot be exported from Stradwin into other formats as easily. The user interface of Analyze is also more powerful than that of Stradwin for segmentation, giving the user more flexibility to modify the segmented contour.

Step by step runthrough

The following set of steps are required for using Analyze with Stradwin files:

- Write all Stradwin images to a sequence of bitmap files
- Load the images into Analyze
- Create an Object Map
- Use the spline tool to outline the lumen
- Save the Object Map as a series of bitmap images
- Convert the bitmap images to a Stradwin image file
- Threshold the images in Stradwin to produce spatially registered 3D contours.

B.1 Write all Stradwin images to a sequence of bitmap files

The Stradwin file required for segmentation should be opened in Stradwin. To export frames from Stradwin, the command “File→Export frames...” should be used. A range of images should be selected (typically 0:N, where N is the highest frame number in the frame counter on the bottom of the Stradwin window) and a location to save the files should then be chosen. “Windows Bitmap” should be chosen in the “Save as type:” field that appears in the file box.

The numbering of the exported frames should be changed using XnView (<http://www.xnview.com/>) or a similar graphics program to ensure that leading zeroes are added to the image file names. Appendix C contains instructions on how to do this.

B.2 Load the images into Analyze

The Analyze program should then be opened. The window shown in figure B.1 should be visible. Then the Import/Export program should be opened (use File→Import/Export...) (figure B.2). The Volume tool (Tools→Volume tool...) should then be opened. With the volume tool, a list of graphic files or other 3D file format files for import into Analyze may be selected. The “Wild Cards” button brings up a file dialog where a directory of images can be chosen (figure B.3). Pressing the “Load” button will load these into the Analyze workspace as a volume file. An icon should appear on the main Analyze window that represents this data. Once this is done, the Volume Tool and Import/Export windows can be closed.

Now that the data is loaded into the Analyze workspace, it is advisable to save it. “File→Save as...” should be used, and a location chosen to save the file (figure B.4).

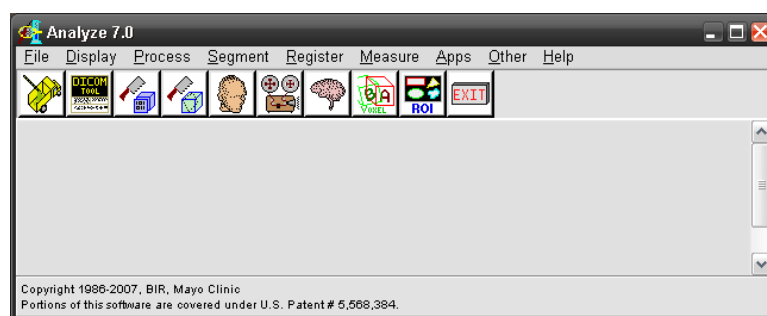


Figure B.1: *The Analyze main screen. All other functions are available from this window.*

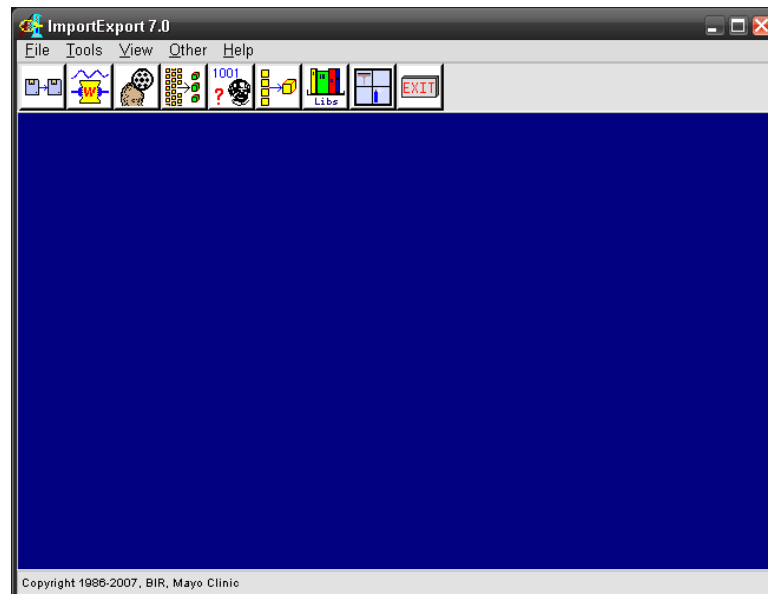


Figure B.2: *The Import/Export tool used to load files of various formats into Analyze.*

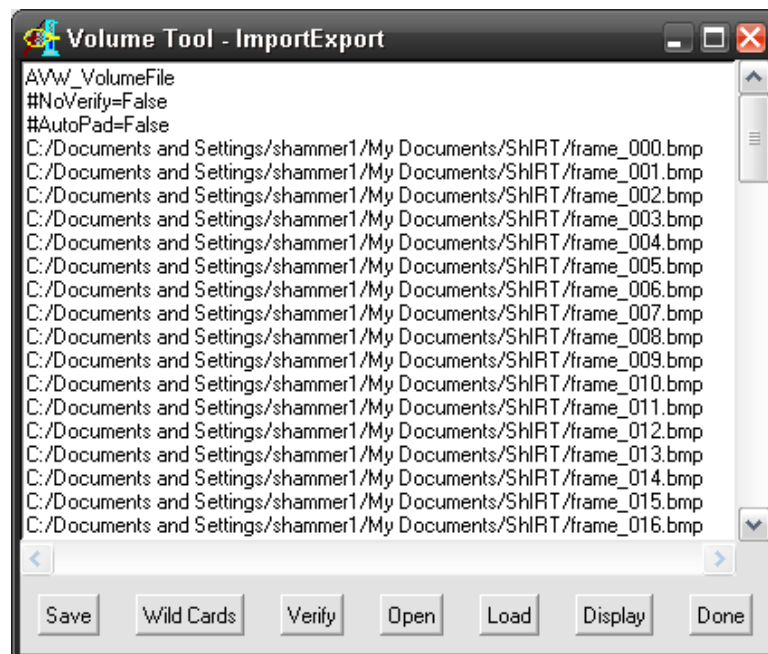


Figure B.3: *The Volume tool, used to load bitmap files into Analyze.*

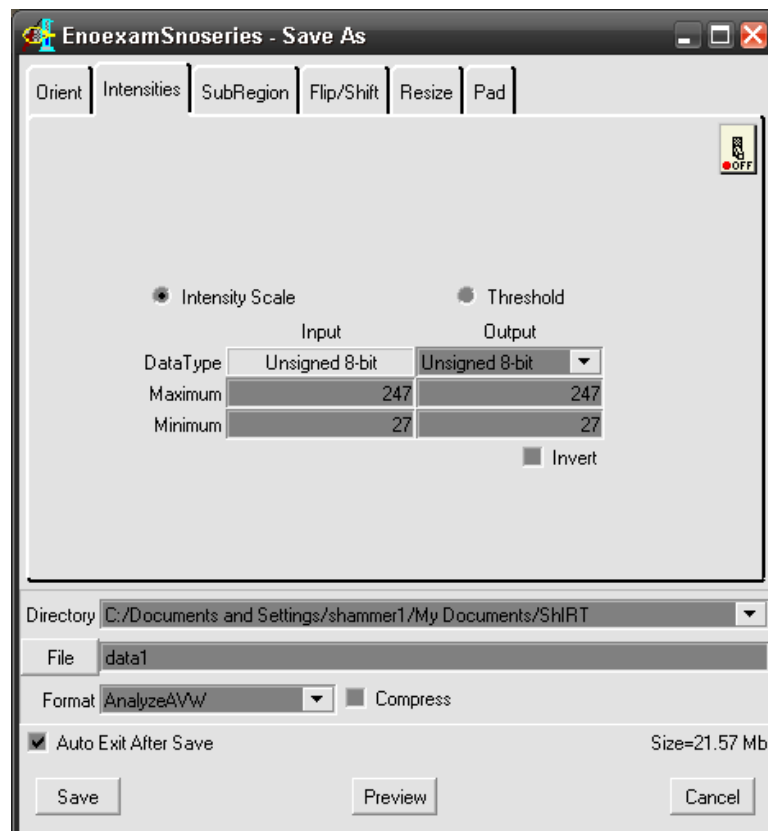


Figure B.4: The Save As... window.

B.3 Create an Object Map

An object map is the filetype used in Analyze to define the location of segmented contours on the ultrasound images. The segmentation program (Segment→Image Edit...) can be used to define an object map and change it for every image of the ultrasound dataset. To do this, the “Change” radio button on the bottom left of the Image Edit window (figure B.5) should be set to “Object Map”. A new object map may be defined by selecting File→Create Object Map (figure B.7). This should be given a meaningful name such as “CommonCarotid”. It is helpful to increase the size of the displayed image. “View→Size...” may be used to increase the displayed size of the image. Increasing the image size will slow down the display of images.



Figure B.5: The Image Edit window.

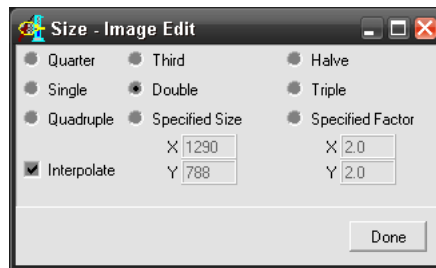


Figure B.6: *The Image Size window.*

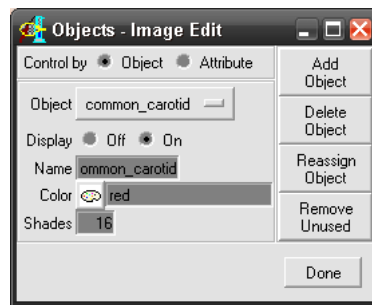


Figure B.7: *The Objects window. Here the name of the current Object Map may be defined, a new Object Map may be created or a currently loaded Object Map may be removed.*

B.4 Use the spline tool to outline the lumen

To segment the dataset a shape should be drawn outlining the lumen using the spline tool (figure B.8). A delayed fill (the icon with a paint can with a clock face next to it) should be placed in the centre of the spline once it has been closed. Once this has been done, the “Apply & Advance” button should be pressed to save the segmented spline to the object map and move to the next image. The spline from the previous image is moved to the next image and can be moved around or modified to suit the new image. The object map should be saved frequently during segmentation.

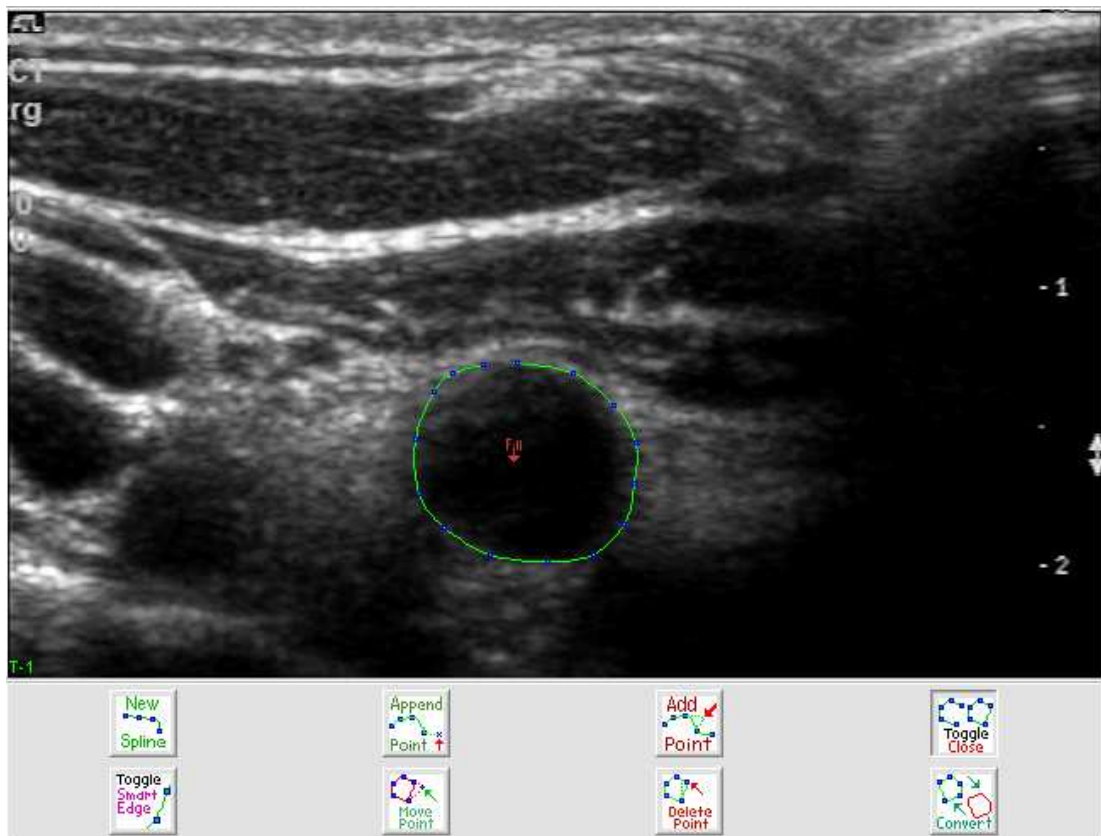


Figure B.8: *The Spline Tool. The various buttons below the image allow the user to add or remove spline points and move spline points around to suit the image. The “Fill” in the centre of the spline is a delayed fill which will fill in the spline outline once the “Apply & Advance” button has been pressed.*

B.5 Save the Object Map as a series of bitmap images

To spatially reconstruct the segmented splines they will have to be imported into Stradwin. To do this the object map will need to be exported as a bitmap file. In the main Analyze window “File→Save as...” should be selected, which opens the window shown in figure B.9. “BMP” should be selected from the Format pull-down menu. Analyze should now save the object file as a set of bitmap images in the directory specified in the “Directory” box.

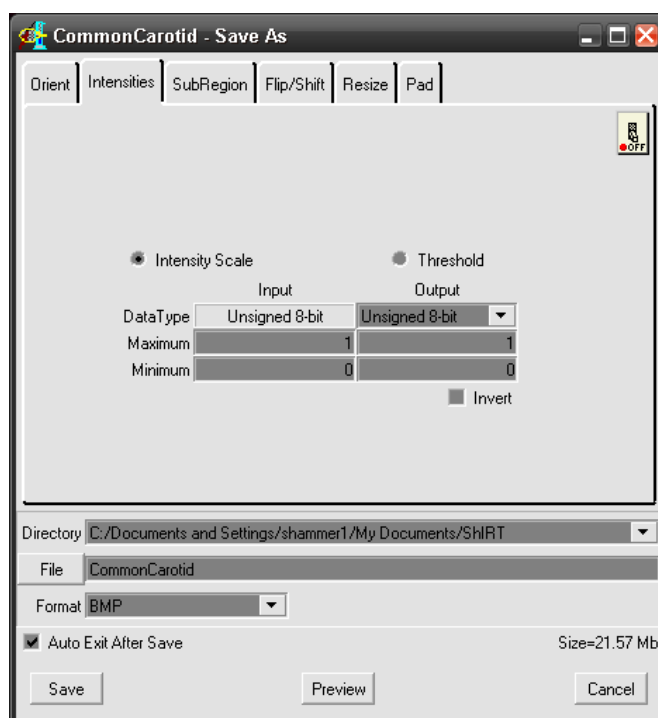


Figure B.9: Save the object map as a series of bitmap images.

B.6 Convert the bitmap images to a Stradwin image file

This step is covered in appendix C. The bitmaps may have to be converted (again using XnView or similar) from the RGB colour space to 256 shades of grey. This can be done using the Sequence Convert function of XnView.

B.7 Threshold the images in Stradwin to produce spatially registered 3D contours

Once valid .sxi and .sw files have been created, the images should be thresholded in Stradwin to produce spatially registered contours. The .sw file should be loaded into Stradwin. The “Draw” task pane should be shown, and the “Use threshold sliders” checkbox selected. The thresholds should be changed so that the filled blob is outlined in pink in every image. As there is no fully automatic threshold segmentation yet available in Stradwin, the user has to move through all the images and click the mouse on the centre of each blob. Stradwin should then draw a contour around the blob (figure B.10). This should be done until every blob is segmented. To save time, it is possible to click on the blob to segment it and use the PageUp or PageDown keys to move

through the images after each click.

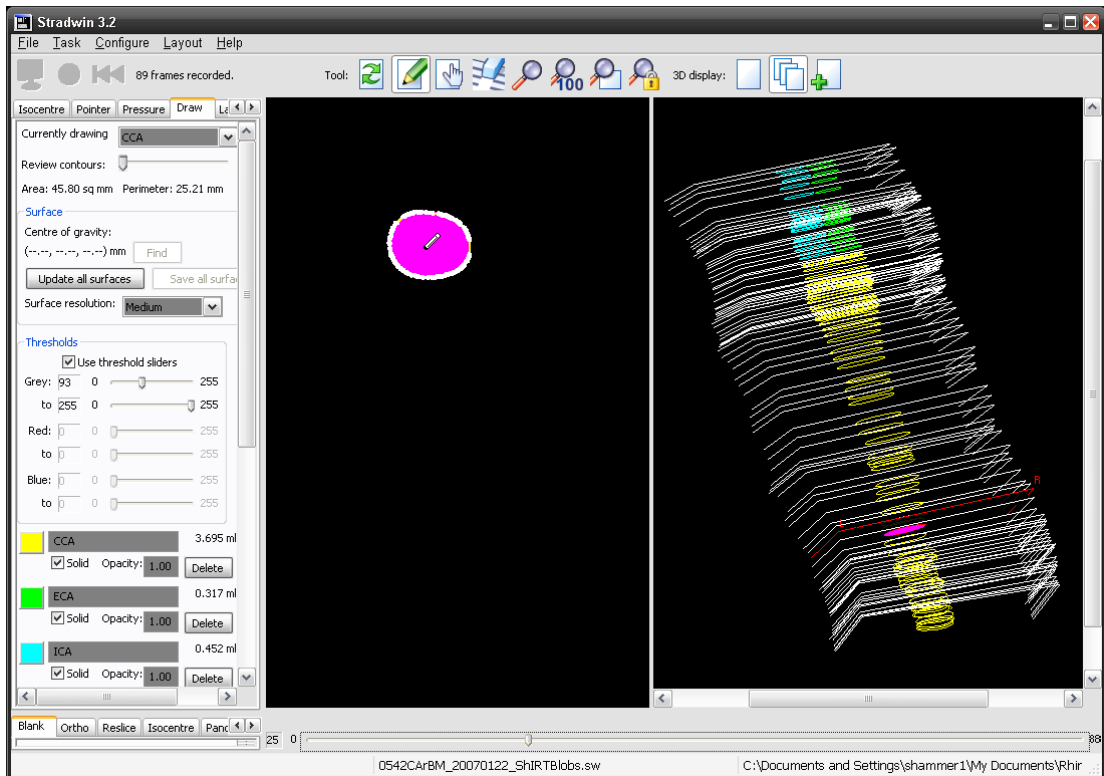


Figure B.10: *Thresholding segmented blobs using Stradwin*

Appendix C

Generating a Stradwin image file from a series of bitmap graphics files

A Stradwin image file (.sxi) often has to be made from a series of bitmap (.bmp) graphics files. This appendix shows how to create a .sxi file from a series of sequentially numbered bitmaps using “BMP2SXIarray.vi” (see Appendix F, section F.2 for documentation of this program).

Step by step runthrough

The following steps are required:

- Save a series of sequentially numbered bitmaps
- Renumber the images if required using XnView
- Run BMP2SXIarray.vi to create a Stradwin image file
- Modify the Stradwin header file (.sw) to suit the new image file.

C.1 Save a series of sequentially-numbered bitmaps

Analyze and ShIRT can save a sequentially-numbered series of bitmap files. Appendix B gives an explanation of how to do this using both programs.

C.2 Renumber the images if required using XnView

If the bitmaps are either numbered incorrectly or are of the wrong type, XnView (<http://www.xnview.com/>) may be used to change them. The bitmaps should be numbered using a format such as `image_###.bmp` with a minimum of three numerals. There should be leading zeroes in each filename where applicable. For example,

```
image_0.bmp  
image_1.bmp  
image_2.bmp  
:  
image_10.bmp
```

is not acceptable, whereas

```
image_000.bmp  
image_001.bmp  
image_002.bmp  
:  
image_010.bmp
```

is acceptable.

In XnView the “Sequence Convert” (Tools→ Sequence Convert...) command can change the numbering of the image sequence and also convert the image to 256 colour greyscale.

C.3 Run BMP2SXIarray.vi to create a Stradwin image file

“BMP2SXIarray.vi” (figure C.1) should be used to convert all the bitmap files in a chosen directory into a Stradwin image file. Note that colour/power Doppler bitmap images can also be converted into .sxi files. The resulting file is placed in the directory of bitmaps with the same name as the directory.

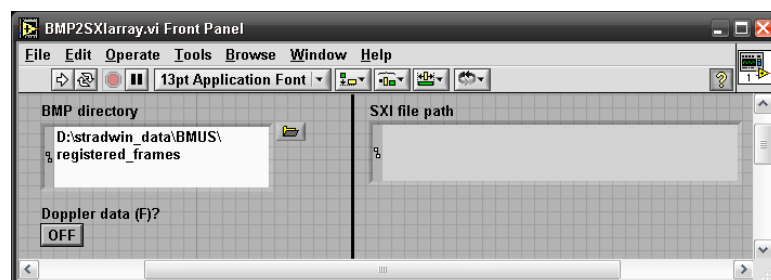


Figure C.1: The front panel of “BMP2SXIarray.vi”

C.4 Modify the Stradwin header file (.sw) to suit the new image file.

To use the image file with Stradwin, a header (.sw) file is required. If a header file from another acquisition is to be used, the RES_BIN_IM_FILENAME resource in the .sw file will need to be changed to match the newly created .sxi file. A text editor such as Windows NotePad or XEmacs (<http://www.xemacs.org>) may be used to modify this value. Once this has been done, double-clicking on the .sw file should open both files in Stradwin.

Appendix D

Development of surface models of bifurcating arteries using Rhino

D.1 Introduction

This appendix contains a step-by-step runthrough of how artery surface models were created using the Rhino solid modelling package. This is the technique used to create the geometries shown in chapter 7 on page 133.

D.2 Importing segmented points into Rhino

The segmented contours from the Stradwin file must be converted into an OBJ file using “SW create OBJ file from segmented file.vi” (figure D.2). Optionally, the centre points of each segmented contour may be imported as an .xyz file using “SW create XYZ file from segmented file.vi” (figure D.2). This allows a centre line to be created which clearly shows misregistered segments. More information about these LabVIEW Virtual Instruments can be found in Appendix F, section F.3.3.

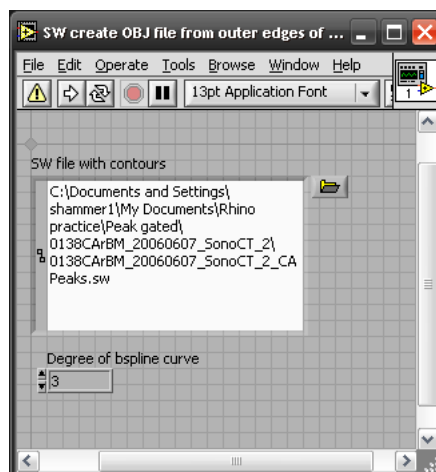


Figure D.1: *SW create OBJ file from outer edges of contours.vi*

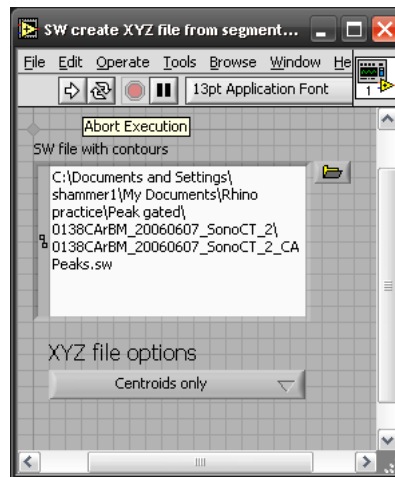


Figure D.2: SW create OBJ file from segmented file.vi

The command “File→Import...” in Rhino must be used to import each of the files that are created. One VI creates a Wavefront Object file from the outer edges of the segmented artery. The other creates an ASCII points file (.xyz) with positions of the centrelines of the artery segments. The two files should be imported into different layers (figure D.3).

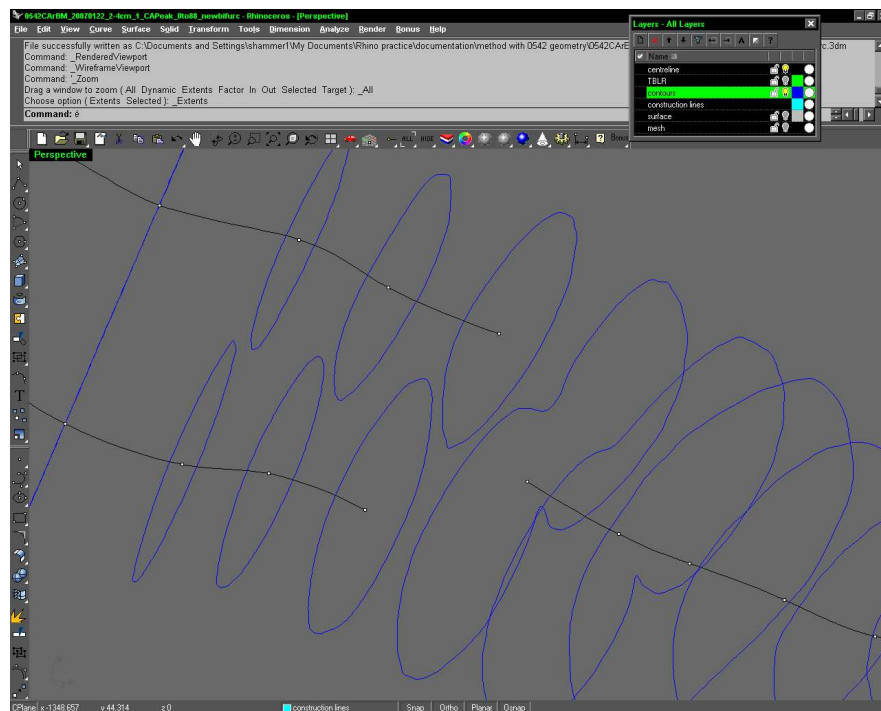


Figure D.3: OBJ and XYZ files imported onto different layers. The OBJ file is imported to “contours” and the XYZ file to “centrelines”

D.3 Rebuilding the segmented contours

By default, the points defining the outline of the artery are converted to an OBJ file by fitting a curve of degree one through them. The contours should be rebuilt with degree 3 curves before meshing. This is done by selecting the contours and using the “Rebuild” command (figure D.4). A point count of 80 or more should be used.

Once the “Rebuild” command has been issued on all the contours, the “Smooth” command should be used to smooth each contour (see figure D.5). The following settings give the best results:

- Smooth X, Y and Z
- “World Coordinates” checked
- “Smooth factor” set to 0.5.

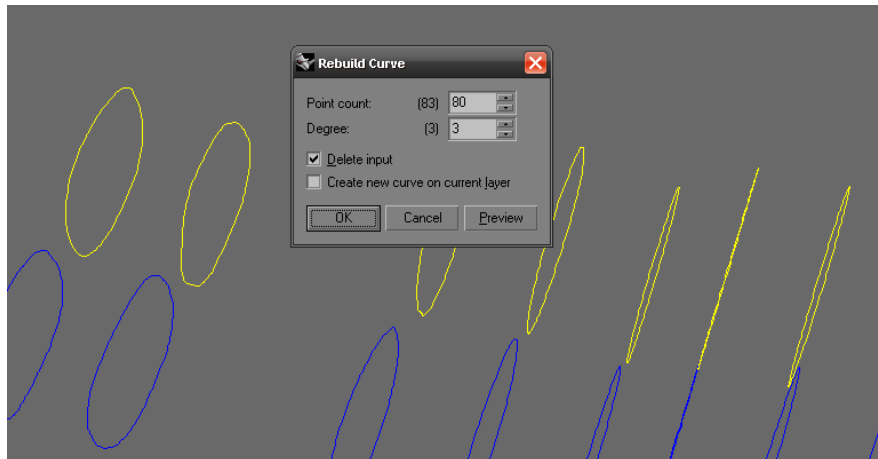


Figure D.4: Rebuilding the imported OBJ file contours using the “Rebuild” command.

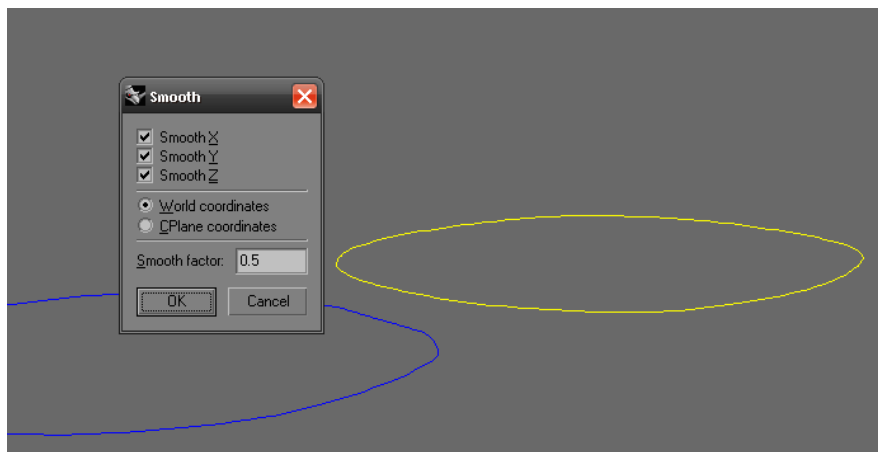
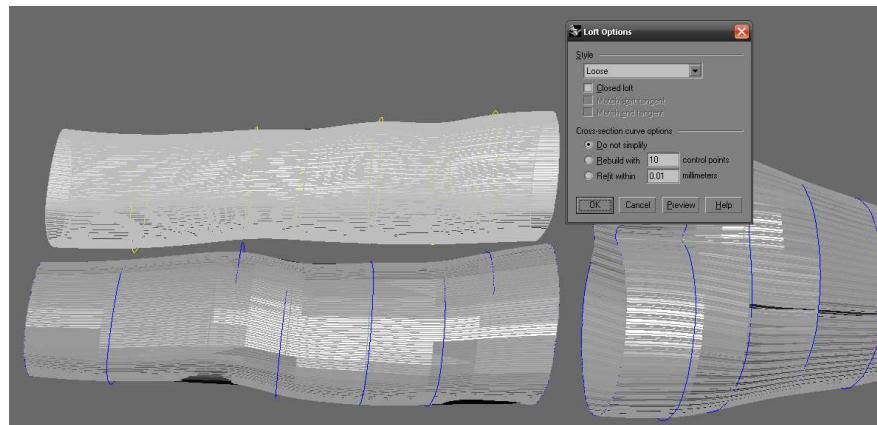


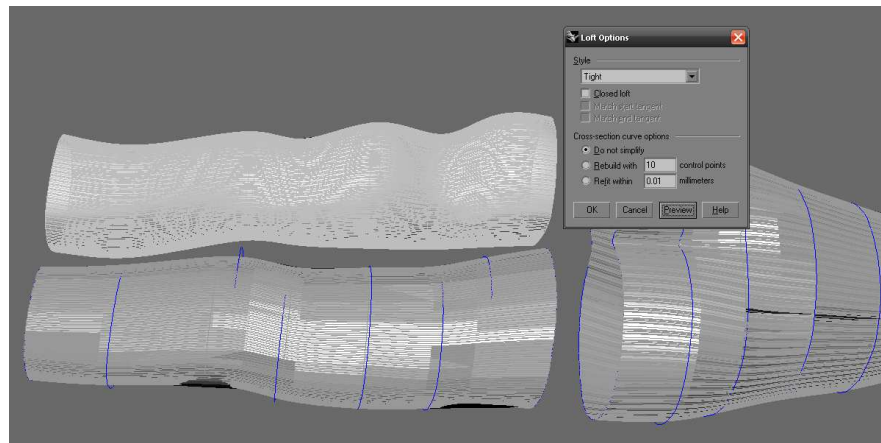
Figure D.5: Smoothing the imported OBJ file contours using the “Smooth” command.

D.4 Removing misregistered contours

It will be obvious from an inspection of the location of the contours and the smoothness of curvature of the centrelines that some contours may be misregistered. These may be removed by selecting them and deleting them. The centreline points corresponding to any deleted curves should also be deleted, and the curve should be redrawn (using the CurveThroughPt command) without the deleted points.



(a) Loose lofting



(b) Tight lofting

Figure D.6: Two methods of lofting the artery contours, showing the effect of loose lofting compared to tight lofting. The newly lofted artery section is shown at the top of each image in light grey with the artery contours highlighted in yellow.

D.5 Lofting the CCA/ICA/ECA

The CCA, ICA and ECA should be lofted separately using the “Loft” command. The “Loose” option gives the smoothest contours for unregistered data. The effect of this option may be compared to the “Tight” option to see its effect on the smoothness of the surface (see figure D.6). “Do not simplify” should be selected in the “Cross-section curves options” section of the “Loft Options” dialog box. There will be a gap in between the three vessels corresponding to the root of the bifurcation. This will be filled in manually next.

D.6 Filling the bifurcation area

D.6.1 Extracting wireframes from the lofted artery sections

First, the “ExtractWireframe” command should be used to extract the wireframe component of the three surfaces of the ICA, ECA and CCA (see figure D.7). The following commands should be used to create three short sections as shown in this image:

- The “ExtractWireframe” command should be used on each artery section.
- The “Split” command should be used to trim the lower parts of the vertical wireframes from the longer upper parts. This makes the wireframes easier to move and makes navigation of the model easier.
- Each set of wireframes corresponding to each section of the artery should be grouped by selecting the wireframes and using the “Group” command (Ctrl+G).

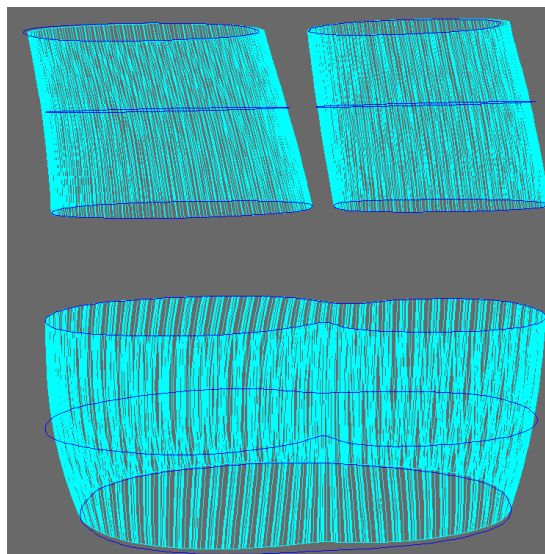


Figure D.7: Using “ExtractWireframe” to form the shape of the three lofted arteries.

D.6.2 Connecting wireframes using interpolated curves

After this, several of the upper ECA and ICA wireframe curves should be connected to the lower wireframes of the CCA section using interpolated curves (“InterpCrv”) (figure D.8). These will look like straight lines when first created. To change their curvature to match the general

shape of the upper and lower sections, the “Match” command should be used (see figure D.9). Curvature or Tangency matching give the best results.

It is helpful to group each set of interpolated curves after they have been created. This makes it easier to hide them when working on other parts of the geometry.

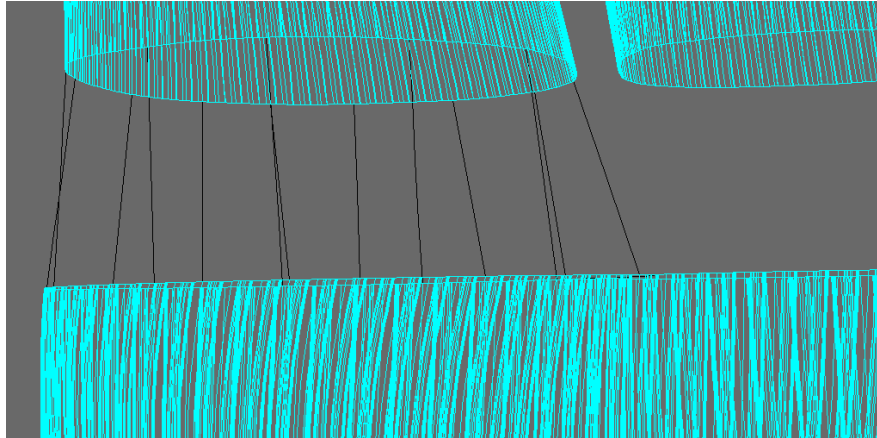


Figure D.8: *Joining the upper and lower wireframes using the “InterpCrv” command.*

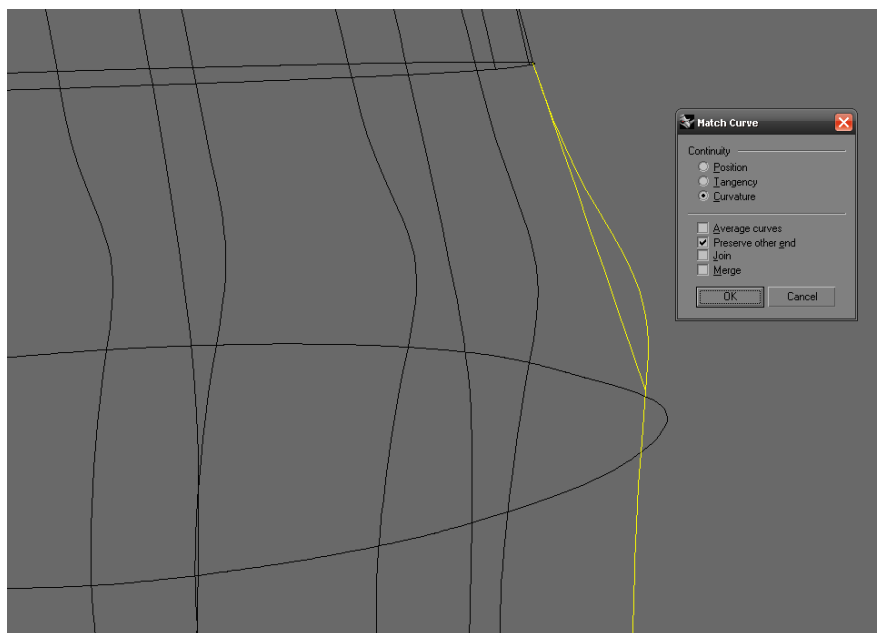


Figure D.9: *Matching the curvature of the interpolated curves using the “Match” command.*

D.6.3 Creating a network surface between the upper part of the CCA and the ECA/ICA

The upper planar extracted wireframe of the CCA section of the artery should be split using the interpolated curves drawn in section (D.6.2). An interpolated curve should be drawn between the two ends of the cut section which corresponds to each side. The “Match” command should be used to match the curvature of the interpolated curve to the two ends of the planar section (figure D.10). The middle section of this curve should start at the centre of the curve corresponding to the centre of the bifurcation at the top of the CCA. If this starts anywhere else, the shape of the bifurcation will not be clearly defined. The interpolated curve should be joined to the other curve using the “Join” command. A network surface (“NetworkSrf”) can then be created using the upper and lower planar curves and the interpolated curves in between (see figure D.11). This should be done for both the ECA and the ICA.



Figure D.10: *Creating the upper curve that creates the start of the bifurcation outline at the top of the CCA.*

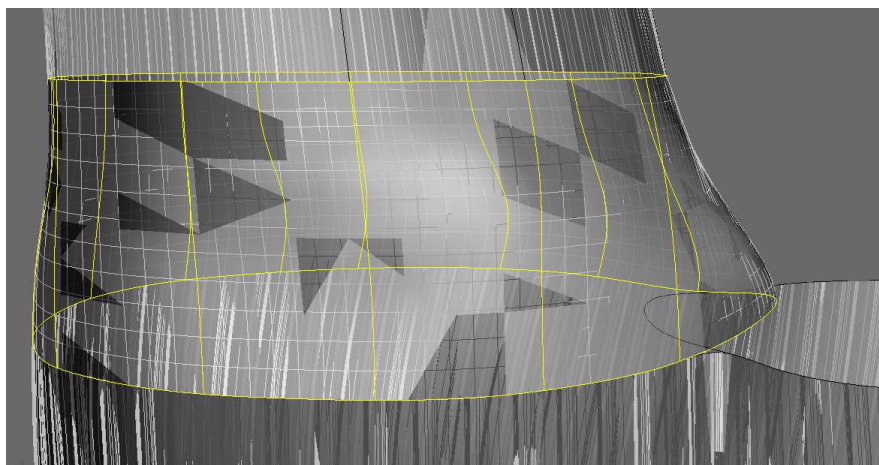


Figure D.11: *Creating a network surface to match the top of the CCA to the bottom of the ECA.*

D.6.4 Splitting the bifurcation segments

An overlapping pair of surfaces should now be left (figure D.12). The Split command (“Split”) may be used to remove the overlapping section of the bifurcation (figure D.13).

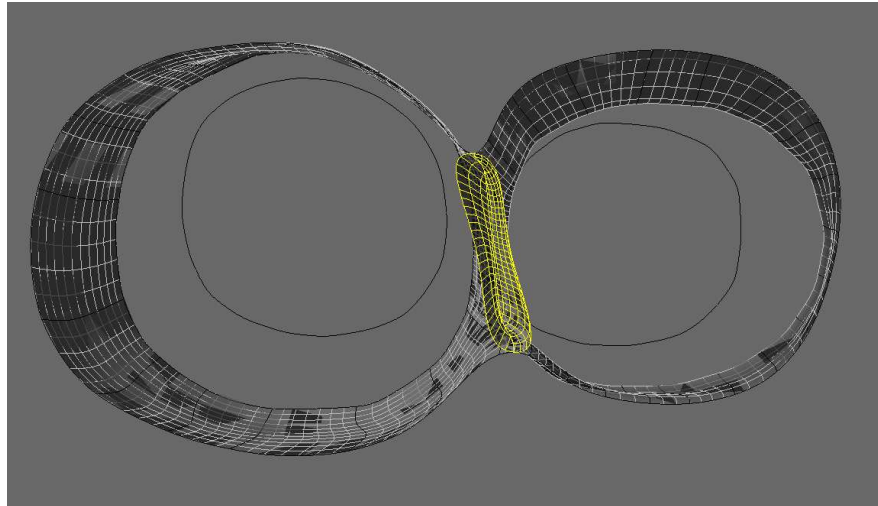


Figure D.12: *The bifurcation region before splitting.*



Figure D.13: *The bifurcation region after splitting.*

D.6.5 Creating a smoothed bifurcation surface

An approximate shape of the bifurcation has now been sketched out due to the overlap of the two extensions added to the ICA and ECA lofted surfaces. This needs to be smoothed to produce realistic flow patterns in this area. Firstly, the wireframes should be extracted from the

two overlapping surfaces (figure D.14).

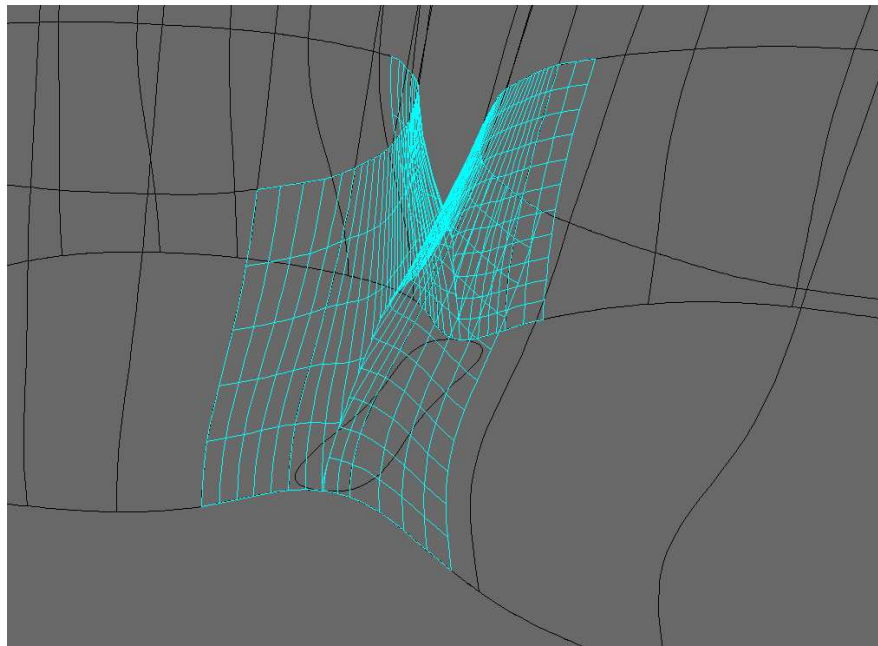


Figure D.14: *Extracted wireframes on the bifurcation region.*

After this, interpolated curves (“InterpCrv”) will need to be drawn between the two sides of the extracted wireframes. These should correspond to the positions of the horizontal lines on each side. The “Match” command should be used to match the curvature of the new lines to the curvature of each side of the bifurcation (see figure D.15). This should be done all the way along the bifurcation. The “InterpCrvOnSrf” command should be used to connect these lines together. The surfaces at each side should be selected in turn to draw the line onto. The end points of the middle bifurcation lines should be connected using this command (see figure D.16). This command ensures the curvature of the line connecting the lines in the middle of the bifurcation matches that of the surfaces at each side.

Once the two side rails of the bifurcation are drawn, a network surface (“NetworkSrf”) should be created using the bifurcation central lines and the two side rails (figure D.17).

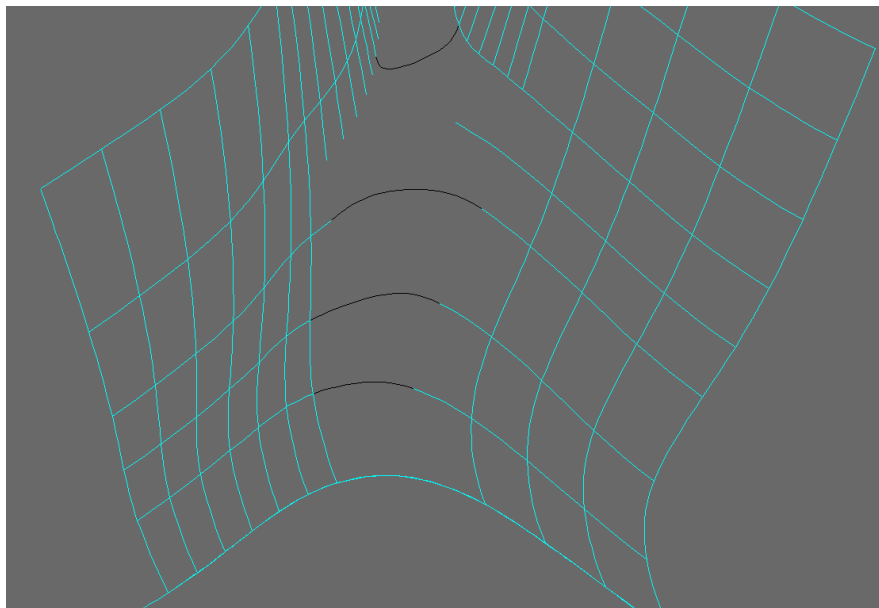


Figure D.15: *Matched interpolated curves that will make up the shape of the bifurcation surface.*

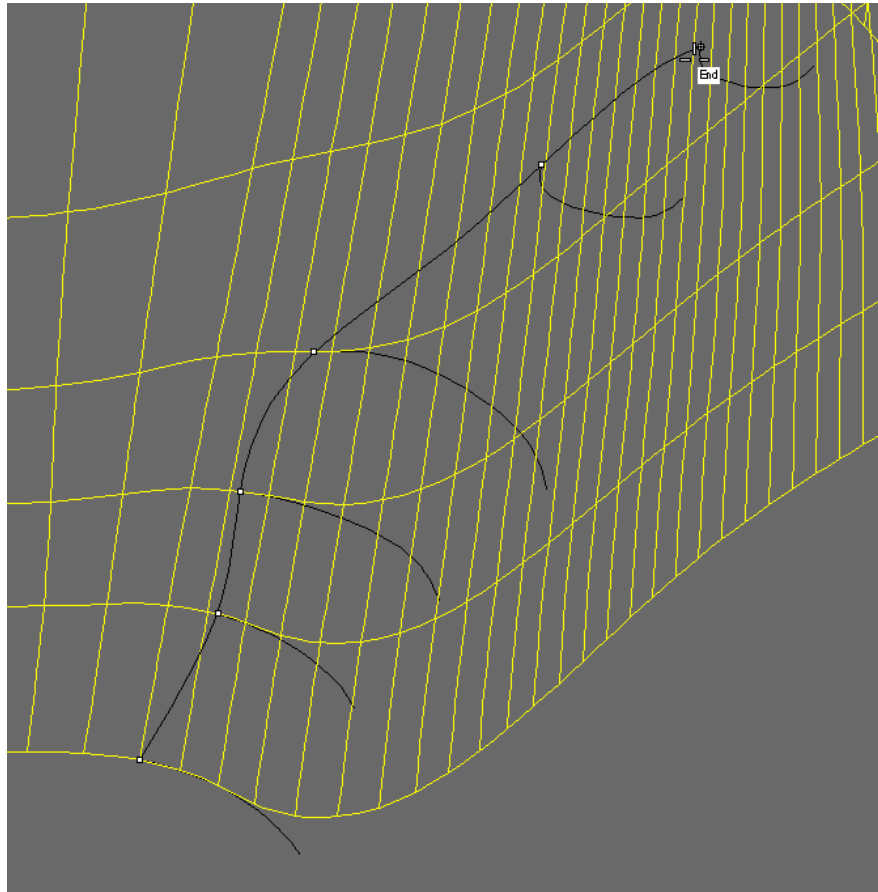


Figure D.16: *Joining the central bifurcation lines with the “InterpCrvOnSrf” command. The line is endpoint connected to the central lines.*

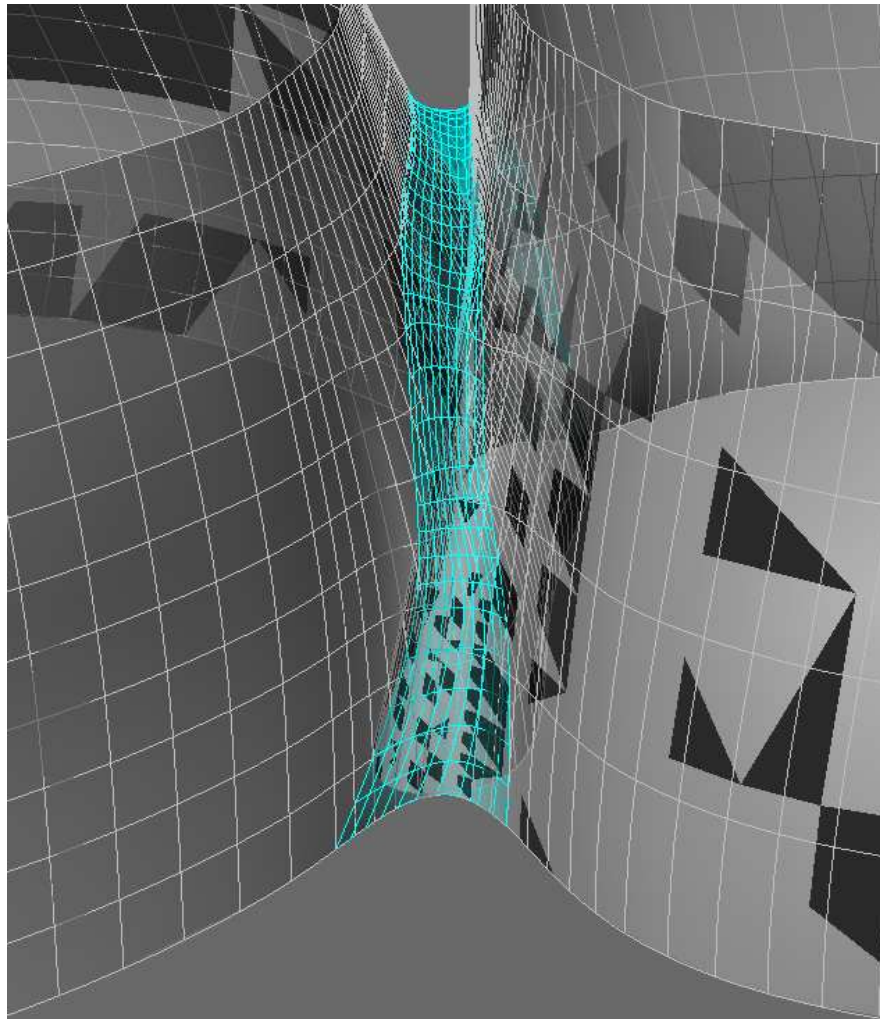


Figure D.17: *The surface which will become the region joining the two side sections of the bifurcation.*

D.6.6 Splitting and joining the bifurcation surfaces

The “Split” command should be used to divide the side surfaces of the bifurcation using the two rail curves that made up the sides of the bifurcation central region surface (figure D.18). The two small inner surfaces that are left should be deleted. The three surfaces that remain should be joined using the “Join” command. If the interface between the bifurcation network surface and the other surfaces appear prominent, the “MatchSrf” command should be used to adapt the curvature of each side of the bifurcation surface to the other surfaces (figure D.19).

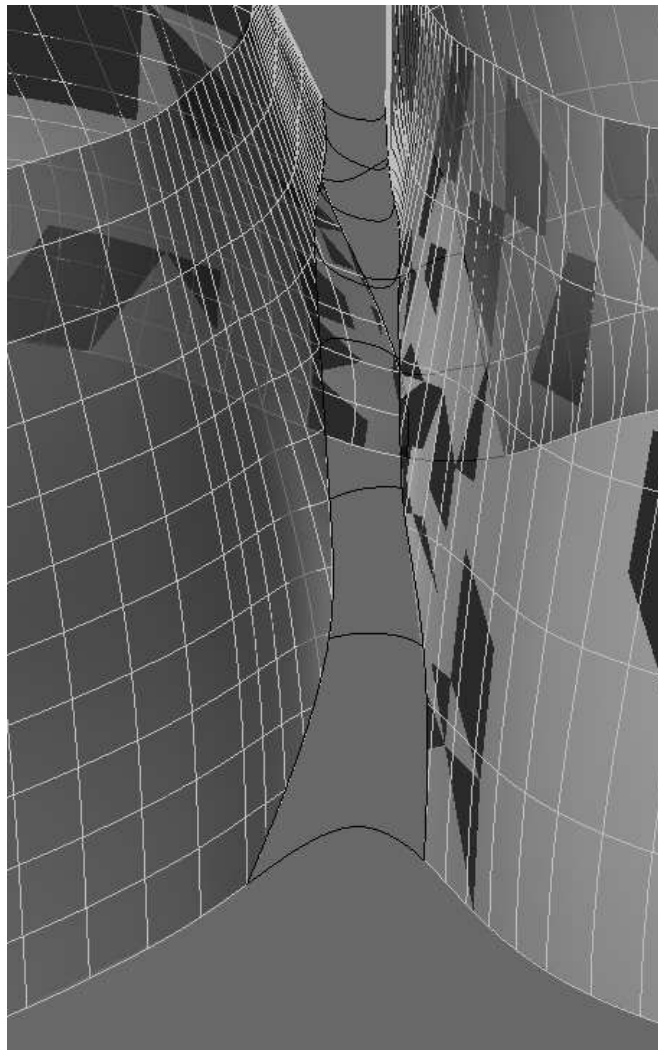


Figure D.18: *Using the side rail curves of the bifurcation to split the side surfaces.*

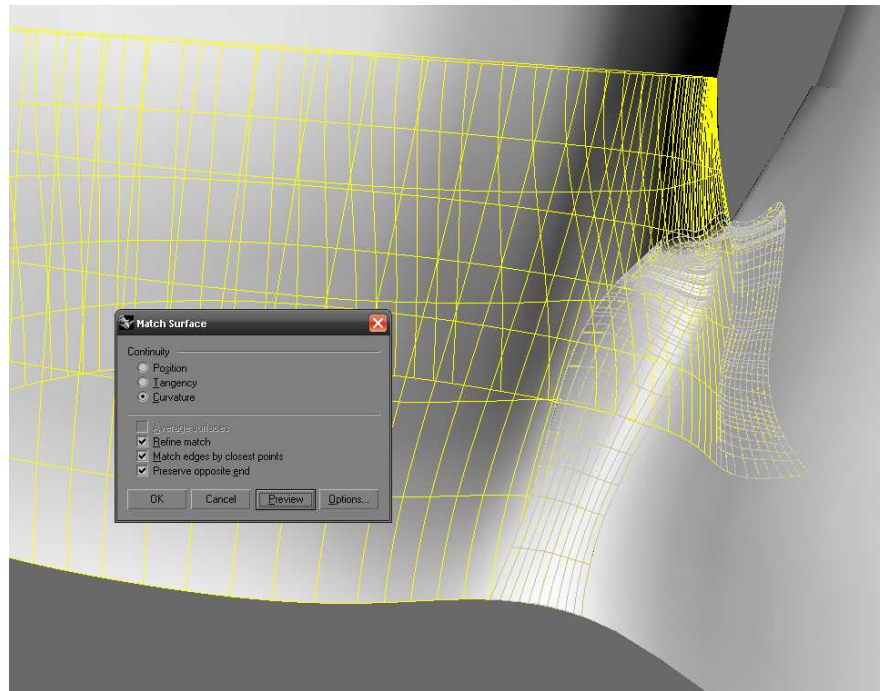


Figure D.19: Matching the curvature or tangency of the bifurcation surface using “MatchSrf”.

D.6.7 Tidying and checking the mesh

The “MatchSrf” command should be used to ensure the curvature of the separate surfaces are the same if required. “Zebra” should be used to map zebra stripes to the surface to find discontinuities in the surface (figure D.20). Any surfaces that are not smooth enough or do not appear correct should be recreated.

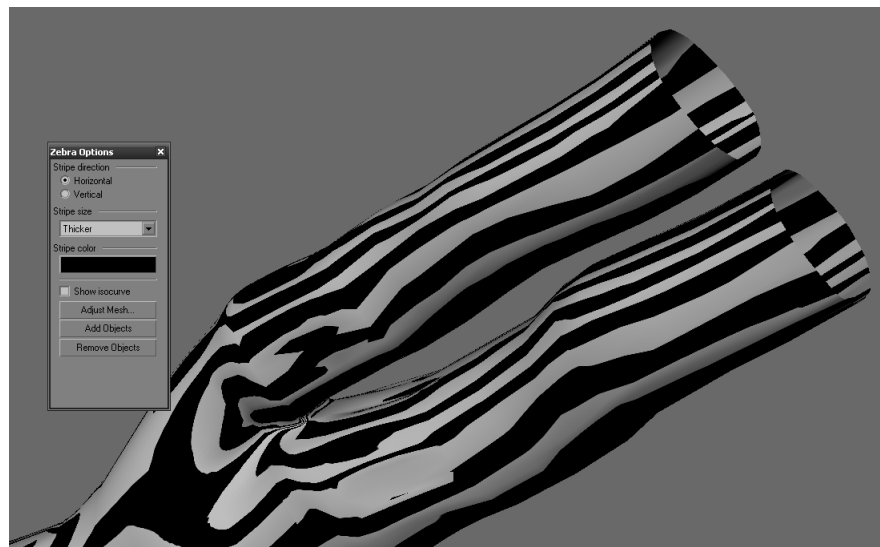


Figure D.20: *Checking the curvature and the continuity of the surface sections using “Zebra”.*

D.6.8 Joining all the surfaces

Planar surfaces should be created at the ends of the artery (“PlanarSrf” command). These make the geometry watertight for forming a valid STL file later on. All of the surfaces should be joined together. The consistency and curvature can be checked using the “Zebra” command.

D.7 Meshing the geometry and exporting it to STL

The “MeshSrf” command should be used to create a mesh using the surface model that has been created. The mesh should be selected, then the “Export” command should be used to export it to an STL file for further processing using Materialise Magics (see figure D.21).

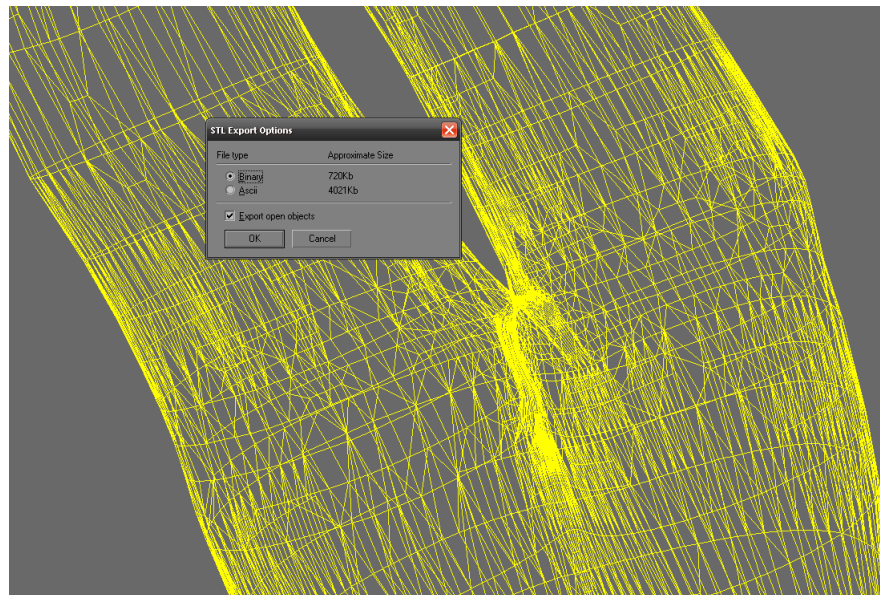


Figure D.21: *Exporting the created mesh to an STL file. The “Export open objects” option should be used in case the surface mesh is not fully closed.*

Appendix E

Remeshing STL files with Materialise Magics

Materialise Magics (Materialise NV, Leuven, Belgium. <http://www.materialise.com>) is a powerful mesh editing tool used throughout the rapid prototyping industry. It is also widely used to edit mesh files for import into CFD and FEA simulations. Many CAD or solid modelling packages can produce mesh files using the STL format. However these mesh files are frequently not tidy enough for successful import into CFD packages such as Fluent. The following problems are routinely encountered in mesh files generated in this way:

- Overlapping triangles
- Sharp and very small triangles
- Inverted normals (sections of the model are inside out)
- Fine mesh, leading to an unwieldy file size that is too large to import.

Materialise Magics can solve many of these problems with its sophisticated mesh editing tools. This appendix contains a brief run-through of how to edit a mesh file created in Rhino to allow successful import into GAMBIT, the pre-processor of the Fluent CFD package.

E.1 Create a solid model in Rhino and export it as an STL file

This step is covered in appendix D.

E.2 Load the STL file into Magics

In Magics, the *File*→*Import...* command should be used to load the STL mesh file created in Rhino. The mesh file should appear in the main window of Magics.

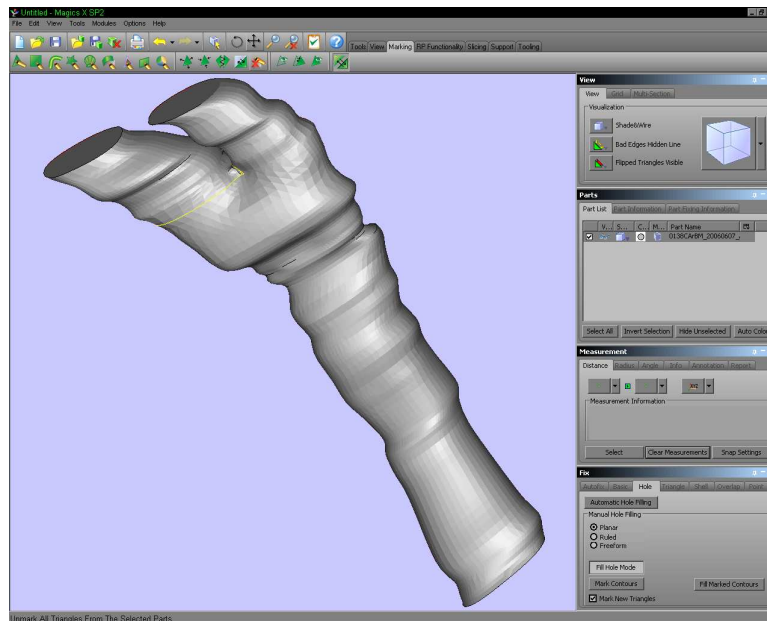


Figure E.1: Importing the STL file into Magics

E.3 Automatic fixing with the Fix Wizard

Some parts of the STL file are often not generated correctly using Rhino. The mesh may be “watertight” (there are no holes in the mesh) but some triangles may overlap, be very sharp or have inverted normals (the normal of the triangle points outside the mesh instead of inside). Many of these problems can be repaired using the Fix Wizard function (*Tools*→*Fix Wizard...*(Ctrl+F)) (figure E.2). This automatically checks for the problems listed in the main window and can automatically fix them for the user. In most cases a few applications of the Fix Wizard will produce a valid geometry for remeshing. However sometimes the mesh generated by Rhino needs further manual fixing. This requires careful use of the manual triangle editing and hole filling tools. The Magics help file contains more information on how to use these.

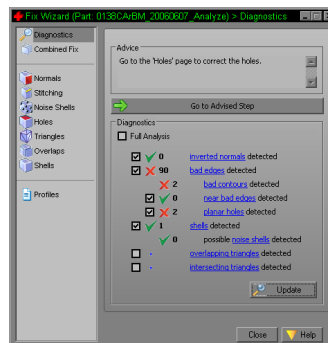


Figure E.2: The Fix Wizard window.

E.4 Slice the outlets and/or inlets parallel to the vessel centreline

Before remeshing begins, the shape of the artery mesh should be corrected. The Remesh functions do not change the shape of the mesh. If the mesh has a very sharply pointed inlet or outlets GAMBIT (the mesh preprocessor for the Fluent CFD package) cannot distinguish the outlet/inlet face from the wall of the artery. Inlet/outlets should be trimmed to produce an outlet that is perpendicular to the centre line of the relevant artery section. This is done using the Cut & Punch tool (*Tools*→*Cut & Punch...*(Ctrl+X)) (figure E.3). The geometry should be rotated to the correct orientation and a cut line can be defined. The line acts in a similar manner to a cheese wire: it will slice straight through the mesh. Magics automatically fills the holes that are created to produce a watertight mesh.

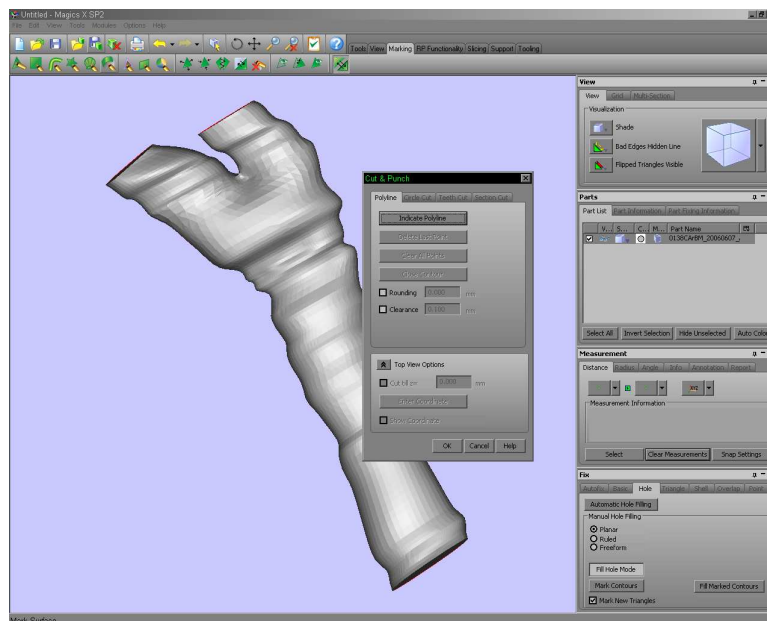


Figure E.3: Using *Cut & Punch* to slice the vessel outlets.

E.5 Remesh operations

Remeshing aims to make the mesh more consistent and uniform. Rhino creates a mesh with varying densities depending on the size of details in the artery solid model. This can be difficult to import into GAMBIT as a result. Remeshing doesn't significantly change the size or shape of the model. Open the remesh module (*Modules*→*Remesh...*(Ctrl+M)) (figure E.4). Remeshing should not be carried out on all of the model. If remeshing is carried out on the flat planes at the inlet and outlet(s) the shape of the mesh will be changed significantly. GAMBIT requires a

flat plane at each end to define an inlet or outlet to the artery model. The marking tools (on the tab at the top of the screen) should be used to mark all the triangles in the mesh. The flat planes should then be unmarked using the Mark Plane tool (figure E.5).

Before remeshing, a normal triangle reduction should be performed (*Tools*→*Triangle Reduction*→*Normal*(Alt+N) - see table E.1 for the settings required for this function). This unifies smaller triangles into larger triangles. A remesh performed without this step would require more processing time.

Once this has been done, a split-based remesh should be performed (*Tools*→*Auto Remesh*→*Split-based method*(Alt+S)). The settings for this function are listed in table E.2. Once the remesh operation is finished, a quality-preserving triangle reduction should be performed (*Tools*→*Triangle Reduction*→*Normal*(Alt+N)). Table E.3 gives the settings for this function. Any sharp triangles from this process should then be filtered (*Tools*→*Triangle Reduction*→*Filter Sharp Triangles...*(Table E.4)).

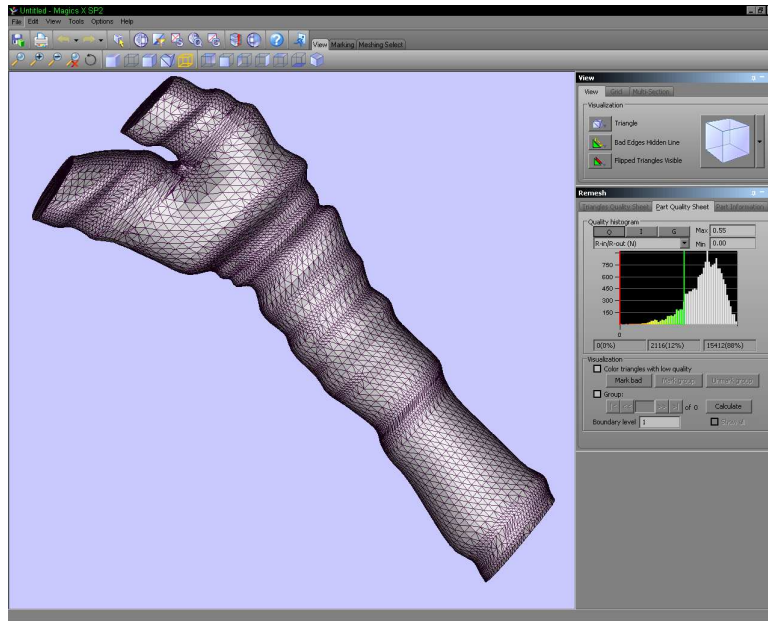


Figure E.4: The Remesh window

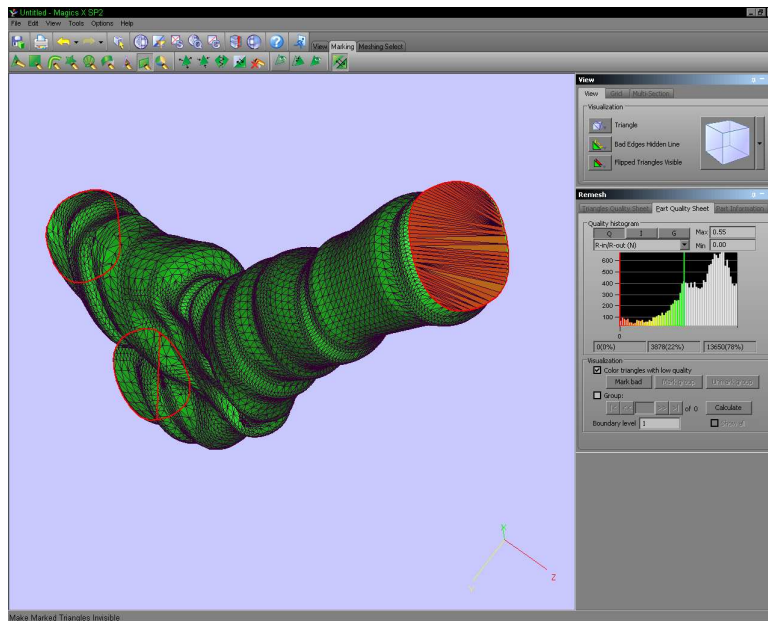


Figure E.5: Any remesh operation should be done locally. The ends of the geometry should be unmarked to prevent shape change at the inlet/outlets.

Tab	Local
Smallest detail	0.1 mm
Maximum angle	10 °
Number of iteration	5

Table E.1: Normal triangle reduction options

Quality Threshold	0.55
Maximum geometry error	0.10 mm
Minimum edge length	0.50 mm
Number of iterations	10
Number of move iterations	1
Maximum edge length	5.00 mm
Preserve initial mesh quality	False
Local	True

Table E.2: *Split based remesh options*

Quality threshold	0.55
Number of iterations	6
Maximum geometry error	0.05 mm
Maximum edge length	5.00 mm
Skip bad edges	False
Local	True

Table E.3: *Quality preserving triangle reduction options*

Filter	0.050 mm
Angle	5.0 °
Collapse	True

Table E.4: *Filter sharp triangles options*

E.6 Save remeshed file

The mesh file should now be correctly remeshed. The file should then be saved with “_remesh” appended to the filename for clarity, as an STL file (*File*→*Save part as...*(Ctrl+S)). It should be noted that Magics can save the mesh file as a Fluent mesh file, but GAMBIT cannot import this type of file.

Appendix F

Software documentation

F.1 Introduction

This appendix contains documentation for all the software developed in relation to the results presented in this thesis. Where a particular piece of software is considered relevant to the conclusions presented in this thesis, or where replication of the results presented here would require knowledge of how to use the software, documentation for each LabVIEW Virtual Instrument (VI) is included.

The symbol “~” is used for shorthand for the location of the author’s Subversion repository held at the School of Engineering and Electronics (SEE). This is available within SEE from

```
https://svn.see.ed.ac.uk/see/users/shammer1
```

The symbol “*” refers to the location of version 7.1 of the National Instruments LabVIEW development environment. This may vary from PC to PC. On a typical installation this path will be

```
C:\Program Files\National Instruments\LabVIEW 7.1
```

Some VIs were developed using the OpenG toolkit (version 2.00α3). More information on the OpenG toolkit is available at <http://www.openg.org>.

F.2 BMP2SXIarray.vi

This VI is used to convert a list of bitmap files (.bmp) to a Stradwin image file (.sxi). A directory name is required for an input. It is assumed that the bitmaps are in that directory. Bitmaps must

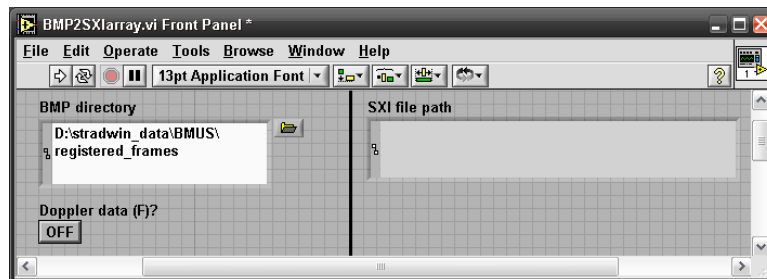
be 8-bit format (256 levels of grey) for a valid result. The .sxi file is saved in the input directory with the name of the directory.

This VI is useful for converting images segmented manually using Analyse (see chapter 6 and Appendix B) and ShIRT (see chapter 6) into Stradwin files, allowing a spatially registered segmented dataset to be created.

F.2.1 Connector Pane



F.2.2 Front Panel



F.2.3 List of SubVIs and Express VIs



Merge Errors.vi

*\vi.lib\Utility\error.llb\Merge Errors.vi



Write Characters To File with error.vi

~\Sandpit\LV utilities\Write Characters To File with error.vi



2D U8 array to raw data.vi

~\Sandpit\convert._sx.&._sw\BMP to SW\2D U8 array to raw data.vi



Read BMP File.vi

*\vi.lib\picture\bmp.llb\Read BMP File.vi



Unflatten Pixmap.vi

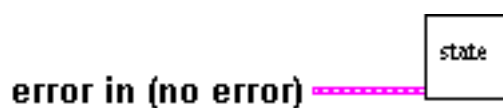
*\vi.lib\picture\pixmap.llb\Unflatten Pixmap.vi

F.3 SW threshold and segment images SM.vi

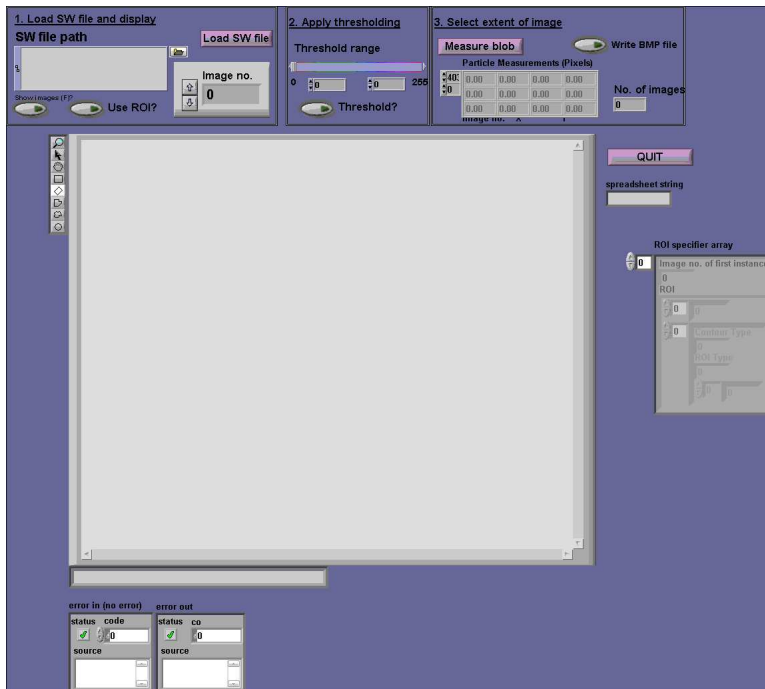
This VI was used to automatically segment Stradwin files by thresholding the images. This selects only a subset of the image according to the brightness values found in the image. This process can be carried out manually using the Stradwin program, but is time-consuming for large datasets.

This VI was used to calculate the area of the vessel in the flow phantoms used in chapter 5.

F.3.1 Connector Pane



F.3.2 Front Panel



F.3.3 List of SubVIs and Express VIs



Merge Errors.vi

*\vi.lib\Utility\error.llb\Merge Errors.vi



SW threshold and segment images SM CASEs.ctl

~\Sandpit\StradWorks\Threshold SW file\SW threshold and segment images SM CASEs.ctl



SW_read image.vi

~\Sandpit\convert_sx_&_sw\SW_read image.vi



IMAQ ArrayToColorImage

*\vi.lib\Vision\Color.llb\IMAQ ArrayToColorImage



IMAQ Create

*\vi.lib\Vision\Basics.llb\IMAQ Create



IMAQ Dispose

*\vi.lib\Vision\Basics.llb\IMAQ Dispose



IMAQ Cast Image

*\vi.lib\Vision\Management.llb\IMAQ Cast Image



IMAQ Threshold

*\vi.lib\Vision\Process.llb\IMAQ Threshold



IMAQ ROIToMask

*\vi.lib\Vision\ROI Tools.llb\IMAQ ROIToMask



IMAQ Copy

*\vi.lib\Vision\Management.llb\IMAQ Copy



IMAQ WindDraw

*\vi.lib\Vision\Display.llb\IMAQ WindDraw



IMAQ Image.ctl

*\vi.lib\vision\Image Controls.llb\IMAQ Image.ctl



IMAQ Mask

*\vi.lib\Vision\Operator.llb\IMAQ Mask



IMAQ UserLookup

*\vi.lib\Vision\Process.llb\IMAQ UserLookup



IMAQ FillImage

*\vi.lib\vision\Pixel Manipulation.llb\IMAQ FillImage



IMAQ GetPalette

*\vi.lib\Vision\Display.llb\IMAQ GetPalette



SW measure phantom area.vi

~\Sandpit\StradWorks\Threshold SW file\SW measure phantom area.vi



ROI and image number array.ctl

~\Sandpit\StradWorks\Threshold SW file\ROI and image number array.ctl

**Check ROI.vi**

~\Sandpit\StradWorks\Threshold SW file\Check ROI.vi

**ROI cluster to ROI array.vi**

~\Sandpit\StradWorks\Threshold SW file\ROI cluster to ROI array.vi

**SW_parse_sw&sx_file.vi**

~\Sandpit\convert_sx_&_sw\SW_parse_sw&sx_file.vi

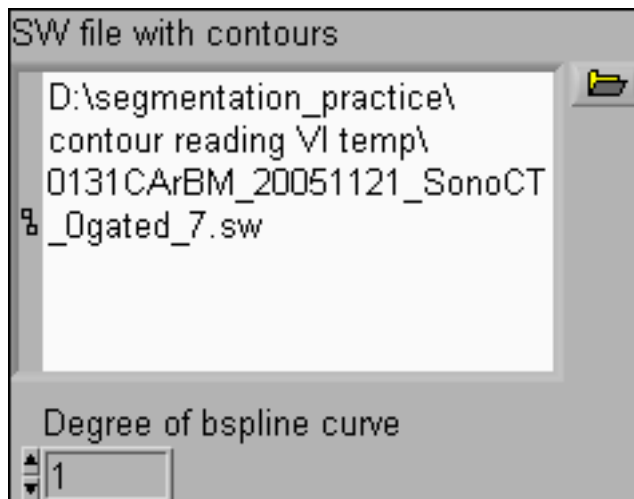
F.4 SW create OBJ file from segmented file.vi

A vital stage in creating a segmented spatially registered geometry using a solid modelling package is that of converting the points and curves which represent segmented lumen outlines into a file format which can be imported into the package. This VI converts segmented outlines in a Stradwin file into Wavefront Object files with a .obj extension. These files contain curves fitted to the lumen outlines which can be used as the basis of an artery mesh model following the guidelines given in appendix D.

F.4.1 Connector Pane



F.4.2 Front Panel



F.4.3 List of SubVIs and Express VIs



SW read all contours.vi

~\Sandpit\StradWorks\SW contour utilities\read all contours\SW read all contours.vi



SW contour 3D transform using x-y-z matrix.vi

~\Sandpit\StradWorks\SW contour utilities\read all contours\SW contour 3D transform using x-y-z matrix.vi



SW convert 3D contour to OBJ file.vi

~\Sandpit\StradWorks\SW contour utilities\read all contours\SW convert 3D contour to OBJ file.vi

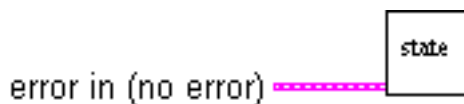
F.5 SW gate to sxp peaks.vi

Automatic gating of a Stradwin file is performed using this VI. A Stradx phase file (with a .sxp extension) must first be created according to the instructions included with Stradx. The phase file is then used with this VI to create a list of images which are found at the peaks (or optionally troughs) of the phase file.

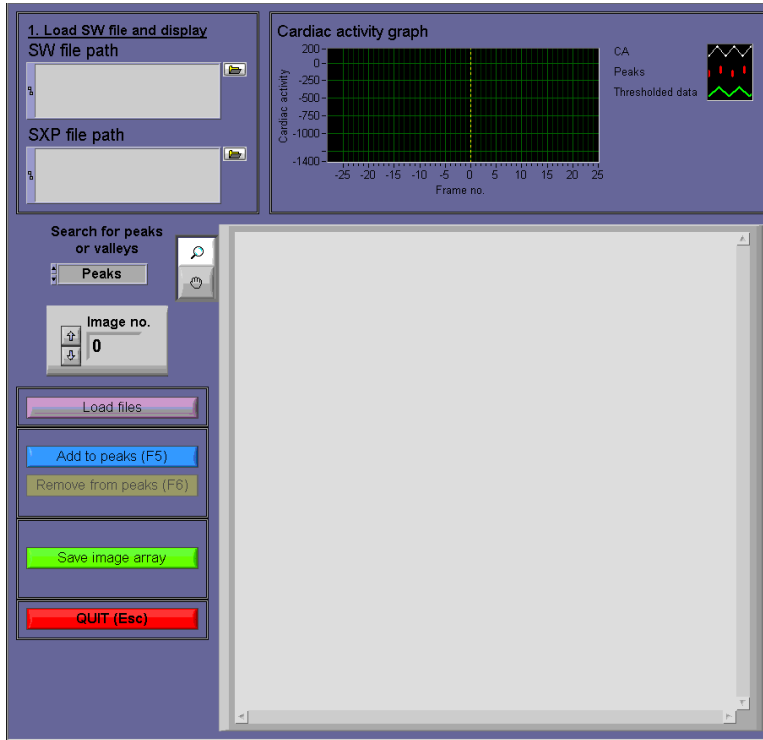
The user can sort through all of the selected peaks or troughs to manually remove any which the program has misidentified. Once this has been done, the list of peak images is saved as a text file for use with “SW_SelectSW.vi”.

All of the gated Stradwin files used for CFD simulation and solid modelling found in chapters 5, 4 and 7 were gated using this VI.

F.5.1 Connector Pane



F.5.2 Front Panel



F.5.3 List of SubVIs and Express VIs



Merge Errors.vi

*\vi.lib\Utility\error.llb\Merge Errors.vi



SW_read image.vi

~\Sandpit\convert_sx_&_sw\SW_read image.vi



IMAQ Create

*\vi.lib\Vision\Basics.llb\IMAQ Create



IMAQ Dispose

*\vi.lib\Vision\Basics.llb\IMAQ Dispose



IMAQ Cast Image

*\vi.lib\Vision\Management.llb\IMAQ Cast Image



IMAQ Image.ctl

*\vi.lib\vision\Image Controls.llb\IMAQ Image.ctl



IMAQ GetPalette

*\vi.lib\vision\Display.llb\IMAQ GetPalette



SW gate to sxp peaks CASEs.ctl

~\Sandpit\StradWorks\SelectSW\SW gate to sxp peaks CASEs.ctl



SW_Read SXP file.vi

~\Sandpit\convert.sx.&.sw\Read SXP file\SW_Read SXP file.vi



IMAQ ArrayToColorImage

*\vi.lib\Vision\Color.llb\IMAQ ArrayToColorImage



Strip Path Extension...ogtk.vi

*\user.lib_OpenG.lib\file\file.llb\Strip Path Extension...ogtk.vi



Strip Path Extension - Path...ogtk.vi

*\user.lib_OpenG.lib\file\file.llb\Strip Path Extension - Path...ogtk.vi



Write To Spreadsheet File.vi

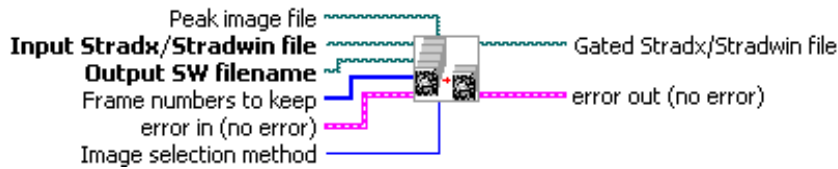
*\vi.lib\Utility\file.llb\Write To Spreadsheet File.vi

F.6 SW_SelectSW.vi

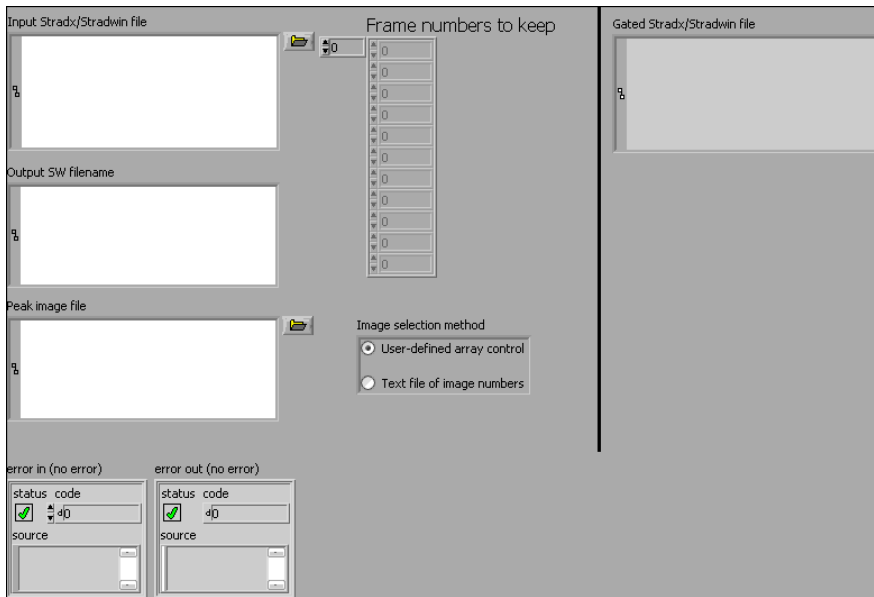
SelectSW acts in a similar way to selectsx, the tool included with Stradx. It takes an array of frame numbers from the input stradwin/stradx file, and then saves a .sw and .sxi file with only those frames.

This uses text files with a list of images found from “SW gate to sxp peaks.vi” shown in section F.5.

F.6.1 Connector Pane



F.6.2 Front Panel



F.6.3 List of SubVIs and Express VIs



SW_parse_sw&sx_file.vi

~\convert_sx_sw\SW_parse_swsx_file.vi



Read Characters From File with error.vi

~\LV utilities\Read Characters From File with error.vi



Convert File Extension..ogtk.vi

*\user.lib_OpenG.lib\file\file.llb\Convert File Extension..ogtk.vi



Convert File Extension (Path)..ogtk.vi

*\user.lib_OpenG.lib\file\file.llb\Convert File Extension (Path)..ogtk.vi



Merge Errors.vi

*\vi.lib\Utility\error.llb\Merge Errors.vi



Write Characters To File with error.vi

~\LV utilities\Write Characters To File with error.vi



Search and Replace Pattern.vi

*\vi.lib\Utility\error.llb\Search and Replace Pattern.vi



Strip Path...ogtk.vi

*\user.lib_OpenG.lib\file\file.llb\Strip Path...ogtk.vi

**Strip Path - Traditional...ogtk.vi**

*\user.lib_OpenG.lib\file\file.llb\Strip Path - Traditional...ogtk.vi

**Read From Spreadsheet File.vi**

*\vi.lib\Utility\file.llb\Read From Spreadsheet File.vi

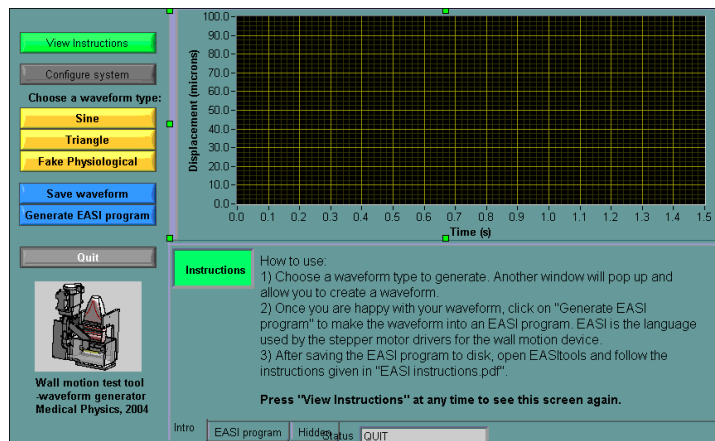
F.7 state demo with fake physio.vi

This is the top-end GUI used to create custom wall motion waveforms for the wall motion test phantom described in chapter 8. The user may import a saved waveform (for example from *in-vivo* data) as a tab-delimited text file, or create their own waveform using the included tools. The characteristics of the test phantom controller can also be changed such as the stepper motor step size, acceleration and stepper motor velocity.

F.7.1 Connector Pane



F.7.2 Front Panel



F.7.3 List of SubVIs and Express VIs



MR and ballscrew diameter chooser.vi

~\Sandpit\AWM test tool\MR and ballscrew diameter chooser.vi



generate EASI waveform GUI.vi

~\Sandpit\AWM test tool\generate EASI waveform GUI.vi



generate EASI program no LOOP.vi

~\Sandpit\AWM test tool\generate EASI program no LOOP.vi

**Write Characters To File.vi**

*\vi.lib\Utility\file.llb\Write Characters To File.vi

**Write To Spreadsheet File.vi**

*\vi.lib\Utility\file.llb\Write To Spreadsheet File.vi

**generate fake physio EASI waveform GUI.vi**

~\Sandpit\AWM test tool\generate fake physio EASI waveform GUI.vi

F.8 SW evaluate segmentation with Udupa methods using BMPs.vi

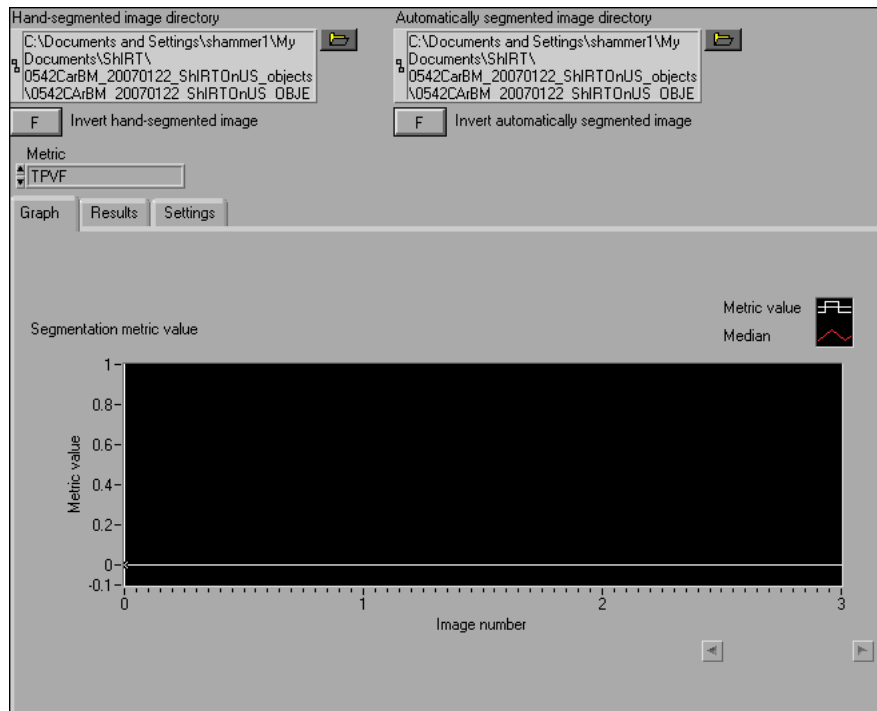
The normalized segmentation error of two images, one hand-segmented and the other automatically segmented, is calculated by this VI (using an algorithm described in Hammoude, A. (2001). "An empirical parameter selection method for endocardial border identification algorithms." *Computerized Medical Imaging and Graphics* 25(1): 33). A directory of bitmap image files (.bmp) is required for each input, as well as the sizes of pixels in the image. The sizes of each pixel can be found in the Stradwin file (.sw) on the lines marked RES_XSCALE and RES_YSCALE in cm/pixel.

This code was used in chapter 6.

F.8.1 Connector Pane



F.8.2 Front Panel



F.8.3 List of SubVIs and Express VIs



IMAQ Create

*\vi.lib\vision\Basics.llb\IMAQ Create.vi



IMAQ ReadFile

*\vi.lib\Vision\Files.llb\IMAQ ReadFile.vi



IMAQ Inverse

*\vi.lib\Vision\Process.llb\IMAQ Inverse.vi



IMAQ Browser Setup

*\vi.lib\Vision\Browser.llb\IMAQ Browser Setup.vi



IMAQ Browser Insert

*\vi.lib\Vision\Browser.llb\IMAQ Browser Insert.vi



IMAQ WindDraw

*\vi.lib\Vision\Display.llb\IMAQ WindDraw.vi



IMAQ Dispose

*\vi.lib\vision\Basics.llb\IMAQ Dispose.vi



IMAQ WindSetup

*\vi.lib\Vision\Display.llb\IMAQ WindSetup.vi



Merge Errors.vi

*\vi.lib\Utility\error.llb\Merge Errors.vi



IMAQ Image.ctl

*\vi.lib\vision\Image Controls.llb\IMAQ Image.ctl



Median.vi

*\vi.lib\Analysis\baseanly.llb\Median.vi



Udupa segmentation metrics.vi

~\Sandpit\StradWorks\segmentation evaluation\Udupa method\Udupa segmentation metrics.vi



Mean.vi

*\vi.lib\Analysis\baseanly.llb\Mean.vi



Calculate Udupa scene areas.vi

~\Sandpit\StradWorks\segmentation evaluation\Udupa method\Calculate Udupa scene areas.vi

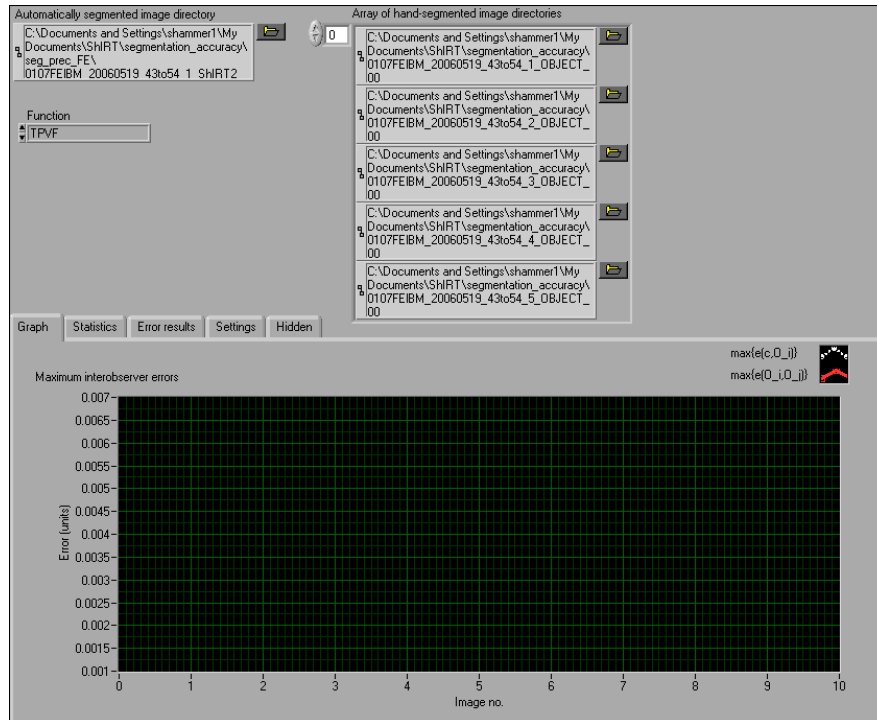
F.9 calculate Udupa interobserver percent statistic.vi

This VI calculates the interobserver percent statistic. It is designed to be used to compare an automatically segmented directory of bitmap images to a set of several directories of manually segmented bitmap images. The segmentation metric used to assess the multiple segmentations can be chosen from those defined in chapter 6.

F.9.1 Connector Pane



F.9.2 Front Panel



F.9.3 List of SubVIs and Express VIs



Merge Errors.vi

*\vi.lib\Utility\error.llb\Merge Errors.vi



Confidence Interval using Inverse t.vi

~\Sandpit\StradWorks\segmentation evaluation\Confidence Interval using Inverse t.vi



Mean.vi

*\vi.lib\Analysis\baseanly.llb\Mean.vi

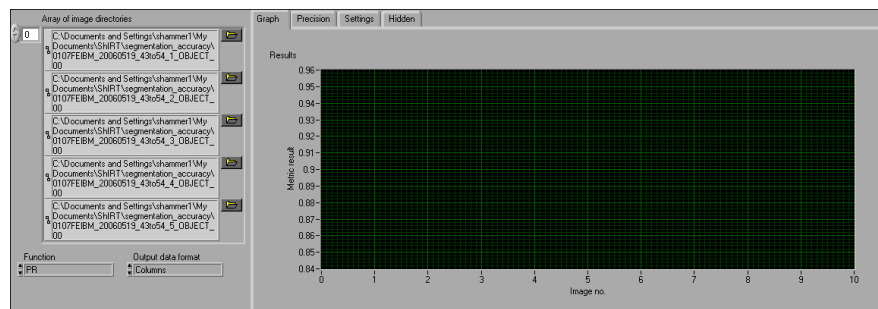
**SW evaluate segmentation with Udupa methods using BMPs.vi**

~\Sandpit\StradWorks\segmentation evaluation\Udupa method\SW evaluate segmentation with Udupa methods using BMPs.vi

F.10 calculate Udupa segmentation precision.vi

This VI allows the user to calculate the precision of a set of segmentations. Each segmentation should be performed using the same segmentation method on the same image dataset. Each segmentation should be saved as a series of binary bitmap images with the area inside the segmented outline coloured in white and the area outside coloured in black. Each series of bitmaps should be in a separate directory.

This VI was used in chapter 6

F.10.1 Connector Pane**F.10.2 Front Panel**

F.10.3 List of SubVIs and Express VIs



Merge Errors.vi

~\vi.lib\Utility\error.llb\Merge Errors.vi



SW evaluate segmentation with Udupa methods using BMPs.vi

*\Sandpit\StradWorks\segmentation evaluation\Udupa method\SW evaluate segmentation with Udupa methods using BMPs.vi

References

- [1] WHO, “The Atlas of Heart Disease and Stroke,” 2005. http://www.who.int/cardiovascular_diseases/resources/atlas/en/.
- [2] H. C. Stary, A. B. Chandler, S. Glagov, J. R. Guyton, J. Insull, W., M. E. Rosenfeld, S. A. Schaffer, C. J. Schwartz, W. D. Wagner, and R. W. Wissler, “A definition of initial, fatty streak, and intermediate lesions of atherosclerosis. a report from the Committee on Vascular Lesions of the Council on Arteriosclerosis, American Heart Association,” *Circulation*, vol. 89, no. 5, pp. 2462–2478, 1994.
- [3] S. G. Frangos, V. Gahtan, and B. Sumpio, “Localization of atherosclerosis: Role of hemodynamics,” *Arch Surg*, vol. 134, no. 10, pp. 1142–1149, 1999.
- [4] T. Igari, S. Hoshino, F. Iwaya, H. Satokawa, H. Midorikawa, S. Takase, and Y. Hoshino, “Results of 256 consecutive abdominal aortic aneurysm repairs using extraperitoneal approach,” *Cardiovascular Surgery*, vol. 9, no. 3, pp. 249–253, 2001.
- [5] J. May, G. H. White, R. Waugh, M. S. Stephen, X. Chaufour, W. Yu, and J. P. Harris, “Endovascular treatment of abdominal aortic aneurysms,” *Cardiovascular Surgery*, vol. 7, no. 5, pp. 484–490, 1999.
- [6] R. B. Rutherford, “Options in the surgical management of aorto-iliac occlusive disease: a changing perspective,” *Cardiovascular Surgery*, vol. 7, no. 1, pp. 5–12, 1999.
- [7] C. Westbrook and C. Kaut, *MRI in practice*. Oxford: Blackwell Science, 2nd ed. ed., 1998.
- [8] P. M. Rothwell, S. A. Gutnikov, and C. P. Warlow, “Reanalysis of the final results of the European Carotid Surgery Trial,” *Stroke*, vol. 34, no. 2, pp. 514–523, 2003.
- [9] I. N. Staikov, M. Arnold, H. Mattle, L. Remonda, M. Sturzenegger, R. W. Baumgartner, and G. Schroth, “Comparison of the ECST, CC, and NASCET grading methods and ultrasound for assessing carotid stenosis,” *Journal of Neurology*, vol. 247, no. 9, pp. 681–686, 2000.
- [10] C. F. Bladin, A. V. Alexandrov, J. Murphy, R. Maggisano, and J. W. Norris, “Carotid stenosis index : A new method of measuring internal carotid artery stenosis,” *Stroke*, vol. 26, no. 2, pp. 230–234, 1995.
- [11] J. G. Lijmer, M. G. M. Hunink, J. J. A. M. van den Dungen, J. Loonstra, and A. J. Smit, “ROC analysis of noninvasive tests for peripheral arterial disease,” *Ultrasound in Medicine & Biology*, vol. 22, no. 4, pp. 391–398, 1996.
- [12] UKSAT authors, “Mortality results for randomised controlled trial of early elective surgery or ultrasonographic surveillance for small abdominal aortic aneurysms,” *The Lancet*, vol. 352, no. 9141, pp. 1649–1655, 1998.

- [13] F. A. Lederle, G. R. Johnson, S. E. Wilson, D. J. Ballard, J. Jordan, William D., J. Blebea, F. N. Littooy, J. A. Freischlag, D. Bandyk, J. H. Rapp, A. A. Salam, and I. for the Veterans Affairs Cooperative Study, "Rupture rate of large abdominal aortic aneurysms in patients refusing or unfit for elective repair," *JAMA*, vol. 287, no. 22, pp. 2968–2972, 2002.
- [14] S. C. Nicholls, J. B. Gardner, M. H. Meissner, and K. H. Johansen, "Rupture in small abdominal aortic aneurysms," *Journal of vascular surgery : official publication, the Society for Vascular Surgery [and] International Society for Cardiovascular Surgery, North American Chapter*, vol. 28, no. 5, pp. 884–888, 1998. 0741-5214.
- [15] C. P. Oates, *Cardiovascular Haemodynamics and Doppler Waveforms Explained*. London: Greenwich Medical Media Ltd., 1 ed., 2001.
- [16] O. Bonnefous, A. Criton, L. Germond, and E. Denis, "New TDI developments for vascular and cardiac applications," in *IEEE Ultrasonics Symposium*, vol. 2, pp. 1285–1290, 2000.
- [17] P. N. T. Wells, "Ultrasound imaging," *Physics In Medicine And Biology*, vol. 51, no. 13, pp. R83–R98, 2006.
- [18] R. Steel, T. L. Poepping, R. S. Thompson, and C. Macaskill, "Origins of the edge shadowing artefact in medical ultrasound imaging," *Ultrasound in Medicine & Biology*, vol. 30, no. 9, pp. 1153–1162, 2004.
- [19] P. R. Hoskins, A. Thrush, K. Martin, and T. A. Whittingham, *Diagnostic Ultrasound : Physics and Equipment*. London: Greenwich Medical Media Ltd., 1 ed., 2003.
- [20] D. H. Evans and W. N. McDicken, *Doppler Ultrasound Physics, Instrumentation and Signal Processing*. Wiley, 2 ed., 2000.
- [21] W. N. McDicken, *Diagnostic Ultrasonics : Principles and Use of Instruments*. Edinburgh: Churchill Livingstone, 3 ed., 1991.
- [22] P. L. Carson, ed., *Standard Methods for Calibration of 2D and 3D Spatial Measurement Capabilities of Pulse Echo Ultrasound Imaging Systems*. The American Institute of Ultrasound in Medicine, 2004.
- [23] R. Kern, K. Szabo, M. Hennerici, and S. Meairs, "Characterization of carotid artery plaques using real-time compound B-mode ultrasound," *Stroke*, vol. 35, no. 4, pp. 870–875, 2004.
- [24] C. J. C. Cash, G. M. Treece, L. H. Berman, A. H. Gee, and R. W. Prager, "3D reconstruction of the skeletal anatomy of the normal neonatal foot using 3D ultrasound," *British Journal of Radiology*, vol. 78, no. 931, pp. 587–595, 2005.
- [25] A. Hammoude, "Endocardial border identification in two-dimensional echocardiographic images: review of methods," *Computerized Medical Imaging and Graphics*, vol. 22, no. 3, pp. 181–193, 1998.

- [26] K. W. Lee, N. B. Wood, and X. Y. Xu, "Ultrasound image-based computer model of a common carotid artery with a plaque," *Medical Engineering & Physics*, vol. 26, no. 10, pp. 823–840, 2004.
- [27] J. A. Noble and D. Boukerroui, "Ultrasound image segmentation: a survey," *Medical Imaging, IEEE Transactions on*, vol. 25, no. 8, pp. 987–1010, 2006.
- [28] C. D. Ainsworth, C. C. Blake, A. Tamayo, V. Beletsky, A. Fenster, and J. D. Spence, "3D ultrasound measurement of change in carotid plaque volume: A tool for rapid evaluation of new therapies," *Stroke*, vol. 36, no. 9, pp. 1904–1909, 2005.
- [29] D. C. Barratt, B. Ariff, K. N. Humphries, S. A. M. Thom, and A. Hughes, "Reconstruction and quantification of the carotid artery bifurcation from 3-D ultrasound images," *IEEE Transactions on Medical Imaging*, vol. 23, no. 5, pp. 567–583, 2004.
- [30] T. C. Poon and R. N. Rohling, "Three-dimensional extended field-of-view ultrasound," *Ultrasound in Medicine & Biology*, vol. 32, no. 3, pp. 357–369, 2006.
- [31] X. Ye, J. A. Noble, and J. Declerck, "3D freehand echocardiography for automatic left ventricle reconstruction and analysis based on multiple acoustic windows," in *Medical Image Computing and Computer-Assisted Intervention - MICCAI 2001* (W. Niessen and M. Viergever, eds.), (Utrecht, The Netherlands), pp. 778–785, Springer-Verlag Heidelberg, 2001.
- [32] W. Lees, "Ultrasound imaging in three and four dimensions," *Seminars in Ultrasound, CT, and MRI*, vol. 22, no. 1, pp. 85–105, 2001.
- [33] F. Lindseth, T. Lang, J. Bang, and T. A. N. Hernes, "Accuracy evaluation of a 3D ultrasound-based neuronavigation system," *Computer Aided Surgery*, vol. 7, no. 4, pp. 197–222, 2002.
- [34] S. Tong, D. B. Downey, H. N. Cardinal, and A. Fenster, "A three-dimensional ultrasound prostate imaging system," *Ultrasound in Medicine & Biology*, vol. 22, no. 6, pp. 735–746, 1996.
- [35] J. A. Shipley, F. A. Duck, D. A. Goddard, M. R. Hillman, M. Halliwell, M. G. Jones, and B. T. Thomas, "Automated quantitative volumetric breast ultrasound data-acquisition system," *Ultrasound in Medicine & Biology*, vol. 31, no. 7, p. 905, 2005.
- [36] A. Fenster and D. B. Downey, "3-D ultrasound imaging: A review," *IEEE Engineering in Medicine and Biology*, pp. 41–51, 1996.
- [37] A. Hernandez, O. Basset, P. Chirossel, and G. Gimenez, "Spatial compounding in ultrasonic imaging using an articulated scan arm," *Ultrasound in Medicine & Biology*, vol. 22, no. 2, pp. 229–238, 1996.
- [38] G. M. Treece, A. H. Gee, R. W. Prager, C. J. C. Cash, and L. H. Berman, "High-definition freehand 3-D ultrasound," *Ultrasound in Medicine & Biology*, vol. 29, no. 4, pp. 529–546, 2003.

- [39] D. C. Barratt, A. H. Davies, A. D. Hughes, S. A. Thom, and K. N. Humphries, "Accuracy of an electromagnetic three-dimensional ultrasound system for carotid artery imaging," *Ultrasound in Medicine & Biology*, vol. 27, no. 10, pp. 1421–1425, 2001.
- [40] M. Hastenteufel, M. Vetter, H.-P. Meinzer, and I. Wolf, "Effect of 3D ultrasound probes on the accuracy of electromagnetic tracking systems," *Ultrasound in Medicine & Biology*, vol. 32, no. 9, pp. 1359–1368, 2006.
- [41] A. Ali and R. Logeswaran, "A visual probe localization and calibration system for cost-effective computer-aided 3D ultrasound," *Computers in Biology and Medicine*, vol. 37, no. 8, pp. 1141–1147, 2007.
- [42] P. Abolmaesumi, S. E. Salcudean, W. H. Zhu, S. P. DiMaio, and M. R. Sirouspour, "A user interface for robot-assisted diagnostic ultrasound," in *IEEE International Conference on Robots and Automation*, (Korea), 2001.
- [43] A. Fenster, D. Lee, S. Sherebrin, R. Rankin, and D. Downey, "Three-dimensional ultrasound imaging of the vasculature," *Ultrasonics*, vol. 36, no. 1-5, pp. 629–633, 1998.
- [44] A. Landry, J. D. Spence, and A. Fenster, "Measurement of carotid plaque volume by 3-dimensional ultrasound," *Stroke*, vol. 35, no. 4, pp. 864–869, 2004.
- [45] A. Landry, J. D. Spence, and A. Fenster, "Quantification of carotid plaque volume measurements using 3D ultrasound imaging," *Ultrasound in Medicine & Biology*, vol. 31, no. 6, pp. 751–762, 2005.
- [46] K. V. Ramnarine, T. Anderson, and P. R. Hoskins, "Construction and geometric stability of physiological flow rate wall-less stenosis phantoms," *Ultrasound in Medicine & Biology*, vol. 27, no. 2, pp. 245–250, 2001.
- [47] T. L. Poepping, H. N. Nikolov, R. N. Rankin, M. Lee, and D. Holdsworth, "An *in-vitro* system for Doppler ultrasound flow studies in the stenosed carotid artery bifurcation," *Ultrasound in Medicine & Biology*, vol. 28, no. 4, pp. 495–506, 2002.
- [48] O. V. Solberg, F. Lindseth, H. Torp, R. E. Blake, and T. A. Nagelhus Hernes, "Freehand 3D ultrasound reconstruction algorithms—a review," *Ultrasound in Medicine & Biology*, vol. 33, no. 7, pp. 991–1009, 2007.
- [49] C. D. Barry, C. P. Allott, N. W. John, P. M. Mellor, P. A. Arundel, D. S. Thomson, and J. C. Waterton, "Three-dimensional freehand ultrasound: Image reconstruction and volume analysis," *Ultrasound in Medicine & Biology*, vol. 23, no. 8, pp. 1209–1224, 1997.
- [50] S. Berg, H. Torp, D. Martens, E. Steen, S. Samstad, I. Hoivik, and B. Olstad, "Dynamic three-dimensional freehand echocardiography using raw digital ultrasound data," *Ultrasound in Medicine & Biology*, vol. 25, no. 5, pp. 745–753, 1999.
- [51] R. Rohling, A. Gee, and L. Berman, "A comparison of freehand three-dimensional ultrasound reconstruction techniques," *Medical Image Analysis*, vol. 3, no. 4, pp. 339–359, 1999.

- [52] A. Roche, X. Pennec, M. Rudolph, D. P. Auer, G. Malandain, S. Ourselin, L. M. Auer, and N. Ayache, "Generalized correlation ratio for rigid registration of 3D ultrasound with MR images," in *Medical Image Computing and Computer-Assisted Intervention MICCAI 2000*, p. 567, Springer-Verlag, 2000.
- [53] R. Prager, A. Gee, G. Treece, and L. Berman, "Freehand 3D ultrasound without voxels: volume measurement and visualisation using the Stradx system," *Ultrasonics*, vol. 40, no. 1-8, pp. 109–115, 2002.
- [54] R. Dammers, F. Stifft, J. H. M. Tordoir, J. M. M. Hameleers, A. P. G. Hoeks, and P. J. E. H. M. Kitslaar, "Shear stress depends on vascular territory: comparison between common carotid and brachial artery," *J Appl Physiol*, vol. 94, no. 2, pp. 485–489, 2003.
- [55] P. Tortoli, T. Morganti, G. Bambi, C. Palombo, and K. V. Ramnarine, "Noninvasive simultaneous assessment of wall shear rate and wall distension in carotid arteries," *Ultrasound in Medicine & Biology*, vol. 32, no. 11, pp. 1661–1670, 2006.
- [56] C. J. Slager, J. J. Wentzel, F. J. H. Gijssen, J. C. H. Schuurbiers, A. C. Van der Wal, A. Van der Steen, and P. Serruys, "The role of shear stress in the generation of rupture-prone vulnerable plaques," *Nature Clinical Practice Cardiovascular Medicine*, vol. 2, no. 8, pp. 401–407, 2005.
- [57] P. F. Davies, "Flow-mediated endothelial mechanotransduction," *Physiological Reviews*, vol. 75, no. 3, pp. 519–560, 1995.
- [58] C. J. Slager, J. J. Wentzel, F. J. H. Gijssen, A. Thury, A. C. Van der Wal, J. A. Schaar, and P. Serruys, "The role of shear stress in the destabilization of vulnerable plaques and related therapeutic implications," *Nature Clinical Practice Cardiovascular Medicine*, vol. 2, no. 9, pp. 456–464, 2005.
- [59] M. M. Thompson, L. Jones, A. Nasim, R. D. Sayers, and P. R. F. Bell, "Angiogenesis in abdominal aortic aneurysms," *European Journal of Vascular and Endovascular Surgery*, vol. 11, no. 4, pp. 464–469, 1996.
- [60] W. R. W. Wilson, M. Anderton, E. C. Schwalbe, J. L. Jones, P. N. Furness, P. R. F. Bell, and M. M. Thompson, "Matrix metalloproteinase-8 and -9 are increased at the site of abdominal aortic aneurysm rupture," *Circulation*, vol. 113, no. 3, pp. 438–445, 2006.
- [61] E. Choke, M. M. Thompson, J. Dawson, W. R. W. Wilson, S. Sayed, I. M. Loftus, and G. W. Cockerill, "Abdominal aortic aneurysm rupture is associated with increased medial neovascularization and overexpression of proangiogenic cytokines," *Arterioscler Thromb Vasc Biol*, vol. 26, no. 9, pp. 2077–2082, 2006.
- [62] D. Birchall, A. Zaman, J. Hacker, G. Davies, and D. Mendelow, "Analysis of haemodynamic disturbance in the atherosclerotic carotid artery using computational fluid dynamics," *European Radiology*, vol. 16, no. 5, pp. 1074–1083, 2006.
- [63] D. A. Steinman, J. S. Milner, C. J. Norley, S. P. Lownie, and D. W. Holdsworth, "Image-based computational simulation of flow dynamics in a giant intracranial aneurysm," *American Journal of Neuroradiology*, vol. 24, no. 4, pp. 559–566, 2003.

- [64] J. Leung, A. Wright, N. Cheshire, J. Crane, S. Thom, A. Hughes, and Y. Xu, "Fluid structure interaction of patient specific abdominal aortic aneurysms: a comparison with solid stress models," *BioMedical Engineering OnLine*, vol. 5, no. 1, p. 33, 2006.
- [65] D. A. Steinman, "Image-based computational fluid dynamics: A new paradigm for monitoring hemodynamics and atherosclerosis," *Current Drug Targets - Cardiovascular and Haematological Disorders*, vol. 4, no. 2, pp. 183–197, 2004.
- [66] A. D. Augst, D. C. Barratt, A. Hughes, S. A. M. Thom, and X. Y. Xu, "Various issues relating to computational fluid dynamics simulations of carotid bifurcation flow based on models reconstructed from three-dimensional ultrasound images," *Proceedings of the Institution of Mechanical Engineers - H*, vol. 217, no. H, pp. 393–403, 2003.
- [67] F. P. Glor, B. Ariff, A. D. Hughes, L. A. Crowe, P. R. Verdonck, D. C. Barratt, S. A. M. Thom, D. N. Firmin, and X. Y. Xu, "Image-based carotid flow reconstruction: a comparison between MRI and ultrasound," *Physiological Measurement*, vol. 25, no. 6, pp. 1495–1509, 2004.
- [68] A. D. Augst, D. C. Barratt, A. Hughes, F. P. Glor, S. A. M. Thom, and X. Y. Xu, "Accuracy and reproducibility of CFD predicted wall shear stress using 3D ultrasound images," *Journal of Biomechanical Engineering*, vol. 125, pp. 218–222, 2003.
- [69] C. J. Slager, J. J. Wentzel, J. C. H. Schuurbijs, J. A. F. Oomen, J. Kloet, R. Krams, C. von Birgelen, W. J. van der Giessen, P. W. Serruys, and P. J. de Feyter, "True 3-dimensional reconstruction of coronary arteries in patients by fusion of angiography and IVUS (ANGUS) and its quantitative validation," *Circulation*, vol. 102, no. 5, pp. 511–516, 2000.
- [70] J. Dineley, S. Meagher, T. L. Poepping, W. N. McDicken, and P. R. Hoskins, "Design and characterisation of a wall motion phantom," *Ultrasound in Medicine & Biology*, vol. 32, no. 9, pp. 1349–1357, 2006.
- [71] W. Dabrowski, J. Dunmore-Buyze, N. Cardinal, and A. Fenster, "A real vessel phantom for flow imaging: 3-D Doppler ultrasound of steady flow," *Ultrasound in Medicine & Biology*, vol. 27, no. 1, pp. 135–141, 2001.
- [72] W. N. McDicken, "A versatile test-object for the calibration of ultrasonic doppler flow instruments," *Ultrasound in Medicine & Biology*, vol. 12, no. 3, pp. 245–249, 1986.
- [73] P. R. Hoskins, T. Anderson, and W. N. McDicken, "A computer controlled flow phantom for generation of physiological Doppler waveforms," *Physics in Medicine and Biology*, vol. 34, no. 11, pp. 1709–1717, 1989.
- [74] F. Forsberg, "Ultrasonic biomedical technology; marketing versus clinical reality," *Ultrasonics*, vol. 42, pp. 17–27, 2004.
- [75] M. J. Starmans-Kool, A. V. Stanton, S. Z. Zhao, X. Y. Xu, S. A. M. Thom, and A. D. Hughes, "Measurement of hemodynamics in human carotid artery using ultrasound and computational fluid dynamics," *Journal Of Applied Physiology*, vol. 92, no. 3, pp. 957–961, 2002.

- [76] B. Dunmire, K. W. Beach, K. H. Labs, M. Plett, and D. E. Strandness, "Cross-beam vector Doppler ultrasound for angle-independent velocity measurements," *Ultrasound in Medicine & Biology*, vol. 26, no. 8, pp. 1213–1235, 2000.
- [77] C. P. Allott, C. D. Barry, R. Pickford, and J. C. Waterton, "Volumetric assessment of carotid artery bifurcation using freehand-acquired, compound 3D ultrasound," *British Journal of Radiology*, vol. 72, no. 855, pp. 289–292, 1999.
- [78] F. P. Glor, B. Ariff, L. A. Crowe, A. Hughes, P. L. Cheong, S. A. M. Thom, P. R. Verdonck, D. N. Firmin, D. C. Barratt, and X. Y. Xu, "Carotid geometry reconstruction: a comparison between MRI and ultrasound," *Medical Physics*, vol. 30, no. 12, pp. 3251–3261, 2003.
- [79] A. Gee, R. Prager, G. Treece, C. Cash, and L. Berman, "Processing and visualizing three-dimensional ultrasound data," *British Journal of Radiology*, vol. 77, no. 2, pp. S186–193, 2004.
- [80] R. W. Prager, R. N. Rohling, A. H. Gee, and L. Berman, "Rapid calibration for 3-D freehand ultrasound," *Ultrasound in Medicine & Biology*, vol. 24, no. 6, pp. 855–869, 1998.
- [81] A. H. Gee, N. E. Houghton, G. M. Treece, and R. W. Prager, "A mechanical instrument for 3D ultrasound probe calibration," *Ultrasound in Medicine & Biology*, vol. 31, no. 4, pp. 505–518, 2005.
- [82] J. R. Jago, T. A. Whittingham, and R. Heslop, "The influence of ultrasound scanner beam width on femur length measurements," *Ultrasound in Medicine & Biology*, vol. 20, no. 8, pp. 699–703, 1994.
- [83] D. D. Frantz, S. R. Kirsch, and A. D. Wiles, "Specifying 3D tracking system accuracy - one manufacturers views," 2004. <http://www.ndieurope.com/markets/respapers/bvm2004.pdf>.
- [84] A. D. Wiles, D. G. Thompson, and D. D. Frantz, "Accuracy assessment and interpretation for optical tracking systems," 2004. <http://www.ndigital.com>.
- [85] L. Mercier, T. Lango, F. Lindseth, and D. L. Collins, "A review of calibration techniques for freehand 3-D ultrasound systems," *Ultrasound in Medicine & Biology*, vol. 31, no. 4, pp. 449–471, 2005.
- [86] M. B. Zerhouni and M. Rachedine, "US Patent # 5196343: Ultrasonic calibration material and method," 04/10/1990 1993.
- [87] F. Rousseau, P. Hellier, and C. Barillo, "Robust and automatic calibration method for 3D freehand ultrasound," in *Medical Image Computing and Computer-Assisted Intervention - MICCAI 2003*, pp. 440–448, 2003.
- [88] G. M. Treece, R. W. Prager, A. H. Gee, and L. Berman, "Correction of probe pressure artifacts in freehand 3D ultrasound," *Medical Image Analysis*, vol. 6, no. 3, pp. 199–214, 2002.

- [89] I. D. Faux and M. J. Pratt, *Computational geometry for design and manufacture*. Ellis Horwood Ltd., 1987.
- [90] M. J. Campell and D. Machin, *Medical Statistics: a commonsense approach*. John Wiley & Sons Ltd., 1990.
- [91] S. K. Nadkarni, D. Boughner, and A. Fenster, "Image-based cardiac gating for three-dimensional intravascular ultrasound imaging," *Ultrasound in Medicine & Biology*, vol. 31, no. 1, pp. 53–63, 2005.
- [92] D. C. Barratt, A. H. Davies, A. D. Hughes, S. A. Thom, and K. N. Humphries, "Optimisation and evaluation of an electromagnetic tracking device for high-accuracy three-dimensional ultrasound imaging of the carotid arteries," *Ultrasound in Medicine & Biology*, vol. 27, no. 7, pp. 957–968, 2001.
- [93] C. J. P. M. Teirlinck, R. A. Bezemer, C. Kollmann, J. Lubbers, P. R. Hoskins, P. Fish, K.-E. Fredfeldt, and U. G. Schaarschmidt, "Development of an example flow test object and comparison of five of these test objects, constructed in various laboratories," *Ultrasonics*, vol. 36, no. 1-5, p. 653, 1998.
- [94] A. R. Groves and R. N. Rohling, "Two-dimensional spatial compounding with warping," *Ultrasound in Medicine & Biology*, vol. 30, no. 7, p. 929, 2004.
- [95] D. C. Barber and R. D. Hose, "Automatic segmentation of medical images using image registration: diagnostic and simulation applications," *Journal of Medical Engineering & Technology*, vol. 29, no. 2, pp. 53 – 63, 2005.
- [96] A. Hammoude, "An empirical parameter selection method for endocardial border identification algorithms," *Computerized Medical Imaging and Graphics*, vol. 25, no. 1, pp. 33–45, 2001.
- [97] V. Chalana and Y. Kim, "A methodology for evaluation of boundary detection algorithms on medical images," *Medical Imaging, IEEE Transactions on*, vol. 16, no. 5, pp. 642–652, 1997.
- [98] J. K. Udupa, V. R. LeBlanc, Y. Zhuge, C. Imielinska, H. Schmidt, L. M. Currie, B. E. Hirsch, and J. Woodburn, "A framework for evaluating image segmentation algorithms," *Computerized Medical Imaging and Graphics*, vol. 30, no. 2, pp. 75–87, 2006.
- [99] C. Alberola-Lopez, M. Martin-Fernandez, and J. Ruiz-Alzola, "Comments on: A methodology for evaluation of boundary detection algorithms on medical images," *Medical Imaging, IEEE Transactions on*, vol. 23, no. 5, pp. 658–660, 2004.
- [100] D. A. Steinman, "Image-based computational fluid dynamics modeling in realistic arterial geometries," *Annals of Biomedical Engineering*, vol. 30, no. 4, pp. 483–497, 2002.
- [101] H. M. Ladak, J. S. Milner, and D. A. Steinman, "Rapid three-dimensional segmentation of the carotid bifurcation from serial MR images," *Journal of Biomechanical Engineering*, vol. 122, pp. 96–99, 2000.

- [102] D. C. Barber, E. Oubel, A. F. Frangi, and D. R. Hose, "Efficient computational fluid dynamics mesh generation by image registration," *Medical Image Analysis*, vol. 11, no. 6, pp. 648–662, 2007.
- [103] C. K. Zarins, D. P. Giddens, B. K. Bharadvaj, V. S. Sottiurai, R. F. Mabon, and S. Glagov, "Carotid bifurcation atherosclerosis. Quantitative correlation of plaque localization with flow velocity profiles and wall shear stress," *Circ Res*, vol. 53, no. 4, pp. 502–514, 1983.
- [104] L. Goubergrits, K. Affeld, J. Fernandez-Britto, and L. Falcon, "Geometry of the human common carotid artery. a vessel cast study of 86 specimens," *Pathology - Research and Practice*, vol. 198, no. 8, pp. 543–551, 2002.
- [105] Q. Long, X. Y. Xu, M. W. Collins, M. Bourne, and T. M. Griffith, "Magnetic resonance image processing and structured grid generation of a human abdominal bifurcation," *Computer Methods and Programs in Biomedicine*, vol. 56, no. 3, p. 249, 1998.
- [106] P. J. Yim, J. J. Cebra, R. Mullick, H. B. Marcos, and P. L. Choyke, "Vessel surface reconstruction with a tubular deformable model," *Medical Imaging, IEEE Transactions on*, vol. 20, no. 12, pp. 1411–1421, 2001.
- [107] J. Seong, B. B. Lieber, and A. K. Wakhloo, "Morphological age-dependent development of the human carotid bifurcation," *Journal of Biomechanics*, vol. 38, no. 3, pp. 453–465, 2005.
- [108] F. P. Glor, B. Ariff, A. D. Hughes, P. R. Verdonck, D. C. Barratt, A. D. Augst, S. A. M. Thom, and X. Y. Xu, "Influence of head position on carotid hemodynamics in young adults," *Am J Physiol Heart Circ Physiol*, vol. 287, no. 4, pp. H1670–1681, 2004.
- [109] M. H. Friedman and L. W. Ehrlich, "Numerical simulation of aortic bifurcation flows: The effect of flow divider curvature," *Journal of Biomechanics*, vol. 17, no. 12, pp. 881–883, 1984.
- [110] X. He and D. N. Ku, "Flow in T-bifurcations: Effect of the sharpness of the flow divider," *Biorheology*, vol. 32, no. 4, pp. 447–458, 1995.
- [111] S. Z. Zhao, X. Y. Xu, A. D. Hughes, S. A. Thom, A. V. Stanton, B. Ariff, and Q. Long, "Blood flow and vessel mechanics in a physiologically realistic model of a human carotid arterial bifurcation," *Journal of Biomechanics*, vol. 33, no. 8, pp. 975–984, 2000.
- [112] J. R. Womersley, "Oscillatory flow in arteries: the constrained elastic tube as a model of arterial flow and pulse transmission," *Physics in Medicine and Biology*, no. 2, p. 178, 1957.
- [113] L. Topoleski, N. Salunke, J. Humphrey, and W. Mergner, "Composition- and history-dependent radial compressive behavior of human atherosclerotic plaque," *Journal of Biomedical Materials Research*, vol. 35, no. 1, pp. 117–127, 1997.
- [114] O. Bonnefous, M. Montaudon, J. Sananes, and E. Denis, "Non-invasive echographic techniques for arterial wall characterisation," in *IEEE Ultrasonics symposium*, pp. 1059–1064, 1996.

- [115] T. Anderson and W. McDicken, "Measurement of tissue motion," *Proceedings of the Institution of Mechanical Engineers, Part H: Journal of Engineering in Medicine*, vol. 213, pp. 181–191, 1999.
- [116] R. H. Selzer, W. J. Mack, P. L. Lee, H. Kwong-Fu, and H. N. Hodis, "Improved common carotid elasticity and intima-media thickness measurements from computer analysis of sequential ultrasound frames," *Atherosclerosis*, vol. 154, no. 1, pp. 185–193, 2001.
- [117] A. R. Ahlgren, F. Hansen, B. Sonesson, and T. Lanne, "Stiffness and diameter of the common carotid artery and abdominal aorta in women," *Ultrasound in Medicine & Biology*, vol. 23, no. 7, pp. 983–988, 1997.
- [118] J. Meinders, P. Brands, J. Willigers, L. Kornet, and A. Hoeks, "Assessment of the spatial homogeneity of artery dimension parameters with high frame rate 2D B-mode," *Ultrasound in Medicine & Biology*, vol. 27, no. 6, pp. 785–794, 2001.
- [119] A. Schmidt-Trucksass, D. Grathwohl, A. Schmid, R. Boragk, C. Upmeier, J. Keul, and M. Huonker, "Assessment of carotid wall motion and stiffness with tissue Doppler imaging," *Ultrasound in Medicine & Biology*, vol. 24, no. 5, pp. 639–646, 1998.
- [120] P. R. Hoskins, "Review of the design and use of flow phantoms," in *Testing of Doppler Ultrasound Systems* (P. R. Hoskins, S. B. Sherriff, and J. A. Evans, eds.), pp. 12–291, Bristol: IPeM, 1994.
- [121] O. Bonnefous, "Arterial wall motion imaging: A new approach for vascular characterisation," *BMUS Bulletin*, vol. 8, no. 4, pp. 19–23, 2000.
- [122] C. P. Oates, "The Doppler shift & speed of sound in blood," *Ultrasound in Medicine & Biology*, vol. 15, no. 1, p. 75, 1989.
- [123] D. Bergel, "The static elastic properties of the arterial wall," *Journal of Physiology*, vol. 156, pp. 445–457, 1961.
- [124] O. Bonnefous, F. Luizy, and S. Kownator, "Arterial Wall Motion imaging: a new ultrasound approach to vascular characterization," *Medica Mundi*, vol. 44, no. 2, pp. 37–43, 2000.
- [125] K. V. Ramnarine, B. Kanber, and R. B. Panerai, "Assessing the performance of vessel wall tracking algorithms: the importance of the test phantom," *Journal of Physics: Conference Series*, vol. 1, pp. 199–204, 2004.
- [126] J. D. Gill, H. M. Ladak, D. A. Steinman, and A. Fenster, "Segmentation of ulcerated plaque: a semi-automatic method for tracking the progression of carotid atherosclerosis," in *Engineering in Medicine and Biology Society, 2000. Proceedings of the 22nd Annual International Conference of the IEEE*, vol. 1, pp. 669–672, 2000.
- [127] J. D. Gill, H. M. Ladak, D. A. Steinman, and A. Fenster, "Accuracy and variability assessment of a semiautomatic technique for segmentation of the carotid arteries from three-dimensional ultrasound images," *Medical Physics*, vol. 27, no. 6, pp. 1333–1342, 2000.

- [128] S. Tong, H. N. Cardinal, D. B. Downey, and A. Fenster, "Analysis of linear, area and volume distortion in 3D ultrasound imaging," *Ultrasound in Medicine & Biology*, vol. 24, no. 3, p. 355, 1998.